ROLE OF IONOSPHERIC CONDUCTANCE

IN MAGNETOSPHERE-IONOSPHERE COUPLING

By

Tapas Bhattacharya

RECOMMENDED:

Dr. William Bristow

Dr. Mark Conde

Dr. Dirk Lummerzheim

Dr. Chung-Sang Ng

Dr. Antonius Otto
Advisory Committee Chair

Dr. Curt Szuberla
Chair, Department of Physics

APPROVED:

Dr. Paul Layer
Dean, College of Natural Science and Mathematics

Dr. John Eichelberger
Dean of the Graduate School

5/15/14

Date

ROLE OF IONOSPHERIC CONDUCTANCE IN MAGNETOSPHERE-IONOSPHERE COUPLING

A

DISSERTATION

Presented to the Faculty

of the University of Alaska Fairbanks

in Partial Fulfillment of the Requirements

for the Degree of

DOCTOR OF PHILOSOPHY

By

Tapas Bhattacharya, M.S.

Fairbanks, Alaska

August 2014

Abstract

Magnetosphere-ionosphere (MI) coupling has been studied for a long time. However, not much work has been done on a systematic understanding of the relation between ionospheric Pedersen conductance, its effect on the evolution and modification of field-aligned currents (FACs), and the influence of conductance and FACs on the formation of parallel electric fields which cause particle precipitation. Though the roles of ionospheric conductance gradients for FACs and parallel electric field evolution are directly related, they are poorly understood. This dissertation advances the understanding of these areas and all results of this study are based on numerical simulations that employ a three-dimensional - two-fluid (ions and neutrals) simulation code.

The first part of this dissertation presents a systematic study of the magnetospheric and ionospheric influences on the evolution and modification of FACs with focus on the role of ionospheric Pedersen conductance and its gradients. FACs are typically generated in the magnetosphere and are carried into the ionosphere by Alfvén waves. During their reflection from the ionosphere these FACs are modified depending on the magnitude and distribution of ionospheric conductance. For conductance gradients along the polarization of the wave, strong Pedersen currents can be generated which in turn enhance the FAC as well.

The second part of this dissertation addresses the properties and evolution of parallel electric fields in an attempt to better understand the formation of discrete auroral arcs in response to the evolution of FACs for predetermined ionospheric conductance patterns. Frequently, auroral acceleration is believed to occur through U or V shaped potentials. Therefore, this part examines the properties of localized parallel electric fields in a uniform magnetic field. It is demonstrated that localized parallel electric fields generate magnetic flux in the absence of source of free energy.

It is also shown that parallel electric fields generated in a FAC in the presence of a (anomalous) resistivity represent a load and can provide physical explanation for the auroral acceleration geometry. The results demonstrate that such electric fields can be significantly enhanced by Alfvén wave reflection where both magnitude and gradients of the ionospheric conductance are important. The strongly enhanced parallel electric field is associated with magnetic reconnection and modifies the FAC system such that thin current layers (with curls and folds) are observed to be embedded in the large scale current system.

Table of Contents

List of Figures

List of Tables

Acknowledgements

I am taking this opportunity to express my sincere thanks to Antonius Otto, my thesis advisor. I find myself extremely lucky to have had this opportunity to work with him. He is not only a great scientiest - he is a wonderful person as well.

I would like to thank the other members of my thesis committee - Dirk Lummerzheim, Mark Conde, Bill Bristow and Chung-Sang Ng who have reviewed my thesis and have provided valuable suggestions and inputs time to time. They were exceptionally supportive and encouraging.

Many people have enriched me in my long academic journey. The person who made me love mathematics in my early school days is my uncle Mukul Chatterjee. Along with him I wish to thank two of my favorite teachers, Himadri Sekhar Mondal and Anil Kr. Saha.

I have found different graduate courses, here at UAF, extremely useful. I have learned a lot from R. Wackerbauer, D. E. Newman, A. Chowdhury, B. Watkins, E. Buelar and D. Sentman. I am thankful to Tom Logan for helping me learn the basics of high performence computing.

I am sincerely thankful to John D Craven - my MS thesis advisor. What I learned from him during my MS were useful during my PhD as well.

I would like to thank Mary and Robert Parsons, Barbara Day, Saundra Stevens and Jeanie Talbot. Mary and Robert tremendously helped me to adjust to life in Fairbanks - they will always remain my special friends. I thankfully acknowledge Barbara's contribution to my admission process at UAF. Saundra took trouble to complete the necessary paperwork. Jeanie made my TAship more enjoyable - she was very supportive in and outside the class hours.

Thanks to the members of the Graduate Office -L aura Bender, Juan Goula and Hope Bickmeyer and the members of the International Programs - Sue Wolfe, Carol Holz and Joanna Cruzan - who have extended tremendous support whenever I have approached them. I am also thankful to Judy Triplehorn, Flora Grabowska and Chisato Jimura of the GI library. Thanks to David Covey and Dolores Baker for their technical support.

I would also like to thank my fellow graduate students. It has been a pleasure sharing graduate school experience with all of them. Settling at UAF as well as Fairbanks would not have been so easy without them. It was fun sharing my office with Richard J Stevens, Eric Adamson, Xuanye Ma, Julia Pilchowski and Min-Shiu Hsieh. I greatly enjoyed our research related discussions with RJ and Xuanye.

I feel extremely thankful to have such wonderful parents like Tarasankar Bhattacharya and Snigdha Bhattacharya. I'm greatful to my elder brother Goutam Bhattacharya for providing crucial support during my academic endeavor. Completing this journey would have been impossible without the support of these three people. I remain thankful to all my family members and friends.

Finally, this page would be incomplete without mentioning my treasured friend Debasmita who made me complete this huge task overcoming many different obstacles in my path. There are many others to whom I am indebted but their names remain unmentioned here as that makes this list too long - almost endless.

Chapter 1
Introduction

The overall dynamics of magnetospheres is often determined by only two boundaries, which are an outer boundary - the magnetopause - to the solar wind, and an inner boundary - the ionosphere - to the neutral atmosphere. The ionospheric boundary is of major importance to the magnetosphere because a large amount of magnetospheric energy is dissipated in the ionosphere, convection in the magnetosphere is moderated through the ionosphere, and the ionosphere is a dominant source of heavy plasma that modifies magnetospheric dynamics, particularly during active periods of time. In addition, the coupling between the magnetosphere and the ionosphere is the cause for discrete auroral activity at high latitudes.

The main focus of this thesis is the exploration of the geophysical processes involving the electrodynamic coupling between the magnetosphere and the ionosphere using the method of numerical simulations. The particular objectives are the role of the ionospheric boundary and of magnetic field-aligned electric currents, which facilitate the coupling. In this coupling, the current systems, which are involved, are the Birkeland and the Pedersen current. Birkeland or the field-aligned currents (FACs) couple the auroral ionosphere and the outer magnetosphere [1]. Pedersen currents close the FACs in the ionosphere. Therefore, the study of the coupled field-aligned and Pedersen currents are critical in understanding the magnetosphere-ionosphere (MI) coupling processes. It is also believed and there is much evidence that localized electric fields parallel to the magnetic field above the auroral ionosphere plays a crucial role in the coupling processes. So the basic physical effects associated with and required for localized parallel electric fields are also studied.

The three basic elements that are combined in this research are the locally uniform or nonuniform low-frequency Alfvénic perturbations imposed by the magnetosphere, a uniform or nonuniform Pedersen conductance in the ionosphere, and the generation of an electric field, parallel to the magnetic field in the magnetosphere. Nonuniform Alfvénic perturbations carry FACs and interact with the electric field and with the ionospheric Pedersen conductance and this interaction is the objective of the presented thesis.

The next sections provide an introduction to physics of the magnetosphere, the ionosphere, the coupling of these two regions, and an extended motivation for this research. This chapter is concluded with an outline of the contents of different chapters of this thesis.

1.1 The magnetosphere

The presence of matter beyond the ionosphere was first known as a result of discovering *whistler* waves by the physicist Barkhausen [2]. He showed that the whistler mode of waves is initiated

by the audio frequency electromagnetic disturbances caused by lightning discharges. These disturbances travel between the two hemispheres propagating along the geomagnetic field lines. Thomas Gold was first to introduce the term *magnetosphere* [3] in 1959. He had proposed this name "for the region above the ionosphere in which the magnetic field of the Earth has a dominant control over the motions of gas and fast charged particles." The new name replaced the term *geomagnetic cavity* introduced earlier by Chapmann and Ferraro. For a general definition of the magnetosphere, Vasyliunas [4] considered "a central object: a distinct well-defined body held together (in most cases) by its own gravity. It is immersed in a tenuous external medium, assumed to be sufficiently ionized that it behaves as a plasma. The magnetosphere is then the region of space around the object within which the object's magnetic field has a dominant influence on the dynamics of the local medium."

So, for a magnetosphere to be present, the central object must have a magnetic field. There are many sources, above and below the Earth's surface, which are responsible for the generation of the geomagnetic field [5]. These include the geomagnetic dynamo, crustal magnetization, the ionospheric dynamo, the ring current, the magnetopause current, the tail current, field-aligned currents, and auroral, or convective, electrojets. Among them, the geomagnetic dynamo is the most important as in its absence the other sources would not exist. Moreover, the effects of the other sources are limited to certain areas of the magnetosphere. To a first approximation, the geomagnetic field is considered to be dipolar with a magnetic moment $\approx 7.95 \times 10^{22}\ Am^{-2}$ [5]. This results in a variation from 90° to 56° of angle between the direction of the dipole axis and the direction of solar wind flow. This fact plays a strong role in the interactions between the solar wind and the Earth's magnetic field [6].

The cavity-like shape of the (Earth's) magnetosphere is the result of the interactions between the Earth's magnetic field and the solar wind plasma (e.g. [7, 6]). On the dayside, the Earth's magnetic field is compressed by the pressure of the solar wind flow and on the other side the magnetic field-lines are pulled along to produce a tail, many hundreds of Earth radii ($R_E \approx 6.4 \times 10^6\ m$) long. Figure 1.1 illustrates the schematic view of the configuration of magnetic field lines inside the magnetosphere and of the plasma flow outside. This figure also shows the different regions and components in and around the magnetosphere of the Earth. The magnetopause is the outer boundary for the magnetosphere, separating it from the shocked solar wind. The location of the magnetopause is determined basically by the conditions of pressure balance. The total pressure (i.e. the magnetic pressure plus the plasma pressure) on both sides of the discontinuity must be the same [4]. A typical value for the stand-off distance of the magnetopause on the dayside (i.e. the nose of the magnetosphere) from the Earth's center is $\approx 10R_E$ [6].

The bow shock is an important feature outside the magnetosphere where the supersonic solar wind

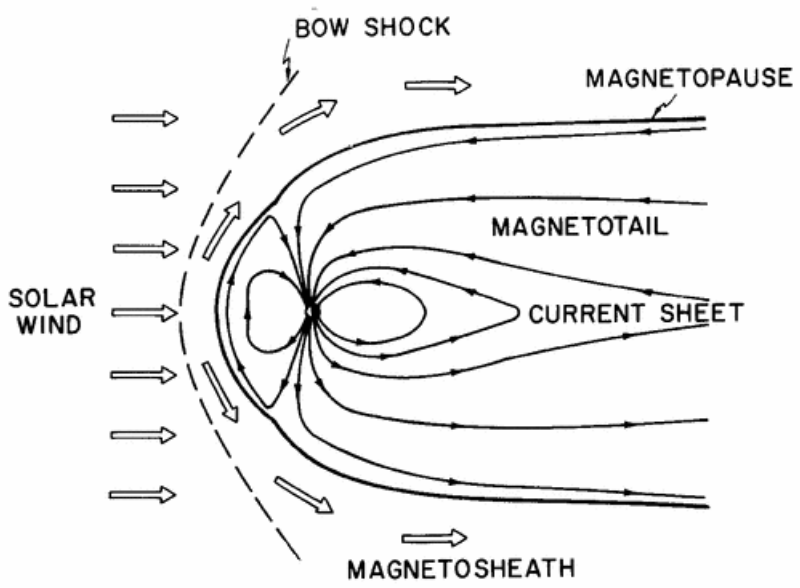

Figure 1.1: Schematic view of the magnetosphere. This diagram illustrates the configuration of magnetic field lines (solid lines with arrows) inside the magnetosphere and of the plasma flow (open arrows) outside, viewed in the noon-midnight meridian plane. (Taken from Vasyliunas, 1983 [8])

speed is slowed down to subsonic speed. It is located 2 to $3R_E$ from the magnetopause, in the upstream direction [9]. The solar wind passes through the bow shock, slows down, and flows mostly around the magnetosphere that acts as an obstacle in its path. In general, only a very minor fraction of the solar wind penetrates the magnetopause. The magnetosheath is the region between the bow shock and the magnetopause. Here the solar wind plasma is deflected and slows down converting its kinetic energy into thermal energy in this region. Due to the heating by the bow shock the temperature of the plasma in this region is 5 to 10 times the temperature of the solar wind [9].

Though the magnetosphere, in general, is considered mostly closed, it is not totally shielded from the solar wind plasma. Particularly when the interplanetary magnetic field (IMF) has a southward component, considerable reconnection of the IMF and the geomagnetic field may take place to produce a magnetically *open magnetosphere*. For northward IMF, reconnection is possible at high latitudes at the magnetopause. Therefore, the magnetopause is not impermeable to the magnetic field and as a consequence it does not remain impermeable to the plasma [4]. The reconnection rate and hence the amount of open flux of the magnetosphere is larger for southward orientation of the IMF. Here, 'open flux' implies the perpendicular magnetic flux that is not closed within the magnetosphere. In fact, it is also believed, based on the satellite data, that "the magnetosphere is

open permanently" (e.g. [10]). Consequences of the different degree of openness are the variation of the size of the auroral oval and strength of auroral precipitation.
The magnetic field lines of the magnetosphere are continued to the interior of the Earth and thus involve the ionosphere as well. So, for any problem of magnetospheric plasma flow the interaction between the magnetosphere and the ionosphere should be considered.
The region of the space surrounding the Earth between the neutral atmosphere and the magnetosphere is called the ionosphere. A description of this region, along with a discussion regarding their characteristics, is given in the next subsection (1.2).

1.2 The ionosphere

The part of the upper atmosphere where the amount of ions and electrons are sufficient to affect the propagation of radio waves is defined as the ionosphere [11]. It is the interface between the neutral atmosphere and the fully ionized magnetosphere. Here the charged particles are created by the ionization of the neutral compounds of the atmosphere. The presence of a conducting layer in the atmosphere was predicted with the discovery that the radio signal propagation did not conform to the expected line-of-sight path. The reflective property of the ionosphere for the long wavelengths ($\geq 15\ m$) has great importance in long-range communications. Though the name 'ionosphere' was introduced first in 1920 and was formally defined in 1950 by a committee of the Institute of Radio Engineers, the existence of a conducting region of the atmosphere responsible for the observed variation of the Earth's magnetic field was speculated by the German mathematician Carl Friedrich Gauss in 1839 [12].

1.2.1 Ionospheric structure and parameters

The neutral atmosphere constitutes the reservoir of the particles for the ionosphere. In general, it is considered that the ionosphere is extended from about 60 km to about 1500 km. When electromagnetic waves, transmitted from the Earth's surface, advance through the ionosphere, they experience a gradual increase of number density (N) of charged particles. Much attention was paid to the effect of this variation at the early days of ionospheric exploration. Solar EUV (*extreme ultra-violet*) radiation and other processes ionize the neutral particles and a certain fraction of the gas remains ionized when ionization and recombination balance each other. Recombination is a process of capturing electrons by ions so that they become neutral.
The number density of neutrals as the source of ions and electrons decreases with increasing altitude. On the other hand, the intensity of radiation from the sun increases with increasing altitude. These two facts along with the recombination rate which depends on the concentrations of electrons, ions, and neutrals at the considered location specifies the altitude profile of the charged particles in the

ionosphere. As a net result, a layer is formed where the plasma density is the maximum. On either side of this layer, the concentration of the charged particles gradually decreases. The altitude of maximum density depends on the causes for the ionization and therefore its location differs between day and night and with the precipitation. In fact, the sun being the prime source of energy for the ionosphere, the ionospheric parameters vary diurnally, seasonally, and with the solar cycle.

In the dense atmosphere, below about 100 km, mean free paths are comparatively much smaller and the molecules collide frequently. Hence the turbulent motion dominates over the diffusive transport of the atmospheric constituents, mixing them evenly. In this part of the atmosphere the densities of the major constituents decrease at same exponential rate with altitude. Above around 110 km, diffusive transport dominates over turbulent transport. Here, with increasing altitude, particles are separated by larger distances and the collisions are rare. The constituents start to become separated under gravity resulting in a diffusive equilibrium as the diffusion of heat and momentum dampens the turbulent motions of the particles. The constituent molecular density decreases with altitude at different rates, faster for the heavier molecules (smaller scale height) and they are stratified according to their own molecular weight.

The force balance for each ion species can obtain an altitude profile of the distribution of different ion species. Here it is done in a simplified manner by studying the distribution of the neutral atmosphere. The fundamental equation for the hydrostatic equilibrium of a parcel of air in the atmosphere can be obtained from two equations. One is obtained from the balance of gravitational force and pressure gradient force and the other is the equation of state. Then a relation for pressure variation with altitude (z) becomes,

$$p = p_0 e^{\left(\frac{-z}{H}\right)} \tag{1.1}$$

where the symbols have their usual meanings. The scale height H is given by,

$$H = \frac{kT}{Mg} \tag{1.2}$$

where M, T, k, and g are, respectively, the mean molecular mass, the temperature, Boltzmann constant, and the acceleration due to gravity. The different ion species show a similar height dependence and hence stratification of ions is similar to that of the neutrals. Note, however, that an ambipolar electric field increases this scale height in the presence of hot electrons. Equation 1.2 shows that the scale height remains fixed if the temperature and mean molecular mass remain unaltered. This can explain the ionospheric ion composition and stratification of the different ion species at different altitudes (temperatures) because different ion species with different mean molecular mass have different scale heights at the same temperature [13]. With altitude, the mean molecular weight decreases monotonically with a dependence on the neutral temperature. Figure 1.2 illustrates a typical altitude profile of ion stratification. In this figure, altitude profiles for the

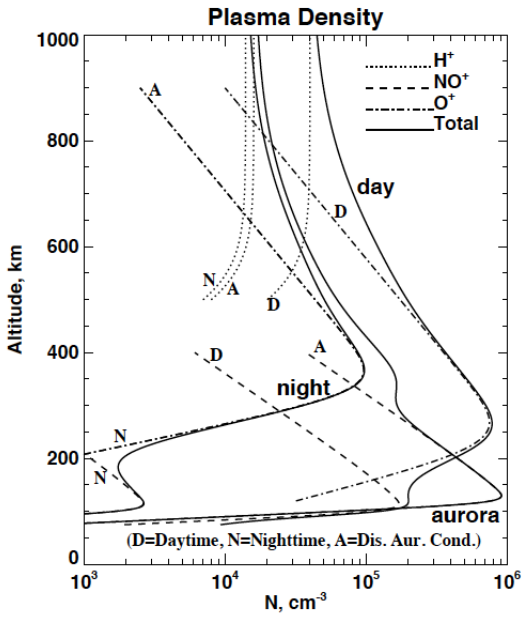

Figure 1.2: Altitude profiles of plasma number densities under three different conditions - at nighttime, at daytime and at the time of discrete auroral arcs. Solid lines show the total number density of the positive ions which is same as the number density of the electrons.

three major ions (H^+, NO^+, and O^+) are shown for three different typical conditions - at nighttime, daytime and at the time of discrete auroral precipitation. Electron density profile is also similar to that of the sum of the number densities of the ionized particles because these two densities are equal to maintain the total charge neutrality of the region and the solid lines represent the profiles for the electrons.

The lower ionosphere is vertically structured in three regions. With increasing altitude and increasing ion concentration they are termed as D, E, and F layers. At daytime, the F-layer is further divided into two layers, F_1 and F_2. These layers differ in their dominant constituents, concentration, sources of ionization, nature of variability, chemistry, and dynamics. A summary of the ionospheric structure is shown in Table 1.1 following Fälthhammar [2]. In this table, typical altitudes, electron densities, ion contents and dominant causes of ionization are summarized.

In the ionosphere one peak for the ionized particle density occurs at about 250 to 300 km as the rate of recombination is minimum in that region and another daytime smaller peak is formed at about 100 km.

Figure 1.3 shows the altitude profile of different neutral components for a medium value of the (exospheric) neutral-temperature ($T_{n,exo}$) ≈ 1044 K between 90 km and 600 km. Close attention needs to be paid to a several aspects in studying the dynamics of ionospheric plasma. The ionosphere is

Table 1.1: Structure of ionosphere: this table summarizes the typical altitudes, electron densities, ion contents and dominating causes of ionization at the different ionospheric layers [2].

Layers	D	E	F1	F2
Altitude (km)	$60-85$	$85-140$	$140-200$	$200-ca1500$
Nighttime electron density (cm^{-3})	$<10^2$	2×10^3	-	$2-5\times10^5$
Daytime electron density (cm^{-3})	10^3	$1-2\times10^5$	$2-5\times10^5$	$0.5-2\times10^6$
Ion species	NO^+, O_2^+	NO^+, O_2^+	NO^+, O_2^+, O^+	O^+, He^+
Cause of Ionization	Lyman-α ($1215\mathring{A}$)	Lyman-β ($1025\mathring{A}$) x-rays	UV	UV

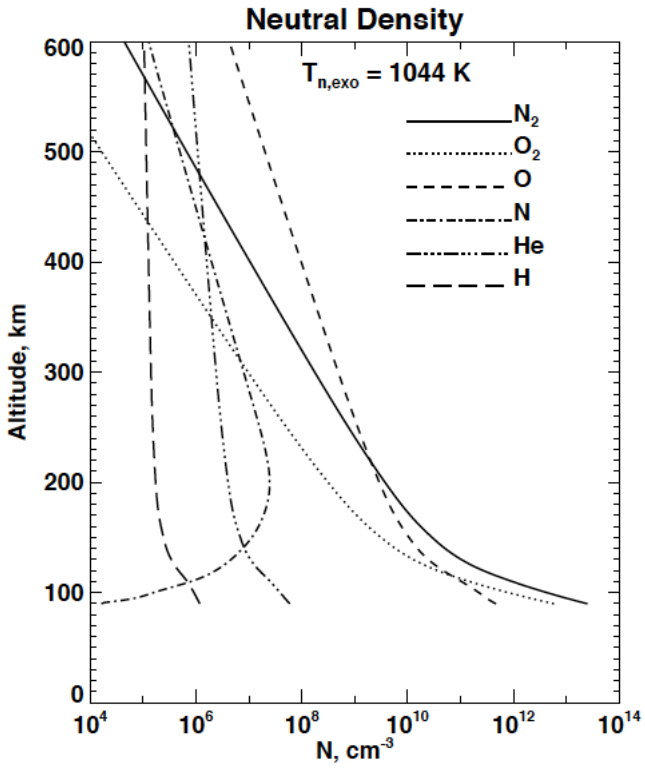

Figure 1.3: Altitude profiles of the neutral densities between 90 km and 600 km for (exospheric) neutral temperature, $T_{n,exo} = 1044\ K$

a partially ionized medium in which the neutrals are dominant and where a magnetic field persists. Charged particles are subject to (1) the gyro-motion around the magnetic field, (2) collisions with the neutrals, and (3) collisions among different kinds of charged particles. In addition to this, their motion is also controlled by the presence of an electric field. Correspondingly, the different ionospheric parameters are of importance. These are the gyro-frequency, collision frequencies between the different species, temperatures of the neutral and charged particles, neutral density, plasma density, plasma frequency etc.

The ionospheric temperature depends on the balance between the various heating and cooling processes in the ionosphere along with the characteristic temporal scales to relax to achieve this balance. In the last more than 60 years, rockets, satellites and ground-based remote sensing devices have been used to explore the upper atmosphere. The observations led to increasingly sophisticated thermospheric temperature models. These models show a sharp increase of the neutral temperature from some minimum value (190 $K \pm 25\ K$) at about 80 to 90 km [14]. This increase continues, typically, up to 300 km and then attains a constant value, the exospheric temperature, $T_{n,exo}$. Value of $T_{n,exo}$ depends on the solar EUV flux that depends, strongly, on the solar activity and its value can be as high as 1500 K. Here the medium is so rarified that even a small amount of energy input can influence the temperature greatly. Altitude profiles of neutral gas temperature (T_n) between $\approx 80\ km$ and 600 km are shown in Figure 1.4 for three typical values of $T_{n,exo}$ (883 K, 1044 K and 1305 K) as low, medium and high values, respectively.

The rates of collisions between the different species and the neutrals, determined by the collision frequencies (ν_{in}, ν_{en}) have strong role on the transfer of momentum and energy between the neutrals and the plasma. These quantities, along with the gyro-frequencies of the charged particles around the magnetic fields (ω_{ge}, ω_{gi}), determine important properties of the ionosphere such as conductivity and energy transfer between plasma and neutrals. The dependence of different collision and gyro frequencies on altitude is shown in Figure 1.5 in the altitude range $\approx 80\ km$ to 400 km for $T_{n,exo} = 1044\ K$. The properties of the ions and the electrons are significantly different in the region marked by the two horizontal dotted lines. The upper line shows the crossing of ω_{gi} and ν_{in} while the lower line shows the crossing of ω_{ge} and ν_{en}. In this height range the ion collision frequency is higher than the corresponding gyro frequency and therefore the ions are not magnetized. As a result, the ions, mostly drift along the direction of electric field. For the electrons, the situation is just opposite and therefore the magnetized electrons, in this part of the ionosphere, follow, largely, the $\mathbf{E} \times \mathbf{B}$ drift.

The gyro-frequency (ω_g) for a particle with charge q and mass m is qB/m which is much higher for electrons than for ions. Here, B is the strength of the magnetic field. The gyro-frequencies do not vary much with altitude because of the slow variation of the magnetic field. Conductivity, having

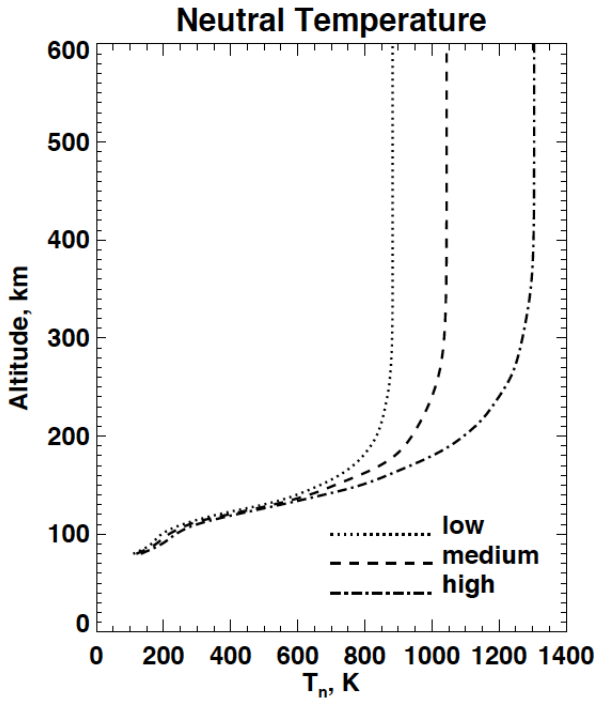

Figure 1.4: Examples of altitude profiles of neutral temperatures for three typical values of exospheric temperature ($T_{n,exo}$). These represent low (883 K), medium (1044 K) and high (1305 K) values of $T_{n,exo}$.

an important role in this research, is discussed separately in the next section.

1.2.1.1 Ionospheric Conductivity

Ionospheric conductivity plays a critical role in the study of the coupling between the ionosphere and the magnetosphere. In this research the influence of the magnitude and gradient of the height integrated Pedersen conductivity (i.e., the Pedersen conductance) is investigated.

In the absence of any magnetic field, the relation between the current density ($\mathbf{j}$) and the electric field ($\mathbf{E}$) can be expressed as

$$\mathbf{j} = \sigma \mathbf{E}, \tag{1.3}$$

where σ is the conductivity. In presence of an electric field, the charged particles move with uninterrupted acceleration $\left(= \frac{qE}{m}\right)$, if there are no collisions. Here, q and m are the charge and mass, respectively, of the particle. In collision-dominated ionosphere, collisions between the neutrals and the charged particles impede their motions. In the absence of a magnetic field, this motion can be expressed by $q_s \mathbf{E} = m_s \nu_{sn} (\mathbf{v}_s - \mathbf{v}_n)$ for species s particle. Thus the collision frequencies have an important role in the determination of conductivity. The current density, for the plasma,

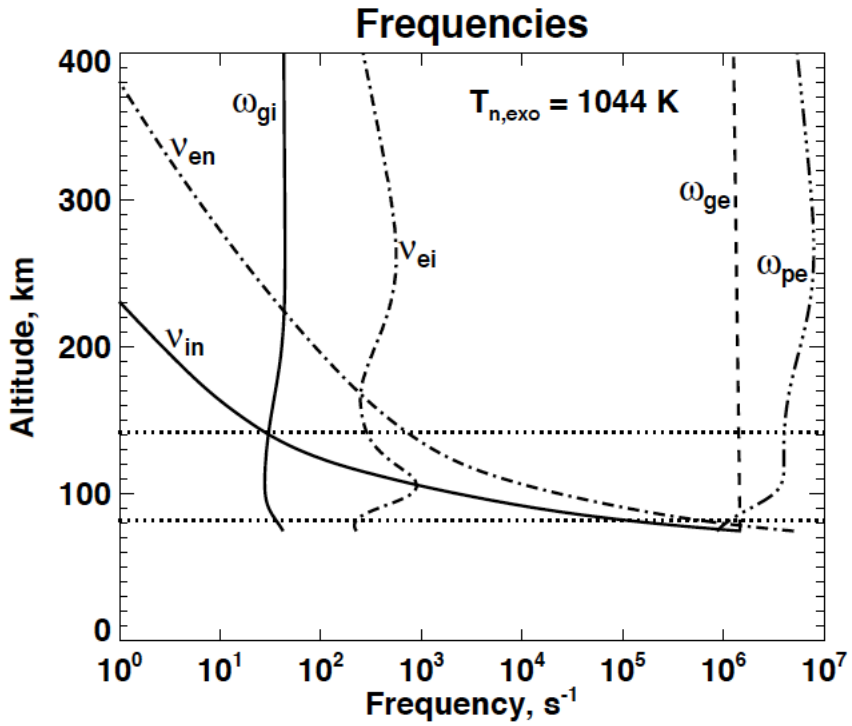

Figure 1.5: Altitude profiles of different ionospheric frequencies at $T_{n,exo} = 1044\ K$. Gyro-frequencies and collision frequencies are represented, respectively, by ω_g and ν, with appropriate subcripts.

can also be estimated from the mean (steady state) velocities of the charged particle components with respect to the neutrals. If $\mathbf{v}_i$ and $\mathbf{v}_e$ are the mean velocities of the ions and the electrons, respectively, then the current density is

$$\mathbf{j} = n_i \mathbf{v}_i q_i + n_e \mathbf{v}_e q_e = n(\mathbf{v}_i q_i + \mathbf{v}_e q_e). \tag{1.4}$$

Here, subscripts i and e are representing the similar quantities for the (positive) ions and electrons, respectively. This expression, in terms of collision frequencies (ν_{in} and ν_{en}) between the charged particles (ions and electrons) and neutrals, becomes

$$\mathbf{j} = ne^2 \left(\frac{1}{m_i \nu_{in}} + \frac{1}{m_e \nu_{en}} \right) \mathbf{E}, \tag{1.5}$$

where, $n \approx n_e \approx n_i$ to ensure the charge neutrality. Comparing Equations 1.3 and 1.5, it can be concluded that the expression for conductivity in absence of magnetic field becomes

$$\sigma = ne^2 \left(\frac{1}{m_i \nu_{in}} + \frac{1}{m_e \nu_{en}} \right). \tag{1.6}$$

The situation is different in the presence of a magnetic field ($\mathbf{B}$). The motion of the charged particles in presence of a magnetic field is not isotropic. Moving charges experience the magnetic

force ($= q\mathbf{v} \times \mathbf{B}$) in addition to the force from the electric field ($= q\mathbf{E}$). Since the magnetic force vanishes along the direction of the magnetic field, it is convenient to split the electric field into two components. One component ($\mathbf{E}_\parallel$) along the direction of magnetic field and the other ($\mathbf{E}_\perp$) perpendicular to the magnetic field. Then the relation between the current density and the electric field for the direction along the magnetic field can be expressed as

$$\mathbf{j}_\parallel = \sigma_0 \mathbf{E}_\parallel. \tag{1.7}$$

Here, σ_0, termed as *parallel conductivity*, is the conductivity parallel to the magnetic field when the flow of charged particles becomes anisotropic and it determines the current aligned along the geomagnetic field or the field-aligned current. As the magnetic force along this direction is zero, σ_0 is actually same as σ of Equation 1.6. The effects of $\mathbf{E}_\perp$ on the charged particles are different in collisionless and collision-dominated plasma. In case of collisionless plasma both electrons and ions move in the same direction, that is perpendicular to $\mathbf{E}_\perp$ and $\mathbf{B}$. With the increase of collisions, electrons and ions get decoupled and tend to move in different directions, depending on their magnetization, as explained for the plot of the altitude profiles of frequencies in Figure 1.5. The relative values of the four frequencies (ω_{gi}, ω_{ge}, ν_{in}, and ν_{en}) control the motion of the charged particles when both electric and magnetic fields are present.

In a typical situation, in a collision dominated partially ionized plasma, $\mathbf{j}_\perp$ consists of two components. One component is mostly contributed by the flow of the ions (Pedersen current) along the direction of $\mathbf{E}_\perp$ and the other component, dominated by the electrons (Hall current), along the direction of $-\mathbf{E} \times \mathbf{B}$. In a compact notation, the expression for current density can be written as

$$\mathbf{j} = \bar{\sigma} \cdot \mathbf{E}. \tag{1.8}$$

Here $\bar{\sigma}$, a second order conductivity tensor, is given by

$$\bar{\sigma} = \begin{pmatrix} \sigma_P & -\sigma_H & 0 \\ \sigma_H & \sigma_P & 0 \\ 0 & 0 & \sigma_0 \end{pmatrix} \tag{1.9}$$

assuming the magnetic field to be in the z-direction. In the above expression, σ_P, the *Pedersen conductivity* determines the Pedersen current and σ_H, the *Hall conductivity* governs the Hall current. The expressions for σ_0, σ_P and σ_H are [15]

$$\sigma_0 = \frac{ne^2}{m_e}\left(\frac{1}{\nu_{en}} + \frac{m_e}{m_i}\frac{1}{\nu_{in}}\right) \tag{1.10}$$

$$\sigma_P = \frac{ne^2}{m_e}\left(\frac{\nu_{en}}{\nu_{en}^2 + \omega_{ge}^2} + \frac{m_e}{m_i}\frac{\nu_{in}}{\nu_{in}^2 + \omega_{gi}^2}\right) \tag{1.11}$$

and

$$\sigma_H = -\frac{ne^2}{m_e}\left(\frac{\omega_{ge}}{\nu_{en}^2+\omega_{ge}^2}+\frac{m_e}{m_i}\frac{\omega_{gi}}{\nu_{in}^2+\omega_{gi}^2}\right). \tag{1.12}$$

Figure 1.6 shows the altitude profiles of three conductivities in the altitudes up to 350 km under three different conditions such as average daytime, nighttime and at the time of discrete auroral arcs.

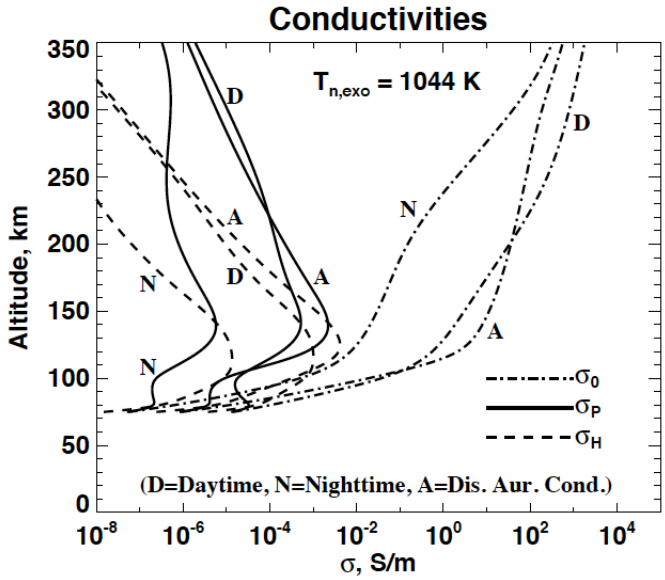

Figure 1.6: Altitude profiles of (ionospheric) *parallel*, *Pedersen*, and *Hall* conductivities.

Equation 1.8 can be expressed in a general form in terms of the different conductivities as

$$\begin{aligned}\mathbf{j} &= \mathbf{j}_\parallel + \mathbf{j}_\perp \\ &= \sigma_0\mathbf{E}_\parallel + [\sigma_P\mathbf{E}_\perp - \sigma_H(\mathbf{E}\times\mathbf{B})/B]\,.\end{aligned} \tag{1.13}$$

In the absence of a magnetic field, the values of ω_{ge} and ω_{gi} become zero and in that case the conductivity becomes isotropic with $\sigma_0 = \sigma_P$ and $\sigma_H = 0$. The different terms in the expressions for the three conductivities, excluding the mass of the individual charged particles, in general, vary greatly under different conditions, the most common being with respect to the altitude. The dependence of the three conductivities on the relative values of ω_g and ν are illustrated in Figure 1.7. In this figure, the three different conductivities, from the conductivity tensor, are plotted as a function of the ratio (ω_{ge}/ν_{en}) of the gyro-frequency to the collision frequency. For a lower value of ω_{ge}/ν_{en}, that is when the collisions are more frequent than the gyrations (e.g. weak magnetic field and more neutrals are present), $\sigma_P >> \sigma_H$ and electrons move in the direction of $\mathbf{E}_\perp$, strengthening the Pedersen current. For a higher values of ω_{ge}/ν_{en}, collisions are less frequent

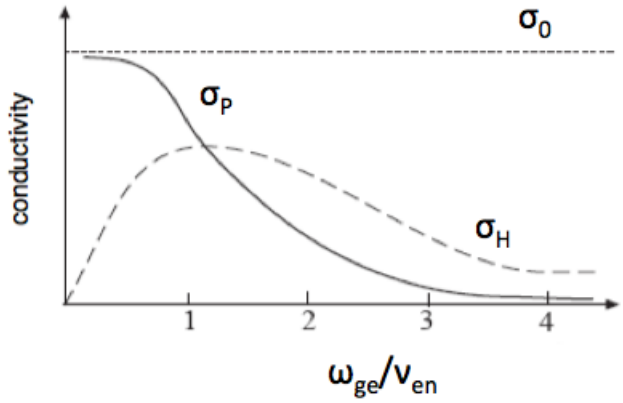

Figure 1.7: Plots showing the variation of different ionospheric conductivities with the ratio between gyro-to-collision frequency (ω_{ge}/ν_{en}) [15].

and the electrons perform, mostly, the $\mathbf{E} \times \mathbf{B}$ drift, supporting the Hall current. When the ratio is ≈ 1, the conductivity is highly anisotropic and both Hall and Pedersen conductivities are equally important.

Across the E-region, the magnetic field can be considered to be constant. Electrons with a very large value of gyro-frequency ($\sim 10^7\ s^{-1}$) basically, contribute to the Hall current. On the other hand, ions, have a low value of gyro-frequency ($\sim 10^2\ s^{-1}$), which is approximately equal to its collisional counterpart at about 125 km [15]. So, below this altitude, ions are forced to move along the direction of $E_\perp$, contributing to the production of Pedersen current.

In this research, the height integrated Pedersen conductivity or the Pedersen conductance is given importance over Hall conductance. FACs, which are of prime importance in this research, are typically closed by the Pedersen current. There are several physical explanations, but a simple one is the following. The $\mathbf{E} \times \mathbf{B}$ drift is equal to ionospheric convection $\mathbf{v}$. However this convection satisfies $\nabla \cdot \mathbf{v} = 0$ otherwise it would result in a compression of the ionospheric magnetic field. Since $\nabla \cdot \mathbf{v} = 0$, it follows that $\nabla \cdot \mathbf{j}_{Hall} = 0$ and there is no vertical (i.e. field-aligned) component to the Hall current. Therefore the Hall current closes in itself and only the Pederson current closes the FAC. It is noted that the simulation does not consider the Hall current which requires high spatial and temporal resolution, and which does not contribute to Joule heating and energy dissipation.

Much of the thesis uses conductance (Σ); i.e., the height integrated values for a conductivity ($\int \sigma \partial z$), because Alfvén wave reflection and convection is mostly determined by conductance for low frequency waves.

Cowling conductance

Cowling conductance (Σ_C) is an effective conductance in which the combination of Pedersen and Hall conductances play a role. The value of Σ_C can be very high at the low latitudes. The strong equatorial electro jet is explained by the formation of Cowling conductance [16].
Cowling conductance is easily understood in a slab geometry as shown in Figure 1.8. A rectangular

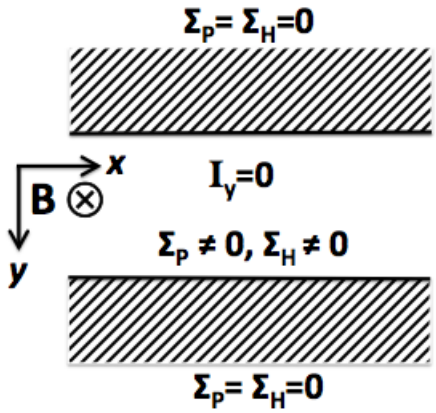

Figure 1.8: Illustration for Cowling conductance using the slab geometry. The conducting zone is bounded by nonconducting regions on both sides and the magnetic field is directed into the plane of the paper.

co-ordinate system (x, y, z) is considered such that the xy-plane coincides with the ground. As shown in this figure, a region with nonzero values of Pedersen and Hall conductances (Σ_P and Σ_H) is considered which is bounded on its two sides (along the y-direction) by nonconducting regions ($\Sigma_P = \Sigma_H = 0$) and the magnetic field is downward (i.e. into the plan of the paper). In this situation the steady state current equations are given by

$$I_x = \Sigma_P E_x + \Sigma_H E_y \tag{1.14}$$

and

$$I_y = \Sigma_H E_x - \Sigma_P E_y = 0. \tag{1.15}$$

Combining the above two equation one can obtain

$$\begin{aligned} I_x &= \left[\Sigma_P + \frac{\Sigma_H^2}{\Sigma_P}\right] E_x \\ &= \Sigma_C E_x \end{aligned} \tag{1.16}$$

where Σ_C is the Cowling conductance and is given by

$$\Sigma_C = \Sigma_P \left[1 + \frac{\Sigma_H^2}{\Sigma_P^2}\right]. \tag{1.17}$$

Hence, if $\Sigma_H > \Sigma_P$ then Cowling conductance, Σ_C, may generate a stronger current in the x-direction, that is in the direction of the Pedersen current. In this research, a geometry similar to what explains the Cowling conductance, is used to explain the generation of an effectively enhanced electric field that produces an enhanced Pedersen current, in the auroral ionosphere.

1.3 Magnetosphere-Ionosphere coupling

The magnetosphere-ionosphere coupling processes involve a wide range of spatial and temporal scales that include the small-scale discrete auroral arcs (a few 100 m) to the global scale plasma convection (a few thousand kilometers). Different models have been proposed to study MI-coupling processes of different scale sizes (e.g. [17, 18, 19, 20, 21, 22, 23, 24, 25, 26, 27, 28, 29, 30]). These models focus on various features of the plasma environment of the Earth such as Ohmic heating in filamentary aurora (e.g. [28]), global model for the F-region ionosphere (e.g. [22]), and substorm model using MI-coupling and tail reconnection (e.g. [24]).

The ionosphere in the auroral zone and the outer magnetosphere are coupled by means of FACs. Magnetic field-aligned electric field associated with these currents are now widely accepted to be responsible for the particle acceleration in the auroral zone [31]. It is well accepted that FACs are mostly generated as a result of stress at the outer magnetosphere developed by plasma convection that is perpendicular to the magnetic field. This stress then propagates in the form of Alfvén waves toward the ionosphere along the auroral field lines. Numerical modeling of MI-coupling by Alfvén waves is an useful means to demonstrate the propagation and evolution of FACs and the production of magnetic field perturbations [29].

Birkeland's proposal (in 1908) about the role of FAC in transferring solar wind energy into the upper atmosphere and the ionosphere was not given much importance for about 60 years. The evidence of FAC was first detected by a low altitude polar orbiting satellite 1963 38C as "transverse magnetic disturbances" [32, 33]. However, Cummings and Dessler were the first to identify a link between these magnetic disturbances and the FAC system [34]. Starting from that time, different experimenters worked in developing the morphology of FACs. Important contributions came from Iijima and Potemra [35, 36, 37], in a number of papers who used the magnetic data from the Triad satellite. In one of these papers [37], they demonstrated the patterns of the FAC system at the high latitudes, for the different levels of geomagnetic activity.

Different (electric) current systems exist in the plasma environment, surrounding the Earth. The examples are the magnetospheric boundary currents, the cross-tail current, the ring current, and the FACs. These currents are generated so that the force balance can be attained between the $\mathbf{j} \times \mathbf{B}$ force, and the force coming from the pressure gradient and inertia [38]. The role of FACs and associated Alfvén waves in MI-coupling is crucial for the transmission of electromagnetic energy

(in the form of Poynting flux) and transverse momentum (i.e. the magnetic tangential stress) from the hot (collisionless) magnetospheric plasma regime to cold dense (collision dominated) plasma of the ionosphere [39].

The auroral ionosphere acts as a partially conducting medium to the Alfvén waves associated with the FACs. In general, Alfvén waves are partially reflected by the ionosphere. The degree of reflection depends on the Pedersen conductance of the ionosphere. The reflection coefficient has a dependence on the wavelength of the incident wave and the coefficient can be high (i.e. close to 1) for very long wavelengths [40]. The reflection of Alfvén wave from the ionosphere has significant effects such as evolution and modification of FACs, to initiate, support, and enhance magnetic reconnection, and formation of parallel electric fields. In this research these effects of low frequency (long wavelength) Alfvén wave reflection are investigated.

The role of parallel electric fields in the gain of energy by the auroral electrons was suggested [41] by Hans Alfvén in 1958. Existence of electric field in a collisionless magnetospheric plasma was not acceptable at that time. This has gained recognition after different in situ observational evidence (e.g. [42]). In general, it was believed that there should not develop any electric field in the magnetosphere because the resistivity (according to the classical theory) in a collisionless plasma is nearly zero along a magnetic field line. After obtaining different evidence of its existence, various theories were proposed on the formation of parallel electric fields. Examples of different proposed causes or mechanisms for the formation of parallel electric fields are anomalous resistivity (e.g. [43]), electric double layer (e.g. [44]), solitary structures (e.g. [45]), magnetic mirror effects ([46]), etc. Relation between the parallel electric field and FAC was under speculation from the early days (e.g. [47]). The resistive term ($\eta \mathbf{j}$) in Ohm's law indicates that if the FAC density is large, this term may introduce parallel electric field. It was suggested that in collisionless magnetosphere, anomalous resistivity may provide the required resistivity ([48, 49]). Some researchers expressed a difference in opinion (e.g. [50]). According to them, anomalous resistivity is far too dissipative in presence of FACs.

Possible role of MI-coupling in auroral arc generation is an area of active research. Lyatsky and Hamza proposed three models for the MI-coupling feedback instability in an attempt to explain the formation of small-scale structures inside a wide arc [51]. Many scientists showed that the magnetospheric convection may be unstable and divided into convection streams (e.g. [52, 53, 54, 55]). Formation of discrete auroral arcs by MI-coupling is a part of this research too.

More detailed discussions on the Alfvén waves, their reflection form the ionosphere, FACs, parallel electric fields, and thin auroral arcs are presented in the respective pertinent chapters.

1.4 Motivation

The ionosphere-magnetosphere coupling makes the ionosphere a major supplier of plasma to the magnetosphere and is of significant importance in understanding different phenomena of space physics. There are many interesting and important issues in this regard. Some of them are: formation of discrete auroral arcs; formation of parallel electric field in the auroral magnetosphere; magnetic reconnection by the reflected Alfvén wave; formation of ion outflow associated with auroral structure; inverted V structure of the energy-latitude plot; precipitation of auroral electrons in a narrow belt around the polar cap; auroral U, V or S-shaped potential structure; acceleration of the current carrying (discharging) electrons on their way to the ionosphere.

The mechanisms involving many of the above mentioned phenomena are among the fundamental open questions of space physics. This research investigates such mechanisms involving FACs and parallel electric field with focus on the role of the ionospheric boundary conditions.

1.5 Outline of the thesis

The introduction to the magnetosphere, the ionosphere and different ionospheric parameters, MI-coupling including the FACs and parallel electric field and, the motivation for this research have been discussed in the present chapter (Chapter 1). This gives a general overview on the magnetosphere, ionospheric structure and different ionospheric parameters with emphasis on the ionospheric conductivity, and significance and different aspects of MI-coupling. Alfvénic perturbations from the magnetosphere are partially reflected by the ionosphere having a considerable Pedersen conductance which determines the Pederson currents and in turn modifies and generates FAC. Such FACs play a central role for the MI coupling on local and global scales. Particularly, FACs are important in relation to parallel electric fields, which in turn are expected to play an important role in the MI coupling. The relation between FACs, ionospheric conductance, and field-aligned electric fields is the central topic of this research. In order to address this topic this thesis is organized as follows.

Chapter 2 describes the basic methodology of this research. It contains two sections. The first section describes the basic numerical methods. This includes the discussions on the basic equations, their normalization, the method of discretization and the order of accuracy, description of the simulation domain and the general boundary conditions. The second section focuses on the implementation of the ionospheric boundary conditions to achieve a desired control on the reflection of magnetospheric Alfvén waves from the ionosphere. This section includes a discussion on Alfvén waves and related dispersion relations, reflection of Alfvén waves from the ionosphere, expressions for the reflection coefficient in terms of the ionospheric Pedersen conductance and the basic results about the reflection from a set uniform ionospheric boundary.

Chapter 3 studies magnetospheric and ionospheric influences on the distribution of FACs. Partic-

ularly, the focus of this chapter is the interaction between the Alfvénic (magnetic and velocity) perturbations from the magnetosphere with the ionosphere assuming different conditions for the Pedersen conductivity. It is demonstrated that a gradient of the Pedersen conductance, its orientation, and the magnitude of Pedersen conductance play a major role in the evolution of the FACs.
Chapter 4 investigates the basic physical effects associated with and required for a localized electric field, aligned with the geomagnetic field. First the presence of a localized (both 3D and 2D) parallel electric field that is not supported by any energy-source is examined. Then a 3D localized resistivity of fixed magnitude is introduced at magnetospheric heights at the location of magnetospheric FAC sheets. The effects and different aspects of the generated parallel electric fields are investigated. Magnetic reconnection is one of the important features illustrated in this investigation.
Chapter 5 uses a current dependent resistivity to demonstrate the formation of parallel electric field and its effects contrary to the use of a fixed-magnitude resistivity, in Chapter 4. This makes the introduced resistivity more realistic because the resistive region is not artificially fixed and can move depending on the evolution of the FAC density. Reconnection can be much stronger in this case compared to the case of fixed resistivity. The investigations are repeated for different magnitudes of uniform or nonuniform Pedersen conductance.
Chapter 6 summarizes the main and significant results of all the simulations. This chapter also includes an overall discussion, and future works.

Chapter 2
Methodology

Introduction

This chapter describes the basic methodology used in the conducted research and contains two sections. The first section (2.1) describes the basic numerical methods. Details on any other numerical approach, specific for some particular section in this thesis, are described in the respective sections of the investigation. The second section (2.2) describes the implementation of the basic boundary conditions for the lower (ionospheric) boundary. This implementation is common to most of the other parts of this research and hence placed in this chapter as a part of the discussion about the general methodology.

2.1 Basic Numerical Methods

This section discusses the basic equations and their different terms, which are significant and important for this research. Then it includes a short discussion on the normalization of the involved quantities. Normalized equations used in this research are described next. Following is a description of the numerical discretization method along with its order of accuracy, a description of the simulation domain and some details about the boundary conditions used for the simulations.

2.1.1 The Basic Equations

In these studies, I used a 3D-2fluid (ions and neutrals) model following Birk and Otto [56]. Note that this does not differentiate between different ion and neutral species. It rather uses an effective ion and neutral mass to account for mass, momentum, and energy density. The derivation of the basic equations from kinetic equations implies the constraints of conservation of mass, momentum and energy. The first basic equation is the continuity equation that determines the evolution of the number density of the fluid as it moves from one place to another. This equation, for both ions and neutrals, can be expressed as

$$\frac{\partial \rho}{\partial t} = -\nabla \cdot (\rho \mathbf{v}) + Q^c. \tag{2.1}$$

Here ρ and $\mathbf{v}$ are the mass density and the fluid velocity, respectively. Q^c denotes the source term of the continuity equation. The source term Q^c is $(\iota - \beta\rho)\rho$ for plasma and $-(\iota - \beta\rho)\rho$ for the neutrals where ι and β denote the ionization frequency and the recombination coefficient, respectively. In this case of interest these terms (Q^c, for the ions and the neutrals) are small enough to allow us to set them equal to zero.

The momentum equation for the plasma component of the fluids is

$$\frac{\partial \rho \mathbf{v}}{\partial t} + \nabla \cdot (\rho \mathbf{v}\mathbf{v}) = -\nabla p + \mathbf{j} \times \mathbf{B} + \rho \mathbf{g} + Q^c \mathbf{v} + Q^p \tag{2.2}$$

with Q^p as the momentum source term which describes friction between the plasma and neutral components. The first three terms on the right hand side represent, respectively, the force due to pressure gradient, the magnetic force, and the force of gravity. For simplicity I will assume the neutral material at rest ($v_n = 0$) but this condition is easily changed. The friction term applies to the bulk of the plasma but contributes also to the electric resistance of the ions because the bulk plasma velocity is defined by the sum of the moments of the different ion species [57]. In this equation p, $\mathbf{j}$, $\mathbf{B}$ and $\mathbf{g}$ are representing the fluid (thermal) pressure, the current density, the magnetic induction vector, and the acceleration due to the gravity, respectively. The momentum source terms, Q^p, for the plasma and the neutrals are $-\rho\nu_{in}(\mathbf{v}-\mathbf{v}_n)$ and $-\rho\nu_{in}(\mathbf{v}_n-\mathbf{v})$, respectively. Here $\mathbf{v}$ and $\mathbf{v}_n$ are the fluid velocity for the plasma and the neutrals, respectively, and ν_{in} is the frequency of collisions between the ions and the neutrals.

We next consider Ohm's law for plasma. In the most general form this law (e.g. [58]) can be expressed as

$$\mathbf{E} + \mathbf{v} \times \mathbf{B} = \eta\mathbf{j} - \frac{1}{ne}\nabla p_e + \frac{1}{ne}\mathbf{j} \times \mathbf{B} + \frac{m_e}{ne^2}\left[\frac{\partial \mathbf{j}}{\partial t} + \nabla \cdot (\mathbf{jv})\right]. \tag{2.3}$$

Here, η and p_e are, respectively, the resistivity and the electron-pressure. Among the other quantities n is the plasma number density and m_e is the mass of an electron. The four terms on the right hand side are, respectively, the resistive term, the electron pressure term, Hall term, and the electron inertia term. Often the less significant terms are dropped and the equation reduces to

$$\mathbf{E} + \mathbf{v} \times \mathbf{B} = \eta\mathbf{j}. \tag{2.4}$$

It should be noted here that for a collisionless plasma (ideal MHD), the resistivity η may be so small as to satisfy $\mathbf{E} + \mathbf{v} \times \mathbf{B} = 0$. This represents the 'frozen-in' condition for the plasma. Now the Equation (2.4) can be rearranged to

$$\mathbf{E} = -(\mathbf{v} \times \mathbf{B}) + \eta\mathbf{j}. \tag{2.5}$$

This expression for $\mathbf{E}$ can then be combined with the Maxwell's (induction) equation (Faraday's law)

$$\frac{\partial \mathbf{B}}{\partial t} = -\nabla \times \mathbf{E} \tag{2.6}$$

and the obtained equation is

$$\frac{\partial \mathbf{B}}{\partial t} = \nabla \times [(\mathbf{v} \times \mathbf{B}) - \eta\mathbf{j}]. \tag{2.7}$$

The relation between the current density ($\mathbf{j}$) and magnetic induction vector ($\mathbf{B}$) is expressed using the MHD form of another Maxwell's equation (Ampere's law)

$$\nabla \times \mathbf{B} = \mu_0\mathbf{j}. \tag{2.8}$$

The next equation that comes from energy conservation is

$$\frac{1}{\gamma-1}\left(\frac{\partial p}{\partial t}+\nabla\cdot p\mathbf{v}\right)=-p\nabla\cdot\mathbf{v}+\eta\mathbf{j}^2+Q^E. \tag{2.9}$$

where γ is the ratio between the two specific heats and Q^E represents the energy source terms and may include thermalization, energy exchanges due to momentum transfer by collisions and by ionization or recombination [56]. After the inclusion of significant source terms and some rearrangements this equation takes the form

$$\frac{\partial p}{\partial t}=-\mathbf{v}\cdot\nabla p-\gamma p\nabla\cdot\mathbf{v}+(\gamma-1)\left[2\eta\mathbf{j}^2-\frac{3\nu_{in}\rho}{m_i+m_n}(T_i-T_n)\right]. \tag{2.10}$$

Here T_i, T_n, m_i and m_n are the temperatures and masses for the ions and neutrals, respectively. The two terms inside the square bracket represent the energy from Ohmic heating and the heat flow due to the thermal contact between the two species. The fundamental constants, their symbols, and values used in this research are given in the following table.

Table 2.1: The fundamental constant quantities, their symbols and the values (used in this research).

Fundamental quantity	**Symbol**	**Value**
mass of electron	m_e	$9.1094\times10^{-31}\ kg$
mass of proton	m_i	$1.6726\times10^{-27}\ kg$
mass of O^+	m_{o+}	$2.66\times10^{-26}\ kg$
elementary charge	e	$1.6022\times10^{-19}\ C$
Ratio of specific heats	γ,γ_n	$5/3$
Permeability of vacuum	μ_0	$4\pi\times10^{-7}\ H\cdot m^{-1}$

2.1.2 Normalization

It is an advantage to normalize (or to scale) the basic equations before implementing the numerical simulations. The normalization directly reveals the magnitude and importance of different transport terms in the basic equation for the given application. Different quantities of the basic equations are measured in typical units. For example **B** is normalized to a typical magnetic field B_0, density ρ to a typical density ρ_0, length scale l to l_0 (for horizontal) or l_{z0} (for vertical) so that $B=B_0\hat{B}$, $\rho=\rho_0\hat{\rho}$, $l=l_0\hat{l}$ and $t=t_{A0}\hat{t}$ etc. Here $\hat{B}$, $\hat{\rho}$, $\hat{l}$ or $\hat{t}$ are the normalized quantities. The choice of the typical units depends on the physical system under investigation.

A few examples of normalization are discussed below:

Magnetic field: The guide field $\mathbf{B}=4\times10^{-5}\ T$ is normalized to $B_0=10^{-5}\ T$. So, in the simulation the guide field assumes a value of $\hat{B_0}=\frac{B}{B_0}=4$. The horizontal magnetic field uses

$B_{0h} = 10^{-7}\ T$ because horizontal perturbations are much smaller than the vertical field. This is justified if a similar ratio is assumed for the length scales in vertical and horizontal directions (see below for the normalization of length scales).

Alfvén speed: Alfvén speed (v_A) is normalized to a typical unit $v_{A0} = B_0(\mu_0\rho_0)^{-\frac{1}{2}}$. Now $\rho_0 = m_0 n_0 = 1.33 \times 10^{-15}\ kg \cdot m^{-3}$ where $m_0 = m_{o+}$, the mass of singly ionized oxygen atom and $n_0 = 5 \times 10^{10}\ m^{-3}$ is the typical value for the number density. So, $v_{A0} = 245\ km \cdot s^{-1}$. In all the cases the Alfvén speed (v_A) is assumed to be 4 (in normalized scale) which represents a physical value for $\hat{v_A} = 980\ km \cdot s^{-1}$.

Length scales (l_{z0} and l_0): In this research $l_{z0} = 100\ km$ for the vertical direction and $l_0 = 1\ km$ for the horizontal directions. The different normalization in the vertical and horizontal directions is motivated mostly by the large vertical (dipole) magnetic field compared to rather small horizontal magnetic perturbation. This is possible because the MI coupling is strongly Alfvénic. A somewhat similar approach is used in the so-called reduced MHD equations, which are applied for instance to the solar magnetic field because the plasma pressure is usually small compared to the magnetic pressure.

Velocities: For the vertical direction the velocities are measured in $v_{A0} = 245\ km \cdot s^{-1}$ where as for the horizontal direction the typical value for the normalization is $(l_0/l_{z0})v_{A0}$ i.e. $2.45\ km \cdot s^{-1}$. Note that the factor of 100 between the vertical and horizontal magnetic field normalization (and the velocities) and the same factor for the vertical and horizontal length scales cancel each other in the characteristic Alfvén times.

Time: The characteristic Alfvén time $t_{A0} = l_{z0}/v_{A0} \approx 0.41\ s$. So, a transit (Alfvén) time $\hat{t} = 30$ is physically same as 12.3 s. As mentioned above, the same result is obtained for the horizontal Alfvén time.

For an extensive list of the normalized quantities see Table 2.2. In the following discussion the hat ($\hat{}$) is omitted such that all quantities are assumed to be normalized.

2.1.3 The Normalized Equations

After normalizing the basic equations (described in the previous part) the dimensionless fluid equations are utilized for the simulation in this research and are given below. The quantities with subscript 'n' are linked with the neutrals where as the quantities without any subscript are for the plasma.

$$\frac{\partial \rho}{\partial t} = -\nabla \cdot \rho \mathbf{v} \tag{2.11}$$

$$\frac{\partial \rho_n}{\partial t} = -\nabla \cdot \rho_n \mathbf{v}_n \tag{2.12}$$

$$\frac{\partial \rho \mathbf{v}}{\partial t} = -\nabla \cdot (\rho \mathbf{v}\mathbf{v}) - \frac{1}{2}\nabla p + \mathbf{j} \times \mathbf{B} - \rho \nu_{in} (\mathbf{v} - \mathbf{v}_n) \tag{2.13}$$

Table 2.2: Physical quantities and their typical units for normalization

Physical quantity	**Typical unit**
B (magnetic field)	B_0
ρ (mass density)	$\rho_0 = m_i n_0$
l (length scale)	l_0
v (velocity)	$v_{A0} = \frac{B_0}{\sqrt{\mu_0 \rho_0}}$ (Alfvén speed)
t (time)	$t_{A0} = \frac{l_0}{v_{A0}}$ (Alfvén time)
p (pressure)	$p_0 = \frac{B_0^2}{2\mu_0}$
E (electric field)	$E_0 = v_{A0} B_0$
j (current density)	$j_0 = \frac{B_0}{\mu_0 l_0?}$
η (resistivity)	η_0
Σ_P (Pedersen conductance)	$\Sigma_{P0} = (v_{A0}\mu_0)^{-1}$

$$\frac{\partial \rho_n \mathbf{v}_n}{\partial t} = -\nabla \cdot (\rho_n \mathbf{v}_n \mathbf{v}_n) - \frac{1}{2}\nabla p_n + \rho_n \mathbf{g} - \rho_n \nu_{in} (\mathbf{v}_n - \mathbf{v}) \tag{2.14}$$

$$\frac{\partial \mathbf{B}}{\partial t} = \nabla \times (\mathbf{v} \times \mathbf{B} - \eta \mathbf{j}) \tag{2.15}$$

$$\frac{\partial p}{\partial t} = -\mathbf{v} \cdot \nabla p - \gamma p \nabla \cdot \mathbf{v} + (\gamma - 1) \left[2\eta \mathbf{j}^2 - \frac{3\nu_{in}\rho}{m_i + m_n} (T_i - T_n) \right] \tag{2.16}$$

$$\frac{\partial p_n}{\partial t} = -\mathbf{v}_n \cdot \nabla p_n - \gamma_n p_n \nabla \cdot \mathbf{v}_n + (\gamma_n - 1) \frac{3\nu_{in}\rho_n}{m_i + m_n} (T_i - T_n) \tag{2.17}$$

$$\mathbf{j} = \nabla \times \mathbf{B} \tag{2.18}$$

For the presented results the neutral velocity is assumed to be 0, and the momentum source terms in Equation (2.14) and the heating/cooling terms in Equation (2.17) are small for the considered time scales. Therefore the neutral equation reduces to the force balance equation in Equation (2.14).

2.1.4 Numerical Discretization and Accuracy

The system under consideration is described by a set of differential equations. Different discretization schemes are suitable for the integrations of different differential equations. The DuFort-Frankel method for discretization that introduces centered differences in both time and space is a relevant

scheme for this research is discussed here. This discretization method is very similar to the Leapfrog scheme. For the discussion of this scheme the following simple linear differential equation, containing both convection and diffusion terms, is considered.

$$\frac{\partial f}{\partial t} + u\frac{\partial f}{\partial x} - D\frac{\partial^2 f}{\partial x^2} = 0. \tag{2.19}$$

Here the constants u and D in this advection-diffusion equation are the velocity and the diffusion coefficient, respectively. The Richardson scheme uses a three-point centered difference formula and produces a second order contribution to the truncation error. The DuFort-Frankel scheme is a simple modification of the Richardson scheme. Using the Richardson discretization method for space and time (about f_i^n) we can obtain

$$\frac{\partial f}{\partial t} = \frac{f_i^{n+1} - f_i^{n-1}}{2\Delta t}, \tag{2.20}$$

$$\frac{\partial f}{\partial x} = \frac{f_{i+1}^{n} - f_{i-1}^{n}}{2\Delta x} \tag{2.21}$$

and

$$\frac{\partial^2 f}{\partial x^2} = \frac{f_{i+1}^{n} - 2f_i^n + f_{i-1}^{n}}{\Delta x^2}. \tag{2.22}$$

The subscript i and the superscript n represent the steps in space and time, respectively and are indicated as the grid-points in the Figure 2.1. So, in discretized form, the Equation (2.19) becomes

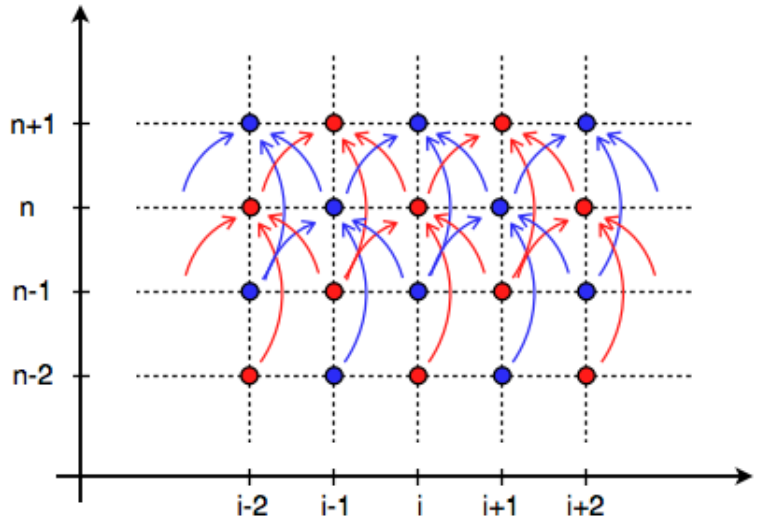

Figure 2.1: Schematic diagram for the DuFort-Frankel scheme. The horizontal axis denotes the spatial steps and the vertical axis denotes the temporal steps.

$$\frac{f_i^{n+1} - f_i^{n-1}}{2\Delta t} + \frac{u(f_{i+1}^n - f_{i-1}^n)}{2\Delta x} - \frac{D\left(f_{i+1}^n - 2f_i^n + f_{i-1}^n\right)}{\Delta x^2} = 0. \tag{2.23}$$

This scheme is of $O(\Delta t^2, \Delta x^2)$ but is unconditionally unstable according to the Von Neumann stability analysis when $D\frac{\Delta t}{\Delta x^2} > 0$ [59]. The unstable behavior of the Richardson scheme can be avoided through a slight modification of the diffusion term, using the DuFort-Frankel scheme which replaces the term $2f_i^n$ in Equation (2.23) with $\left(f_i^{n+1} + f_i^{n-1}\right)$. Thus the equation becomes

$$\frac{f_i^{n+1} - f_i^{n-1}}{2\Delta t} + \frac{u(f_{i+1}^n - f_{i-1}^n)}{2\Delta x} - \frac{D\left(f_{i+1}^n - (f_i^{n+1} + f_i^{n-1}) + f_{i-1}^n\right)}{\Delta x^2} = 0. \tag{2.24}$$

A rearrangement of Equation (2.24) yields

$$f_i^{n+1} - f_i^{n-1} + c\left(f_{i+1}^n - f_{i-1}^n\right) - 2s\left(f_{i+1}^n - f_i^{n+1} - f_i^{n-1} + f_{i-1}^n\right) = 0 \tag{2.25}$$

where c is callled the *Courant number* and is given by

$$c = u\frac{\Delta t}{\Delta x} \tag{2.26}$$

and

$$s = D\frac{\Delta t}{\Delta x^2}. \tag{2.27}$$

The required algorithm from the above equation is

$$f_i^{n+1} = \left(\frac{2s - c}{1 + 2s}\right) f_{i+1}^n + \left(\frac{1 - 2s}{1 + 2s}\right) f_i^{n-1} + \left(\frac{2s + c}{1 + 2s}\right) f_{i-1}^n. \tag{2.28}$$

The update of the value of f_i^{n+1} comes from the values of f_i^{n-1}, f_{i+1}^n and f_{i-1}^n. In Figure 2.1 all these values are represented by blue grid-points. Actually, in this chess-board like pattern of the scheme, information is transported to a blue grid-point from the blue grid-points only and to a red grid-point only from the red grid-points as is evident from Figure 2.1. So, the information at the grid-points represented by two different colors are mutually independent. This implies that the differently colored grid points (meaning odd or even numbered grid-points) can transport information independently and hence they are decoupled in the differencing process. This can lead to strong oscillations on the grid scale when the even and odd grids are combined. However, the actual simulation makes use of the decoupling and employs only one half of the points (either blue or red) thereby saving memory and simulation time.

The discretization is inevitable to solve the differential equations numerically but at the same time this introduces errors in the solutions. The solution to f_i^n is different from the corresponding exact solution. The accuracy of a numerical scheme can be estimated by using the Taylor expansions of the variable about a center location [at grid point (x_i, t_n)]. Expanding all the terms (f_i^{n+1},

f_i^{n-1}, f_{i+1}^n and f_{i-1}^n) in Equation (2.25) and combining them with Equations (2.26) and (2.27) to determine the truncation error yields

$$\frac{\partial f}{\partial t} + u\frac{\partial f}{\partial x} - D\frac{\partial^2 f}{\partial x^2} + \Delta x^2 \left[\frac{u}{6}\left(1-c^2\right)\frac{\partial^3 f}{\partial x^3} + D\left(s^2 - \frac{1}{12}\right)\frac{\partial^4 f}{\partial x^4}\right] + O(\Delta t^4, \Delta x^4) = 0. \qquad (2.29)$$

Hence the leading term of the truncation error is $\Delta x^2 \left[\frac{u}{6}\left(1-c^2\right)\frac{\partial^3 f}{\partial x^3} + D\left(s^2 - \frac{1}{12}\right)\frac{\partial^4 f}{\partial x^4}\right]$ and the scheme is second order accurate with the truncation error of order $O(\Delta x^2)$.
It is important to note that the choice of the time-step (Δt) is restricted by the requirement of numerical stability. According to the CFL (Courant-Friedrichs-Lewy) condition [60] the leapfrog scheme is stable if $c \leq 1$. In order to avoid numerical instability we should maintain

$$\Delta t < \left|\frac{\Delta x}{u}\right|_{min}. \qquad (2.30)$$

The physical meaning of this condition is that any information should not travel more than one spatial step Δx in one time-step Δt [59]. The update of all dependent variables occurs only from next neighbors such that a violation of this stability condition implies an unphysical update of the variable at the respective grid point.

It should be noted that Equation (2.19) reduces to a purely advection or a purely diffusion equation with $u = 0$ or $D = 0$, respectively. In that case we are left with the truncation error as $\frac{u\Delta x^2}{6}\left(1-c^2\right)\frac{\partial^3 f}{\partial x^3}$ or $D\Delta x^2\left(s^2 - \frac{1}{12}\right)\frac{\partial^4 f}{\partial x^4}$, respectively. Thus for an advection equation the truncation error contains only the odd spatial derivatives and the scheme is then free of any numerical diffusion term (i.e. there are no even spatial derivatives). Though this is apparently a positive aspect for this scheme, it actually creates a problem. Every numerical solution of a nonlinear hyperbolic partial differential equation creates two types of errors which can be characterized as numerical dispersion and diffusion [61]. In absence of any damping of such errors through numerical diffusion, the dispersion can generate strong grid oscillations because different wavelengths propagate differently for the part of the spectrum that is close to the grid scale. In order to compensate for the absence of numerical diffusion, small dissipation terms are introduced that effectively damp oscillations close to the numerical grid scale in the code. These dissipation terms are implemented similar to the diffusion term shown in Equation 2.24, however, they are applied if there is oscillation in the local grid points. Hence the inclusion of the diffusion term through the DuFort-Frankel scheme becomes useful to balance the issues with numerical dispersion.

On the other hand if it is a purely diffusion equation then the leading term of the truncation error is $D\Delta x^2\left(s^2 - \frac{1}{12}\right)\frac{\partial^4 f}{\partial x^4}$ and the scheme is second order accurate with the truncation error of order $O(\Delta x^2)$. Then the scheme is unconditionally stable, but not without a price. A consistency analysis shows that the method could be inconsistent. Consistency requires that the truncation

error tends to zero when the time and spatial steps tend to zero [62]. The local truncation error E_i^n is given by

$$E_i^n = \frac{\Delta t^2}{6}\frac{\partial^3 f}{\partial t^3} - D\frac{\Delta x^2}{12}\frac{\partial^4 f}{\partial x^4} + \left(\frac{\Delta t}{\Delta x}\right)^2 \frac{\partial^2 f}{\partial t^2} + ... \tag{2.31}$$

$$= O\left(\Delta t^2, \Delta x^2, \left(\frac{\Delta t}{\Delta x}\right)^2\right). \tag{2.32}$$

It is clear that if Δt and Δx are in linear relation that is if $\Delta t = k\Delta x$ with k as a constant then the truncation error does not vanish for $\Delta t \to 0$ and $\Delta x \to 0$. For achieving consistency we need a time-step $\Delta t = k\Delta x^{1+\varepsilon}$ with $\varepsilon > 0$. Moreover accuracy requirement pose an additional constraint on ε and it can be established that ε is constrained to be in the interval $1/2 \leq \varepsilon \leq 1$ [63].

2.1.5 Simulation Region and Boundary Conditions

The space above the auroral region is explored in this research where the geomagnetic field is close to being vertical (Figure 2.2). The base of the simulation box is assumed to be at an altitude of nearly 100 km. For most considered applications the horizontal extent of the box is within a tens of kms (but can easily be extended to hundreds of km with a corresponding reduction of the horizontal resolution) and the vertical extent is of the order of a few R_e (Earth-radii). So, the simulation region includes both the ionosphere and the magnetosphere. The simulations use a cartesian coordinate system in which x and y are taken perpendicular to the magnetic field. Furthermore, z is along the unperturbed magnetic field $\mathbf{B}$ and in the northern hemisphere $\mathbf{B}$ is uniform and in the negative z-direction in the entire simulation domain. This local simulation ignores the dipolar magnetic field configuration including the divergence (or convergence) of $\mathbf{B}$. Although the chosen magnetic field ignores the dipolar convergence, many aspects such as the formation and evolution of current along the magnetic field, propagation of Alfvén wave and its interaction with a partially conducting ionosphere, can be examined. It is noted that due to this limitation, a few aspects such as the mirror force, variation of Alfvén speed along the magnetic field lines, cannot be included in this study.
The model has the capability to choose between uniform and non-uniform grid distributions. For the different cases, the grid in the y-direction is uniformly spaced at values between 0.1 km and 0.4 km. The x direction uses a uniform or nonuniform grid as specified in the respective applications. The grid distribution in the z-direction is non-uniform and the best resolution in this direction is $\approx$ 20 km in the lower ionosphere. The smoothly varying non-uniform grid spacing is generated using the following equation:

$$z(i_z) = w + a_1 sin(\beta w) + a_2 sin(2\beta w) \tag{2.33}$$

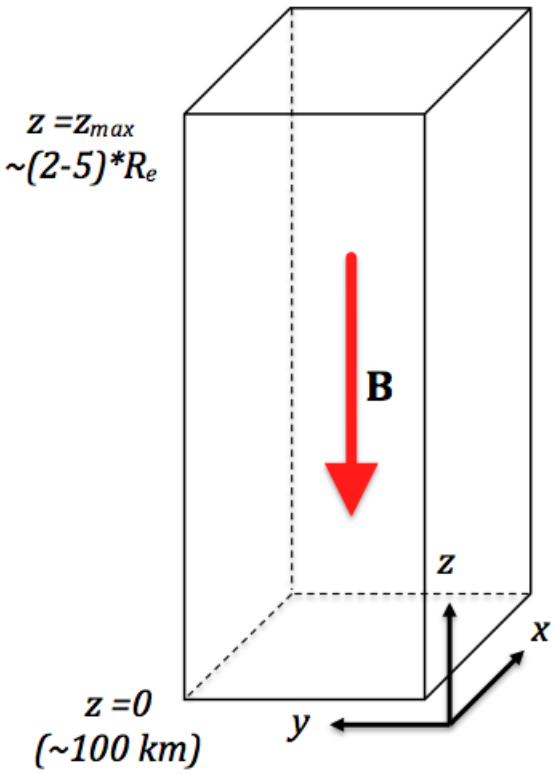

Figure 2.2: Illustration of the simulation domain. The orientations of the coordinate axes, the locations of the lower and upper boundaries and the geomagnetic field are shown.

where, i_z represents the index of a particular grid point. $w = w(i_z) = k_z * (i_z - 2)$ with $k_z = (z_{max} - z_{min})/(n_z - 3)$. Here n_z is the total number of grid points in the z-direction and $\beta = \pi/(z_{max} - z_{min})$. a_1 and a_2 are two constants selected in such a way that the grid spacing varies smoothly in a manner as shown in Figure 2.3. For this plot, typical values of z_{max} and n_z are assumed to be 120 and 303, respectively, but these are not same for all the simulations. Here the slope of the curve $\frac{dz}{di_z}$ increases with increasing grid-index i_z which implies that the resolution in this direction is highest (smallest Δz) at the lower end of the simulation box (for the smallest value of i_z).

Boundary conditions are implemented through a mathematical boundary (single layer of grid points) immediately outside the physical simulation domain. In the horizontal directions the actual physical boundary of the system (ionosphere or magnetosphere) is far from the edge of the simulation box. When appropriate, periodic boundary conditions are used for the x and y-directions. This allows any disturbance to propagate freely through the simulation region. Boundary conditions for the z-direction are case-specific and will be discussed in the appropriate places. Along the

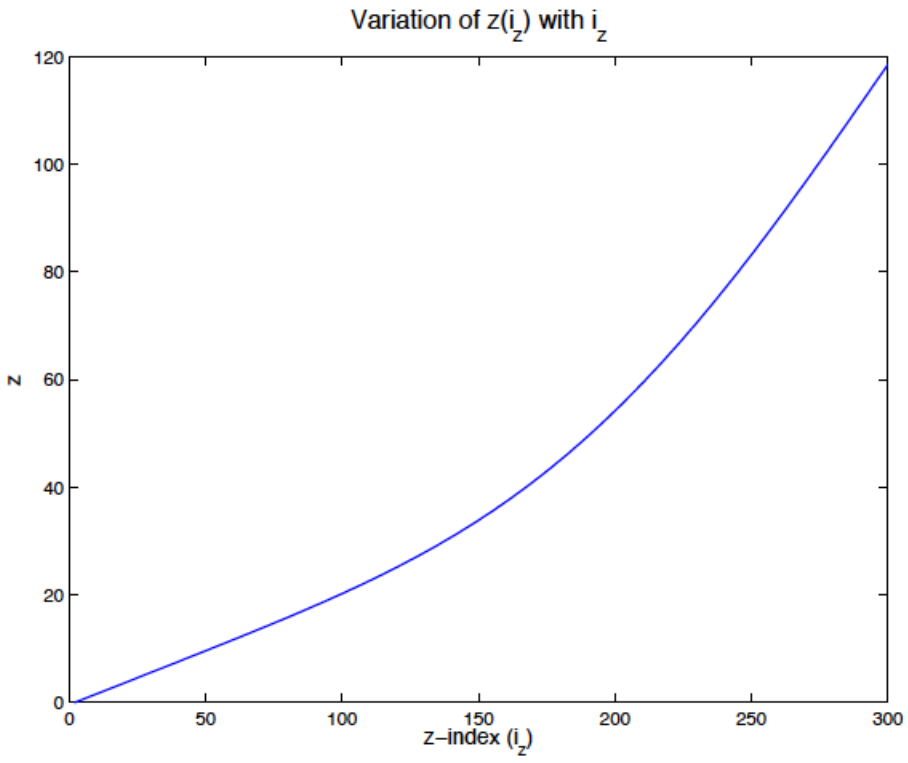

Figure 2.3: An example of non-uniform distribution of grid-points. This figure shows the distribution of the grid-points in the z-direction.

y-direction, the boundary conditions are periodic. Along the x-direction, the boundary conditions are symmetric for the tangential components (of the magnetic field and velocity) where as they are anti-symmetric for their normal components.

Density and resistivity in the simulation domain

The density of the neutrals and the plasma and, the resistivity are important for this study. The neutral density (ρ_n) decreases exponentially with the height (z) from a fixed value ρ_{n0} (at the lower boundary) up to a certain height following the relation

$$\rho_n = \rho_{n0} e^{-\alpha g z} \tag{2.34}$$

with α as a scaling factor. Though this height may not be the same for all the cases, a typical value for it is $z \approx 10$ (in normalized units). Above this height, the neutral density is assumed to remain constant at this minimum value. The plasma density (ρ) is assumed to be constant in the entire range of the simulation domain. ρ is much smaller than ρ_{n0} but is larger than the minimum value of ρ_n.

The resistivity (η) in the simulation domain is contributed by three different terms, in general, and is given by

$$\eta = \eta_{io} + \eta_{bg} + \eta_{loc}. \tag{2.35}$$

Here η_{io} depends on the local neutral density (ρ_n) and therefore is a height dependent term up to a certain height. It is the dominant contribution to the ionospheric resistivity. η_{bg} contributes a low value background resistivity of constant magnitude. η_{loc} is the spatially varying component of the resistivity that reflects the effect of anomalous collisions, for instance in presence of very high current density and may or may not be present in the equation. The expression for η_{io} is given by

$$\eta_{io} = \eta_0 \left(\frac{\rho_n}{\rho_{n0}} \right)^2. \tag{2.36}$$

As ρ_n decreases in the upward direction, η_{io} also decreases rapidly with height from η_0 at the ionospheric boundary and becomes negligible beyond a certain height in the ionosphere. At those heights η_{bg} which is much smaller than η_0 becomes dominant. So, η_{bg}, practically represents a very small magnetospheric resistivity. The third term of the Equation 2.35 is used to introduce a location dependent resistivity, if necessary.

2.2 Alfvén Wave and its Reflection from the Ionosphere

This section outlines the methodology to implement wave reflection from the ionosphere by controlling the ionospheric conductance as a boundary condition of the simulation. The discovery and past experiments on the Alfvén wave are first discussed in an introductory part. This is followed by a discussion on the dispersion properties of Alfvén waves. The numerical methods to achieve the desired control of the reflection from the ionosphere are described next and the section concludes with some basic results and a summary.

2.2.1 Alfvén Waves

The concept of magnetohydrodynamic (MHD) waves was introduced by Hannes Alfvén more than 70 years ago. This landmark discovery along with some other works earned him the Noble prize in 1970. In 1942, in his famous letter to Nature [64], he described "The Existence of Electromagnetic-Hydrodynamic Waves" in an attempt to explain sunspots and sunspot cycles. He stated that if a conducting liquid is placed in a magnetic field, the motion of the liquid develops an (induced) electro-motive force (E.M.F.) that in turn produces electric currents, and in the presence of a magnetic field, these currents apply mechanical forces to produce changes in the state of motion of the liquid. In fact, this induced current produces change in the magnetic field itself. This is basically the fundamental concept behind MHD. According to Hannes Alfvén, "Thus a kind of combined

electromagnetic-hydrodynamic wave is produced which, so far as I know, has as yet attracted no attention." This was the starting point of a whole new branch of physics - magnetohydrodynamics, in which hydrodynamics and electromagnetism merge. At that point of time it was not possible to verify this fact experimentally. But by the end of the 1950s the technical capabilities to produce high-temperature plasmas on Earth made it possible to confirm the existence of MHD waves. Experimenters such as Allen et al. (1959) [65], Jephcott (1959) [66], Wilcox et al. (1960) [67] etc. used different methods to prove the existence of magnetohydrodynamic waves. Magnetohydrodynamic waves are low frequency waves (frequency $<$ ion gyrofrequency) associated with the ions in a plasma [9] [68]. It is accepted that, for the study of many phenomena in space physics, it is necessary to understand the interactions between the MHD waves of magnetospheric origin and the ionosphere [69] [40].

Among the different modes (transverse, longitudinal) of MHD waves, Alfvén waves are the simplest one. The propagation of Alfvén waves is commonly compared with the propagation of transverse vibration in a string under tension. These are the transverse electromagnetic waves and propagate parallel to the ambient magnetic field. One of the dominant processes in magnetosphere-ionosphere coupling is the propagation of Alfvén waves. Magnetic perturbations may result from temporal change of convection in the magnetosphere. After their generation, these perturbations travel downward in the form of Alfvén waves carrying the change in perpendicular velocity (and the corresponding electric fields). Finally the waves interact with the ionosphere, which behaves on large scales as a conducting shell surrounding the Earth. For a horizontal extent of a few tens of kilometers ($\sim$ the horizontal dimensions of the simulation domain) we approximate the ionosphere to be a flat partially conducting plane. The reflection of the Alfvén waves from the ionosphere is important because the reflected wave (after being superposed with the incident waves) can markedly modify the pattern of the electric field carried with the incident waves [70]. In this research, the ionosphere is located at the lower boundary of the simulation domain. Depending on the conductivity of the ionosphere the waves are reflected fully, partially or not at all - with higher reflection for higher conductivity. Lessard and Knudsen[40] pointed out that the reflection coefficient is typically small if the wavelength of the wave is much smaller compared to the dimension of the ionosphere. They had explored the reflection of Alfvén waves for different ionospheric density profiles and got similar results for all the profiles. However, for long wavelengths, the reflection coefficient can be close to 1 depending on the value of ion-neutral collision frequency (ν_{in}). The focus of this work is on long wavelength (low frequency) Alfvén waves to examine reflection and field-aligned current (FAC) formation. This requires to control the lower (ionospheric) boundary conditions such that any desired amount of reflection of the Alfvén waves reaching the ionosphere may be observed.

2.2.2 The Dispersion Relation for the Alfvén Wave

To derive the dispersion relation for the Alfvén wave propagating along the magnetic field, "0" and "1" are used as the subscripts to represent the equilibrium quantities and the perturbations, respectively. The unperturbed magnetic field and the propagation vector are

$$\mathbf{B}_0 = -B_0\mathbf{e}_z \quad \text{and} \quad \mathbf{k} = k\mathbf{e}_z.$$

The velocity and magnetic field perturbations are

$$\mathbf{v}_1 = -\delta v_y\mathbf{e}_y \quad \text{and} \quad \mathbf{B}_1 = \delta B_y\mathbf{e}_y.$$

The linearized momentum equation (2.2) and the induction equation [combining equations (2.7) and (2.8)] can be written as

$$\frac{\partial\rho\mathbf{v}_1}{\partial t} = \frac{1}{\mu_0}(\nabla\times\mathbf{B}_1)\times\mathbf{B}_0 - \rho\nu_{in}\mathbf{v}_1$$

and

$$\frac{\partial\mathbf{B}_1}{\partial t} = \nabla\times(\mathbf{v}_1\times\mathbf{B}_0) - \nabla\times(\frac{\eta}{\mu_0}\nabla\times\mathbf{B}_1).$$

After substituting wave perturbations we can obtain

$$i\omega\rho\delta v_y = -ik\delta B_y\frac{B_0}{\mu_0} + \nu_{in}\rho\delta v_y$$

and

$$-i\omega\delta B_y = ik\delta v_y B_0 - \frac{\eta}{\mu_0}k^2\delta B_y.$$

Let us consider the terms of relative dominance at different altitudes.

When resistive interaction is dominant: For the magnetospheric altitudes where the ion-neutral collisions are insignificant, that is, for $\nu_{in} = 0$ and $\eta \neq 0$, the above two equations yield

$$\omega\left(\omega + ik^2\frac{\eta}{\mu_0}\right) = k^2v_A^2.$$

Here, $\frac{B_0}{\sqrt{\mu_0\rho}}$ is replaced by v_A, the Alfvén speed. So, in this case the dispersion relation becomes

$$\omega = -ik^2\frac{\eta}{2\mu_0} \pm \sqrt{k^2v_A^2 - k^4\frac{\eta^2}{4\mu_0^2}}. \tag{2.37}$$

This relation shows that the waves can propagate only when $kv_A > \frac{k^2\eta}{2\mu_0}$. It may be noted here that $\frac{\mu_0}{k^2\eta}$ is the resistive diffusion time for the wavelength, λ $(= 2\pi/k)$. Thus the condition for the Alfvénic propagation at the magnetospheric altitudes is that the wavelength must be big enough such that the diffusion time for its wavelength is longer than the period of the wave.

When ion-neutral collision is dominant: At the altitudes close to the ionosphere, ion-neutral collision term is dominant. Taking $\nu_{in} \neq 0$ and $\eta = 0$, we can obtain

$$\omega\left(\omega + i\nu_{in}\right) = k^2 v_A^2$$

and the corresponding dispersion relation is

$$\omega = -i\frac{\nu_{in}}{2} \pm \sqrt{k^2 v_A^2 - \frac{\nu_{in}^2}{4}}. \tag{2.38}$$

This relation shows that the wave can propagate for $k > \frac{\nu_{in}}{2v_A}$ that is when the wavelength $\lambda < \frac{4\pi v_A}{\nu_{in}}$.

So, it is seen that the resistive dispersion relation demonstrates that the short wavelengths are largely dissipated by the finite resistivity before they can actually be reflected which is consistent with the finding of low reflection coefficient by Knudsen [69]. The dissipation relation implies strong dissipation for $\lambda < \frac{\pi\eta}{\mu_0 v_A}$. Here it should be noted that $\frac{1}{\mu_0 v_A}$ is the Alfvénic impedance. In contrast, the ion-neutral friction shows that all waves are damped by the friction but the long-wavelength waves with $\lambda > \frac{4\pi v_A}{\nu_{in}}$ stop propagating such that they are partially reflected.

2.2.3 Numerical Methods

The basic equations are discussed in chapter-2. For this part of the research I try to generate Alfvén waves at the magnetospheric region. For this purpose, uniform magnetic perturbations are introduced near the upper part of the simulation domain at the initial stage of the simulation. The magnetic perturbation has the form:

$$\delta B_y = \frac{\delta B_{y0}}{2}\left[1 + tanh\left(\frac{z - 0.8 z_{max}}{2}\right)\right] \tag{2.39}$$

and the associated velocity perturbation, consistent for the generation of Alfvén waves, is

$$\delta v_y = -\frac{v_A}{B_0}\delta B_y \tag{2.40}$$

where v_A is the Alfvén speed. So, initially these perturbations are present at the top 20% of the simulation domain. The amplitude of the magnetic perturbation becomes δB_{y0}, which is much smaller ($\approx$ 1%) compared to the magnitude of the guide field B_0 where the guide field $B_z\mathbf{e}_z = -B_0\mathbf{e}_z$. These perturbations travel in the downward z-direction in the form of fixed amplitude, long (infinite) wavelength Alfvén waves (see Figure 2.4). As a first step we need to formulate boundary conditions that reflect typical ionospheric conditions so that we can get the desired amount of reflection of such Alfvén waves after being incident on the ionosphere.

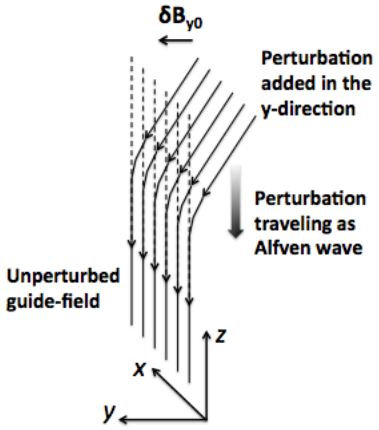

Figure 2.4: Magnetic perturbations propagating in the form of long-wavelength Alfvén waves. Here δB_{y0} is the amplitude of the magnetic field perturbation.

2.2.3.1 Alfvén wave reflection at the ionospheric boundary

To formulate partially reflective boundary conditions for low frequency Alfvén waves, I assume an infinitely long wave ($\lambda \to \infty$). Here the quantities under consideration are independent of the spatial variables x and y. So, assuming z (vertical) to be the only independent spatial variable and taking the perturbations $\delta B = \delta B_y \mathbf{e}_y$ and $\delta v = \delta v_y \mathbf{e}_y$, - the momentum equation and Ohm's law become:

$$\frac{\partial \rho \delta v_y}{\partial t} = -\frac{\partial}{\partial z}(\rho \delta v_z v_y - B_z \delta B_y) - \rho \nu_{in} v_y \tag{2.41}$$

and

$$\frac{\partial \delta B_y}{\partial t} = -(\nabla \times \mathbf{E})_y = \frac{\partial}{\partial z}(\delta v_y B_z - v_z \delta B_y - \eta j_x). \tag{2.42}$$

Here, the magnetic field is $\mathbf{B} = [0, \delta B_y, B_z]$ and for the steady state without any vertical flow the velocity is $\mathbf{v} = [0, \delta v_y, 0]$. With the simplification $\eta j_x = 0$ we obtain

$$\frac{\partial \delta B_y}{\partial z} = \frac{\nu_{in} \rho}{B_z^2} \delta v_y B_z \tag{2.43}$$

and

$$\frac{\partial \delta v_y}{\partial z} = 0. \tag{2.44}$$

The Equation (2.44) implies that the velocity perturbations $\delta v_y = constant$ and so it is independent of the altitude. This is the condition required for a steady state and is consistent with the relation $\nabla \times \mathbf{E} = 0$. Equation (2.43) is equivalent to Ohm's law for the Pedersen current density at the ionosphere because it can be expressed in the form of the x-component of Ohm's law as

$$j_x = \sigma E_x \tag{2.45}$$

with

$$j_x = -\frac{\partial \delta B_y}{\partial z} \tag{2.46}$$

and

$$E_x = -\delta v_y B_z \tag{2.47}$$

such that the ionospheric Pedersen conductivity, σ, is given by

$$\sigma = \frac{\nu_{in}\rho}{B_z^2}. \tag{2.48}$$

The relation in Equation (2.46) can also be obtained from the Ampere's law which is

$$\mathbf{j} = \nabla \times \mathbf{B}. \tag{2.49}$$

Combining Equation (2.45), Equation (2.46) and Equation (2.47),

$$j_x = -\frac{\partial \delta B_y}{\partial z} = -\sigma \delta v_y B_z$$

or,

$$\partial \delta B_y = -j_x \partial z = -\sigma(\delta v_y B_z)\partial z.$$

After integrating the above equation over the entire altitude of the simulation domain and considering the Equation (2.47) we have,

$$\Delta B_y = -I_{P,x} = \Sigma_P(\delta v_y B_z) = -\Sigma_P E_x \tag{2.50}$$

where, $I_{P,x}$ is the height integrated Pedersen current density or the Pedersen current, and is given by

$$I_{P,x} = \int j_x \partial z$$

and Σ_P is the height integrated Pedersen conductivity or the Pedersen conductance, and is given by

$$\Sigma_P = \int \sigma \partial z.$$

So, the Equation (2.50) gives the x-component of a relation that satisfies,

$$\mathbf{I}_P = \Sigma_P \mathbf{E} \tag{2.51}$$

which is Ohm's law for the Pedersen current at the lower ionosphere. The ionosphere is a conducting layer above which the plasma density is lower and is relatively nonconducting along the xy-plane and below which there is no plasma. So, this can be considered as a conducting sheet with a thickness much lower than the wavelength of the incident Alfvén waves. In this situation it is appropriate to treat the ionosphere as a partially conducting surface having a Pedersen conductance, Σ_P [70].

2.2.3.2 Pedersen current and the reflection coefficient

Let $B_i(=\delta B_y)$ be the incident magnetic field perturbation traveling in the downward direction and B_r be the magnetic perturbation of the upward reflected wave (see Figure 2.5). Correspondingly the velocity perturbations are $v_i = -B_i\frac{v_A}{B_0}$ and $v_r = B_r\frac{v_A}{B_0}$. Here the sign changes due to the change of direction of the propagation vector ($\mathbf{k}$) after reflection. In Figure 2.5 the times are given by t_0,

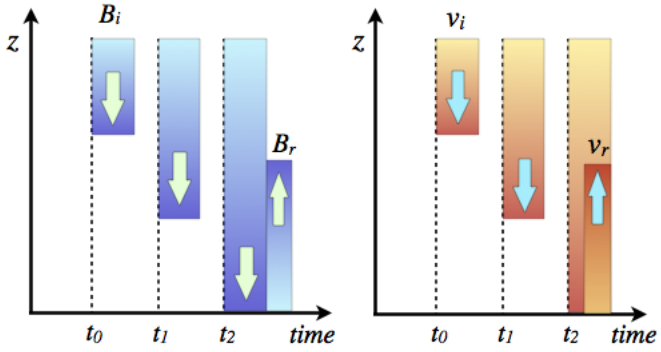

Figure 2.5: Schematic view of the reflection of Alfvénic perturbations. Illustration of the reflection of the magnetic (left) and the velocity (right) perturbations traveling in the form of Alfvén waves. Important to note that the the reflected velocity perturbation has a different sign from its incident counter part.

t_1 and t_2 with $t_0 < t_1 < t_2$. Here t_1 depicts a time before reflection and t_2 is a time when reflection has already taken place. After the reflection the incident (incoming) and reflected (outgoing) waves superpose. As the sign remains unchanged for the magnetic perturbations, after the superposition the magnetic perturbation is enhanced in magnitude where as the superposed value of the velocity perturbation is diminished due to the sign change. In this example (Figure 2.5) the ionosphere has a reflection coefficient $\left(r = \frac{B_r}{B_i}\right)$ of 0.63. After reflection the total magnetic perturbation is given by

$$(B_i + B_r) = (v_i + v_r)B_z\Sigma_P = -I_{P,x} = -\Sigma_P E$$

following Equation (2.50). The substitution for v_i and v_r yields

$$(B_i + B_r) = (-B_i + B_r)\frac{v_A}{B_0}B_z\Sigma_P.$$

Remembering that $B_z = -B_0$ we obtain

$$(B_i + B_r) = (B_i - B_r)v_A\Sigma_P$$

or,

$$B_r(v_A\Sigma_P + 1) = B_i(v_A\Sigma_P - 1).$$

From this we can derive an expression for the reflection coefficient:

$$r = \frac{B_r}{B_i} = \frac{v_A \Sigma_P - 1}{v_A \Sigma_P + 1} \tag{2.52}$$

or,

$$r = \frac{\Sigma_P - \frac{1}{v_A}}{\Sigma_P + \frac{1}{v_A}}. \tag{2.53}$$

So for a fixed value of the Alfvén speed (v_A) the reflection coefficient (r) should be determined by the Pedersen conductance (Σ_P) only. This kind of expression for the reflection coefficient was first derived by Manfred Scholer (1970) [71] in an attempt to investigate the process of momentum exchange between the artificially generated ion-clouds and the ambient magnetospheric plasma.
It may be noted that in the above derivations, involving the Pedersen conductance and the reflection coefficient, normalized equations are used where as the standard SI system is followed in the discussion on the dispersion relations for the Alfvén waves in Subsection 2.2.2 .

2.2.3.3 Setting the lower boundary at a desired level of reflecion

Though the Pedersen current is mostly confined to the physical boundary (that is at grid index $i_z = 2$) some currents also flow in next few grid levels. So, to evaluate the Pedersen current we need to include some of the lower grid levels. I explored this and verified that an acceptable height integrated value of $I_{P,x}$ can be obtained if grid-index up to $i_z = 9$ is taken. That means

$$I_{P,x} = -(\delta B_{y,i_z=9} - \delta B_{y,i_z=1}) = -\Sigma_P \delta v_{y,i_z=2} B_z. \tag{2.54}$$

To apply this I set the boundary condition for v_y such that

$$\delta v_{y,i_z=2} = \frac{\delta B_{y,i_z=9}}{\Sigma_P B_z} \tag{2.55}$$

with

$$\delta B_{y,i_z=1} = 0 \quad \text{and} \quad \delta v_{y,i_z=1} = \delta v_{y,i_z=2}.$$

The last condition ensures the consistency with $\nabla \times \mathbf{E} = 0$. The value of Σ_P is obtained from Equation (2.53) as

$$\Sigma_P = \frac{1}{v_A}\left(\frac{1+r}{1-r}\right). \tag{2.56}$$

In this work the Alfvén speed is $v_A = 4$ (in normalized unit). So, for example, to produce a 50% reflection (or $r = 0.5$) of the incident perturbation we need to take $\Sigma_P = 0.75$. This corresponds to a physical value of 2.44 *mho*. Now, it is possible to derive a direct relation involving the Pedersen current (I_P) and the reflection coefficient (r)

2.2.3.4 Relation showing the dependence of $I_{P,x}$ on r

The superposed velocity perturbation, after the reflection, becomes $\delta v_{y0}(-1+r)$. Using this in Equation 2.47, the expression for I_P [as in Equations (2.50) or (2.51)] can be written as

$$I_{P,x} = \Sigma_P E_x = -\Sigma_P(-1+r)\delta v_{y0} B_z. \tag{2.57}$$

Combining with Equation 2.53 the above equation can take the form

$$I_{P,x} = \frac{\delta v_{y0} B_z}{v_A}(1+r). \tag{2.58}$$

It may be noted that the quantities outside the parenthesis are constants. Hence the value of $I_{P,x}$ becomes proportional to $(1+r)$.

2.2.4 Basic Results and Summary

It should be noted that all quantities are in typical (normalized) units. Using (2.56) we set the Pedersen conductance Σ_P, in this case, equal to 2.25 to achieve a reflection coefficient, $r = 0.8$. Then we switch on the magnetic and velocity perturbations, described in Equation (2.39) and (2.40) at the top 20% of the simulation domain. That implies that the initial perturbations are of magnetospheric origin. These fixed amplitude ($\delta B_{y0} = 0.04$ and $\delta v_{y0} = 0.04$ - in normalized units), long (infinite) wavelength waves travel downward and reach the ionosphere which is at the lower boundary of the simulation region and is capable of reflecting 80% of the incident perturbations. So, here, with respect to our previous notations, $B_i = 0.04$ and $v_i = -0.04$. After reflection, the amplitude of the superposed magnetic and velocity perturbations are supposed to be approximately $\delta B_{y0}(1+r) = 0.04 \times (1+0.8) = 0.72$ and $\delta v_{y0}(-1+r) = 0.04 \times (-1+0.8) = -0.008$, respectively. Figure 2.6 plots of the altitude profiles of the propagating magnetic perturbation. The corresponding velocity perturbations are shown in Figure 2.7 in the same time sequence from $t = 0$ to 56. The waves reach the ionosphere at time $t = 30$ and the plots illustrated the profile of the waves before and after the reflection. After the reflection the amplitudes of the waves at the altitude $z = 20$ gives $\delta B_y = 0.07153$ and $\delta v_y = -0.0084$. Comparing these values with their expected (analytical) values confirms that we have achieved the desired control over the conductivity or reflection from the ionosphere. This achievement is important for this research as I am going to make use of this imposed conductivity of the ionosphere to investigate the effects of ionospheric conductance on the modification of FACs and on dynamic processes above the ionosphere that strongly depend on the magnitude of field-aligned electric currents and thus on the ionospheric conductance.

Figure 2.8 shows the variation of the x-component of the Pedersen current density (j_x) with altitude near the lower boundary at time $t = 56$ and at the middle of the simulation domain both for low

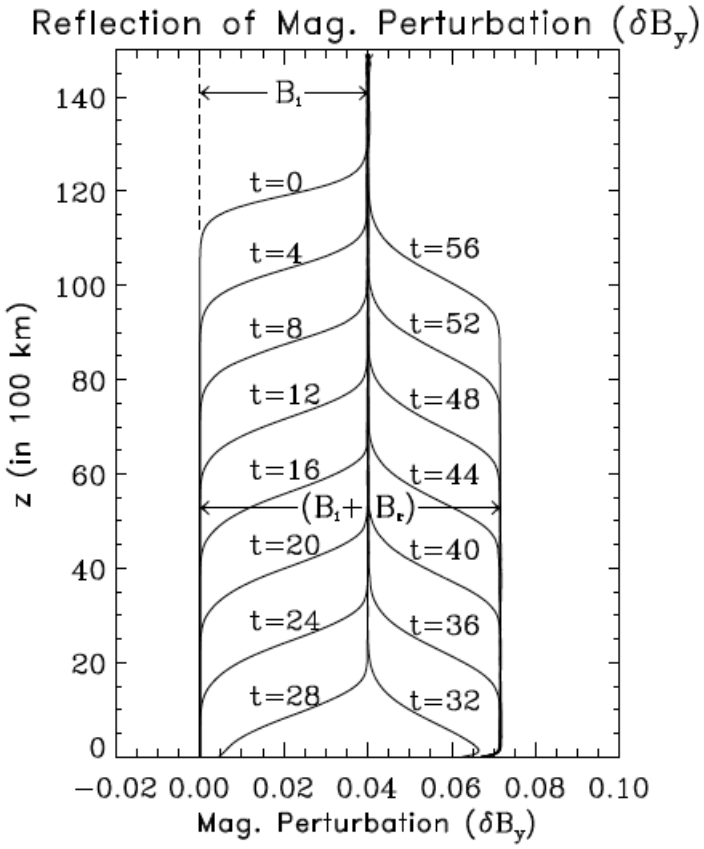

Figure 2.6: Reflection of the magnetic perturbations - simulation result. Altitude profiles of magnetic perturbation traveling in the form of Alfvén waves from the ionosphere. Plotted in a time sequence from $t = 0$ to $t = 56$ at an interval of $\Delta t = 4$. The reflection starts at $t = 30$. So, $t > 30$ depicts the reflected waves.

($r = 0.2$) and high ($r = 0.8$) conductance ionosphere. It is evident from this vertical profile that the magnitude of j_x is much higher at the lowest grid level than its magnitudes above it. From nearly 0.17 (normalized value) at $z = 0$ (the physical boundary) it falls sharply to about 0.01 at the next grid level at $z = 0.2$. The negative sign indicates that the current flows in the negative x-direction which is consistent with our expectation.

A vector-plot is shown at the same time ($t = 56$) in Figure 2.9. This plot shows the current densities perpendicular to the equilibrium magnetic field (in z-direction) in the xy-plane at grid points $i_z = 2$ (i.e. at $z = 0$ - the physical boundary). This plot indicates that the y-component of the current density is negligible and that the x-component is uniformly distributed on this plane. In these Figures the plot-titles imply that the vectors shown in the plots are the resultant of the x and y components of the mentioned quantities (here, the current density). It should be noted

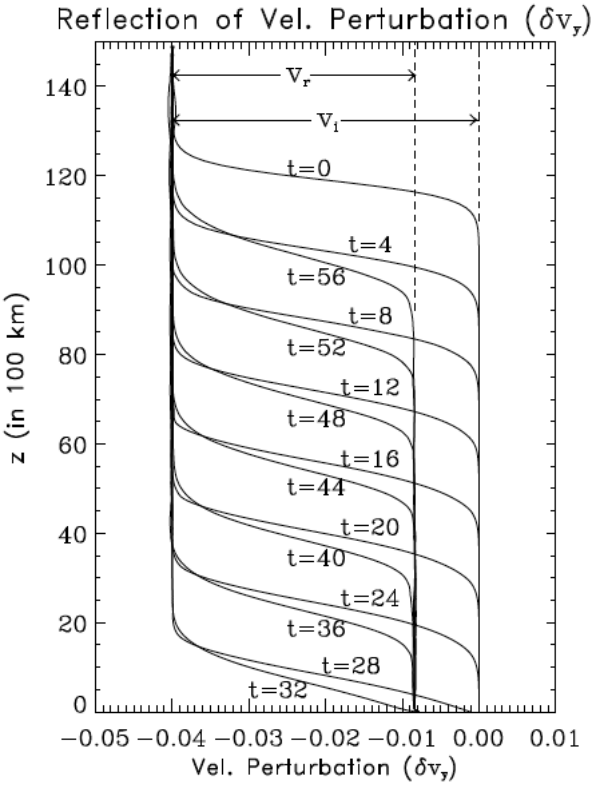

Figure 2.7: Reflection of the velocity perturbations - simulation result. Altitude profiles of velocity perturbation traveling in the form of Alfvén waves from the ionosphere. Plotted in a time sequence from $t = 0$ to $t = 56$ at an interval of $\Delta t = 4$. The reflection starts at $t = 30$. So, $t > 30$ depicts the reflected waves.

that the value for the magnitude of the plotted vectors is shown on the right upper corner outside the plot. Another vector-plot for the Pedersen current, $I_{P,x}$, at the same time ($t = 56$) is shown in Figure 2.10. As derived, this is also directed along negative-x direction and is equal in magnitude of $\delta B_{y,i_z=9}$.

It is concluded that a desired control of the ionospheric boundary conditions has been achieved. This introduces the capability to control the amount of reflection of the Alfvén wave from the ionosphere in the simulation. This is actually achieved by the imposition of an estimated value of height integrated Pedersen conductivity at the lower boundary. In the next chapter the effect of the height integrated Pedersen (ionospheric) conductivity on the magnetospheric FACs and the effect of the gradient in height integrated (ionospheric) Pedersen conductivity and its orientation on the generation of ionospheric FACs will be studied.

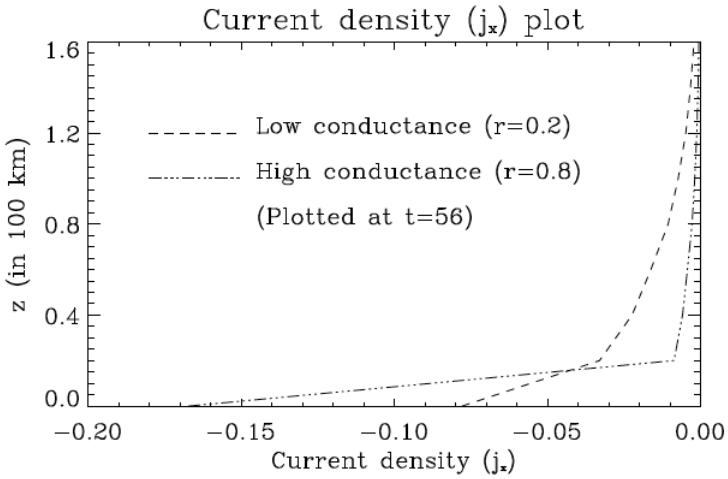

Figure 2.8: Variation of the current density, j_x, with altitude near the ionospheric boundary. These plots show that the currents are mostly confined at the lowest grid level (the physical boundary at $z = 0$) and is along the negative x-direction.

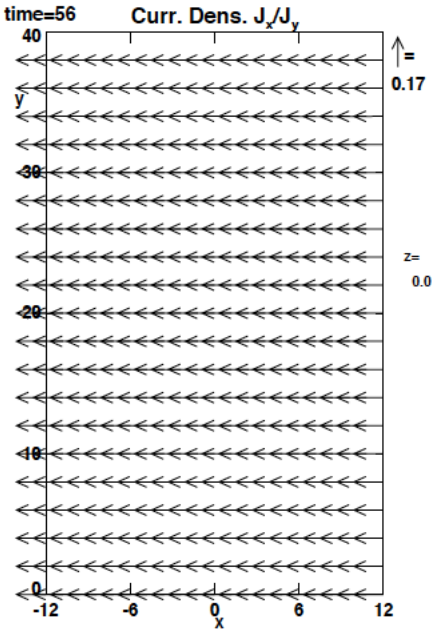

Figure 2.9: Plot of Pedersen current density at the physical boundary (lowest grid point, $z = 0$) plotted in the xy-plane.

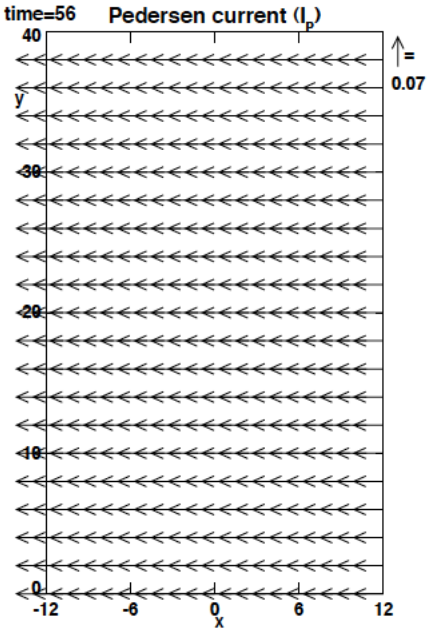

Figure 2.10: Plot of Pedersen current ($I_{P,x}$) that is flowing in the ionosphere

Chapter 3
Magnetospheric and ionospheric influences on the distribution of field-aligned currents

Introduction

The formation and distribution of field-aligned current (FAC) is of major importance to understand the coupling between the ionosphere and the magnetosphere. Physical causes for FACs are mostly in the magnetosphere. However, the actual distribution and evolution of FAC is determined also by the ionospheric conductance because the reflection of Alfvénic perturbations, associated with FACs, modifies the magnetic perturbations above the ionosphere, and therefore the intensity and distribution of the associated currents. Therefore this chapter explores the interactions between the Alfvénic magnetic and velocity perturbations from the magnetosphere (associated with FACs) and different patterns of the Pedersen conductance in the ionosphere. An introduction to the role and importance of FACs is included in the first section (3.1) followed by the numerical methods used for the simulations. A brief description of the methods for the generation of the magnetospheric perturbations and the associated FAC of different origins is added at the beginning of this section. The next part of this section includes several cases consisting of different combinations of magnetospheric perturbation and ionospheric conductance patterns. The interaction between the FACs from a magnetospheric source and the ionosphere, having a uniform Pedersen conductance, is considered first. This is followed by two cases in which the magnetospheric source perturbation is homogeneous, i.e., carries no FACs, and such currents evolve only through a nonuniform ionospheric response (conductance). And then their dependence on the patterns of the ionospheric Pedersen conductance is studied. One additional case of higher complexity (non-uniform magnetospheric source and nonuniform ionospheric conductance) is considered for a better understanding of the role of the Pedersen conductance at the ionospheric boundary. This chapter is concluded with a summary and discussion of all the main results.

3.1 Field-aligned current

Current along the geomagnetic field lines or the field-aligned current (FAC) is one of the most important aspects in the coupling of the magnetosphere and the ionosphere. It is now well accepted that the field-aligned or Birkeland currents play important role in many magnetospheric phenomena (e.g. Russell [49]) and is considered as the primary mechanism for the dissipation of the energy in the solar wind into the upper atmosphere and the ionosphere during the solar wind-magnetosphere-ionosphere coupling processes [72]. The Norwegian scientist K Birkeland first proposed the importance of the current systems parallel to the magnetic field, for the coupling

between the magnetosphere and the ionosphere in the first decade of the last century (1908). However, the idea did not receive much recognition until it was established by the in situ observations of intense fluctuations of transverse magnetic field in the auroral ionosphere with the satellite 1963 38C by Zmuda [32]. This also established the proposal made by Dungey [73] that the oscillations from the outer part of the geomagnetic field propagate as hydrodynamic waves.

Studies on FACs were conducted by direct measurements using satellites and rockets and indirect measurements using ground based magnetometers. Birkeland's proposal earned more appreciation after the detection of the longitudinal extent of the FAC and its magnitude ($\sim 10^5$ A) by Cummings and Dessler [34]. Gradually, more information about the configuration of the FAC system was obtained by different experimenters (e.g. [74, 75, 76, 37]). They inferred that the FACs consist of one or more pairs of oppositely directed flows. There are general patterns for the flow, which are also time dependent. Zmuda and Armstrong [74] used satellite data to establish that (through out the auroral oval) the magnetic perturbations are eastward between around 1400 and 2300 DLT (dipole local time) with the upward FAC at the poleward side of the auroral oval and downward at the equatorward side. Hence the closing ionospheric Pedersen current is northward in this region. The pattern is just the opposite between around 2400 and 1000 DLT. In this sector the magnetic perturbations are westward with upward FAC being observed at the equatorward side and the downward current being observed at the poleward side of the region. The ionospheric Pedersen closing current becomes southward in that case. These observations demonstrated a reversal of the pattern between 2300 and 2400 DLT but the interval between about 1000 to 1400 DLT is characterized by continuous disturbances without a specific pattern. The first polar orbited satellite TRIAD supplied magnetometer data showing large magnetic perturbation in the east-west direction. The east-west components of perturbation indicate the presence of a current in the vertical direction (that is the FAC). Iijima and Potemra [37] used the data obtained from the TRIAD mission to establish the average global scale FAC system (see Figure 3.1) when the IMF (interplanetary magnetic field) has a southward component. Figure 3.1 shows the most characteristic features of FACs at times (a) when the state of the magnetosphere is quiet and (b) when larger disturbances are present. The features of the FACs depicted in Figure 3.1 are common to both the hemispheres but an additional current system, the so-called cusp current, has a strong dependence on the IMF and is opposite in the two hemispheres for strong perturbations in the transverse magnetic field [77]. It is mostly accepted that the FACs are of magnetospheric origin and are formed in response to the stress exerted by the solar wind on the magnetosphere [72]. A schematic diagram showing combined field-aligned and ionospheric current systems is represented in Figure 3.2.

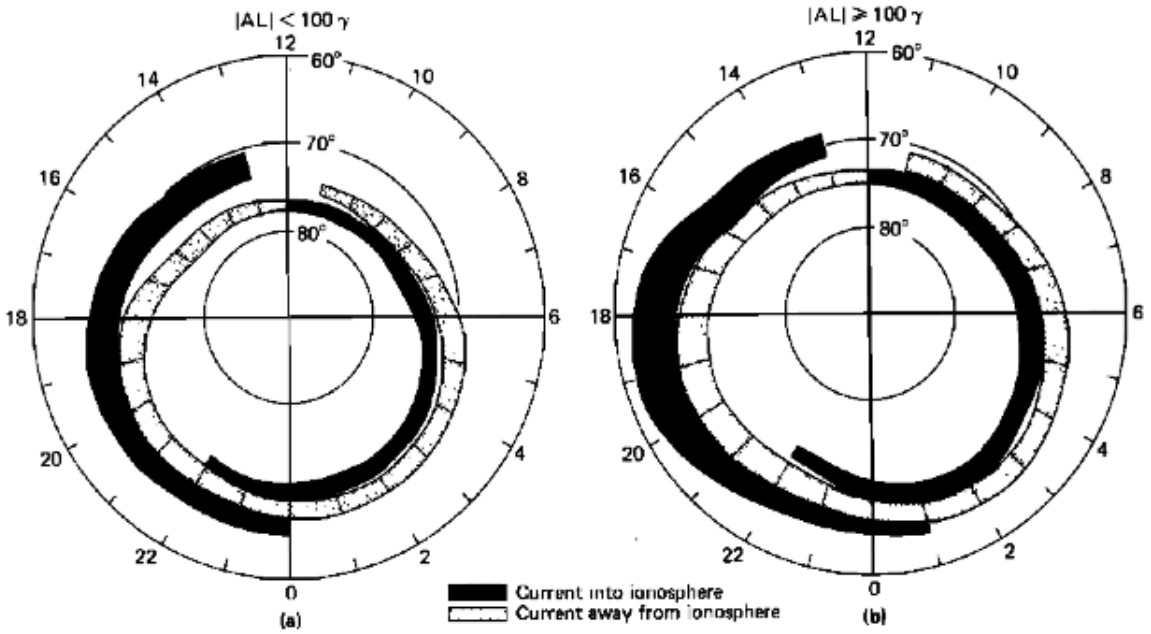

Figure 3.1: Distribution of the FACs at high latitudes. In the same region of the auroral oval, FACs always exist in two overlapping rings. During quiet times the pattern of FAC occurs at higher latitude with less latitudinal extent. The currents from the inner and the outer rings are called region-1 current and region-2 current, respectively (Taken from Iijima and Potemra, 1978 [37]).

3.2 Numerical methods

In all the cases discussed in this chapter, magnetic and velocity perturbations are introduced at the magnetospheric boundary assuming a primary magnetospheric driver. The exact magnetospheric cause for the FAC generation is unspecified because it is irrelevant for the goal to investigate the modification of FACs by the ionospheric conductance. These magnetospheric perturbations can locally be uniform or nonuniform in the xy-plane and propagate downward along the negative z-direction parallel to the magnetic field. Note that the configuration chooses the magnetic field for the northern hemisphere but results can easily be applied to the southern hemisphere by mirroring the configuration. When the Alfvénic perturbation reaches the ionosphere, it is reflected by a uniform or nonuniform Pedersen conductance. Therefore interaction of different choices of magnetospheric perturbations with the ionosphere depends on the assumed horizontal distribution of the Pedersen conductance. Obviously, any nonuniform magnetic perturbations are equivalent to a FAC imposed at the magnetospheric boundary, which is explained in the next section followed by an introduction on FAC of ionospheric origin.

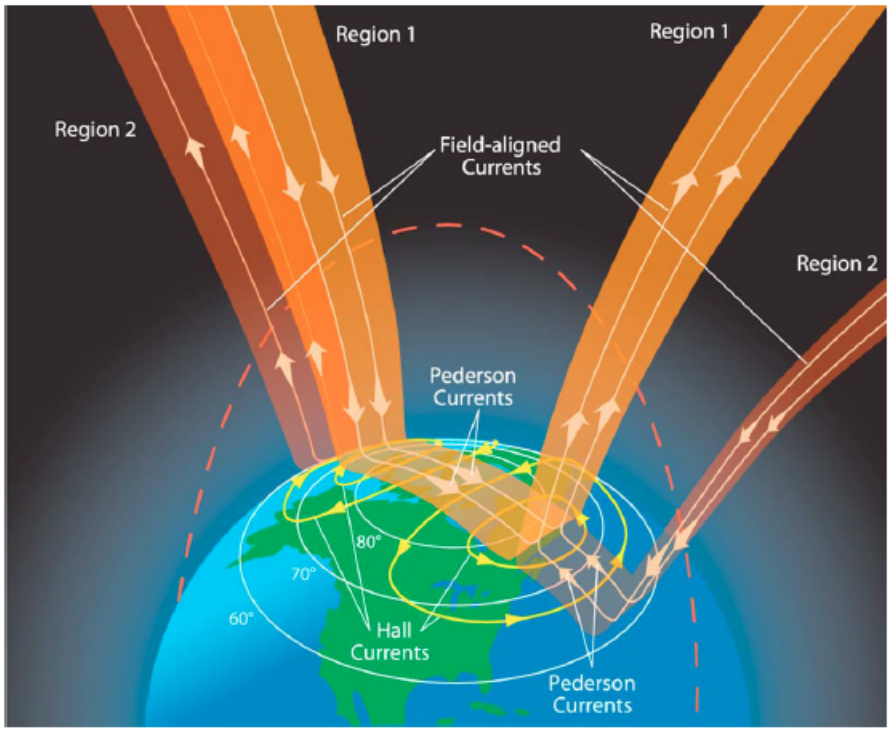

Figure 3.2: A schematic view of the combined field-aligned and ionospheric current systems (Taken from Le et. al., 2010 [72]).

Field-Aligned Currents of Magnetospheric Origin

In a warm magnetized plasma three fundamental magnetohydrodynamic (MHD) waves can exist [78]. These are the fast and slow magnetosonic waves and the shear Alfvén wave. FAC is carried only by the shear Alfvén wave [79]. For the cases of this research where a magnetospheric source for a FAC is imposed (case I and IV), this current is generated close to the magnetospheric boundary by a shear of the magnetic field perturbation applied in the $\pm y$-direction as illustrated in Figure 3.3. Correspondingly, homogeneous magnetic perturbation used in Equation 2.39 is replaced by a perturbation with a gradient in the x-direction at the beginning of the simulation close to magnetospheric boundary. This perturbation is given by

$$\delta B_y = \frac{\delta B_{y0}}{2}\left[1 + tanh\left(\frac{z - 0.8 z_{max}}{4}\right)\right] tanh\left(\frac{x}{0.5}\right) \tag{3.1}$$

and the associated velocity perturbation, for the generation of downward propagating Alfvén waves, follows the same relation as Equation (2.40) and is given by

$$\delta v_y = -\frac{v_A}{B_0}\delta B_y \tag{3.2}$$

where v_A is the Alfvén speed and B_0 is the magnitude of the guide-field. The quantities δB_{y0}, v_A and B_0 are constants for all the cases and have the same values (0.04, 4.0, and 4.0, respectively, in

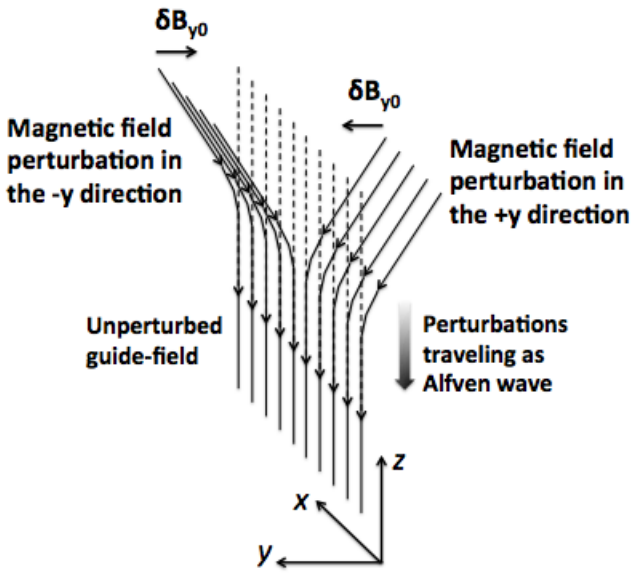

Figure 3.3: A sketch showing the nonuniform (sheared) magnetic perturbations traveling from the magnetosphere toward the ionosphere. These Alfvénic perturbations in the $\pm y$-direction generate FACs at the junction between the oppositely directed magnetic fields.

the normalized units) as in Chapter 2.

These Alfvénic perturbations are nonuniform along the x-direction, that is, the perturbations are oppositely directed in the $\pm y$-directions across a thin boundary at $x = 0$. After launching, these waves travel downward and eventually reach the ionospheric boundary. The dotted lines, or, the solid lines in the lower part of the diagram represent the unperturbed geomagnetic field. At the junction between the oppositely directed perturbations the gradient in the magnetic field $\left(\frac{\partial \delta B_y}{\partial x}\right)$ implies the z-component of $\nabla \times \mathbf{B}$ which is carried by the Alfvén waves into the ionosphere. This results in a FAC that propagates toward the ionosphere following Ampere‘s law [Equation (2.18)]. The following study considers 4 combinations of magnetospheric source perturbation and ionospheric conductance patterns. The sketch in Figure 3.4 illustrates these patterns, used for the different cases. The second column of the table shows the type of magnetic perturbation, initially imposed at the top (magnetospheric) part of the simulation domain in the xy-plane. Red arrows show the directions of these perturbations. Patterns of the ionospheric Pedersen conductance, imposed at the lower (ionospheric) boundary, are shown in the third column. Darker shade represents the higher conductance than the lighter one. It is noted that Cases I and IV consider the presence of a magnetospheric source of FACs to interact with different ionospheric boundary conditions. At the ionospheric boundary, the Pedersen conductance is varied in different ways and the effects of different ionospheric boundary conditions on this FAC are studied. In case I the ionospheric

	Initially imposed magnetic perturbation at the top part of the simulation domain	Imposed Pedersen conductance at the lower (ionospheric) boundary
Case I	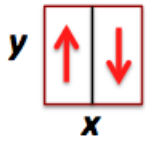	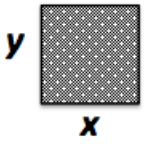
Case II	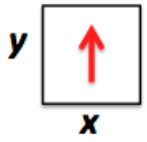	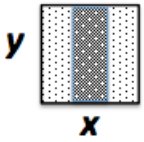
Case III	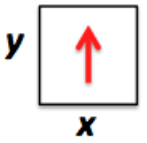	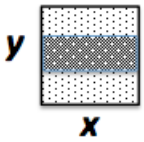
Case IV	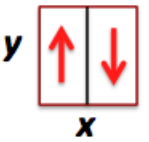	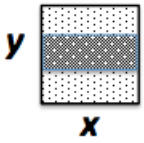

Figure 3.4: Sketch illustrating the 4 combinations of magnetospheric source perturbation and ionospheric conductance pattern. Initially imposed magnetic perturbation at the magnetospheric level is shown in the second column. Red arrows show the directions of this perturbations in xy-plane. Patterns of the imposed ionospheric Pedersen conductance are shown in the third column. Darker shade represents higher conductance than the lighter one.

Pedersen conductance is uniform but in all other cases the conductance has a gradient in the x or y-directions.

Though FACs are mostly of magnetospheric origin they may originate from the ionosphere too. In case II and III, simple Alfvénic perturbations travel from the magnetosphere without initial FACs. Here, FAC forms in response to the reflection of the simple Alfvénic perturbations through a nonuniform Pedersen conductance. In case II the imposed ionospheric Pedersen conductance has a gradient in the x-direction while in case III and IV, the gradient is chosen to be in the y-direction. One additional case study is illustrated in the summary, which is not included in the above table. In that case the simple magnetospheric perturbations without any FAC travel toward the ionosphere with a high conductance patch in a low conductance background.

3.2.1 Case I: Nonuniform magnetospheric perturbations and uniform ionospheric Pedersen conductance

In this case, the effects of a uniform Pedersen conductance, at the lower (ionospheric) boundary of the simulation region, on a FAC (imposed from the magnetosphere) are considered. Therefore, this class of cases can serve also as a reference for other inhomogeneous ionospheric conductance patterns.

The simulation domain has x-axis extending from -12 to 12 (in km), y-axis from 0 to 40 (in km) and z-axis from 0 to 120 (in 100 km). The nonuniform magnetic and velocity perturbations (as illustrated in Figure 3.3) are along the y-axis following Equations 3.1 and 3.2.

At the lower ionospheric boundary, a uniform Pedersen conductance is assumed in the simulation. The value of this imposed Pedersen conductance, Σ_P, is set to 2.25 and corresponds to a reflection coefficient, $r \approx 0.8$. In physical units this Pedersen conductance corresponds to a value ≈ 7.31 mho. Equation (3.1) indicates that the magnetic perturbations are both in the $\pm y$-directions. The magnetic perturbation is along the negative y-direction for $x > 0$ and is along the positive y-direction when $x < 0$ and is initialized (i.e. at time, $t = 0$), approximately, in the top 20% of the simulation domain (from $z \approx 96$ to $z = 120$).

The velocity perturbations are, accordingly, consistent [Equation (3.2)] with downward propagating Alfvén waves. This kind of perturbation develops, for instance, if convection in the magnetosphere has a gradient perpendicular to the local magnetic field. With this initial condition a pair of Alfvén waves travel along the magnetic field carrying a FAC down and reach the lower boundary eventually at time, $t \approx 24$. Figures 3.5 and 3.6 show snap-shots of the propagation of the magnetic field and velocity perturbations at time, $t = 18$ before they have reached the lower (ionospheric) boundary. These plots are taken in the xz-plane in the middle of the simulation domain (at $y = 20$). Though the gradient of the plotted quantities in the x-direction (between the opposite polarities of the Alfvénic perturbations) appear discontinuous, it actually has a width of 1 length-unit. This width can be chosen to be of any desired value. Within 18 Alfvén times the fronts of the incident perturbations travel down to $z \approx 24$ from their initial positions ($z \approx 96$). In these plots, the portion of the simulation domain below $z \approx 24$ is unperturbed and above this altitude the perturbations are of opposite sign on the two sides of $x = 0$. The nonzero values of $\frac{\partial \delta B_y}{\partial x}$ around $x = 0$ in the perturbed region implie the presence of a current sheet, in the yz-plane, following Ampere's law. Since the unperturbed magnetic field is also in the negative z-direction, the current from the Alfvénic perturbation is aligned with the magnetic field which is illustrated by the plots in Figure 3.7. These plots show the component of current density ($j_\parallel$) that is parallel to the direction of the magnetic field ($\mathbf{B}$) in two orthogonal cuts through the simulation domain (a) in the xz-plane

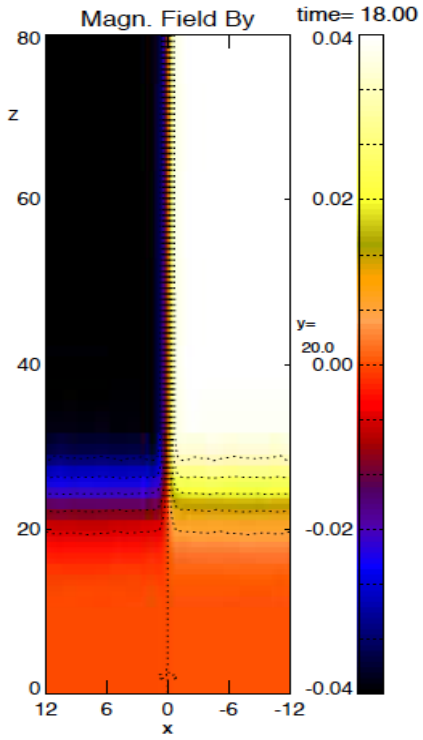

Figure 3.5: Case I: Plot of incident magnetic perturbation (δB_y) in the xz-plane at $y = 20$ before the reflection at time $t = 18$.

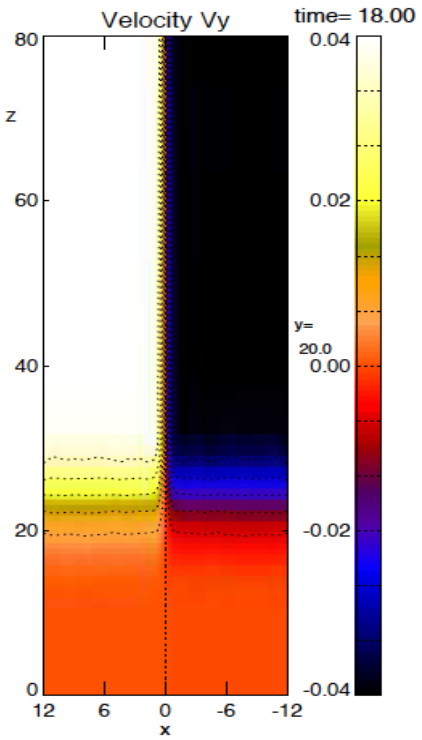

Figure 3.6: Case I: Plot of incident velocity perturbation (δv_y) in the xz-plane at $y = 20$ before the reflection at time $t = 18$.

and (b) in the xy-plane at time, $t = 18$. Our choice of the guide field in the negative z-direction (northern hemisphere) implies that, a downward FAC is represented by a positive $j_\parallel$ (for an upward FAC, $j_\parallel$ is negative). The plots (in Figure 3.7) show that the magnitude of the normalized value of (downward) $j_\parallel$ is ≈ 0.064 at the central plane of the current sheet. Note that the FAC shown in Figure 3.7 is closed by a perpendicular current at the leading edge of the Alfvén wave. This current is easily determined through Ampere's law and is consistent with the expected polarization current due to the temporal change of the electric field at the Alfvén wave front.

As described in the previous cases (in Chapter 2), the pair of Alfvénic perturbations are reflected by the ionosphere having a high value of Pedersen conductance. So, the superposed magnetic perturbations, $(1 + r)\delta B_{y0}$, attain the enhanced values but they have opposite ($\pm y$) directions on the two sides of $x = 0$ as the reflected waves propagate in the upward direction. This is illustrated in Figure 3.8. The corresponding plot for the velocity perturbations is shown in Figure 3.9. The superposed reflected velocity perturbation has a polarity opposite to incoming wave such that the total amplitude is $(-1 + r)\delta v_{y0}$. The two plots are taken at the same location as in Figures 3.5 and 3.6, at time, $t = 36$, that is 12 Alfvén times after the incident waves reach the lower boundary. At

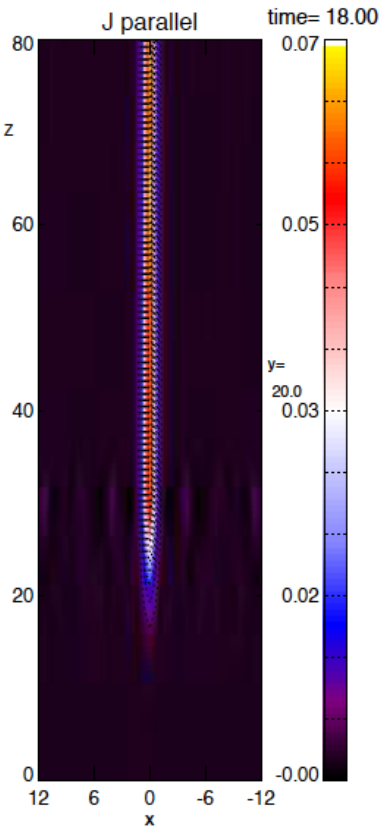

(a) $j_{\|}$-plot in the xz-plane at $y = 20$.

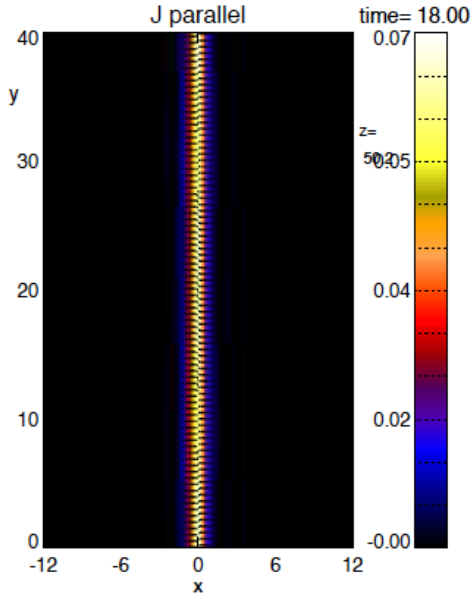

(b) $j_{\|}$-plot in the xy-plane at $z = 50$.

Figure 3.7: Case I: Magnetospheric FAC-sheet carried by the pair of Alfvén waves traveling downward. Plots of FAC density ($j_{\|}$) are taken at $t = 18$ before the start of reflection (at $t = 24$). The magnitude of $j_{\|}$ is ≈ 0.064 (normalized) at the central plane of the current sheet. (a) Plot in the xz-plane at $y = 20$. (b) Plot in the xy-plane at $z = 50$.

this time, the reflected wave front has travelled up to $z \approx 48$. Figure 3.10 shows the x-profiles at $y = 20$ for the magnetic field and the velocity above the ionosphere at $z = 36$ to compare incident and reflected wave perturbations. These x-profiles show the changes in the quantities (δB_y and δv_y) between $t = 25$ (incident perturbations) and $t = 45$ (total perturbations after reflection). The magnitude of δB_y increases from ≈ 0.04 to ≈ 0.072. The corresponding change of δv_y is from 0.040 to 0.008. The larger magnitude of the magnetic perturbation, after reflection, implies an increase of the z-component of the current density $j_z = \frac{\partial \delta B_y}{\partial x}$ at $x = 0$. This enhancement of the FAC, after reflection at the ionospheric boundary, is illustrated in Figure 3.11. This figure shows the color-plots for $j_{\|}$ (a) in the xz-plane and (b) in the xy-plane at time $t = 36$ which implies that these snap-shots are also taken about 12 Alfvén times after the reflection. In the first plot [Figure 3.11a] the modified FAC is observed up to an altitude of $z \approx 48$ that is covered by the reflected

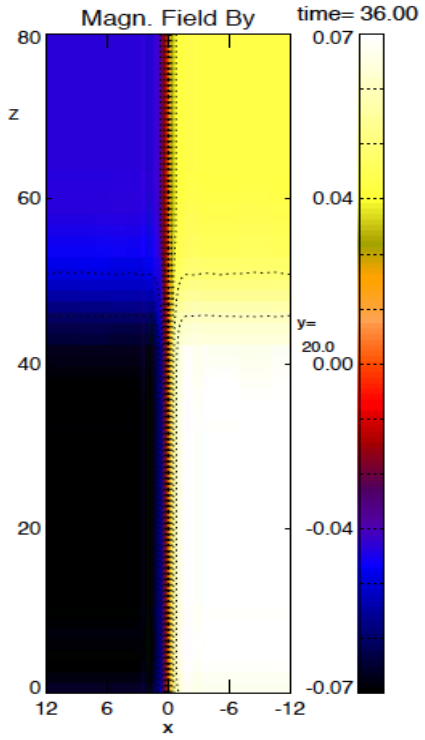

Figure 3.8: Case I: Plot of total magnetic perturbation (δB_y) after reflection in the xz-plane at $y = 20$ at time $t = 36$.

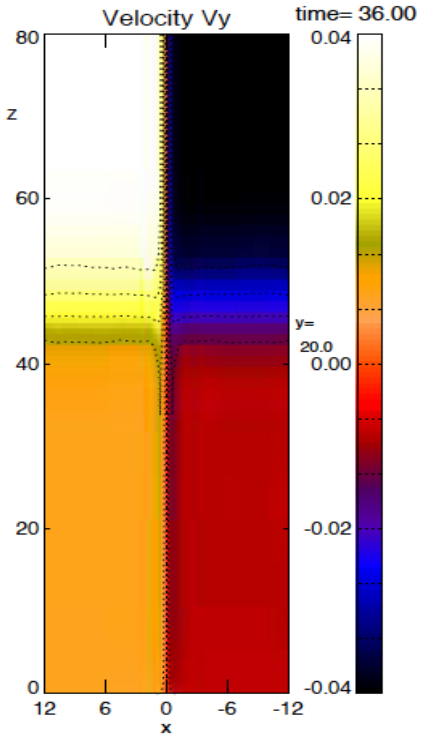

Figure 3.9: Case I: Plot of total velocity perturbation (δv_y) after reflection in the xz-plane at $y = 20$ at time $t = 36$.

waves and the magnitude of this FAC density, $j_{\|}$, is ≈ 0.105 (in normalized units) at the central plane of the current sheet.

The FAC at this time is closed through two perpendicular currents. One of which is again a polarization current at the leading edge of the reflected wave. The other is the Pedersen current at the ionospheric boundary of the simulation.

For the FACs, before and after the reflection, Figure 3.12 is added. This figure shows the time-evolution of the x-profile of $j_{\|}$ at $z = 36$ between times $t = 25$ and $t = 45$. At the chosen altitude only the incident perturbations are present at time, $t = 25$ and at time, $t = 45$ the $j_{\|}$ contains the contributions from the incident and the reflected waves. The magnitudes of the FAC densities before and after the reflection demonstrate an increase of $\approx 64\%$ at the central plane.

Considering the case that was discussed in Chapter 2, the generation of the Pedersen current (to close the FAC), is expected at the ionospheric boundary. It is already seen (in Chapter 2) that this current is mostly confined to the lowest grid levels at the physical boundary of the simulation domain. A vector plot of the current density in the xy-plane, at the lower boundary, is shown in Figure 3.13. This plot shows the presence of two oppositely directed Pedersen current densities,

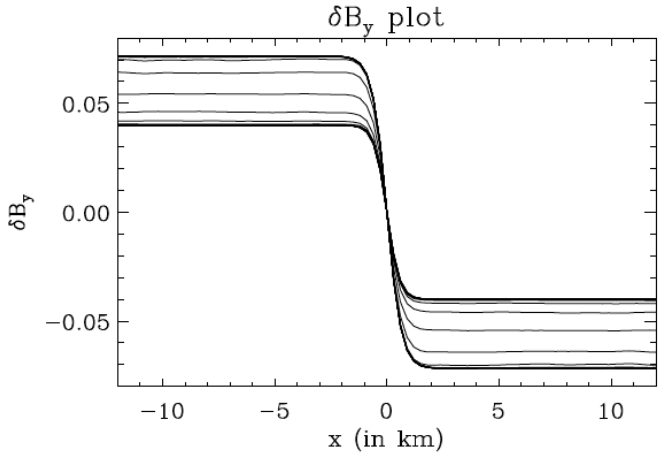

(a) Magnitude of magnetic perturbation increases (from 0.04 to 0.072) on reflection.

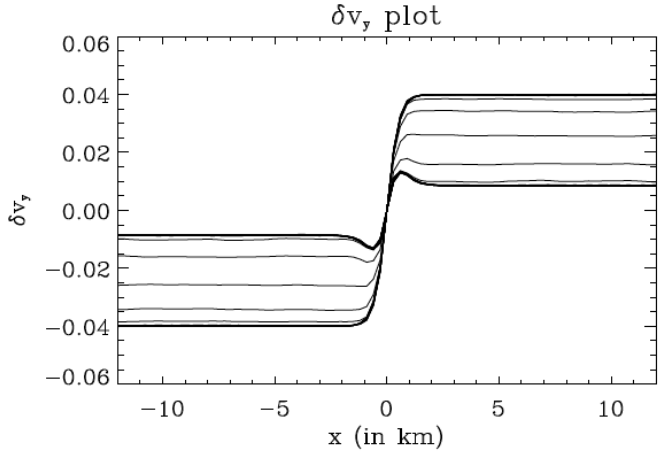

(b) Magnitude of velocity perturbation decreases (from 0.04 to 0.008) on reflection.

Figure 3.10: Case I: Changes of magnetic and velocity perturbations after reflection from the ionosphere. Both plots show the x-profiles at $y = 20$ and $z = 36$. (a) Magnitude of magnetic perturbation becomes larger after reflection. (b) Magnitude of velocity perturbation becomes smaller after reflection.

j_x, at the lower (physical) boundary of the simulation domain. These Pedersen currents, directed away from $x = 0$, connect to the downward FAC, at their junction (i.e. at $x = 0$), (Figure 3.11b) to satisfy the conservation of electric current ($\nabla \cdot \mathbf{j} = 0$). Near the lower boundary, the electric field is $E_x = -\delta v_y B_z$. This electric field along with the imposed Pedersen conductance (Σ_P) produces the (height integrated) Pedersen current ($I_{P,x}$) as $I_{P,x} = \Sigma_P E_x$. Equation (2.58) illustrated the dependence of the Pedersen current ($I_{P,x}$) on the reflection coefficient (r). The plot in Figure 3.14

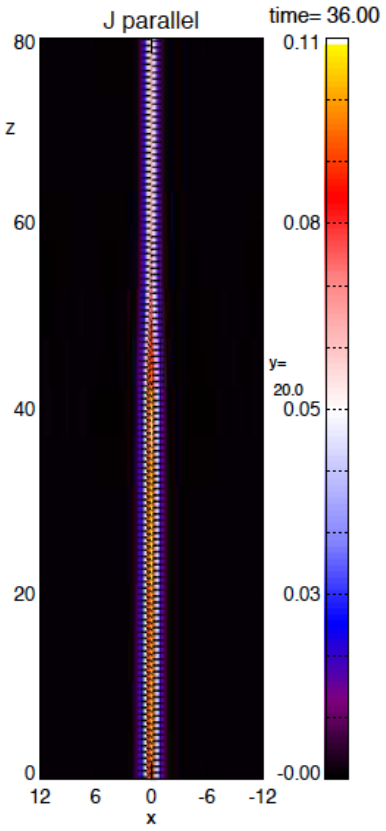

(a) $j_{\|}$-plot in the xz-plane at $y = 20$.

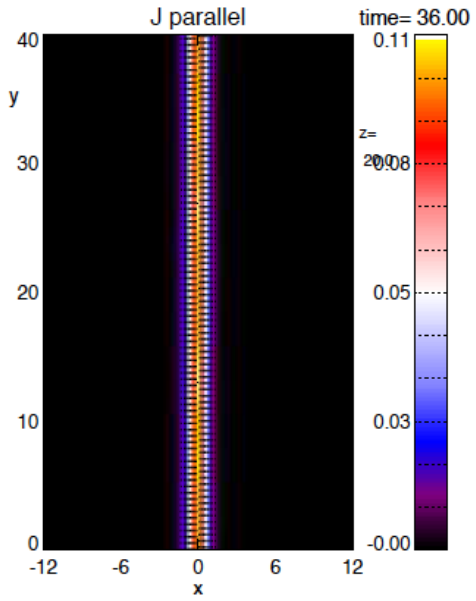

(b) $j_{\|}$-plot in the xy-plane at $z = 50$.

Figure 3.11: Case I: FAC-sheet carried by the superposed (total) Alfvén waves. Plotts of $j_{\|}$ are taken at $t = 36$ after the reflection (at $t = 24$). The magnitude of current density is ≈ 0.105 (normalized) at the central plane of the current sheet. (a) Plotted in the xz-plane at $y = 20$. (b) Plotted in the xy-plane at $z = 20$.

shows the x-profile of Pedersen current ($I_{P,x}$) at the middle of the simulation domain. The lineplots represent the x-profiles at times starting from $t = 23$ with $\Delta t = 1$. The current is positive for $x > 0$ and negative when $x < 0$ having a magnitude of ≈ 0.071 (at steady state) on both the sides of the central plane. The value of the current is consistent with the Equation (2.58).

This result demonstrate that the boundary conditions at the ionosphere plays a strong role for the modification of FACs with a generator in the magnetosphere and for the magnitude of the associated Pedersen currents at the ionospheric boundary. An ionosphere with high Pedersen conductance is able to amplify such FACs significantly and correspondingly, can generate stronger Pedersen currents. Vice versa a Pedersen conductance lower than the Alfvénic conductance can lower the net FAC and the respective Pederson currents. The generated Pedersen current is found consistent with the relation between $I_{P,x}$ and r (Equation (2.58)), derived in Chapter 2. If the

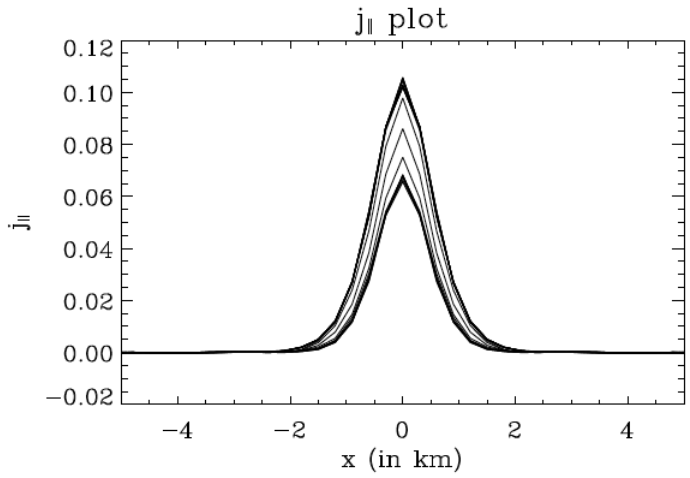

Figure 3.12: Case I: Plot showing the time-evolution of the x-profile of the FAC density ($j_{\parallel}$) at $y = 20$ and at an altitude $z = 36$, between time $t = 25$ and 45. The value of $j_{\parallel}$ increases monotonically by about 64% after reflection.

Pedersen conductance of the ionosphere is very low, the ionosphere cannot reflect the waves efficiently. In that situation, the FACs remain almost unchanged or negligibly enhanced and the associated Pedersen current is also zero or very small. In the next section, the interaction between a homogeneous Alfvénic perturbation from the magnetosphere and an ionospheric boundary with a nonuniform Pedersen conductance is considered.

3.2.2 Case II: Uniform magnetospheric perturbations and nonuniform ionospheric Pedersen conductance (gradient in the x-direction)

In this case, the homogeneous Alfvénic perturbations, in the y-direction, are imposed at the magnetospheric simulation boundary and the ionosphere has a Pedersen conductance which is nonuniform with a gradient in the x-direction as indicated in Figure 3.4. That is, the direction of the conductance-gradient is perpendicular to the direction of the magnetic field and velocity polarization.

The simulation domain is same as that described in case I, except that the boundaries in the x-direction are taken at $x = -15$ and $x = 15$. The profile of the Pedersen conductance along the x-direction is illustrated in Figure 3.15. The profile assumes a strip of high conductance bound by regions of much lower conductance. The conductance is changed gradually between low and high values. The profile of the chosen Pedersen conductance is determined by

$$\Sigma(x) = \frac{(\Sigma_{P,2} - \Sigma_{P,1})}{2} tanh\left(\frac{x - (-6)}{3}\right) + \frac{(\Sigma_{P,2} + \Sigma_{P,1})}{2} \tag{3.3}$$

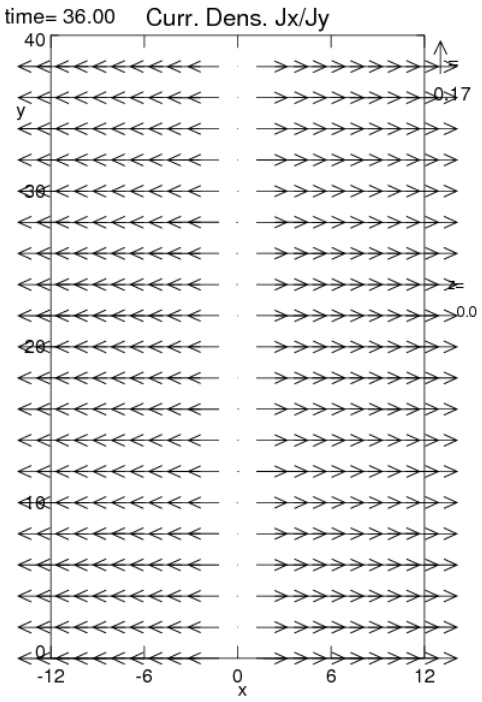

Figure 3.13: Case I: Vector plot of the current density (j) in the xy-plane at the lower boundary (i.e. $z = 0$) after the reflection (at $t = 36$). This plot shows the presence of two oppositely directed j_x on the two sides of $x = 0$.

for $x < 0$, and

$$\Sigma(x) = -\frac{(\Sigma_{P,2} - \Sigma_{P,1})}{2} tanh\left(\frac{x - (+6)}{3}\right) + \frac{(\Sigma_{P,2} + \Sigma_{P,1})}{2} \tag{3.4}$$

for $x \geq 0$.

The background value of the Pedersen conductance is $\Sigma_{P,1} = 0.375$ on the two sides of the central strip within which the conductance is $\Sigma_{P,2} = 2.25$. For convenience the central part with the higher conductance will be referred as region 2 (extending from -6 to 6 on the x-axis) and the remaining part with lower conductance on its two sides as region 1. With the chosen values of Σ_P, the reflection coefficient (r) at region 1 is ≈ 0.2 ($\approx 20\%$ reflection of the incident waves) and at region 2 is ≈ 0.8 ($\approx 80\%$ reflection of the incident waves).

The height (z) profiles of the magnetic and velocity perturbations are the same as in case I except for their x-dependence and are given by the Equations (2.39) and (2.40). So, before reaching the ionospheric boundary, from the moment of launching, the Alfvén waves propagate downward in the way this was described in Chapter 2.

It may be noted here, that the underlying dynamics is two-dimensional (independent of y) in this case. It does not matter where a cut is chosen to show the results. From the geometry of this case,

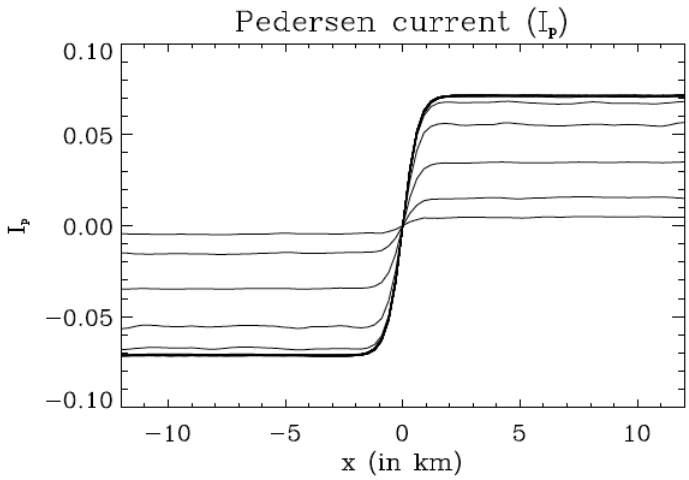

Figure 3.14: Case I: Plot of x-profiles of the ionospheric Pedersen current ($I_{P,x}$). This plot shows the presence of two oppositely directed $I_{P,x}$s on the two sides of $x = 0$.

it is concluded that the plots in a xz-plane for any y-value or in a xy-plane for any z-value would not be different. The physics of Alfvén wave reflection can be fully derived from the one-dimensional results in chapter 2. This was also true for case I. The purpose of these simulations (cases I & II) is to confirm the expectations from the 1D results (of Chapter 1).

As discussed in Chapter-2, the incident and reflected perturbations superpose to produce the net values of the magnetic and velocity perturbations along the y-direction after the reflection from the ionosphere. These net values of the magnetic and the velocity perturbations [$\delta B_{y0}(1 + r)$ and $\delta v_{y0}(-1 + r)$, respectively] are obviously different above region 1 and region 2. With Alfvén speed $v_A = 4$, the perturbations reach the ionosphere at time $t \approx 24$ and after this time the reflected waves (perturbations) propagate in the upward direction.

Superposed magnetic field and velocity, after the reflection at the ionosphere, are shown in color-plots in Figure 3.16 and Figure 3.17, respectively. These plots are taken on the xz-planes at the middle of the simulation domain (at $y = 20$) at time, $t = 36$. As the reflection starts at time, $t \approx 24$ the waves reach $z \approx 48$ in a time of 12 Alfvén times after being reflected at the ionosphere. The two Figures (3.16 and 3.17) show that the perturbations have different values above region 1 and region 2 up to an altitude covered by the reflected waves. Therefore the superposed (total) value of the magnetic field [$\delta B_{y0}(1 + r)$] above region 2 is much larger than that above region 1. The situation is just opposite for the velocity perturbation. Higher values of the Pedersen condcutances cause smaller magnitude of the superposed velocity perturbation [$\delta v_{y0}(-1+r)$] above region 2 than above region 1.

The x-profiles of the equilibrium values of the total magnetic and velocity perturbations (after

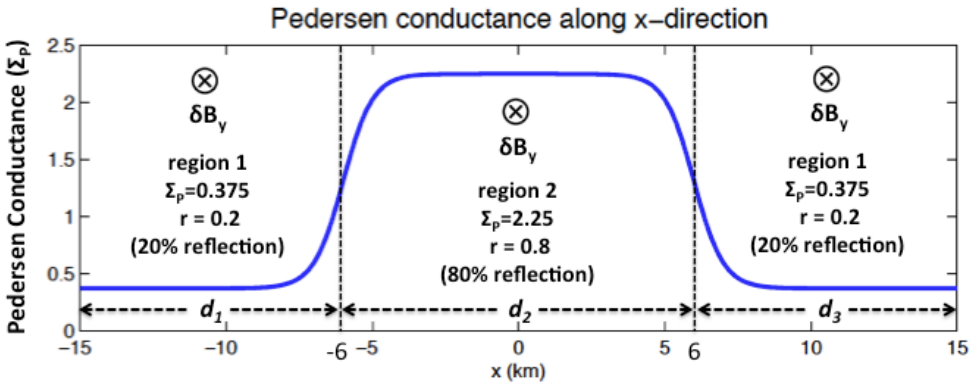

Figure 3.15: Case II: x-profile of the Pedersen conductance imposed at the ionospheric boundary. Here the magnetic and velocity perturbations (δB_y and δv_y) are perpendicular to the direction of the conductance gradient.

reflection) above the ionosphere (at $z = 20$) are shown in Figure 3.18 and Figure 3.19. These line-plots show that as the leading edge of the perturbation wave reaches a sufficient height (here, $z = 20$ between time $t = 24$ and 52), the superposed perturbations gradually attain an equilibrium value above region 1 and region 2 depending on its conductance (or reflection coefficient) values. Figure 3.18 demonstrates a gradient of the y-component of the magnetic field along the x-direction $\left(\frac{\partial \delta B_y}{\partial x}\right)$ at the boundaries between region 1 and region 2 conductances. It is noted that $B_y = \delta B_y$ because the unperturbed field has no B_y-component. This gradient (Ampere's law) implies the evolution of two field-aligned vertical current sheets at the conductance boundaries with oppositely directed z-components of the current density as shown in Figure 3.20. In this figure, we see an upward (antiparallel) current at $x = -6$ and a downward current layer at $x = 6$. These two FACs extend up to the altitude of the wave front of the reflected waves.

The ionospheric closure of these two FACs is shown in Figure 3.21. This figure shows the current densities at the lower physical boundary ($z = 0$, ionospheric) of the simulation box. Arrows show the combined x & y components of the current density and the color indicates the z-component (j_z) which is nearly same as the FACs ($j_\parallel$) in magnitude. This confirms the presence of the upward and downward FACs at the two conductance boundaries. In this figure, the arrows, representing the Pedersen current density, j_x, in the high conductance region between $x = -6$ and $x = 6$, are larger than those in the low conductance areas. This indicates the presence of a stronger Pedersen current across the region 2, with a higher value of Pedersen conductance.

Figure 3.22 shows the x-profiles of the Pedersen current density at the ionospheric boundary at the middle of the simulation domain and Figure 3.23 shows the corresponding Pedersen current in the ionosphere. The reflection conditions for the Alfvén waves imply that, the Pedersen current ($I_{P,x}$)

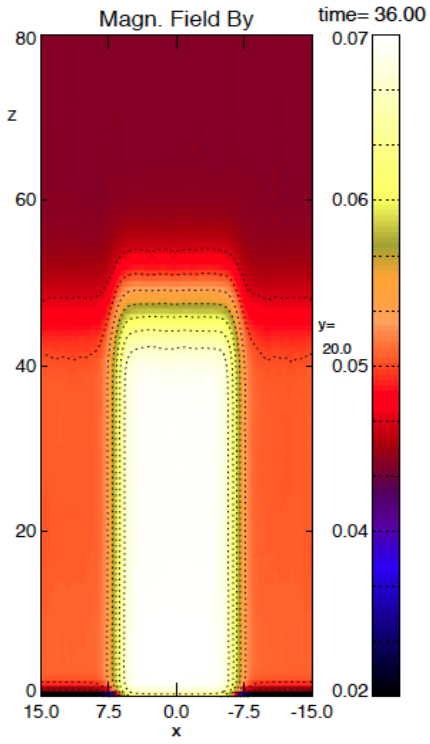

Figure 3.16: Case II: Plot of magnetic perturbation (δB_y) after reflection in the xz-plane at $y = 20$ at time $t = 36$.

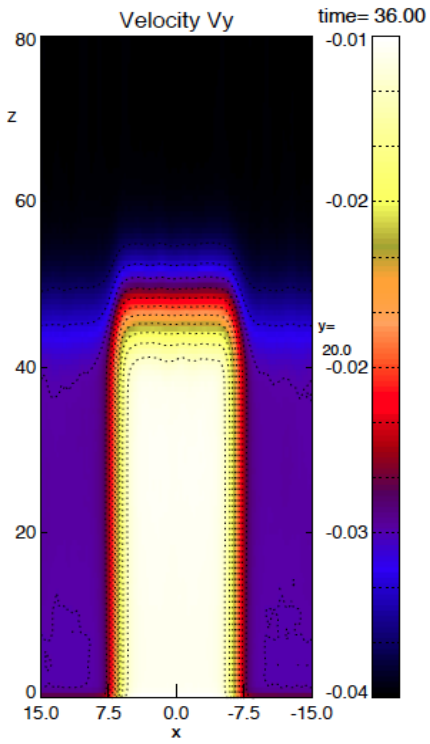

Figure 3.17: Case II: Plot of velocity perturbation (δv_y) after reflection in the xz-plane at $y = 20$ at time $t = 36$.

is proportional to $(1 + r)$. Therefore, the expected ratio of the values of $I_{P,x}$ in the two regions (region 1 and 2) is $I_{P,x,2}/I_{P,x,1} \approx (1 + 0.8)/(1 + 0.2) = 1.5$. Figure 3.23 shows the values of $I_{P,x,2}$ (in region 2) and $I_{P,x,1}$ (in region 1) as 0.0715 and 0.0473, respectively. This results in a ratio of ≈ 1.51 for $I_{P,x,2}/I_{P,x,1}$. This demonstrates that the Pedersen currents are indeed consistent with the values of the Pedersen conductance of the respective regions, in case II. The closure of the field aligned current at the leading edge of the Alfvén waves is again through polarization currents as mentioned for case I.

Most of these results, similar to the results for case I, are fully consistent with the one-dimensional reflection of Alfvén waves by a partially conducting boundary. For instance, reflection conditions are, within the numerical accuracy, the same as obtained in Chapter 2. The reason for the consistency is the geometry, i.e., the polarization of the Alfvén wave is along the y-direction and is exactly aligned with the conductance boundaries. Therefore a flux tube, that is set in motion by the Alfvén wave, is always exposed to the same conductance at its ionospheric foot point. Therefore, effects that can induce any two-dimensionality are negligible. Even though the system is two-dimensional the interaction of the Alfvén wave is one-dimensional and the two dimensional system could be

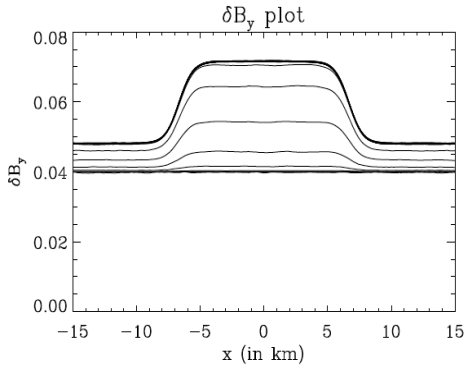

Figure 3.18: Case II: x-profile of total magnetic perturbation (after reflection) above the ionospheric boundary at $z = 20$ at equilibrium. Plotted between $t = 24$ and 52.

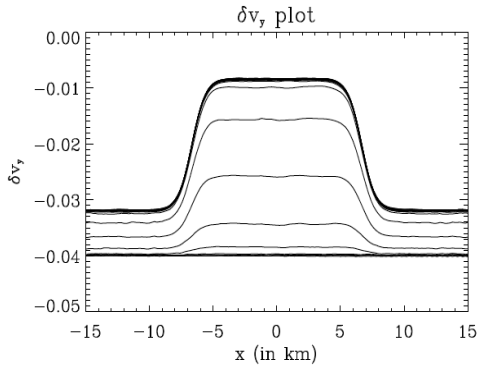

Figure 3.19: Case II: x-profile of total velocity perturbation (after reflection) above the ionospheric boundary at $z = 20$ at equilibrium. Plotted between $t = 24$ and 52.

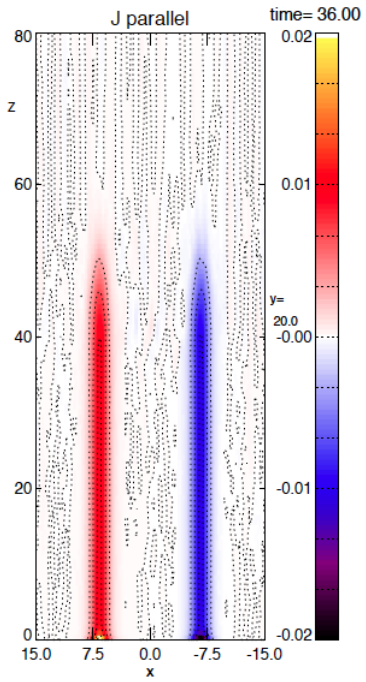

Figure 3.20: Case II: Generated FAC after reflection of the Alfvénic perturbations, at the locations of strong conductance gradient, in case II. These currents are present up to $z = 48$, that is, the region covered by the reflected waves. At $x = -6$, it is upward and at $x = +6$, it is downward. Plotted in the xz-plane at $y = 0$.

modeled by stacked field lines, where each has reflection conditions according to the specific value of the conductance at the ionospheric boundary. The next section considers a set of cases where

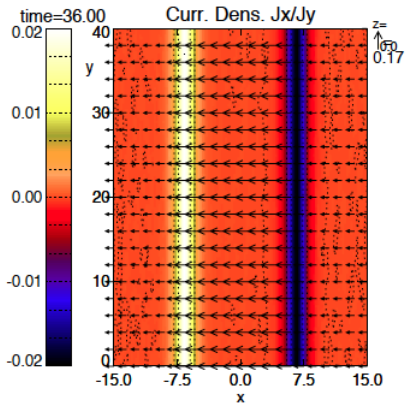

Figure 3.21: Case II: In the ionosphere, strong Pedersen current closes the FACs in region 2. The magnitude of the currents is shown by the arrow at the upper right corner outside the plot. Colors represent the z-components of the current that is perpendicular to the plane of the paper. Plotted in the xy-plane at $z = 0$ at time $t = 36$.

the polarization of the Alfvén wave is not aligned with a conductance boundary.

3.2.3 Case III: Uniform magnetospheric perturbations and nonuniform ionospheric Pedersen conductance (gradient in the y-direction)

In case III, the simulation domain differs from that in case I only in the boundaries along the y-direction. Here, these boundaries are located at $y = 0$ and $y = 60$ and it is noted that the system is periodic in the y-direction. As in case II, here too, a strip with imposed higher value of Pedersen conductance $\Sigma_{P,2}$ (region 2), is interlaid in a background (region 1) having a much lower value of Pedersen conductance $\Sigma_{P,1}$ but with a different orientation relative to the Alfvén wave polarization (see Figure 3.4). The following equations determine the choice of the conductance profile.

$$\Sigma(y) = \frac{(\Sigma_{P,2} - \Sigma_{P,1})}{2} tanh\left(\frac{y - 17}{3?}\right) + \frac{(\Sigma_{P,2} + \Sigma_{P,1})}{2} \tag{3.5}$$

for $y < 30$, and

$$\Sigma(y) = -\frac{(\Sigma_{P,2} - \Sigma_{P,1})}{2} tanh\left(\frac{y - 43}{3?}\right) + \frac{(\Sigma_{P,2} + \Sigma_{P,1})}{2} \tag{3.6}$$

for $y \geq 30$.

This choice determines a strip of high conductance $\Sigma_{P,2}$ $(= 2.25)$ between $y = 17$ and $y = 43$. Outside of this strip, the conductance has a lower value of $\Sigma_{P,1}$ $(= 0.375)$ as illustrated in Figure 3.24. Correspondingly the reflection coefficients (r) in region 1 and region 2 are ≈ 0.2 and ≈ 0.8, respectively. In this figure, the direction of magnetic perturbation or polarization (δB_y) is indicated by arrows. The widths of the different zones, along the y-direction, are marked as d_1, d_2, and d_3.

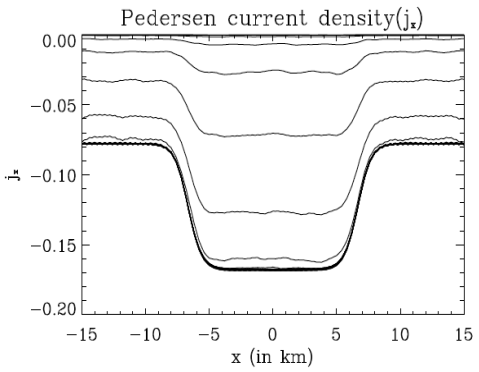

Figure 3.22: Case II: x-profiles of Pedersen current density (j_x) at the ionospheric boundary between time $t = 22$ and 52.

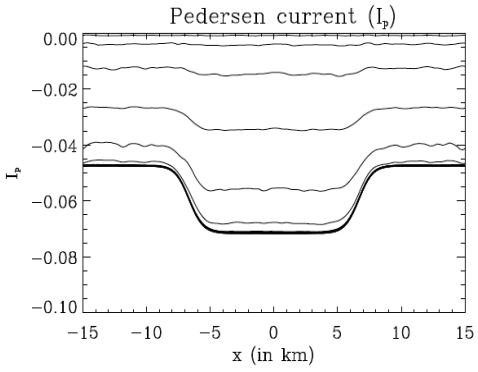

Figure 3.23: Case II: x-profiles of the ionospheric Pedersen current ($I_{P,x}$) between time $t = 22$ and 52.

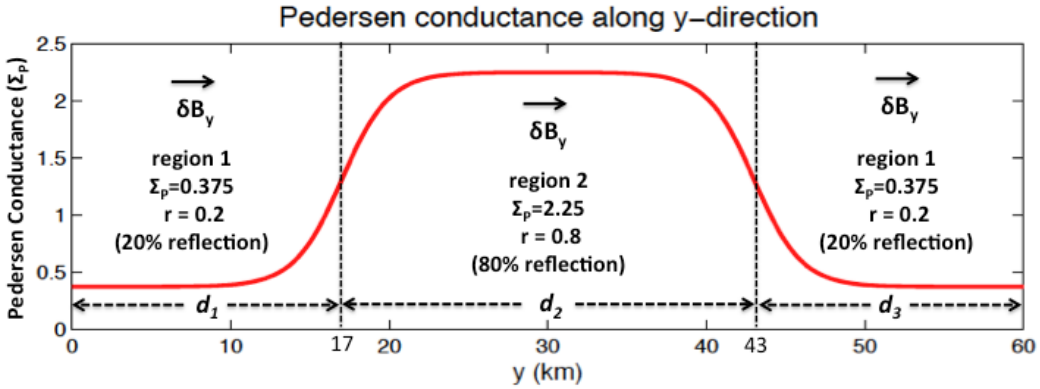

Figure 3.24: Case III: y-profile of the Pedersen conductance imposed at the ionospheric boundary. Here the magnetic and velocity perturbations (δB_y and δv_y) are parallel to the y-direction (direction of the magnetic perturbation is shown by the arrows).

As in case II, the magnetic and velocity perturbations are uniform and the initial conditions for the magnetic field and the velocity are identical to case II. Note that in this case no significant FACs are expected because the configuration (incident wave and conductance pattern) has no gradient along x.

After reflection from the ionosphere, the incident and reflected perturbations, δB_y and δv_y, are superposed but these superposed waves have very different properties compared to case II. A plot of the total magnetic perturbation is shown in Figure 3.25. This figure is a snap-shot at time $t = 36$ and shows the superposed waves (perturbations) about 12 Alfvén-times after reflection (at $t \approx 24$). At this time the reflected wavefronts reach a height of $z \approx 48$ and above this height only the incident perturbations are present. Comparing Figure 3.25 and Figure 3.16 it is evident that

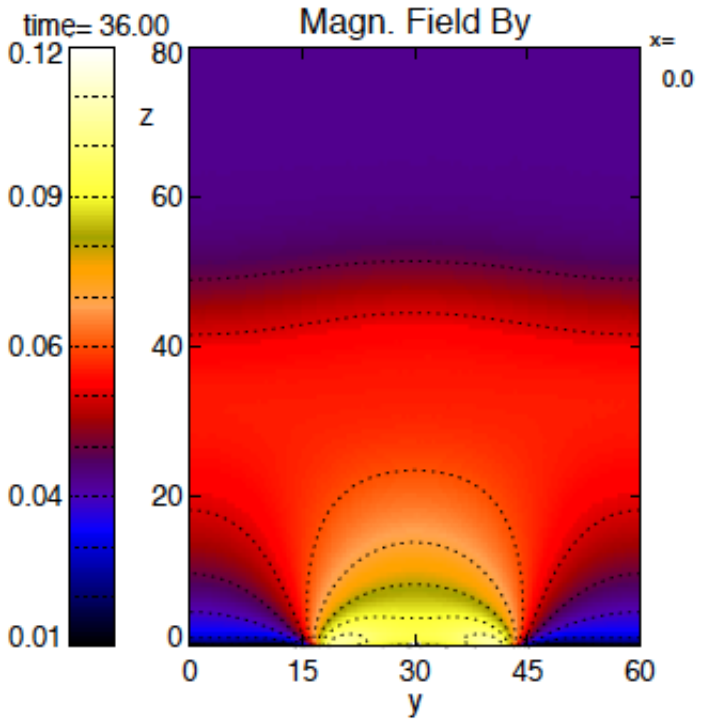

Figure 3.25: Case III: Plot of total magnetic perturbation (δB_y) after reflection in the yz-plane at $x = 0$. The superposed magnetic perturbation covers up to $z = 48$ at the time ($t = 36$) of the plot.

the upward propagations of the reflected (and superposed) magnetic perturbations, in case II and case III, are different. However, in case III, the perturbation is nonuniform with a dome shaped maximum right above the enhanced conductance region (and confined by the region) and with a strong gradient in the vertical direction that is not associated with the edge of the wave front. Also slightly above the ionosphere, the perturbation is not anymore confined to the perimeter of the high conductance region but spread out over the entire length of the simulation domain along y.

The time variation of the magnetic perturbation, near the ionospheric boundary is different from the variation at a higher level. Figure 3.26 illustrates the time evolution of the y-profile of δB_y at $z = 1.6$ starting from the beginning of reflection at times, $t = 28$ to 72. In this figure, the plots are separated by $\Delta t = 4$. Immediately after the reflection, the values of δB_y is consistent with the local reflection conditions imposed by Σ_P. These values are ≈ 0.046 and ≈ 0.072, respectively, in region 1 and region 2. But, gradually, δB_y increases to a higher value in region 2 and decreases to a lower value in region 1 to reach a steady state value. The equilibrium values of δB_y in regions 1 and 2 are ≈ 0.023 and ≈ 0.118, respectively. The significance of these plots is further discussed later.

The structure shown in Figure 3.25 is further examined in Figure 3.27 showing the propagation

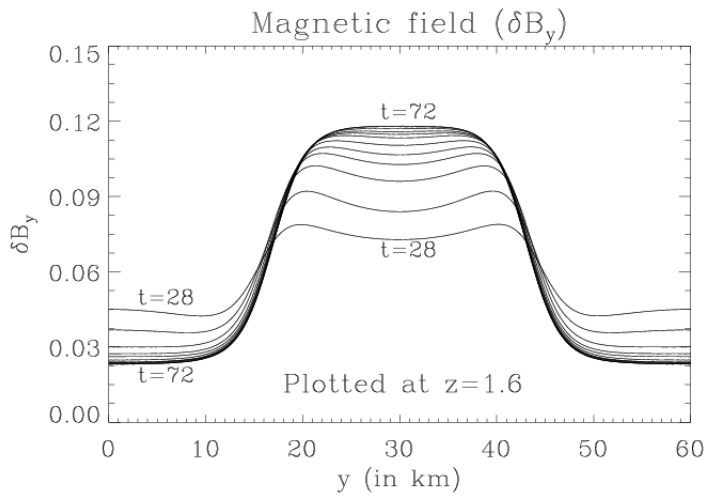

Figure 3.26: Case III: Monotonic time evolution of the y-profile of magnetic perturbation (δB_y) near the ionospheric boundary after reflection. Plots are taken at $x = 0$ and $z = 1.6$ between times $t = 28$ and 72 in an interval of $4t_{A0}$. The equilibrium value of δB_y in region 2 is higher than its initial value while it is smaller than the initial value in region 1.

of the magnetic perturbation in a series of snapshots (in a cut at $x = 0$). The 6 plots show the evolution of the magnetic field between $t = 28$ and $t = 48$ at intervals of 4 Alfvén times. These plots show the persistence of the dome shaped magnetic field perturbation close to the lower boundary while the perturbation becomes uniform at larger distances as time proceeds.

Figure 3.28 illustrates the evolution of the velocity perturbation in a series of snapshots above the conducting ionosphere in the yz-plane at $x = 0$ at intervals of 4 Alfvén times (from $t = 28$ to $t = 48$). These plots illustrate that the velocity perturbation evolves quite differently from the magnetic field perturbation. While a dome shaped velocity structure is clearly present early after the reflection, this structure fades at later times and the velocity perturbation becomes fairly uniform in the entire region above the differently conducting boundary regions.

The evolution of velocity perturbations with time, at the ionospheric boundary (on the xy-plane) is shown in Figure 3.29. This figure shows the plots of total velocity at the ionospheric boundary at four different times ($t = 28,\ 32,\ 36$ & 40) after the reflection.

Two interesting aspects are evident from the magnetic field and velocity results (Figures 3.27, 3.28, and 3.29). Firstly, at the lower boundary and early after the reflection, the magnetic and velocity perturbations appear consistent with the local reflection conditions implied by the local values of the imposed conductance, Σ_P. This implies that both magnetic and velocity perturbations are different above regions 1 and 2 conductances. But, secondly, the velocity perturbation (δv_y) assumes a uniform value covering both the regions (1 and 2) at later times. This implies the

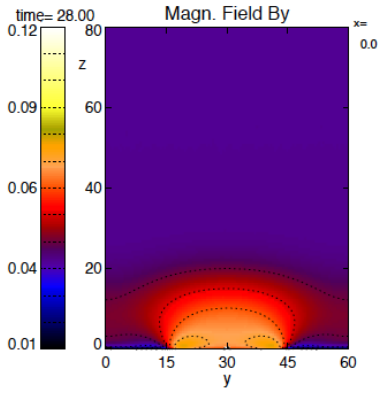

(a) $t = 28$

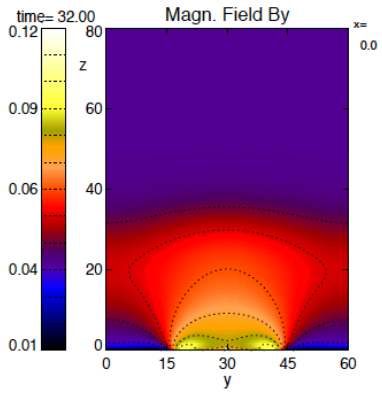

(b) $t = 32$

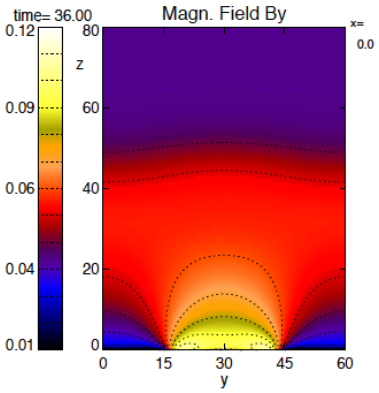

(c) $t = 36$

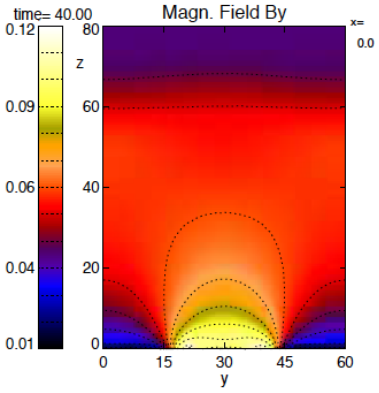

(d) $t = 40$

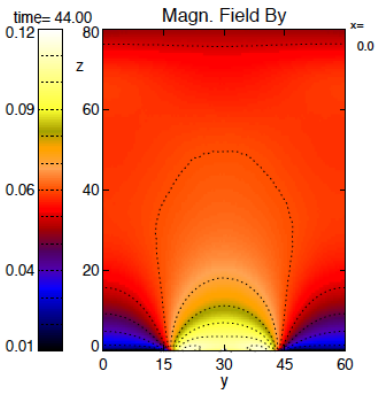

(e) $t = 44$

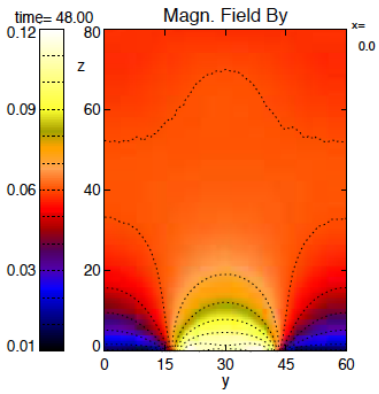

(f) $t = 48$

Figure 3.27: Case III: Time evolution of magnetic perturbation after reflection. The plots in the yz-plane are taken at the middle of the simulation domain ($x = 0$) at different times (shown below the plots).

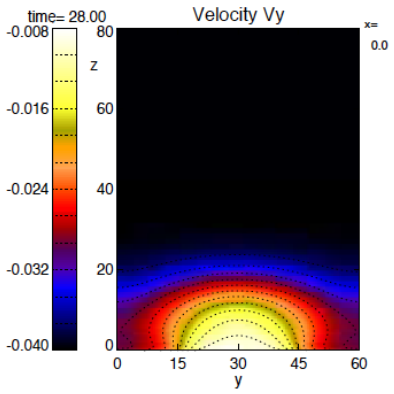

(a) $t = 28$

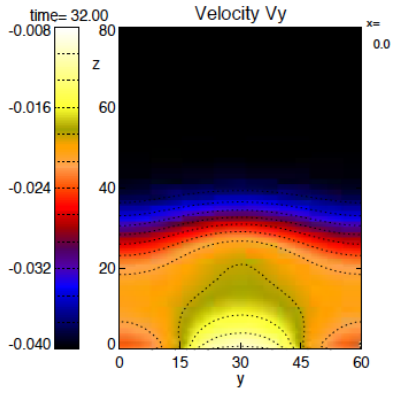

(b) $t = 32$

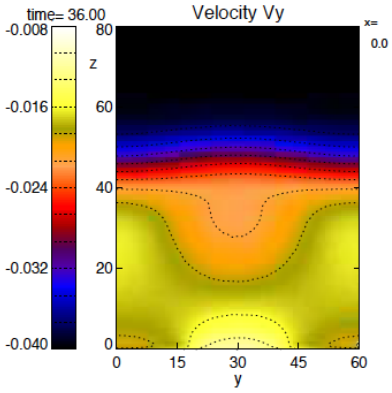

(c) $t = 36$

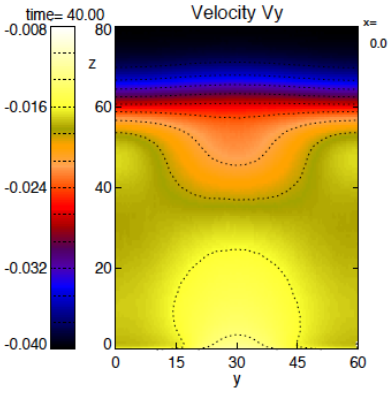

(d) $t = 40$

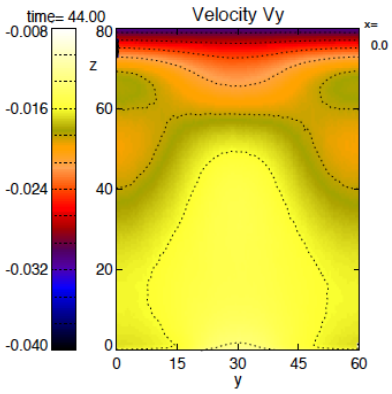

(e) $t = 44$

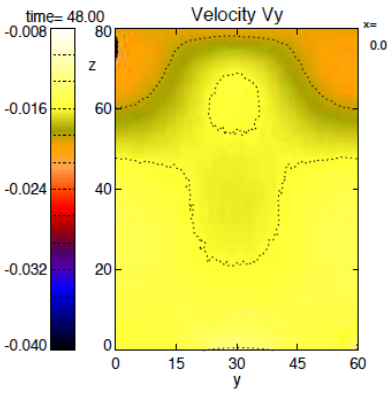

(f) $t = 48$

Figure 3.28: Case III: Time evolution of velocity perturbation after reflection. The plots in the yz-plane are taken at the middle of the simulation domain ($x = 0$) at different times (shown below the plots).

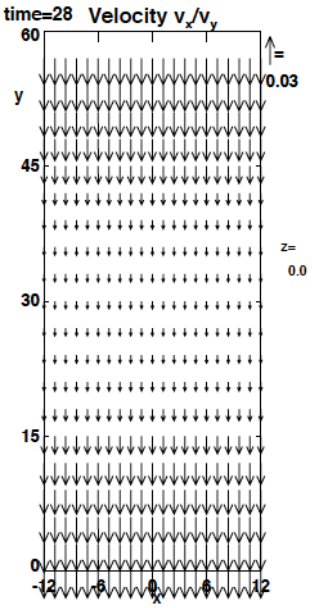

(a) $t = 28$

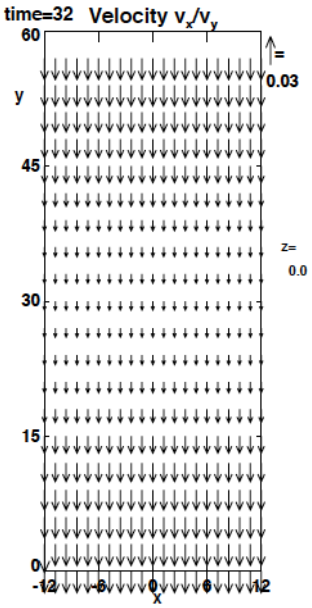

(b) $t = 32$

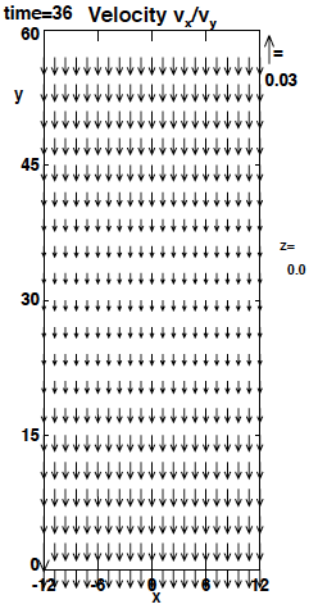

(c) $t = 36$

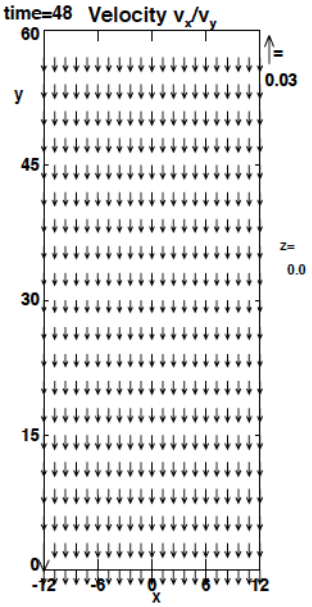

(d) $t = 48$

Figure 3.29: Case III: Variation of velocity perturbation at the ionospheric boundary with time after reflection. The plots in the xy-plane at $z = 0$ are taken at different times (shown below the plots). The velocity gradually becomes uniform over the different zones.

existence of a uniform steady state value for the electric field ($E_x = -\delta v_y B_z$) above both regions at the ionospheric boundary, according to Equation (2.47), because the strength of the guide field, B_z, remains constant and unchanged. This steady state is assumed on a time scale of 4 to 8 t_{A0} which is approximately the fast mode travel time over the width of the different conductance strips. Figure 3.30 illustrates the change of the y-profile of the velocity perturbation (δv_y), at the ionospheric boundary at $z = 0$, with time. Each line in the figure shows a snapshot of the velocity

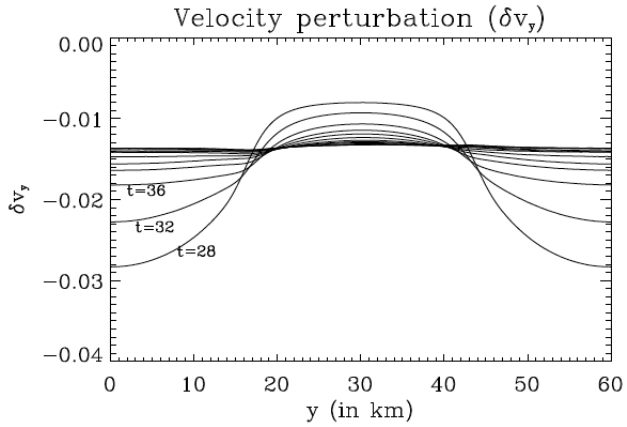

Figure 3.30: Case III: Time evolution of the y-profile of total velocity perturbation at the lower boundary (at $z = 0$) after reflection. The line plots are separated by 4 Alfvén times and gradually attain a uniform steady value (≈ 0.0135) at equilibrium.

profile and the profiles are separated by time-intervals of 4 Alfvén times. The profile converges to a steady-state value of the perturbation of $\delta v_y \approx -0.0135$ (in normalized unit). Plots for the electric field is expected to follow a similar pattern and is shown in the later part. Based on Alfvén wave reflection, a uniform velocity perturbation of the same value should only be obtained if the entire lower boundary is set at a certain uniform value of the Pedersen conductance (Σ_P).

A closer inspection reveals that this value of Σ_P is same as the width-average value ($\Sigma_{P,average}$) of the applied Pedersen conductance (Σ_P) such that

$$\Sigma_{P,average} = \frac{d_1\Sigma_{P,1} + d_2\Sigma_{P,2} + d_3\Sigma_{P,1}}{d_1 + d_2 + d_3} \tag{3.7}$$

where d_1, d_2 and d_3 are the widths of the zones with different values of Σ_P as shown in Figure 3.24. For the present case $d_1 = d_3 = 17$ and $d_2 = 26$ with $\Sigma_{P,1} = 0.375$ and $\Sigma_{P,2} = 2.25$. Using Equation 3.7, the average value of the Pedersen conductance ($\Sigma_{P,average}$), is nearly 1.1875. A plot of the total velocity perturbation, δv_y, after reflection using a uniform conductance of $\Sigma_P = 1.1875$, is shown in Figure 3.31. This value of Σ_P produces a reflection coefficient (r) ≈ 0.65, according to Equation (2.53) and the corresponding value of total velocity is $\delta v_y = -0.0136$ which is in excellent agreement with the steady state value of the total velocity perturbation for the different conductance strips.

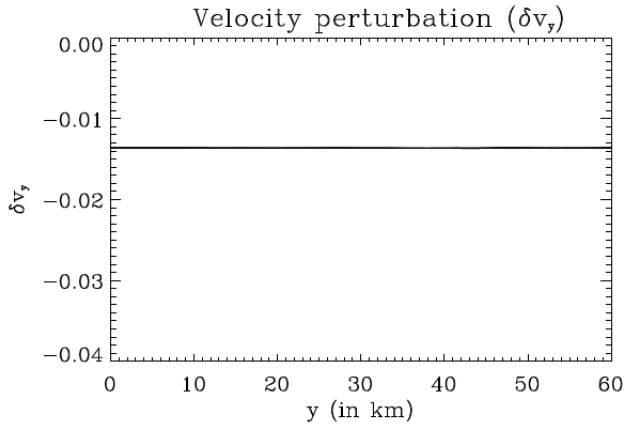

Figure 3.31: Case III: y-profile of the total velocity perturbation at the lower boundary for average uniform Pedersen conductance $\Sigma_{P,average} = 1.1875$. This value is obtained following Equation 3.7. The line plots attain a uniform value ($\delta v_y = \approx 0.0136$) after the reflection.

This result implies that the steady state electric field, E_x, in case III, depends on the relative widths of region 2 and region 1 along with the values of the ionospheric conductance. Therefore, the Pedersen currents ($I_{P,x}$) are different for the different regions because $I_{P,x} = \Sigma_P E_x$. As the value of Σ_P is much higher in the middle zone (region 2), $I_{P,x}$ also has a larger magnitude in the region 2.

Following the discussion and results shown in the previous chapter (Subsection 2.2.4) the Pedersen current $I_{P,x} = -\delta B_{y,i_z=9}$. Therefore the y-profiles of δB_y at $z(9) = 1.6$ in Figure 3.26 exactly represent the corresponding plots for magnitude of $I_{P,x}$ and the discussion on δB_y there become applicable for $I_{P,x}$. The negative sign in $I_{P,x} = -\delta B_{y,i_z=9}$ implies that the Pedersen current is in the negative x-direction. These results then demonstrate that the Pederesen current is enhanced by more than 50% compared to the simple reflection conditions and is about 5 times the value in the low conductance region for this example.

With the increase in the height integrated Pedersen current, in region 2, a high value (compared to that in case II) of the Pedersen current density, j_x, is also expected. In Figure 3.33, the y-profile of the Pedersen current density, j_x, at the ionospheric boundary is illustrated by the green line, after the equilibrium is attained (at $t = 72$). The full description of that figure is given in the next section. This plot shows the presence of a strong Pedersen current density in region 2 accompanied by a much smaller Pedersen current density in region 1 at the ionospheric boundary. So, it can be concluded that the orientation of a gradient in Pedersen conductance has a strong influence on the Pedersen current. It is interesting to study the influence of the width, d_2, on the value of $I_{P,x}$ and j_x, which is explored in the next section.

Influence of the width of the middle-zone (with higher conductance)

The width of region 2 (in case III) is now varied to study its effects on the strength of the Pedersen current. It is anticipated that a decrease of the width, d_2, of the high conductance region 2 should increase the stationary value of the electric field (E_x) which should enhance the value of the Pedersen current ($I_{P,x}$) in both region 1 and region 2. That is, a decrease of d_2 and the corresponding increase of d_1 and d_3, keeping the total width of the entire zone ($d_1 + d_2 + d_3$) unchanged, reduces the value of $\Sigma_{P,average}$ or the average reflection coefficient ($r_{average}$). The total velocity perturbation, after reflection, is $(-1 + r_{average})\delta v_{y0}$, such that a decrease of $r_{average}$ results in an increase of the velocity perturbation.

This, in turn, produces a larger (and uniform) magnitude of E_x, in the steady state, as shown in Figure 3.32. The plots in this figure show the change of the y-profile with time, at the lower boundary and at $x = 0$. The widths (d_2) of region 2 are chosen from (a) $y = 13$ to 47 ($d_2 = 34$), (b) from $y = 17$ to 43 ($d_2 = 26$) and, (c) from $y = 21$ to 39 ($d_2 = 18$). In these three cases, the middle zones are refered as *wide*, *medium*, and *narrow*, respectively. The plots indicate that the decrease of the width of the region 2 enhances the magnitude of uniform stationary value of E_x to 0.047 for (a), 0.055 for (b) and 0.067 for (c). This results in larger Pedersen currents in both regions as the region 2 becomes narrower.

Figure 3.33 illustrates the y-profile of the Pedersen current density, j_x, at the ionospheric boundary ($z = 0$) for these three cases. This figure indicates that, unlike case II, the narrowing of the high conductance (middle) zone (d_2) has a great influence on the strength of the Pedersen current when the Alfvén wave polarization is parallel to the gradient of the Pedersen conductance.

For convenience, the estimated quantities for the average values of the Pedersen conductance ($\Sigma_{P,average}$), the reflection coefficients ($r_{average}$), the steady state (uniform) values of the velocity perturbations at the lower boundary (δv_y), the steady state electric fields (E_x) at the lower boundary, and the height integrated Pedersen currents in region 1 ($I_{P,x,1}$) and in region 2 ($I_{P,x,2}$) are shown in Table 3.1. The columns for $I_{P,x,1}$ and $I_{P,x,2}$ show extra quantities within the parenthesis. These are the values from the simulation results.

The plots in Figure 3.34 show the Pedersen currents for the three different widths of region 2. The values obtained from the simulations are close to the estimated values but for the region 1s, the values are slightly bigger than the estimated values while they are marginally smaller for the region 2s.

An influence of the width of the highly conducting layer is not expected for situations corresponding to case II where the wave polarization is perpendicular to the gradient of the conductance. In this case (III) Alfvén wave reflection conditions have been shown to agree well with our simulation result

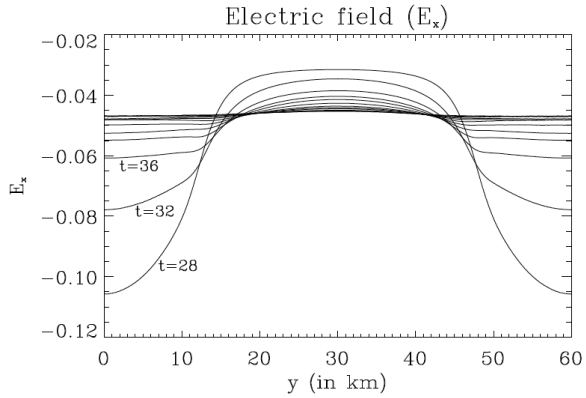

(a) region 2: *wide* ($y = 13$ to 47). Equilibrium value of $E_x \approx -0.047$.

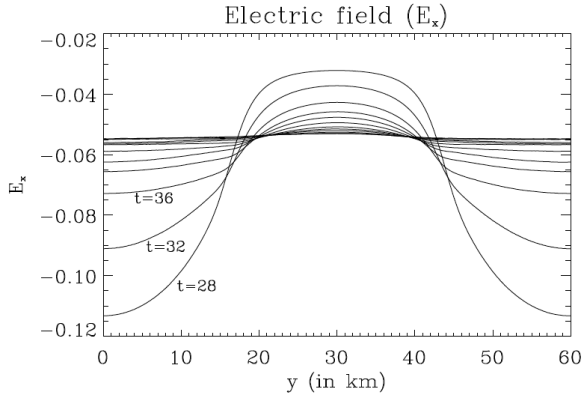

(b) region 2: *medium* ($y = 17$ to 43). Equilibrium value of $E_x \approx -0.055$.

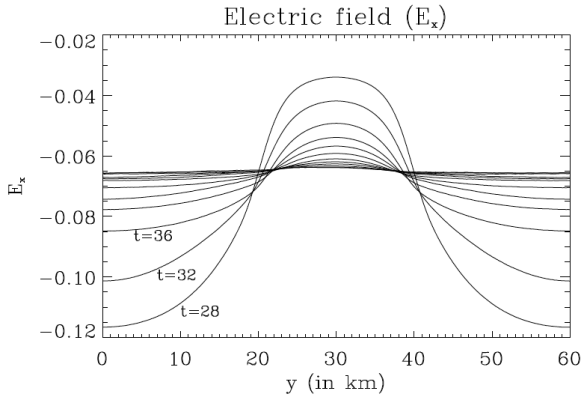

(c) region 2: *narrow* ($y = 21$ to 39). Equilibrium value of $E_x \approx -0.067$.

Figure 3.32: Case III: Time evolutions of y-profiles of the electric fields (E_x) for different widths (d_2) of region 2. With decreasing width the magnitude of the equilibrium value of the electric field (E_x) increases.

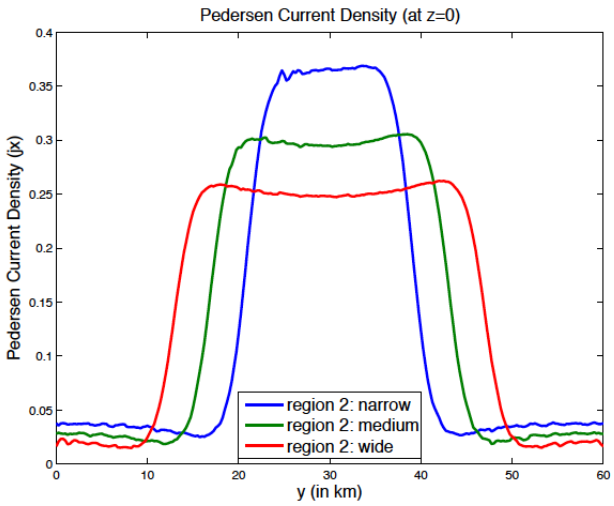

Figure 3.33: Case III: Comparison of Pedersen current densities (j_x) for different widths (d_2) of region 2 (having higher Pedersen conductance).

within the numerical accuracy. However, to further manifest this argument, Figure 3.35 shows the invariance of the value of $j_{\parallel}$ with change of the value of d_2 in case II. In these plots the region 2s are from $x = -9$ to $x = +9$ for the *wide*-width, from $x = -6$ to $x = +6$ for the *medium*-width and from $x = -3$ to $x = +3$ for the *narrow*-width. This figure shows the x-profiles of $j_{\parallel}$ at $z = 20$ and at the middle of the simulation domain (i.e. at $y = 20$). In these three plots identical upward and downward FACs are observed, without any difference except in their on the x-axis. When the fully superposed waves travel past the height at which the plots are taken (here, $z = 20$), the magnitudes of $j_{\parallel}$ attain ≈ 0.01 (normalized value) for all the 3 cases. Consequently, the Pedersen current, that closes the upward and downward FACs at the ionosphere, are expected to be the same. A similar comparison with the plots of the Pedersen currents ($I_{P,x}$) for the different widths of region 2 is shown in Figure 3.36. In these plots, the x-profiles of the Pedersen currents for the different values of d_2 are shown. These plots confirm that the change of d_2 has no effect on the magnitudes of $I_{P,x}$ in case II. The magnitudes of $I_{P,x}$ for different values of d_2 remain ≈ 0.071 in region 2 and ≈ 0.047 in region 1. So, their ratio also remains constant at ≈ 1.51. These results show that the values of $I_{P,x}$ remain consistent with the values of Σ_P for the different zones and follow the relation shown in Equation (2.58) irrespective of the width of region 2, in case II. In the next section, the interaction of the nonuniform magnetospheric perturbations with the ionosphere having a nonuniform Pedersen conductance is studied.

Table 3.1: Case III: Variation of different quantities with the change of d_2. This table shows the average values of Pedersen conductance ($\Sigma_{P,average}$), reflection coefficient ($r_{average}$), the superposed values of the velocity perturbation (δv_y) at $z = 0$ at equilibrium, the electric field (E_x) at $z = 0$ at equilibrium, and the Pedersen currents in region 1 and region 2 ($I_{P,x,1}$ and $I_{P,x,2}$) for different widths (d_2) of the region 2 in case III.

conductance pattern	$\Sigma_{P,average}$	$r_{average}$	δv_y	E_x	$I_{P,x,1}$	$I_{P,x,2}$
region 2: *wide* $d_2 = 34$ & $d_1 = d_3 = 13$	1.44	0.70	-0.012	0.048	0.018 (0.021)	0.108 (0.099)
region 2: *medium* $d_2 = 26$ & $d_1 = d_3 = 17$	1.19	0.65	-0.014	0.056	0.021 (0.024)	0.126 (0.117)
region 2: *narrow* $d_2 = 18$ & $d_1 = d_3 = 21$	0.94	0.58	-0.017	0.067	0.025 (0.028)	0.151 (0.134)

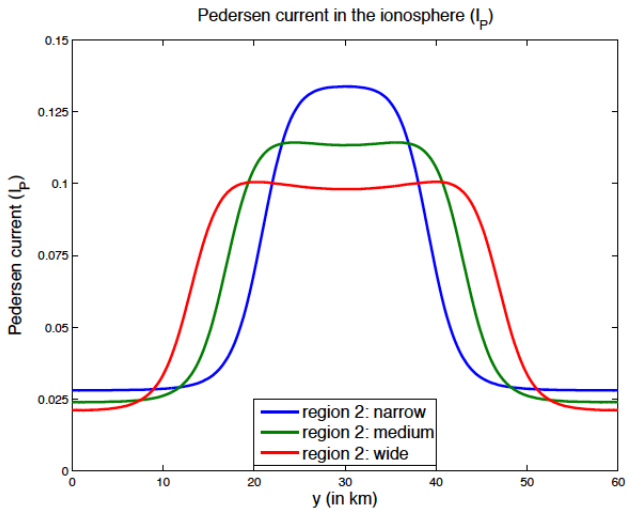

Figure 3.34: Case III: Comparison of ionospheric Pedersen currents ($I_{P,x}$) for different widths d_2 of region 2 (having higher Pedersen conductance).

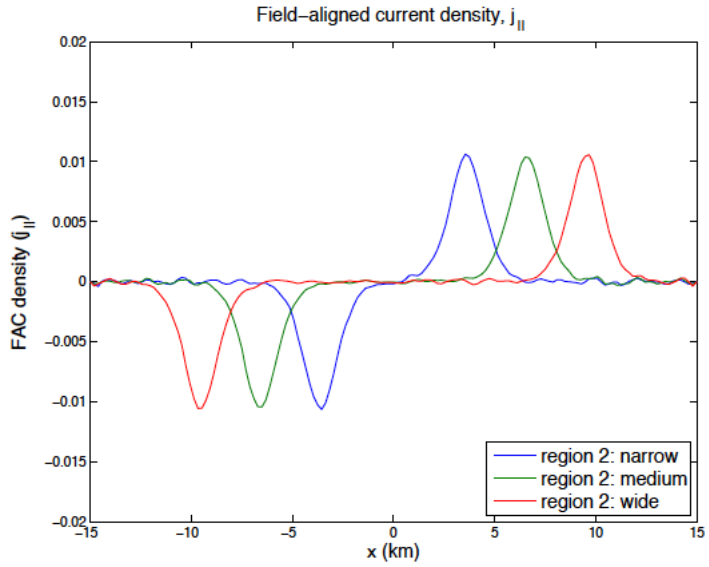

Figure 3.35: Case II: x-profiles of the FAC densities ($j_{\|}$) for different widths d_2 of region 2 at $z = 20$ and $y = 20$ at time $t = 52$. The magnitudes of $j_{\|}$ remain same in spite of the width-change.

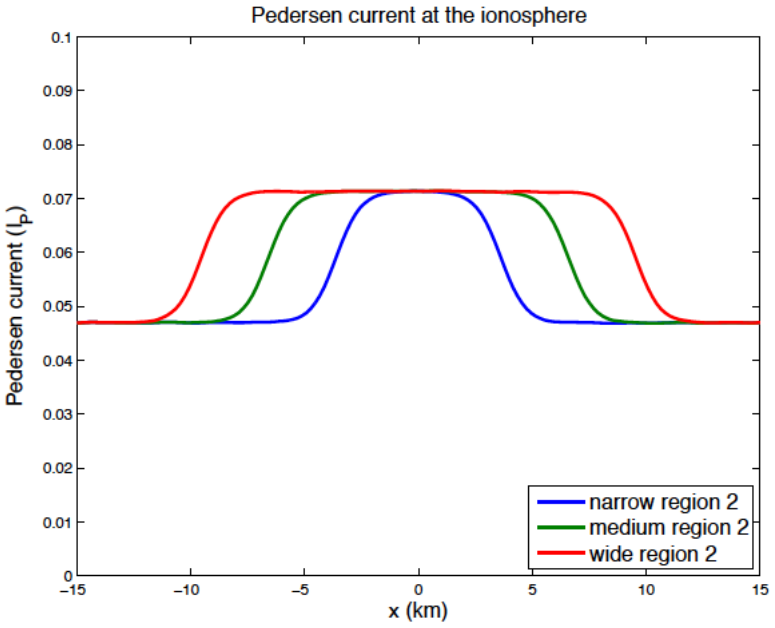

Figure 3.36: Case II: Comparison of ionospheric Pedersen current ($I_{P,x}$) for different widths d_2 of region 2. These plots show that the magnitude of $I_{P,x}$ does not change with d_2 in this case and remain consistent with the local values of Σ_P.

3.2.4 Case IV: Nonuniform magnetospheric perturbations and nonuniform ionospheric Pedersen conductance (gradient in the y-direction)

In view of the prior results, it appears interesting to examine a case where a FAC imposed by a magnetospheric generator interacts with an ionospheric conductance gradient. Case IV is, effectively, a combined form of case I (with respect to the magnetospheric perturbations) and case III (with respect to the ionospheric Pedersen conductances) as shown in Figure 3.4. Here the simulation domain is exactly the same as that used in case I. The perturbations from the magnetosphere are also the same as those used in case I (as illustrated in Figure 3.3) following Equations (3.1) and (3.2). This case is different from the case I at the lower boundary only. Instead of a uniform Pedersen conductance a nonuniform Pedersen conductance having the pattern used in case III is used here. So, the ionospheric boundary has a Pedersen conductance with a gradient in the y-direction as illustrated in Figure 3.24 with some minor differences including the values of d_1, d_2 or d_3 which will be mentioned shortly.

As illustrated in the figure, a strip of high conductance separates two regions with a much lower conductance value. Equations (3.8) and (3.9) determine the profile of Pedersen conductance at the ionospheric boundary as a function of y.

$$\Sigma(y) = \frac{(\Sigma_{P,2} - \Sigma_{P,1})}{2} tanh\left(\frac{y-12}{3}\right) + \frac{(\Sigma_{P,2} + \Sigma_{P,1})}{2} \tag{3.8}$$

for $y < 20$ and,

$$\Sigma(y) = -\frac{(\Sigma_{P,2} - \Sigma_{P,1})}{2} tanh\left(\frac{y-28}{3}\right) + \frac{(\Sigma_{P,2} + \Sigma_{P,1})}{2} \tag{3.9}$$

for $y \geq 20$ such that region 2, having the higher Pedersen conductance, $\Sigma_{P,2} = 2.25$, extends from 12 to 28 along y. The background conductance, $\Sigma_{P,1} = 0.375$. With the chosen values, the reflection coefficient (r) at region 1 is ≈ 0.2 ($\approx 20\%$ reflection of the incident waves) and at region 2 is ≈ 0.8 ($\approx 80\%$ reflection of the incident waves). Thus the ionosphere has a nonuniform Pedersen conductance with a gradient in the y-direcion as in case III.

On either side of $x = 0$, the configuration is similar to the simulation setup for case III. But in these two halves, the polarization of the Alfvén waves are in the opposite directions. Thus, it is expected that away from the boundary, at $x = 0$, the results are similar to those in case III.

The evolution of the magnetic and velocity perturbation for this case (IV) is the same as for case I before reflection (Figures 3.5 and 3.6) because the magnetospheric boundary is the same. For the same reason the FAC transport is the same before reflection from the ionospheric boundary (see Figure 3.7).

The reflection at the lower ionospheric boundary is expected to be interesting in this case because the conductance gradient can cause a large Pedersen current as illustrated in case III. The effect

is explored. First, by the total magnetic field perturbation, after the reflection, at four different altitudes, in Figure 3.37. These plots show the total magnetic field perturbation, at time, $t = 36$,

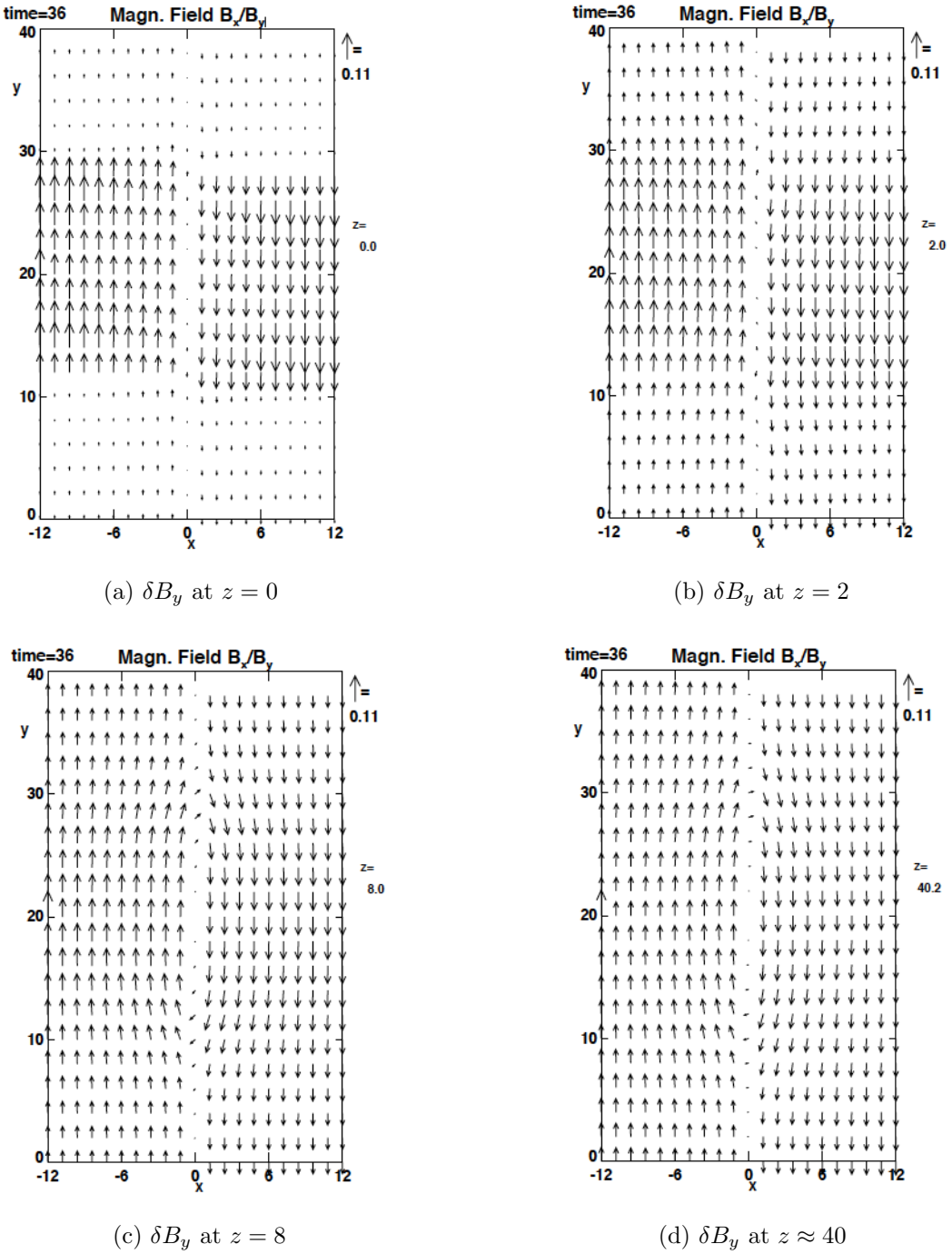

(a) δB_y at $z = 0$

(b) δB_y at $z = 2$

(c) δB_y at $z = 8$

(d) δB_y at $z \approx 40$

Figure 3.37: Case IV: Plots of total magnetic perturbations at different altitudes above the ionospheric boundary. These plots at $t = 36$ in the xy-planes at four different altitudes (shown below the plots) illustrate that the magnetic perturbations gradually attain a uniform value with increasing height in case VI.

and at the altitudes $z = 0$, $z = 2$, $z = 8$, and $z \approx 40$. The figure demonstrates that the magnetic field perturbations near the lower boundary, are different in different conductance zones and do not change, significantly, with time. A closer inspection reveals that the perturbation values are consistent with the imposed ionospheric reflection condition only close to the central vertical plane (at $x = 0$). Away from $x = 0$, the magnetic perturbation gradually increases and decreases, respectively, in region 2 and 1 from its estimated value following $\delta B_y = \delta B_{y0}(1 + r)$, at a slow rate. However, the magnetic perturbation clearly varies with height similar to case III (although in opposite directions on the two sides of $x = 0$ boundary). On both sides of this boundary, the magnetic perturbation, gradually, attains some intermediate uniform value with increasing height.

A plot of magnetic perturbation representing a cut in the yz-plane at $x = -6$ at the same time ($t = 36$) provides additional insight in Figure 3.38. The figure demonstrates that the magnetic

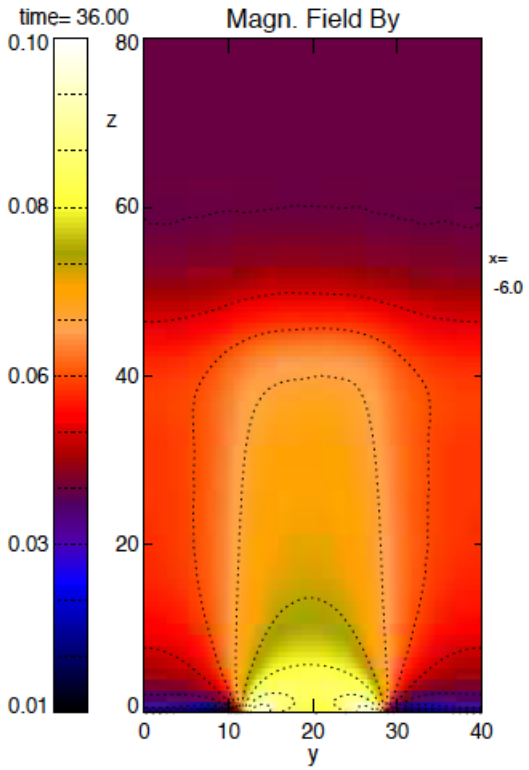

Figure 3.38: Case IV: Plot of total magnetic perturbation (δB_y) after reflection. This plot is taken in the yz-plane $atx = -6$. The total magnetic perturbation covers up to $z = 48$ at the time ($t = 36$) of the plot.

perturbation tends to be more uniform (in the two regions) with increasing altitude. It is seen that this tendency is stronger, away from the junction-plane between the oppositely directed perturbations at $x = 0$. A similar phenomenon happens on the other half of the simulation domain (that is

from $x = 0$ to $x = 12$) with the perturbation-direction being opposite.

The time evolutions of the x-profiles of δB_y, close to the ionospheric boundary, in region 1 and 2 are not similar and have some interesting feature. Figure 3.39 illustrates the variation of x-profiles δB_y with time at $z(9) = 1.6$ in the two regions. In both regions and on both sides of $x = 0$, the

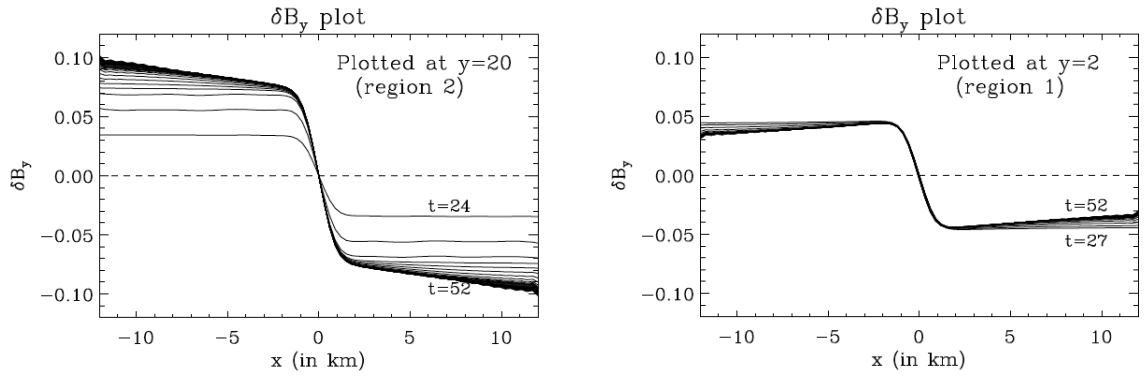

(a) At $y = 20$ (in region 2).

(b) At $y = 2$ (in region 1).

Figure 3.39: Case IV: Time evolutions of the x-profiles of magnetic perturbation (δB_y) above ionospheric boundary ($z = 1.6$) (a) at $y = 20$ (region 2) and (b) at $y = 2$ (region 1). In both cases, the equilibrium values of δB_y develop a small gradient outside the current sheet too.

magnetic perturbations attain the estimated (based on the value of Σ_P in that region) total value after reflection (at $t \approx 27$). But after that, δB_y gradually develops a small gradient $\left(\frac{\partial \delta B_y}{\partial x}\right)$ along the x-direction while reaching the equilibrium. In region 1 and 2, the gradients, $\frac{\partial \delta B_y}{\partial x} > 0$ and $\frac{\partial \delta B_y}{\partial x} < 0$, respectively. Following Ampere's law ($\nabla \times \mathbf{B} = \mathbf{j}$) there should be a small amount of FAC ($j_\parallel$) outside the current sheet also, due to the nonzero value of this gradient. This is verified from the plots for $j_\parallel$ in the later part.

In order to examine the velocity perturbation, Figure 3.40 shows plots in the xy-plane at the lower boundary and at three other altitudes. In case III the velocity was to assume a uniform equilibrium value over the entire region of the ionosphere after a short time from the start of the reflection. In the present case, the velocity perturbation remains different over regions 1 and 2, at least at the locations close to the central plane at $x = 0$, also at later times. Instead of assuming a uniform flow across the conductance boundaries as in case III, a part of the flow is deflected here. At the high conductance boundaries, the convection develops strong vortices, which deflect a large fraction of the flow into the opposite direction across the incoming FAC region. Figure 3.40 indicates that this horizontal convection profile is almost uniform in altitude. This impression is confirmed by Figure 3.41 which shows the altitude profile of the velocity perturbation in the yz-plane at $x = -6$ and time $t = 36$. This plot illustrates that the total velocity perturbation, after the reflection is indeed

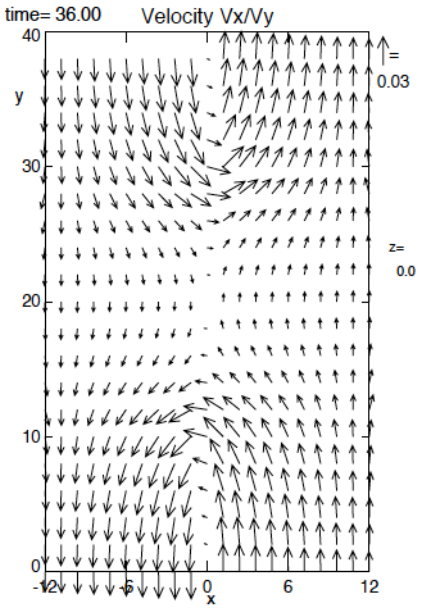

(a) δv_y at $z = 0$

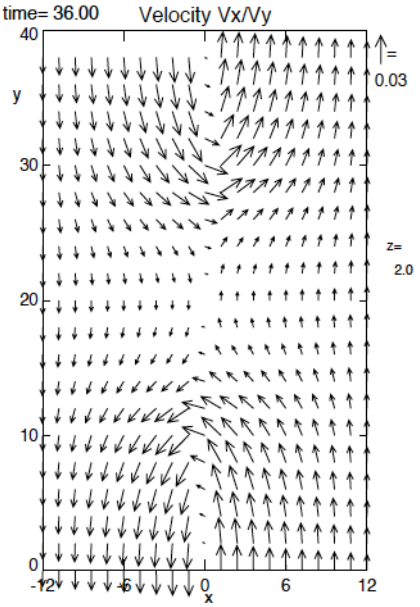

(b) δv_y at $z = 2$

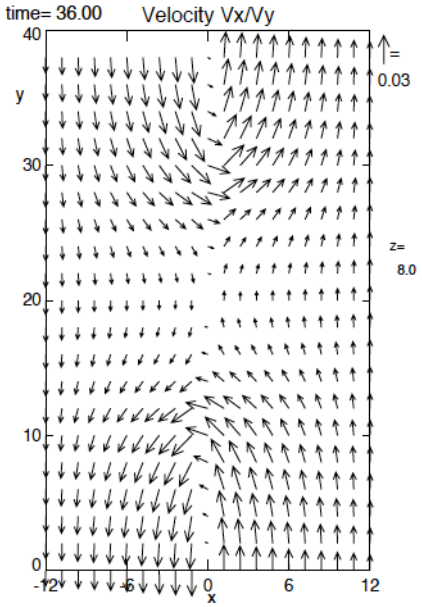

(c) δv_y at $z = 8$

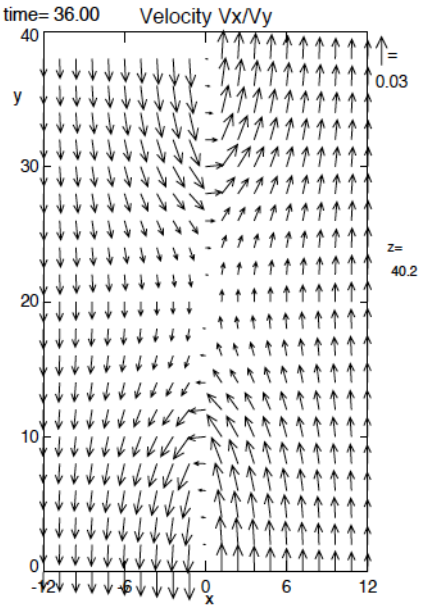

(d) δv_y at $z \approx 40$

Figure 3.40: Case IV: Plots of total velocity perturbations at different altitudes above the ionospheric boundary. These plots at $t = 36$ in the xy-planes at different altitudes (shown below the plots) illustrate that the velocity perturbations remain different in different conductance regions with increasing height.

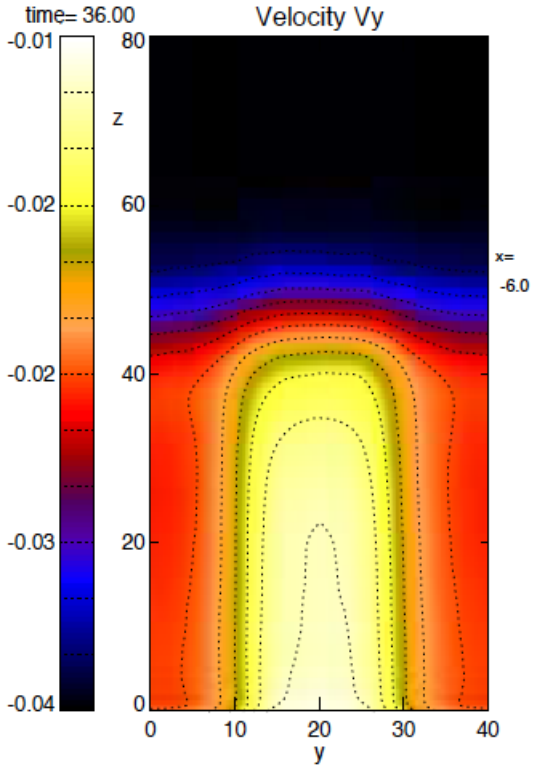

Figure 3.41: Case IV: Plot of total velocity perturbation (δv_y) after reflection. This plot is taken in the yz-plane at $x = -6$. The total velocity perturbation covers up to $z = 48$ at the time ($t = 36$) of the plot.

fairly uniform in height.

Further insight is provided by Figure 3.42. Figures 3.42a and 3.42b illustrate the y-profiles of the velocity perturbations (δv_y), respectively, at $x = -1.5$ and $x = -12$. Here different lines represent the y-profiles at different times between $t = 32$ and $t = 52$. Comparing these two plots, it is seen that the total velocity perturbation is distinctly different over the two conductance regions close to the central plane at $x = 0$ and varies little with time. With increasing distance from this central plane, the perturbation tends to be more uniform. The average magnitude of velocity perturbation (shown in the respective plots by dotted lines) decreases from 0.0187 at $x = -1.5$ to 0.0165 at $x = -12$. This trend is consistent such that far away from the central plane, the velocity approaches the uniform stationary value of $\delta v_y \approx -0.01456$ as was observed in case III (as shown in Figure 3.30). These plots also indicate that the velocity increases with the distance from $x = 0$ in region 2 and decreases in region 1. Note that the electric field (E_x) profile is similar to the velocity profile because it is given by $E_x = -\delta v_y B_z$ and the B_z (dipole) component remains basically unchanged. So, in region 2 the magnitude of Pedersen current, $I_{P,x}, (= \Sigma_P E_x)$ is expected to increase with the

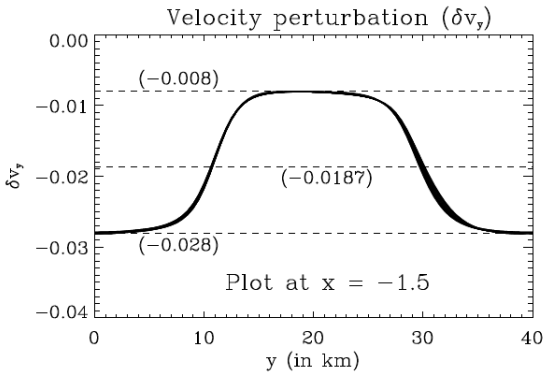

(a) Near the central plane at $x = 0$.

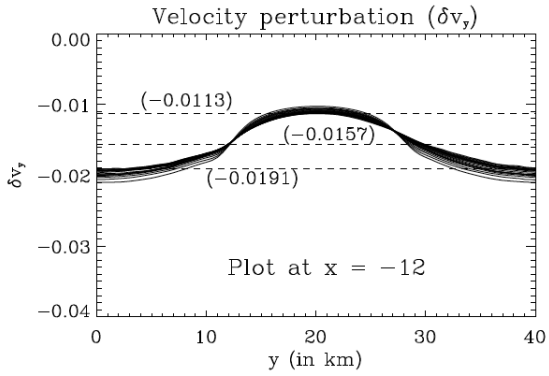

(b) Far from the central plane at $x = 0$.

Figure 3.42: Case IV: y-profiles of the total velocity pertubarions (δv_y) at two different locations on the x-axis: (a) at $x = -1.5$, that is, near the central plane through $x = 0$ and (b) at $x = -12$, that is, away from the central plane. The velocity perturbations are different over the different zones. But become uniform gradually as the observation is shifted away from the central plane. Dotted lines show the maximum, minimum, and average values of δv_y.

distance from $x = 0$ plane and vice versa in region 1.

The modification of the magnetospheric FAC at the lower boundary is illustrated in Figure 3.43. The figure shows the x-profiles of FAC density ($j_\parallel$) at $z = 36$ (a) before reflection at $t = 25$, (b) after reflection (at $t = 45$) above the low conductance region (at $y = 2$), and (c) after reflection (at $t = 45$) above the high conductance region ($y = 20$). Before reflection, the FAC (or $j_\parallel$) is same as the FAC for case I (Figure 3.7). After the reflection the figure shows an increase of $\approx 15\%$ in the peak value of the modified $j_\parallel$ above region 1. Similarly, the corresponding increase above the high conductance region is $\approx 61\%$. So, it can be concluded that the magnetospheric FAC-sheet turns into a nonuniform one after the reflection from the ionosphere and the distribution of $j_\parallel$ along y must be nonuniform as well.

When closely inspected, Figure 3.43 shows the presence of a small amount of FAC outside the central current sheet supporting the expectations from the plots of Figure 3.39. For a better understanding, the part of Figure 3.43 near the lower boundary, is shown (magnified) again in Figure 3.44. These plots confirm the presence of a positive $j_\parallel$ (i.e. negative j_z) in region 2 and a negative $j_\parallel$ (i.e. positive j_z) in region 1 outside the central current sheet which is consistent with the observations from Figures 3.39 and 3.42. This additional FACs modify the distribution of the Pedersen current and therefore it is also interesting to examine the Pedersen current distribution in the different regions. It should be noted that the plots for the x-profile of δB_y at $z(9) = 1.6$ in Figure 3.39 represents the Pedersen current ($I_{P,x}$) with the change of sign of the plotted quantity.

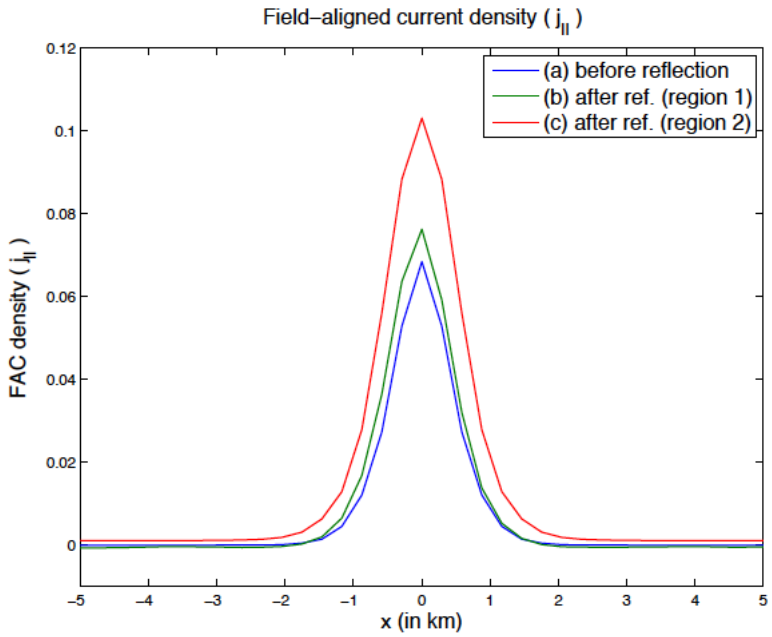

Figure 3.43: Case IV: x-profiles of the FAC density ($j_{\|}$) at $z = 36$ before and after reflection. The peak values of $j_{\|}$ are (a) ≈ 0.064 before the reflection at $t = 25$ (b) ≈ 0.077 after the reflection at $t = 45$ above region 1 (at $y = 2$) and (c) ≈ 0.106 after the reflection at $t = 45$ above region 2 (at $y = 20$).

The positive value of $j_{\|}$ for region 2 enhances the Pedersen current ($I_{P,x}$) with increasing distance from $x = 0$ plane while the negative $j_{\|}$ reduces the value of $I_{P,x}$ with increasing distance from the central plane in region 1.

Figure 3.45 shows a plot of the Pedersen current density (j_x) in the xy-plane at the ionospheric boundary after reflection at time $t = 36$. Arrows show the combined x & y components. The z-component of the current density (j_z) which is nearly same as the FAC density ($j_{\|}$) in magnitude, is represented by the colors. So, the colors effectively confirm the presence of a nonuniform FAC sheet at the junction between the two oppositely directed perturbations. This figure demonstrates - not surprisingly - that the Pedersen current density, j_x, above region 2, is much stronger than above the low conductance region.

A closer examination again reveals that the strengths of both j_x and $I_{P,x}$, in any particular zone, are not uniform along the x direction (away from x=0). Figure 3.46 shows the y-profile of $I_{P,x}$ at two different cuts (at $x = -1.5$ and $x = -12$) at the lower boundary. These plots show Pedersen current profiles from the beginning of complete reflection at time $t = 27$ to $t = 52$ in intervals of 1 t_{A0}. The dotted lines represent the estimated values of $I_{P,x}$ based on the reflection condition (Σ_P) of the two regions. Figure 3.46a shows that, the values of $I_{P,x}$ are almost consistent with the

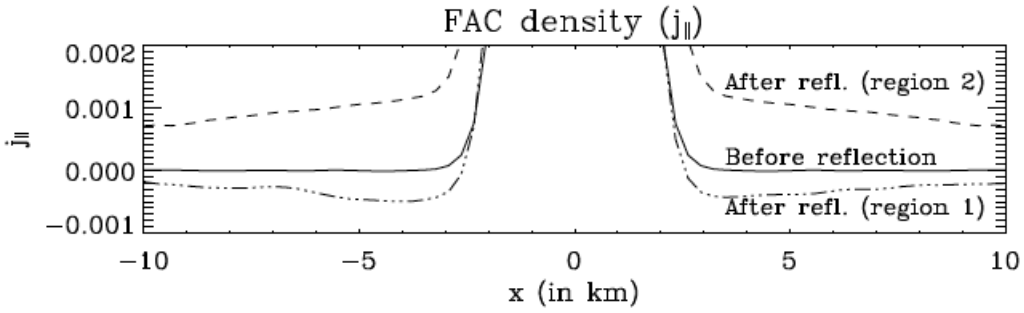

Figure 3.44: Case IV: x-profiles of the FAC density ($j_{\parallel}$) outside the central FAC-sheetat $z = 36$. These plots illustrate that after reflection, downward (in region 2) and upward (in region 1) FACs are generated outside the central current sheet.

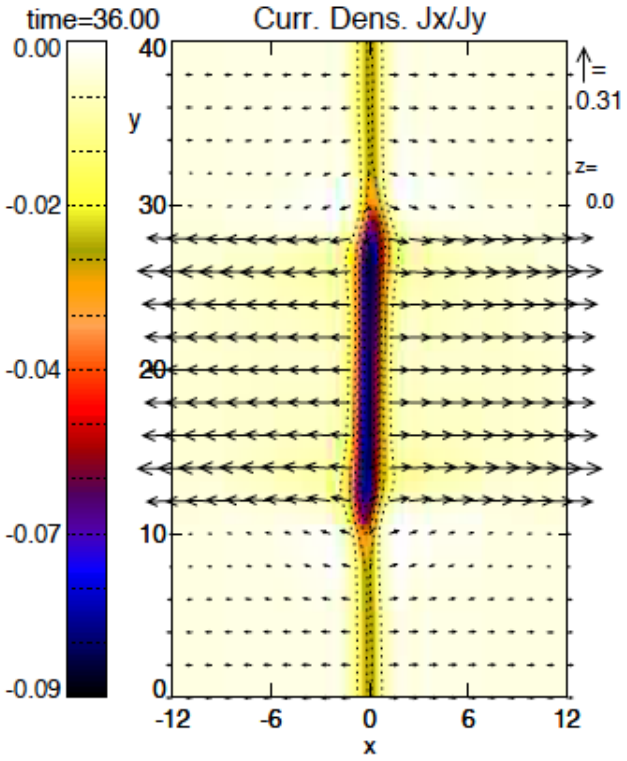

Figure 3.45: Case IV: Current densities at the ionospheric boundary after reflection. Arrows show the combined x and y-components and the colors show the z-component. j_x and j_z are much stronger in region 2 than in region 1.

reflection condition and do not change much with time close to the $x = 0$ boundary. Figure 3.46b shows the y-profile of $I_{P,x}$ at $x = -12$ i.e. farther away from the central plane. In both regions, values of $I_{P,x}$ are consistent with the reflection conditions, only at the beginning of the reflection. As the steady state is attained, the values (of $I_{P,x}$) gradually increases and decreases, respectively,

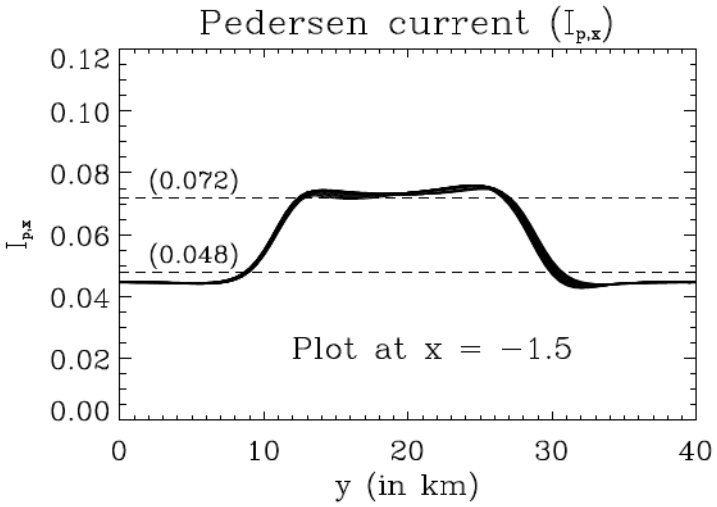

(a) At $x = -1.5$ (near the central-plane).

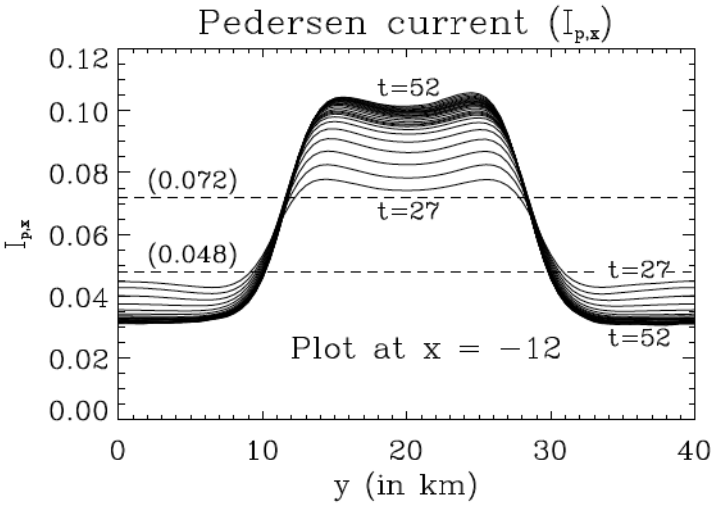

(b) At $x = -12$ (far from the central-plane).

Figure 3.46: Case IV: y-profiles of Pedersen current ($I_{P,x}$) at two different locations on the x-axis: (a) at $x = -1.5$ (near the central plane) and (b) at $x = -12$ (far from the central plane). Value of $I_{P,x}$ increases and decreases (monotonically), respectively, in the region 2 & 1 with increasing distance from the central plane. Plotted from $t = 27$ to $t = 52$ in intervals of 1 t_{A0}. Dotted lines show the values consistent with Σ_P for simple Alfvén waves.

in regions 2 and 1 with time. These observations are consistent with the previous results (e.g. Figure 3.39 and 3.44).

Varying the width of high conductance region

The width of region 2 is varied in the same way as it was done in case III. The high conductance width discussed thus far is referred to as the the *medium* width and two more runs with a narrower, and a wider high conductance zone are considered for comparison. Qualitatively the results for a different width of the high conductance zone are the same as in the reference *medium* width case. Convection is partly reflected and develops vortices at the high conductance boundaries and similar patterns of the magnetic and velocity profiles develop in the different conductance zones. The most important quantitative difference is the gradient of the Pederson current along the x-direction as illustrated in the results in Figure 3.47. The first and third plots show the x-profiles of $I_{P,x}$ in

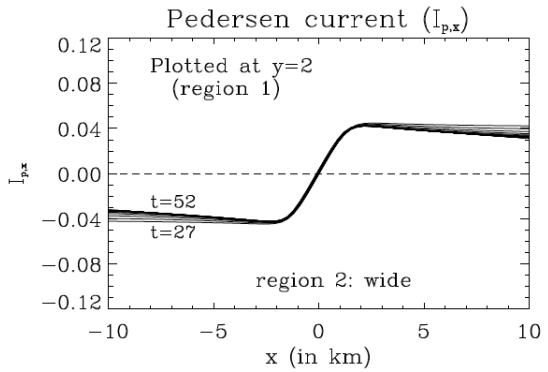

(a) $I_{P,x}$ in region 1 when region 2 is *wide*.

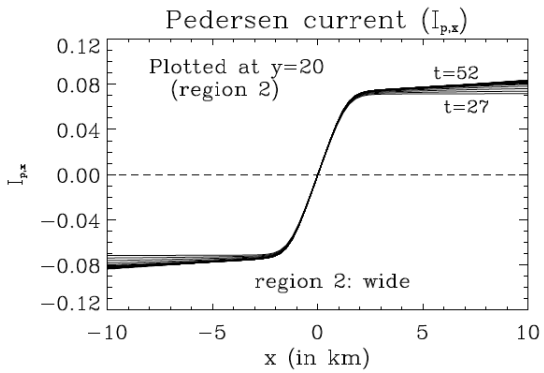

(b) $I_{P,x}$ in region 2 when region 2 is *wide*.

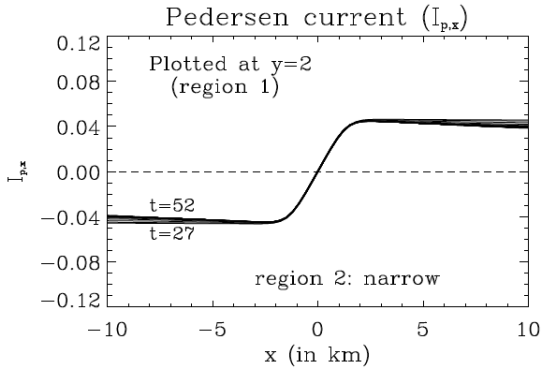

(c) $I_{P,x}$ in region 1 when region 2 is *narrow*.

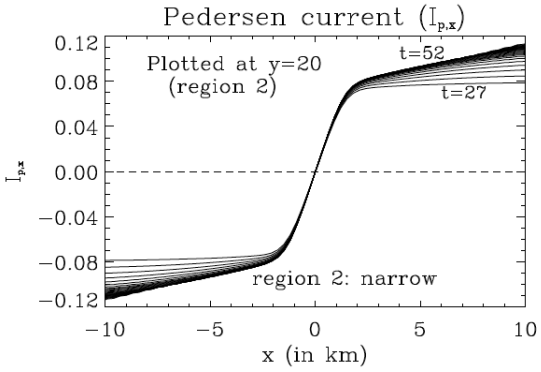

(d) $I_{P,x}$ in region 2 when region 2 is *narrow*.

Figure 3.47: Case IV: Time evolutions of x-profiles of Pedersen currents ($I_{P,x}$) in different regions. Different lines represent the plots in region 1 (a & c) and 2 (b & d) at times between $t = 32$ and 52 with $\Delta t = 1$. The gradient of δB_y along x is more significant in the region 2 for *narrow* d_2 and develop larger FAC outside the current sheet.

region 1 when this zone is, respectively, *wide* and *narrow* compared to the reference case. On both sides of the central plane, the magnitude of $I_{P,x}$ decreases with increasing distance from $x = 0$

and with time by a small amount from the value th.at is implied by simple Alfvén wave reflection. Conversely, in region 2, the magnitude of $I_{P,x}$ increases with increasing distance from $x = 0$ and with time. The magnitude of this gradient of $I_{P,x}$ along the x-direction is higher for the case with a *narrow* high conductance region. The plots in Figure 3.47 cover the time from $t = 27$ to 52 and different lines present results $1t_{A0}$ apart. This demonstrates that near the central plane the values (of $I_{P,x}$ or, j_x) are consistent with Σ_P. Away from the central plane, the values increase in region 2 and approach the steady state conditions defined by case III, i.e., with no field aligned current imposed by magnetospheric conditions.

3.3 Summary and discussion

A FAC can be generated (e.g. Figure 3.7) in the magnetosphere by sheared magnetic field perturbations (here, with a polarization in the $\pm y$-direction) propagating downward as a pair of simple Alfvén waves. This FAC sheet, carried by the pair of Alfvén waves, is then modified after the reflection from the ionosphere (e.g. Figure 3.11). The degree and nature of the modification depends on the pattern of the imposed ionospheric Pedersen conductance. With the change of the FAC, the associated Pedersen current also changes. The ionosphere having a uniform Pedersen conductance of high value ($\Sigma_P = 2.25$ or $r \approx 0.8$) is used in case I. In this case the FAC density at the central plane (at $x = 0$) of the current sheet increases by about 66% after the reflection. Associated Pedersen current ($I_{P,x}$) follows the relation $I_{P,x} = \frac{\delta v_{y0} B_z}{v_A}(1 + r)$ [Equation (2.58)]. Therefore $I_{P,x}$ becomes proportional to $(1+r)$ as the other quantities, δv_y, B_z and v_A are assumed to be constants and thus depends on the imposed ionospheric Pedersen conductance. In all the other three cases, the ionosphere has a nonuniform Pedersen conductance with a strip of high conductance region interlaid in a low conductance background but the directions of its gradient are not same in all of them. In addition, cases II and III use a uniform Alfvénic perturbation (that do not impose a FAC) in order to examine the role of ionospheric conductance gradients relative to the polarization of incoming Alfvén wave.

In case II, the conductance gradient is along the x-direction with a high value in the middle zone and low value on the two sides of it. Therefore the direction of conductance-gradient is perpendicular to the magnetic field and velocity polarization. The magnetospheric perturbations (in the magnetic field and velocity) travel downward in the form of simple Alfvén waves. Due to the different degrees of reflection at the ionospheric boundary, the upward propagating superposed perturbations contribute to a nonzero value of the z-componet of $\nabla \times \mathbf{B}$ $\left(= \frac{\partial \delta B_y}{\partial x}\right)$. This results in the production of FAC at the two locations of the conductance-gradient on the x-axis. Consistently, a strong Pedersen current is generated at the lower boundary in order to close these FACs. In this case, also, the Pedersen current is related to the imposed reflection conditions being proportional

to $(1+r)$. This relation is not violated if the width of region 2 is varied.

The results of case III are highly significant. In this case the magnetospheric perturbation is uniform and the orientation of the gradient of Pedersen conductance is in the same direction as the Alfvén wave polarization. This geometry resembles a situation in which the Cowling conductance becomes significant. In case of Cowling conductance, a stronger ionospheric current is obtained due to the enhancement of the effective conductance in the ionosphere. In addition to the primary electric field (E_x), the $\mathbf{E}\times\mathbf{B}$ force, on the ions and electrons develop a secondary electric field (E_y) in the perpendicular direction. The Hall current corresponding to E_y enhances the net Pedersen current resulting in an enhanced Pedersen conductance termed as Cowling conductance.

In case III, a stronger ionospheric (Pedersen) current is also obtained, but this is due to the enhancement of the effective electric field. The incident perturbation has same velocity at all points in the xy-plane. After reflection the velocity above the high conductance zone (region 2) becomes much smaller than that above the low conductance zone (region 1). However this cannot be a steady state solution considering the incompressibility of the fluids. If the velocities are different across the junction between the two regions then the continuity equation (2.11) is violated for an elementary volume located right above the ionopsheric boundary, at the junction of different conductance regions. As a consequence, the velocity assumes a uniform steady state value over the entire region, which corresponds to an ionospheric boundary with the width-average value for the imposed conductances. Following $\mathbf{E}=-\mathbf{v}\times\mathbf{B}$ the entire boundary offer uniform electric field (E_x) and the ionospheric Pedersen current ($I_{P,x}=\Sigma_P E_x$) become proportional to the imposed conductance (Σ_P).

There is another significant difference that exists between case III and Cowling conductance. Unlike the case of Cowling conductance, in case III, the effective electric field and hence the net Pedersen current becomes stronger if the width of the region having the higher Pedersen conductance becomes narrower. The mechanism that is responsible for the enhancement of the Pedersen current in case III can be summarized as:

- After reflection, the steady state velocity perturbation assumes the average value of the imposed Pedersen conductance ($\Sigma_{P,average}$) or, the average value of the reflection coefficient ($r_{average}$) over the entire region of the ionosphere. Thus, the superposed velocity perturbation, after reflection is $\delta v_{y,out}=\delta v_{y,in}(1-r_{average})$, where $\delta v_{y,in}$ is the incident perturbation.
- So, in the steady state, a uniform electric field (E_x) is established, over the entire region such that $E_x=-\delta v_{y,out}B_z$.
- The Pedersen current, in different zones are developed following, $I_{P,x,1}=\Sigma_{P,1}E_x$ and $I_{P,x,2}=\Sigma_{P,2}E_x$.

- With the decrease of the width of the zone with the higher conductance, the average values of the conductance, $\Sigma_{P,average}$ or the reflection coefficient, $r_{average}$, decreases.
- This leads to an increase in the magnitude of $\delta v_{y,out}$ which in turn increases the magnitude of steady state (uniform) electric field, E_x.
- Thus the Pedersen currents increase in both the zones. But the increase is more prominent where the imposed Pedersen conductance is higher (i.e. in the region 2).

In case IV, FAC of magnetospheric origin propagate in the downward direction and interact with the ionosphere. The gradient of the imposed Pedersen conductance is aligned with the Alfvén wave polarization. The results in this case are qualitatively different from the cases I and III combined, or in other words they cannot be obtained by a simple superposition of these two cases. In this case, small FACs are also observed to be generated outside the magnetospheric current sheet. The velocity perturbation (and hence the electric field, E_x) does not attain a uniform steady state value as in case III but instead they are nonuniform over different regions. Both, the steady state magnetic and velocity perturbations represent a truly three-dimensional configuration. Convection in this configuration is partially deflected from the high conductance zone. However this nonuniformity tends to be gradually reduced as the observations are shifted away from the central plane (at $x = 0$). In region 2, on both sides of and close to the current sheet, the velocity (δv_y) and electric field (E_x) are consistent with the imposed reflection condition. However, the magnitude of velocity and electric field both increases with increasing distance from $x = 0$ plane before reaching a steady state. These steady state values approach the corresponding estimated values as in case III. This increasing electric field results in an enhancement of Pedersen current and the magnitude of Pedersen current gradually grows larger with increasing distance from the $x = 0$ plane. At locations close to the central plane ($x = 0$), the Pedersen currents are consistent with the imposed reflection conditions. Following current continuity, FACs are generated outside the central current sheet. This is consistent with the fact that gradient in the magnetic field $\left(\frac{\partial \delta B_y}{\partial x}\right)$ develops outside the current sheet.

In region 1, the magnitude of velocity decreases with increasing distance from $x = 0$ plane in an attempt to reach the width-average value as in case III. Consequently, the magnitudes of the electric field (E_x), the Pedersen current ($I_{P,x}$) decrease. The current continuity is ensured here by upward FAC (negative $j_{\parallel}$) outside the central current sheet. Consistently, a negative gradient in the magnetic field $\left(\frac{\partial \delta B_y}{\partial x}\right)$ develops on two sides of this current sheet.

So, it may be concluded that, though, in general, FACs are of magnetospheric origin, these currents can also originate from the ionosphere or can be strongly modified by the ionospheric conductance gradients. The ionospheric Pedersen conductance plays an important role in the modification and

amplification of FACs. The gradient of the Pedersen conductance and its orientation play a critical role for the amplification of any FAC. When the simple Alfvénic perturbations are reflected by the ionosphere with a nonuniform Pedersen conductance with a gradient parallel to the incoming wave polarization, the relative widths of the different zones play an important role in the amplification and modification of the FACs. One such example could be the transition from high to low conductance at the terminator for flow in the polar cap. In this study, the situations are idealized, however, the real situation is much more complex. Different interesting flow-patterns may develop depending on the nature of perturbations and, pattern and shape of the conductance gradient. One such example is discussed next.

A high conductance patch in a low conductance background

For this case, a square base is considered for the simulations with both the horizontal extents (of x & y) from -12 to 12. At the central part of this base, a circular patch (region 2, and will be mentioned as *patch* hereafter) of high Pedersen conductance ($\Sigma_{P,2} = 2.25$) is imposed inside a low conductance ($\Sigma_{P,1} = 0.375$) background (region 1). The values of corresponding reflection coefficients, r_2 and r_1 are 0.8 and 0.2, respectively. The value of Σ_P changes linearly between the high and low values in an annular zone inside the *patch*.

Simple magnetospheric perturbations (as in case II and III) travel toward the ionosphere and reflected back. The results are presented using different plots. The steady state magnetic and velocity perturbations are shown in Figure 3.48. The plots show the magnetic and velocity perturbations

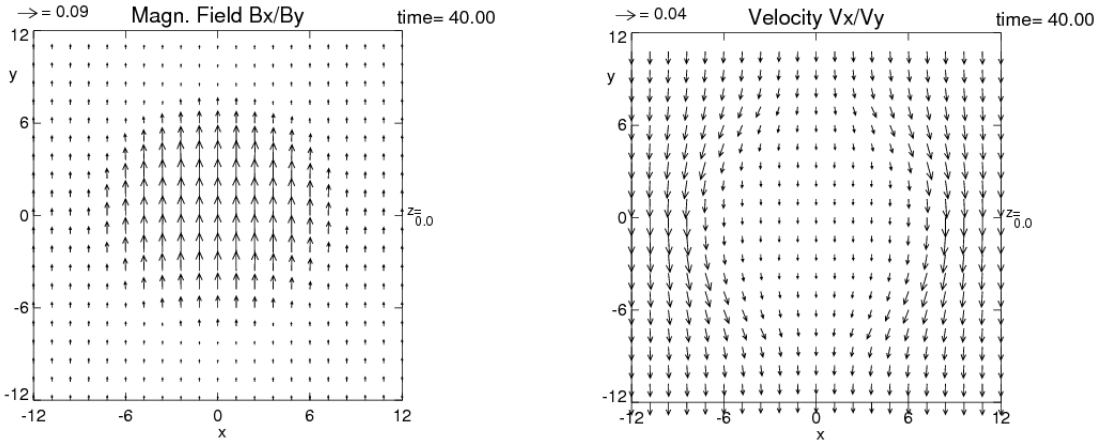

(a) (b)

Figure 3.48: Plots of total (a) magnetic and (b) velocity perturbations at $z = 0$ (after reflection) in the xy-plane and at time $t = 40$ for a patch of high conductance at the lower boundary. The plots are taken at $\Delta t = 16$ after the start of reflection.

in the xy-plane at the lower boundary ($z = 0$) at $t = 40$ that is $\Delta t = 16$ after the start of the reflection. Due to the reflection, the magnetic perturbation becomes stronger above region 2 (i.e. the *patch*) than above region 1. On the other hand, the velocity perturbation becomes stronger above region 1 than above the *patch*. The perturbations remain so with the lapse of time. This case can be compared to case III as these two are similar at least in one aspect. In case III the polarization of the perturbations is in the same direction as the gradient of Pedersen conductance along the entire boundary of region 2. Here, in this case, this is true but only at the boundaries between the two regions along the line $x = 0$.

With increasing height, the magnetic perturbation gradually becomes more uniform toward some intermediate value in the entire region but the velocity perturbation does not change significantly. Plots for magnetic and velocity perturbations at $z = 20$ at the same time, $t = 40$, are shown in Figure 3.49. The reflected perturbations reach this height at $t \approx 29$. So, these plots show the per-

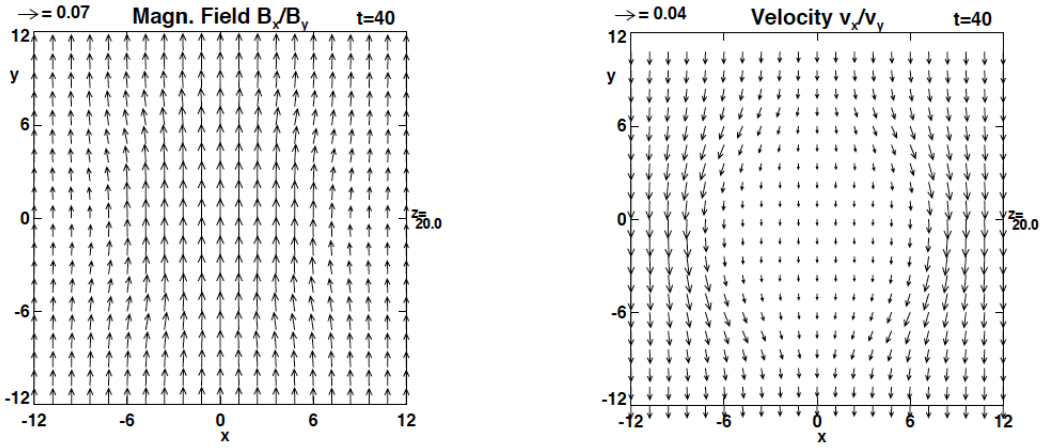

(a) (b)

Figure 3.49: Plots of total (a) magnetic and (b) velocity perturbations at $z = 20$ (after reflection) in the xy-plane and at time $t = 40$ for a patch of high conductance at the lower boundary. The plots are taken at $\Delta t = 12$ after the start of reflection.

turbations after $\Delta t \approx 11$ from the superposition of incident and reflected waves. At the ionospheric boundary, the plasma velocity decreases due to the presence of the high conductance region on its path. Therefore, a part of the plasma flow is obstructed and changes the flow-directions to move around the *patch* because of the incompressibility of the fluid. Note that this kind of solution was not possible in case III. Combined with the magnetic field, B_z, the velocity develops nonuniform electric fields at the ionospheric boundary according to $E_x = -\delta v_y B_z$. Though inside the *patch* the electric field is weaker compared to the electric field outside, the combined effect of this electric field and the Pedersen conductance results in the production of stronger Pedersen current inside

the *patch* according to Ohm's law. The generated current pattern is illustrated in Figure 3.50. This figure shows the plots for the parallel and perpendicular current densities. The plot in Figure

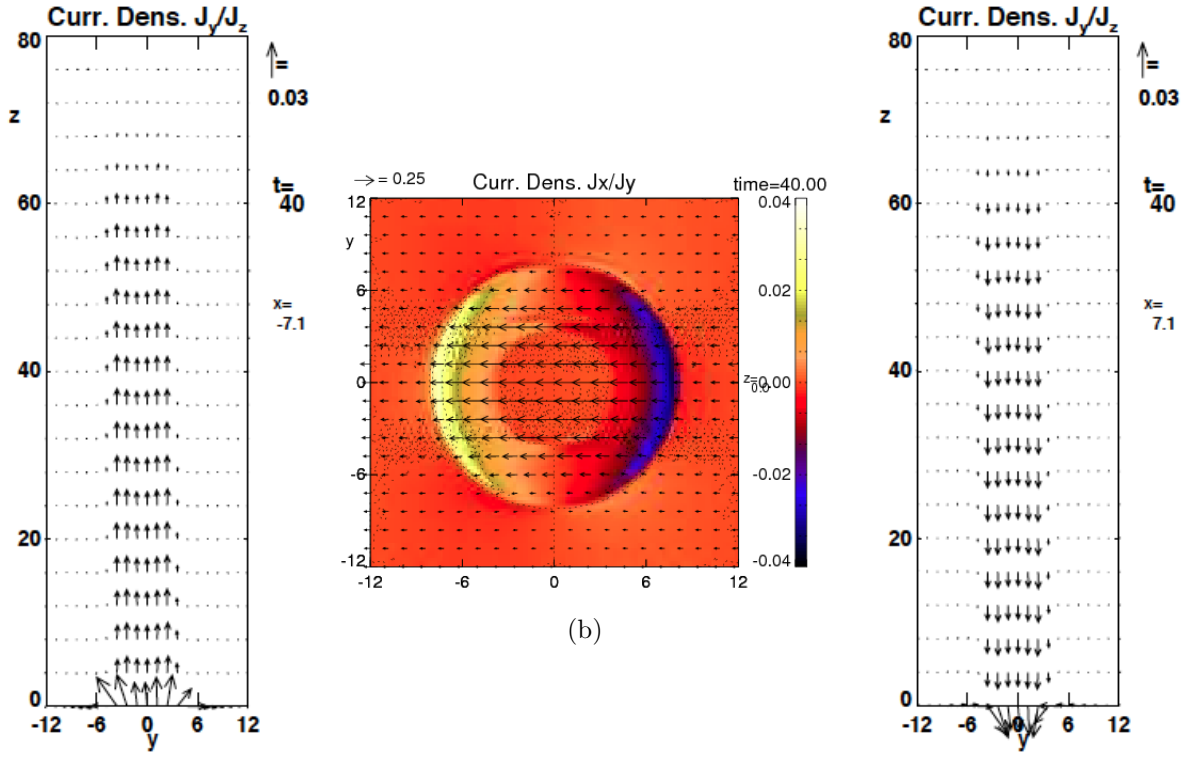

(a) (b) (c)

Figure 3.50: Current distributions for high conductance *patch* at the ionospheric boundary. (b) Plot of Pedersen current density, j_x, in the xy-plane at $z = 0$ and (a) & (c) plots of negative of FAC density j_z, in the yz planes at $x = -7.1$ and $x = 7.1$, and at time $t = 40$. In (b) colors also show the presence of FAC at the edges of the *patch*. The plots are taken at $\Delta t = 16$ after the start of reflection.

3.50b illustrates the stronger Pedersen current inside the *patch* at the ionospheric boundary ($z = 0$) which closes the FACs present at the two edges of the *patch* (indicated by the colors in Figure 3.50) in the up and downward directions as illustrated in all the three plots in Figures 3.50. Figures 3.50a and 3.50c show the vector plots for the FAC densities at the *patch*-boundary in yz-planes at $x = -7.1$ and $x = 7.1$, respectively. These two plots also illustrate that at the snapshot time of the plots, the waves have travelled up to a height of ≈ 64 after the reflection from the lower boundary. It is possible to explore the current distributions in different other combinations of the magnetospheric perturbations and ionospheric conductance patterns utilizing the simulation methods followed in this chapter.

Chapter 4

Basic properties and effects of the localized electric field that is parallel to the geomagnetic field

Introduction

The formation of magnetic field-aligned electric field (commonly termed as *parallel electric field*) in the auroral zone is one of the fundamental unsolved problems of space plasma physics. Though the physics for the formation of parallel electric field is unresolved there is experimental evidence that parallel electric fields exist along the field lines connected to discrete auroral arcs (e.g. [80]). The immediate cause of the Aurora has been known for a long time. The energetic particles (mainly, electrons) having energies of a few keV precipitate into the upper atmosphere and excite the ambient molecules. These excited molecules, in turn, lower their energy by emitting light (e.g. [2]). However, the source of energy for these particles remains as a difficult problem to answer.

In a paper [41], in 1958, Alfvén suggested that the auroral electrons gain their energy by falling through electric double layers, an electric potential structure. The phenomenon, electric double layer, had been known from the plasma experiments in the laboratory. It was observed that in such a double layer a strong and localized potential drop could exist in a collisionless plasma. At that time, however, this theory was not accepted seriously for space plasma. The existence of a potential drop in space couldn‘t be imagined. It was considered that as the plasma in space is highly conducting, any potential drop would be *short-circuited* immediately. Some theoretical works suggest that the electric fields, $\mathbf{E}$, parallel to the magnetic field, $\mathbf{B}$, are zero or very small to account for the observations in the magnetosphere and the magnetosphere under steady conditions i.e. $\mathbf{E} \cdot \mathbf{B}/|B| = E_{\|} \sim 0$ [81]. But this assumption is apparently violated in the auroral region. By now, the existance of parallel electric fields is observationally established. For example, in 2005 Ergun et.al. [42] reported measurements of "intense, localized parallel electric field in association with inertial Alfvén waves and accelerated electron fluxes in space plasma."

Although parallel electric fields are unlikely to exist on large scales, localized electric fields parallel to the magnetic field are of fundamental importance for many space plasma boundaries. They are the cause for particle acceleration in discrete auroral arcs, and they also represent a key element in the definition of magnetic reconnection. In the auroral region, localized parallel electric fields occur in a very strong dipole magnetic field where magnetic perturbations associated with field-aligned electric currents are minor in comparison. Often parallel electric fields are depicted as the effect of U or V shaped electric potentials [82]. The notion of a parallel electric field based on an electric potential, however, bears some major physical questions because a potential implies $\frac{\partial \mathbf{B}}{\partial t} = 0$ and therefore an electrostatic process. Typically, such processes are micro-physical in that they occur

on temporal scales much faster than the large scale evolution.

In this chapter, basic physical aspects associated with and required for localized parallel electric fields are examined. This study illustrates the basic two-dimensional and three-dimensional physics of localized parallel electric fields and addresses the following questions:

1. Can localized parallel electric field form in constant or potential (dipole) magnetic fields?
2. What are the basic physical effects of localized parallel electric fields associated with field-aligned electric currents?

A brief introduction to the parallel electric field and thin auroral arc are given in the next section. The following sections consist of numerical methods and results for the simulations of the different cases involving the localized parallel electric fields. The last section includes the summary and the discussion about the works of this chapter.

4.1 Parallel electric fields

The presence of a parallel electric field must be consistent with generalized Ohm's law (Equation 2.3). Although the precise physical process for the formation of a parallel electric field is microphysical, general Ohm's law provides important constraints and insight into the properties of a parallel electric field. In order to discuss these, Equation 4.1 presents general Ohm's law in normalized form that is all quantities are normalized to typical values as discussed in Chapter 2 (Subsection 2.1.2). This equation is given by

$$\mathbf{E}+\mathbf{v}\times\mathbf{B}=\eta\mathbf{j}-\left(\frac{c}{\omega_{pi}L_0}\right)\nabla p_e+\left(\frac{c}{\omega_{pi}L_0}\right)\mathbf{j}\times\mathbf{B}+\left(\frac{c}{\omega_{pe}L_0}\right)^2\left[\frac{\partial\mathbf{j}}{\partial t}+\nabla\cdot(\mathbf{jv})\right] \tag{4.1}$$

where, ω_{pi} and ω_{pe} are the plasma frequencies for, respectively, the ions and electrons and $c = 1/\sqrt{\mu_0\epsilon_0}$. Here, c/ω_{pi} is the ion inertial scale, c/ω_{pe} is the electron inertial scale (or plasma skin depth), and L_0 is some typical length scale. The third term on the right side, the Hall term, cannot contribute a parallel electric field as the direction of $\mathbf{j}\times\mathbf{B}$ has to be perpendicular to the direction of $\mathbf{B}$. The other three terms may contribute to the presence of parallel electric fields. The first term, i.e. the *resistive term* may introduce parallel electric field when the field-aligned current (FAC) density is large. Typically the resistivity is based on classical collisions, however, a so-called anomalous resistivity can occur for the case of very large drift speeds of the current carriers. When this drift speed surpasses a typical plasma speed (ion acoustic speed, Alfvén speed, electron thermal speed) turbulence based on the respective micro-instability occurs which has the tendency to reduce the respective drift and therefore acts as a resistivity. Ion-acoustic, two stream, and, lower-hybrid instabilities are the examples of such instabilities. The *Electron pressure term* is the second on the right side. For the normalized equation, the coefficient of ∇p_e is $\frac{c}{\omega_{pi}L_0}$. Therefore, the *electron pressure term* is significant if $L_0 \approx c/\omega_{pi}$ i.e. when electron pressure gradient exists on

the ion inertial scale. Note that this has been shown to operate during kinetic reconnection but only for very small guide magnetic fields whereas the guide field (dipole field) in the auroral acceleration region is very large. Similarly, the fourth term scales with $\left(\frac{c}{\omega_{pe}L_0}\right)^2$. This *electron inertial term* may contribute to the parallel electric field if $L_0 \approx c/\omega_{pe}$. This term directly involves the electron inertia, however, the respective relevant length scale is by a factor of $\sqrt{(m_e/m_i)}$ smaller than the ion inertial term. This discussion demonstrates that the physics of any parallel electric field formation requires very small inertial scales or very large drift velocities of electric current carrier (which are expected only for very thin current sheets).

The existence of parallel electric fields has great significance in space plasma physics. The consequence of their existence are (1) violation of frozen-in field condition (2) rapid acceleration of the charged particles, and (3) rapid release of magnetically stored energy [83].

The concept of frozen-in condition for the magnetic field lines was introduced by Hannes Alfvén along with the MHD waves that bear his name. A short time after the publication of the paper on MHD waves [64], Alfvén interpreted the waves in an associated paper [84]. An excerpt from this paper reads, "Suppose that we have a homogeneous magnetic field in a perfectly conducting fluid... . In view of the infinite conductivity, every motion (perpendicular to the field) of the liquid in relation to the lines of force is forbidden because it would give infinite eddy currents. Thus the matter of the liquid is *fastened* to the lines of force... ." In modern terminology *frozen-in* is considered more appealing than *fastened*. Illustrations by Alfvén and Fälthammar [85] show the frozen-in condition and its violation in Figures 4.1 and 4.2. The first figure shows that under the frozen-in condition any two plasma elements on a common magnetic field line at a certain instant will be on a common magnetic field line at any other instant. However, this condition is based on assumptions, which are not always valid and should be used with care. Figure 4.2 illustrates the concept that, in presence of parallel electric field, the frozen-in condition is no more valid. The shaded area represents non-vanishing $E_\parallel$ that is responsible for the decoupling of the plasma elements on the same magnetic field lines. Violation of this condition has serious consequences. Firstly, the plasma elements on a common magnetic field line may no longer remain on a common line and secondly, the mapping of electric field along the magnetic field lines fails [83].

A magnetic field cannot accelerate a charged particle significantly along its own direction because the magnetic force on a moving charge is always perpendicular to the velocity vector. Hence a charged particle may be accelerated parallel to the magnetic field only by an electrostatic electric field. There are basically two ways for achieving acceleration by the charged particles [85]. These are (1) stochastic or multi-step acceleration and (2) direct, one-step, acceleration. An example of the apparent exception to this general rule is the magnetic mirror force where a charged particle may change its motion while moving along a magnetic field of varying strength.

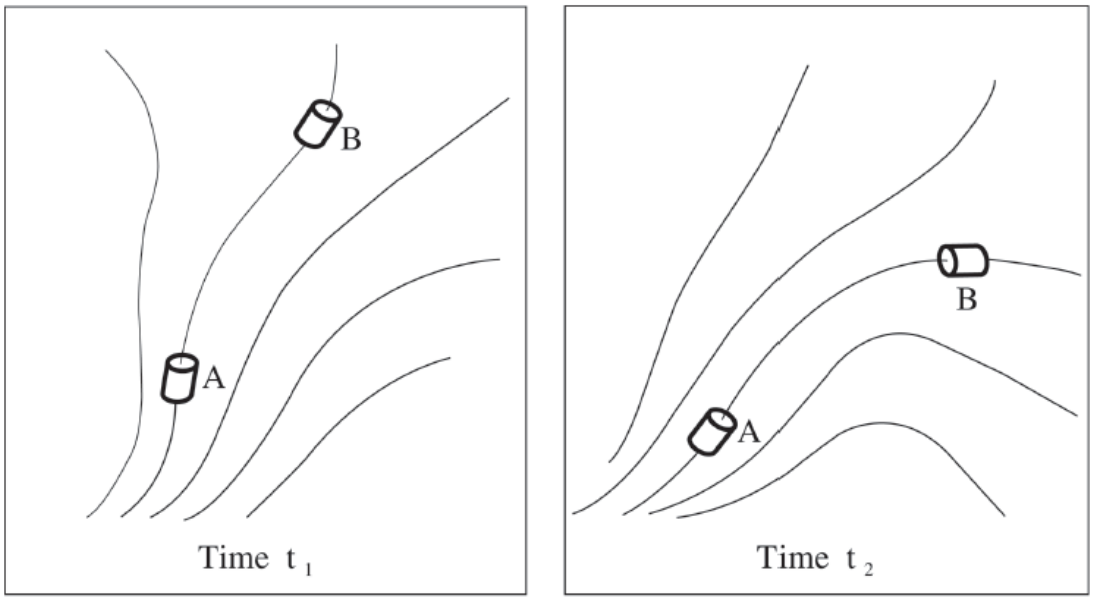

Figure 4.1: Illustrations of plasma *frozen-in* magnetic field. Two elements of plasma, A and B, that are at any one time, t_1, on a common magnetic field will remain on a common line at some other time, t_2 [85].

According to the classical theory of resistivity there should be a negligible amount of resistivity along the magnetic field lines in the collisionless plasma of the magnetosphere and hence Alfvén's proposal in favor of the parallel electric fields was almost universally dismissed. After successful launches of the artificial satellites and space probes in the late fifties, scientists started to think about performing experiments on space research using different measuring instruments and detectors [86]. The results from the direct measurements in space have drastically changed the concepts about the physical processes of the space environment that has become accessible to the sounding rockets and spacecrafts. Alfvén's theory was finally exonerated by the experimental proofs of its existence.

In 1960, McIlwain [87] experimented to determine the nature of particles producing visible auroras, with the help of rocket-borne detectors. He suggested an electrostatic acceleration mechanism to be responsible for the detected presence of monoenergetic electrons. This kind of observations of monoenergetic electron fluxes was also made by some other experimenters (e.g. [88, 89]). There was also other experimental evidence in favor of the existence of parallel electric fields. A group of such examples are the Barium cloud experiments (e.g. [90, 91, 92, 93, 94]) in which a cloud was formed by releasing barium along a magnetic field and then the motion of the cloud (Ba^+), accelerated away from the Earth, was tracked. Existence of parallel electric fields above a certain height was inferred from the gain in parallel velocity by the ions [90] [91]. These experiments estimated

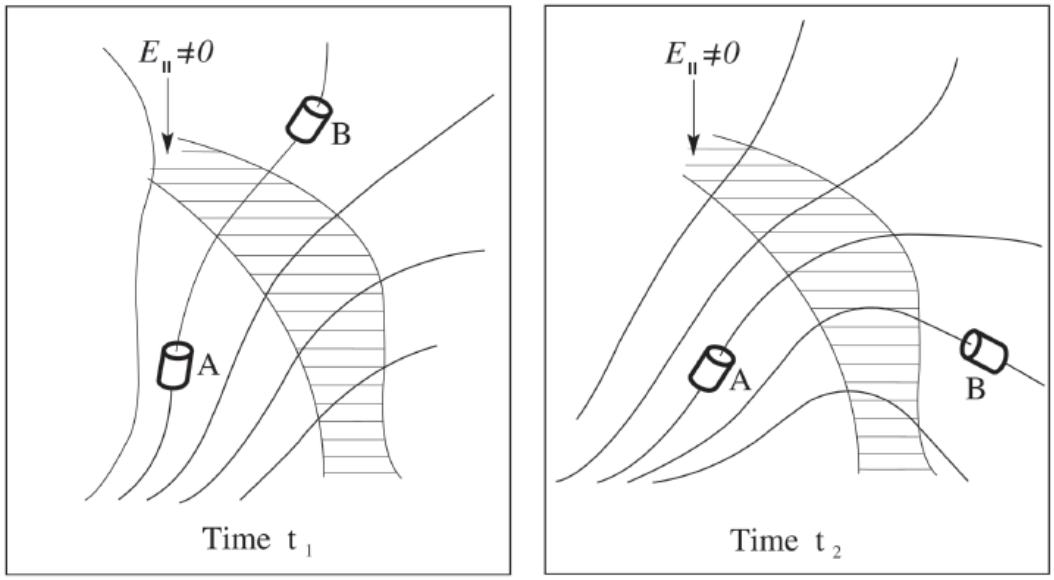

Figure 4.2: Illustrations of violation of *frozen-in* magnetic field condition. Two elements of plasma, A nad B, that are at any one time, t_1, on a common magnetic field will be on different lines at some other time, t_2 - happening in presence of *parallel electric field* ($E_{\parallel}$) [85].

the presence of a $\sim 1\ kV$ potential drop over less than $\sim 200km$ (e.g. [92]). Note that although the term potential is commonly used, these experiments really demonstrated the presence of a parallel electric field which when integrated yields an energy change of about 1 keV over a distance of about 200 km. Different ground based observations (e.g. EISCAT radar observation [95]) also supported the existence of parallel electric fields. Evidence from different types of observations established the existence of parallel electric field beyond doubt. This led to different theories for the possible causes of the formation of parallel electric fields (e.g. [96], [97]).

One of the earliest identified possible causes for the formation of parallel electric field was *anomalous resistivity* [43]. It was suggested that parallel electric field, supported by anomalous resistivity can accelerate the auroral electrons. Papadopoulos [48] gave an early review of anomalous resistivity for the ionosphere. In collisional plasma binary collisions take place. But in case of collisionless plasma, interactions between the particles and the waves, can replace the role of binary collisions, which is represented by the term *anomalous collision* [98]. An instability always acts to reduce its original cause. Therefore, wave turbulence caused by a fast particle drift or large current density reduces the average momentum of the current carriers, effectively introducing a resistivity. The Buneman instability or the ion-acoustic instability are two such examples. Different opinions are still there regarding the role of anomalous resistivity in sustaining parallel electric fields (e.g. [99, 50]).

Another proposed mechanism to support a parallel electric field is the formation of *electric double*

layers. An early review on this topic was given by Block [44]. A double layer consists of two parallel (not necessarily plane) space charge layers, which contain equal, but opposite charges. S3-3 satellite made the first direct measurements of such a phenomenon in 1970 [100, 101]. They found a large number of tiny double layers, each with a potential drop of $\sim 1V$. The observations indicated the presence of thousands of such layers in series along the auroral field lines to account for the potential drop of the order of *kilovolt* and could explain the acceleration of auroral electrons and (upward) ions in terms of parallel electric field [102]. Later, observations from S3-3 satellite were supported by other observations, - for example, by the observations on Viking or on DE 1 & DE 2 (magnetically conjugate) satellites. Figure 4.3 represents the equipotential surfaces considering the double-layers to be connected to large-scale U-shaped structure associated with auroral arcs [102]. The variation of potential along the magnetic field is shown near the lower left side of the

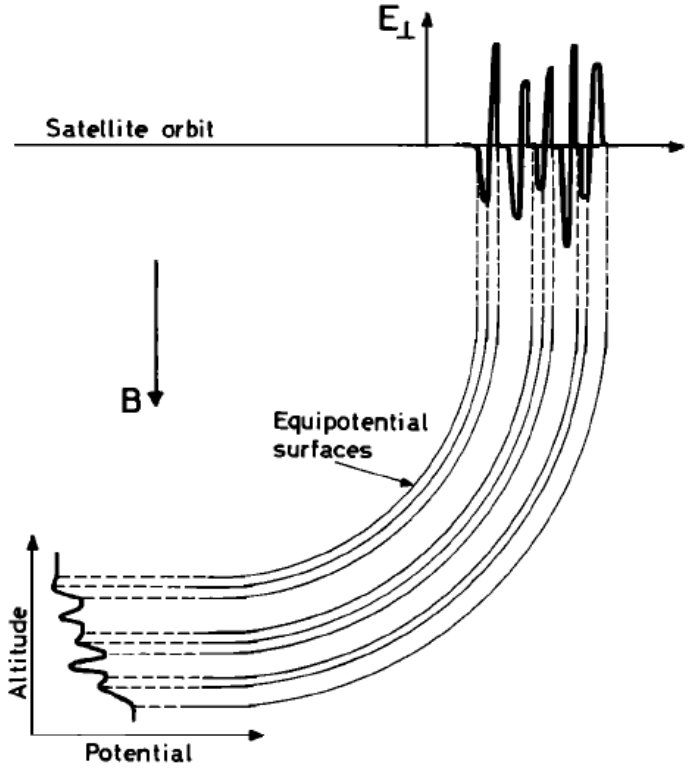

Figure 4.3: Illustrations of *electric double layer*. Variation of potential (lower left) along the magnetic field and of perpendicular electric field (upper right) at a higher altitude are shown [102].

figure. Note that double layers also require a current across the electric space charges and can form as a result of micro-turbulence. As such they can also be considered a mechanism for anomalous resistivity.

Some other suggested mechanisms [83] in favor of supporting parallel electric fields are *solitary*

structures (e.g. [45]), *magnetic mirror effect* (e.g. [46]), *collisionless thermoelectric effect* (e.g. [103, 104]), *scarcity of charged carriers* (e.g. [105]) and *dynamic trapping* (e.g. [106]) .

4.1.1 Thin Auroral Arcs

Auroral arcs are related to the FAC sheets which closely depend on the parallel electric field. The thinness of auroral arcs has captured the interest of many researchers. With the development and improvement of auroral photography and imaging systems, thicknesses have been determined with better precision. An early report from Elvey [107] estimated the thickness of the auroral arc "to be one-fourth the diameter of the moon, which was nearby." That implied the thickness was not more than 250 m. Akasofu [108] reported from the study of the photographs of auroral arcs that they could be $\sim 200m$ wide. The first statistical data came form Maggs and Devis [109]. They had studied 581 auroral structures for 5 nights in 1966 and 1967 during which local *Kp-index* ranged from 3 to 6. According to their report, 50% of the measured structures were below 230 m in thickness. They concluded that structures thinner than 70 m would exist though those could not be measured due to some (instrumental) limitations. They also inferred that "auroral structures tend to become thinner as their brightness increases." More recent report came from Borovsky [97]. He examined twenty-one theoretical mechanisms for the formation of aurora in their ability to predict the thickness of auroral arcs. His prediction indicated the need of more careful theoretical investigations as no theory of auroral arcs could successfully explain the observed narrow structures of aurora. Later Haerendel [110] sought a solution to this problem from formation of auroral cavity. He suggested an erosion of cool plasma (from the topside ionosphere) by a propagating auroral acceleration region where the upwelling ions from the leading edge of the auroral cavity could lead to a local enhancement of the parallel potential drop and thereby the auroral electron flux. Otto [111, 112] presented the *current striation model* for the formation of very thin auroral arcs which provided explanations for some other morphological properties. The model assumed the presence of anomalous resistivity in a sheet of FAC that allows for 3D reconnection process. The foot-points of (newly) reconnected magnetic field lines would be the locations of the auroral display.

4.2 Numerical methods

This chapter will explore the general concept of field-aligned electric fields and the role of electric current layer for the formation of such fields. Therefore the first set of case studies (case I and II) explores the general conditions for the formation of parallel electric fields and the concept of a field aligned electric potential. The basic geometry in this first set of studies explores the situation where a parallel electric field is imposed onto a vacuum fields because the concept of field-aligned

potentials does not provide a relation of how such a potential is connected to electric current or if such currents are necessary at all. In contrast the third case (III) introduces a parallel electric field caused by a localized resistive term in a field aligned electric current layer.

The basic equations described in Chapter 2 are further modified to make suitable for these studies. In cases I and II, localized electric fields ($E_{\parallel}$) parallel to the guide field are introduced at about $1R_e$ (Earth-radius) above the Earth's surface. The effects of the presence of localized $E_{\parallel}$ are then studied. In case III, localized resistivity, of a fixed magnitude, is introduced in a FAC sheet (having current density, $j_{\parallel}$) in the form of a 3D blob. This results in the production of a localized $E_{\parallel}$. The shape of the introduced quantities (i.e. the electric field or the resistivity), in different cases, are specified through a three-dimensional profile parameter. This profile parameter is used to conduct a controlled simulation experiment with a localized parallel electric field. In all the cases the main magnetic field is the guide field which has the magnitude B_0 in the vertically downward direction. In the next subsections, the simulation domains and the use of profile parameters, for the different cases, are described.

4.2.1 Numerical method: Cases I and II - Localized parallel electric field

In cases I, and II the simulation domain has x and y axes extending from -8 to 8 (in km), and z-axis from 0 to 120 (in 100 km). In both cases a localized electric field of fixed magnitude, aligned with the geomagnetic field, is initiated at an altitude corresponding to $\approx 1R_e$ (Earth-radius) above the Earth's surface and the results are studied.

The schematic views of the localized electric fields for these cases are shown in Figure 4.4. In Figure 4.4a the blue spherical body indicates the presence of a localized $E_{\parallel}$ in the form of a 3D blob for case I. At the central part of it, the parameter has its peak value. Away from the central part, its value decreases gradually and becomes negligible beyond a certain distance. The profile used for the localization is given by

$$E_{loc} = 0.05 \left[\frac{1}{cosh^2\left(\frac{x}{2}\right) cosh^2\left(\frac{y}{2}\right) cosh\left(\frac{z-55}{3}\right)} \right]. \tag{4.2}$$

So, the parameter E_{loc} develops quantities in the form of a blob around the location (0, 0, 55) of the simulation domain, with the peak value 0.05 at the central part (of the blob) which is horizontally at the center of the domain and vertically at ≈ 5500 km above the ionosphere.

In Figure 4.4b the blue cylindrical body is indicating the presence of a 2D rod-like localized $E_{\parallel}$ for case II. The quantity has its peak value along the central axis of the colored part. Away from the axis the value decreases gradually and becomes negligible beyond a certain distance from the axis.

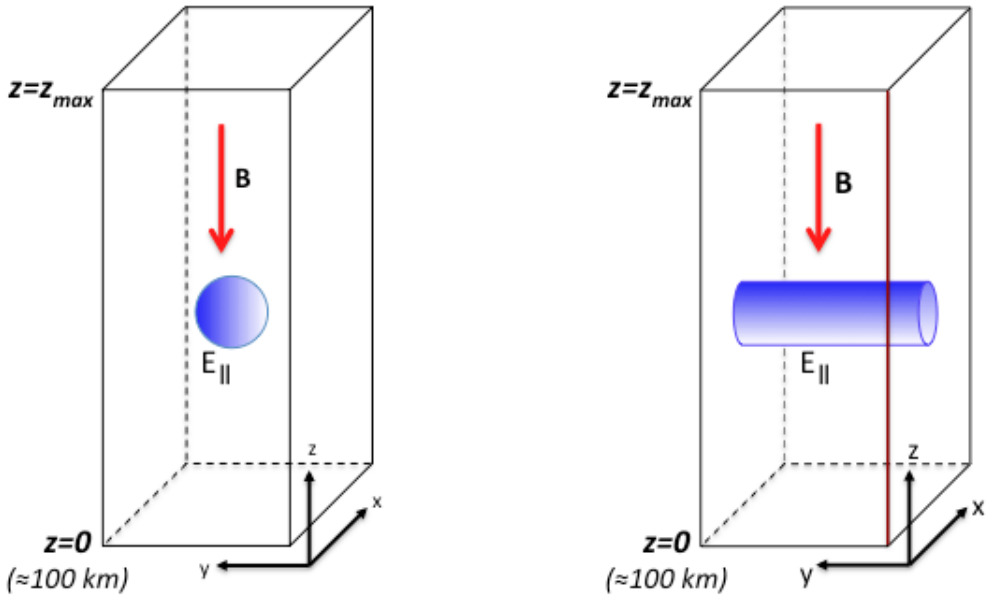

(a) (b)

Figure 4.4: Schematic viewes of introduced localized $E_{\parallel}$ in cases I and II. (a) 3D localization of $E_{\parallel}$ in the form of a blob, for case I and (b) 2D localization of $E_{\parallel}$ in the form of a rod, for case II.

For this case, the profile used for the localized electric field is

$$E_{loc} = 0.05 \left[\frac{1}{cosh^2\left(\frac{x}{2}\right) cosh\left(\frac{z-55}{3}\right)} \right]. \tag{4.3}$$

This profile localizes the parallel electric field in a cylinder geometry with the peak value of 0.05 along a line which is parallel to the y-axis and passes through the point $(0, 0, 55)$. Away from this line, the value drops gradually and is negligible beyond a certain distance.
The parameter E_{loc} is then added to the z-component of Ohm's law in the simulation. Therefore, in both cases I and II the actual electric field in the simulation is given by

$$\mathbf{E} = -(\mathbf{v} \times \mathbf{B}) + \eta \mathbf{j} + \mathbf{e}_z E_{loc}. \tag{4.4}$$

4.2.2 Numerical method: Case III - Localized resistivity

In case III, the simulation domain is larger than that used in case I or II to provide the possibility for longer *run*s without any wave interference at the simulation boundaries. The domain extends from -8 to 8 (in km) in the x-direction, from 0 to 40 (in km) in the y-direction and from 0 to 200 (in 100 km) in the z-direction. At some location near the middle of the simulation domain lies the localized resistivity in the form of a 3D blob. This localized resistivity is introduced by using the

third term η_{loc} of resistivity equation 2.35. The schematic view of the localized fixed resistivity, for case III, is shown in Figure 4.5. In this case the structure of the 3D profile parameter for η_{loc} is

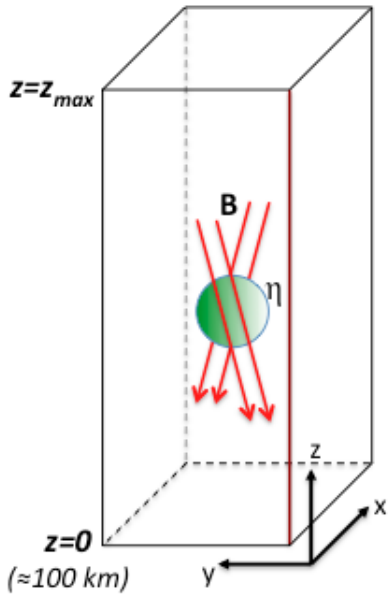

Figure 4.5: Schematic view of introduced localized *resistivity*, η_{loc}, in case III. This diagram shows the 3D localization of resistivity in the form of a blob.

nearly same as that used in case I and is given by

$$\eta_{loc} = 0.05 \left[\frac{1}{cosh^2\left(\frac{x}{2}\right) cosh^2\left(\frac{y-20}{2}\right) cosh^2\left(\frac{z-80}{3}\right)} \right]. \tag{4.5}$$

So, the quantities are localized around $(0, 20, 80)$ with a peak value of 0.05. These quantities are then added to the existing resistivity in the simulation domain. So, a localized high value of resistivity forms in a 3D blob-like pattern at an altitude $\approx 1.25R_e$ above the surface of the Earth where the background resistivity (η_{bg}) is about 4% of this peak value.

Magnetic and velocity perturbations are introduced at the top 16% of the simulation domain, that is in the magnetospheric region, as illustrated in the sketch in Figure 3.3. The introduced sheared magnetic fields that is equivalent to upward FAC layer travels in the downward direction similar to case I (3.2.1) or case IV (3.2.4) of Chapter 3. At the beginning, perturbations cover the portion of domain that is $z \approx 168$ and above. The magnetic perturbations are along the $\pm y$-direction on the two sides of $x = 0$ and the governing equation is

$$\delta B_y = \frac{\delta B_{y0}}{2} \left[tanh\left(\frac{z - 0.8 z_{max}}{4}\right) + 1 \right] tanh(x) \tag{4.6}$$

and the equation for the associated velocity perturbations is given by

$$\delta v_y = -\delta B_y \frac{v_A}{B_0} \tag{4.7}$$

to generate downward propagating Alfvén waves. This is the similar configuration as for the cases I and IV exploring the effect of ionospheric conductance on the evolution of FACs in Subsection 3.2.1 and 3.2.4. The symbols in both the equations have the same meanings as before. The constant quantities δB_{y0}, v_A and B_0 have the values 1.0, 4.0, and 4.0, respectively.

The pair of Alfvén waves, with opposite polarization, carry a sheet of FAC toward the ionosphere. The ionospheric boundary is set at $r \approx 0.8$ by choosing the imposed value of $\Sigma_P = 2.25$. That is the Pedersen conductivity of the ionosphere is set at a uniform high value and about 80% of the incident perturbations are reflected back in the upward direction.

Around the location of the introduced resistivity, both η_{io} and η_{bg} are much smaller than η_{loc}. So, the total resistivity at this location is $\eta = \eta_{io} + \eta_{bg} + \eta_{loc} \approx \eta_{loc}$. Away from this resistive location and at the magnetosheric heights the background resistivity η_{bg} is dominant so that $\eta \approx \eta_{bg}$. Due to the presence of the resistivity in the FAC layer, a parallel electric field ($\approx \eta_{loc} j_\parallel$) is generated so that the effective electric field in the simulation is

$$\mathbf{E} = -(\mathbf{v} \times \mathbf{B}) + \eta \mathbf{j} \approx -(\mathbf{v} \times \mathbf{B}) + \eta_{loc} \mathbf{j} \tag{4.8}$$

for the blob region. But at all other locations at the magnetospheric heights the electric field becomes

$$\mathbf{E} = -(\mathbf{v} \times \mathbf{B}) + \eta \mathbf{j} \approx -(\mathbf{v} \times \mathbf{B}) + \eta_{bg} \mathbf{j}. \tag{4.9}$$

As the peak value of η_{loc} is much bigger than η_{bg}, the total parallel electric field is also localized by the localization of the resistivity. The associated results of all the three cases are explored in the next section.

4.3 Simulation results

4.3.1 Results: Case I - Localized parallel electric field of fixed magnitude in the form of a 3D blob

In case I, the parameter, E_{loc}, is switched on at time, $t = 0$, that is, at the beginning of the simulation and this develops a strong localized electric field in the z-direction. As the geomagnetic field is assumed to be along the z-direction, this, basically, contributes in developing a strong $E_\parallel$. As a result, an immediate generation of the FAC is observed. The plots for the $E_\parallel$ and the associated $j_\parallel$, shortly after the beginning of simulation (at $t = 4$), are shown in Figure 4.6. The plot on the left

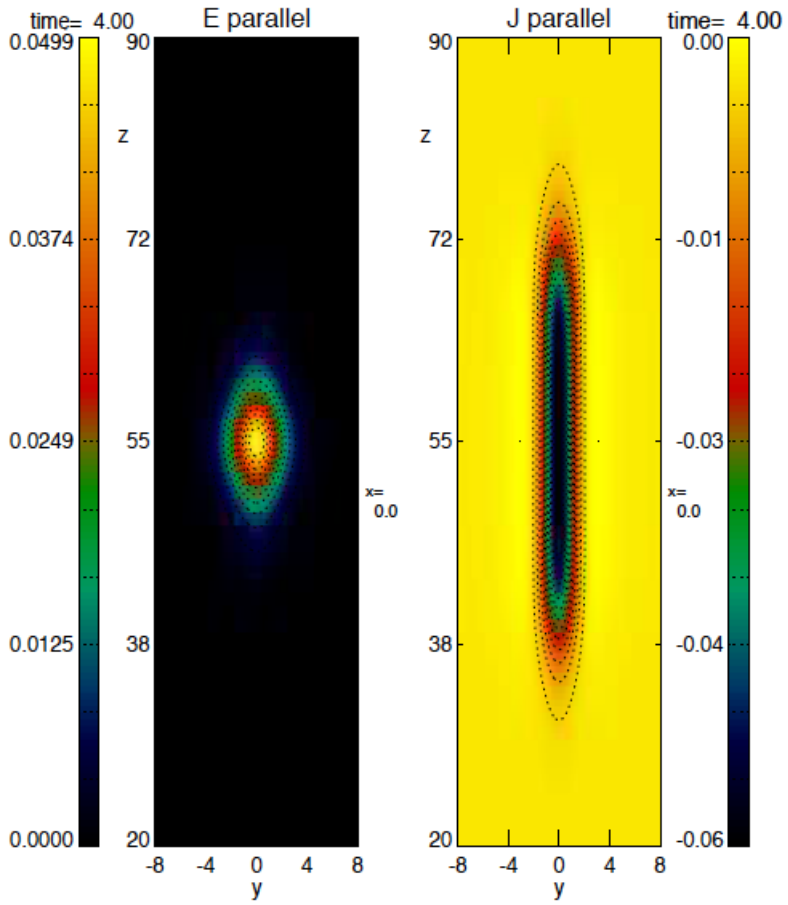

Figure 4.6: Case I: Plots of introduced $E_{\|}$ and generated $j_{\|}$ in the yz-plane at $x = 0$ at time $t = 4$. (Left) Parallel electric field localized around $(0, 0, 55)$ in the form of a 3D blob. Immediately, a strong FAC is generated. (Right) FAC density. Both the plots are taken shortly after the introduction of localized $E_{\|}$.

side of this figure shows the introduced $E_{\|}$, localized around $(0, 0, 55)$, in a cut of the 3D system in the yz-plane at $x = 0$ i.e. at the middle of the domain. The plot on the right side in the same figure shows the FAC density ($j_{\|}$) at the same cut and at the same time ($t = 4$). This plot illustrates the generation of FAC immediately after the introduction of localized $E_{\|}$. Plots of $E_{\|}$ and $j_{\|}$ in the xz-plane at $y = 0$ would produce similar results. These plots also indicate that the source for the FAC is the localized electric field and further inspection shows that the FAC region is expanding along the magnetic field (z-direction) with Alfvén speed.

Figure 4.7 shows the plots of $E_{\|}$ and $j_{\|}$, in the xy-plane at $z \approx 55$, for a better perspective of its shape and location. These plots also consistently indicate the generation of $j_{\|}$ at the location of introduced $E_{\|}$. FACs are closed through polarization currents at the leading edge. Figure 4.6 (right) shows the upward currents in the yz-plane at $x = 0$. The closure of this current (weak,

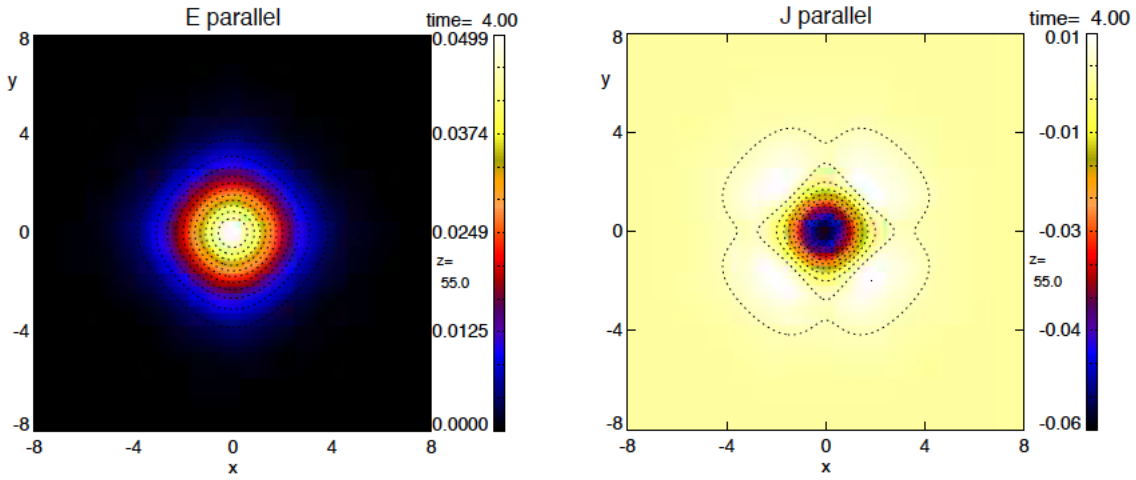

(a) (b)

Figure 4.7: Case I: Plots of introduced $E_{\parallel}$ and generated $j_{\parallel}$ in the xy-plane. (a) Plot of the introduced parallel electric field localized in the form of a 3D blob around $(0, 0, 55)$. (b) Plot of generated FAC density. Both the plots are taken in the xy-plane through $z = 55$ at time $t = 4$ i.e. shortly after the introduction of $E_{\parallel}$.

downward) is evident in Figure 4.7b and the net current in the xy-plane is zero.

The localized electric field perturbation suggests the generation of a magnetic field perturbation based on the induction equation. Figure 4.8 shows the vector-plot for the resultant of the x and y components of magnetic perturbation in the xy-plane at $z = 55$. As in the previous vector-plots,

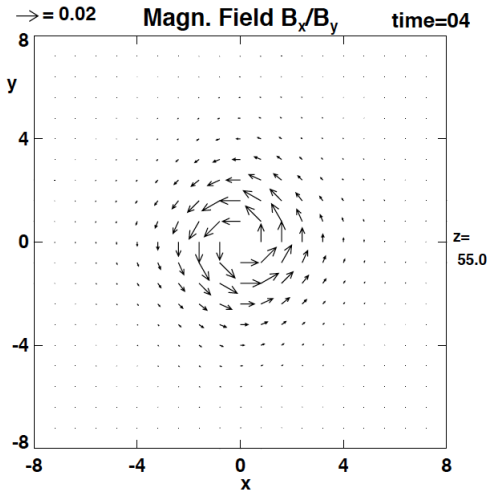

Figure 4.8: Case I: Plot of magnetic perturbation in the xy-plane around the FAC. The plot is taken at $z = 55$ and at time $t = 4$.

the magnitudes of the vectors are obtained from the vector shown outside the upper left corner of the plot. The magnetic perturbation shown in this plot is invariant in height (z) throughout the region covered by the generated FAC. Generation of magnetic perturbation by a localized electric field is farther explained with the help of induction equation in the last section.

The plots of velocity perturbation provide farther insight, consistent with this interpretation. Figure 4.9 shows two vector-plots of velocity perturbations in the xy-planes at distances of $\Delta z \approx \pm 10$ from (i.e. above and below) the location where $E_{\|}$ is introduced. In Figure 4.9a the velocity

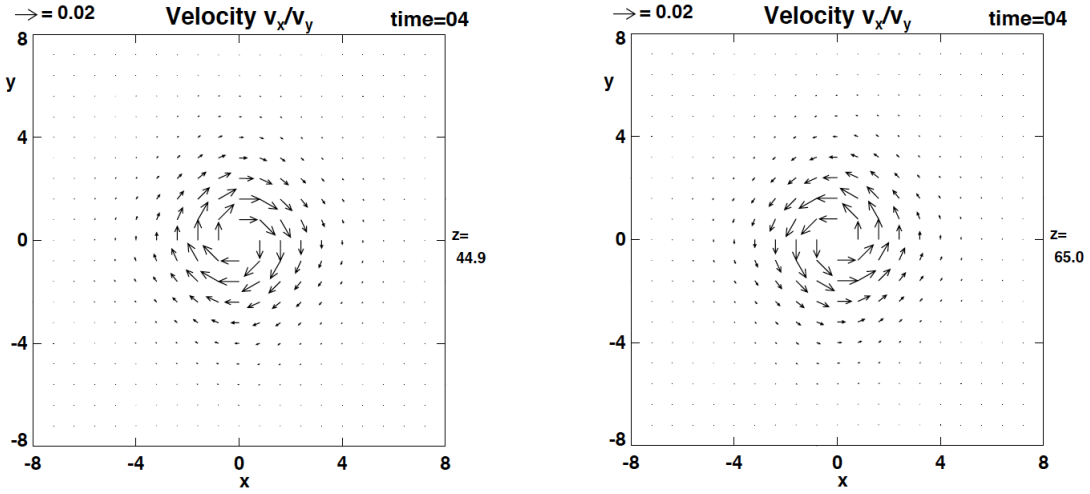

(a) (b)

Figure 4.9: Case I: Plots for velocity perturbations in the xy-plane above and below $z = 55$, the location of the introduced $E_{\|}$, at time $t = 4$. (a) Plotted at $z \approx 45$. (b) Plotted at $z \approx 65$

perturbations, around the current ($j_{\|}$) at $z \approx 45$ are clockwise and the corresponding velocity perturbations at $z \approx 65$ (Figure 4.9b) are counterclockwise. That is exactly the perturbations expected for torsional Alfvén waves with k-vectors in the upward and downward directions carrying energy out of the source region ($z = 55$).

To explore the nature of energy dissipation or generation, Figure 4.10 presents $\mathbf{E} \cdot \mathbf{j}$ in the xy-plane, at $z = 55$, i.e., at a location where the parallel electric field and its associated FAC are present. The plot shows that the dominant value of $\mathbf{E} \cdot \mathbf{j}$ is < 0 at the source region of the FAC where the parallel electric field is localized. The negative value of $\mathbf{E} \cdot \mathbf{j}$ implies a *dynamo action* that is the generation of energy from this region. However, this is unphysical because there is no free source of energy since the magnetic field is uniform. A steady state solution with a localized $E_{parallel}$ requires two converging Alfvén waves (here, torsional) which should exactly match the properties of the expanding waves and carry the energy into the source region from the surrounding. This requires prior knowledge (by the outer world) about the localized $E_{parallel}$ and thus violates causality.

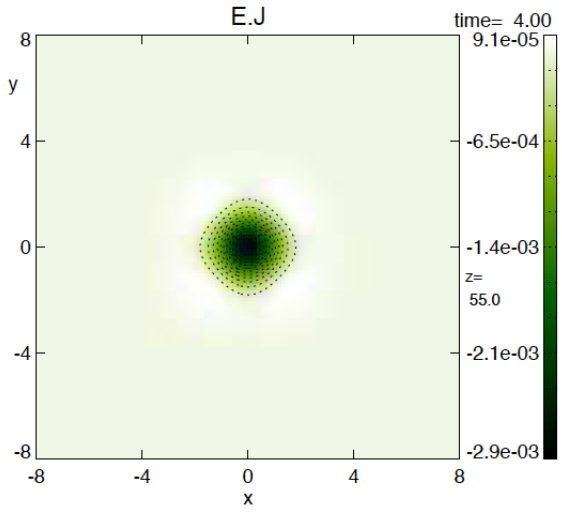

Figure 4.10: Case I: Plot of $\mathbf{E} \cdot \mathbf{j}$ in the xy-plane at $z \approx 55$ at time $t = 4$. The negative values dominate at the location of the introduced parallel electric field.

Therefore this case provides an example that the appearance of localized parallel electric field in absence of any source is not plausible. The next section explores a situation where a parallel electric field is localized in a 2D geometry.

4.3.2 Results: Case II - Localized parallel electric field of fixed magnitude in the form of a 2D cylinder

Figure 4.11 shows the parallel electric field, $E_{\parallel}$, at $t = 4$ in a xz-plane at $y = 0$, that is at the middle of the simulation domain. The plot shows the cross-section of the localized $E_{\parallel}$ having a cylinder like shape centered about $(0, 55)$ on the xz-plane. The results of this appearance of the localized (2D) parallel electric field are studied using the plots of generated FAC and magnetic perturbation. Figure 4.12 shows the presence of $j_{\parallel}$ at the same time $t = 4$. This current is generated along the length of the localized parallel electric field and produces a current sheet. In Figure 4.13, a xy-cut of the FAC is plotted in the plane through the center of the localized parallel electric field. Figures 4.12 and 4.13 together establishes the generation of the current sheet along the location of the introduced parallel electric field.

These figures also demonstrate that the generated FAC has both, parallel and anti-parallel components. This property of up and downward currents is also present in case I although it is not as obvious because the magnitude of the positive parallel current density in case I is much smaller than the antiparallel component. The cause for the presence of both current directions is straightforward in case II, because the total current in the z direction (integrated along x) must be 0 because the magnetic perturbation becomes negligible at large distances from the current layer. This associated

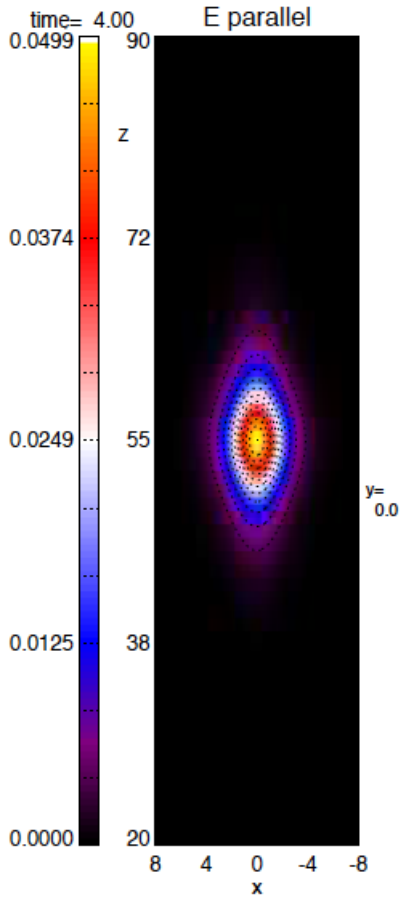

Figure 4.11: Case II: Plot of the introduced $E_{\|}$ in the xz-plane at $y = 0$ at time $t = 4$. The plot shows that the parallel electric field is localized around the point $(0, 55)$ on the xz-plane.

magnetic perturbation is shown in the next two plots. Figure 4.14 shows the plot of y-component of the magnetic field on the xz-plane at $y = 0$ at $t = 4$. As no y-component was present originally, this B_y represents the perturbation in the magnetic field (δB_y). On the two sides of the yz-plane through $x = 0$, the perturbations are in opposite directions. Further insight is provided by the plot of the magnetic field (perturbations) on the xy-plane, shown in Figure 4.15. This is a vector-plot showing the combined x and y-components of the magnetic perturbation at $z \approx 55$ at $t = 4$. It is evident from this figure that the x-component of this perturbation is negligible and the y-component is much weaker than the guide magnetic field. The plots also remain same at any other xy-cut in the region where $j_{\|}$ is present.

The velocity perturbation is examined in Figure 4.16. As in case I, the plots are taken in the xy-planes at distances of $\Delta z \approx \pm 10$ from $z = 55$ that is above and below the location of introduced $E_{\|}$. The directions of δv_y are opposite on the two sides of $x = 0$.

In the plane above $z = 55$, δv_y is positive for $x > 0$ and negative for $x < 0$ and the magnitude

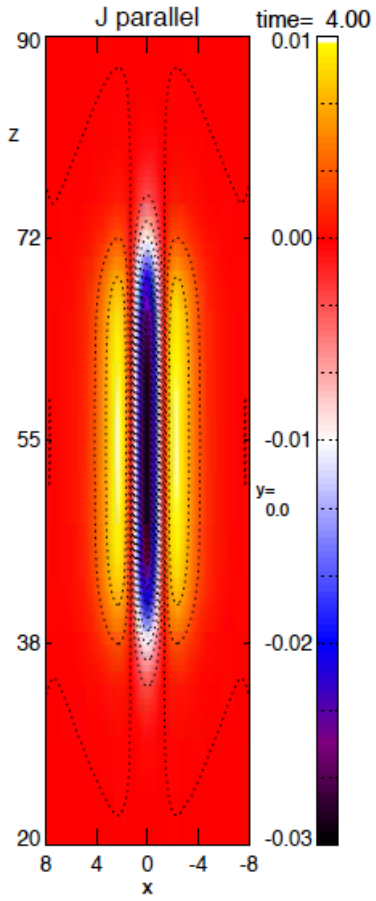

Figure 4.12: Case II: Plot of the generated FAC ($j_{\parallel}$) in the xz-plane at $y = 0$ at time $t = 4$. The generated current gradually covers larger distance along the z-direction.

relative to the magnetic perturbation is consistent with Alfvén waves with a positive k-vector along z, i.e., traveling upward above the localized parallel electric field. The polarity of the velocity perturbation changes below the localized electric field, corresponding to negative k-vectors and propagate in the downward direction. This illustrates that the localized electric field is the source of a magnetic perturbation which is carried out by Alfvén waves traveling up and downward from the source region. The magnetic perturbation induced by the parallel electric field source and propagated by the Alfvén waves is consistent with the FAC density distribution in Figure 4.12.
Again it is instructive in how far this process is a source or sink of magnetic energy. The generation of energy is explored in the plot of $\mathbf{E}\cdot\mathbf{j}$ in the xy-plane at $z \approx 55$ in Figure 4.17. Obviously negative values of $\mathbf{E}\cdot\mathbf{j}$ dominate in the center of the current sheet indicating a net generation of magnetic energy in the absence of any free source of energy. This result is similar to the result obtained in case I and violates causality. Different from the cases I and II, the following section considers a case where a localized parallel electric field is caused by the interaction of a FAC and introduced

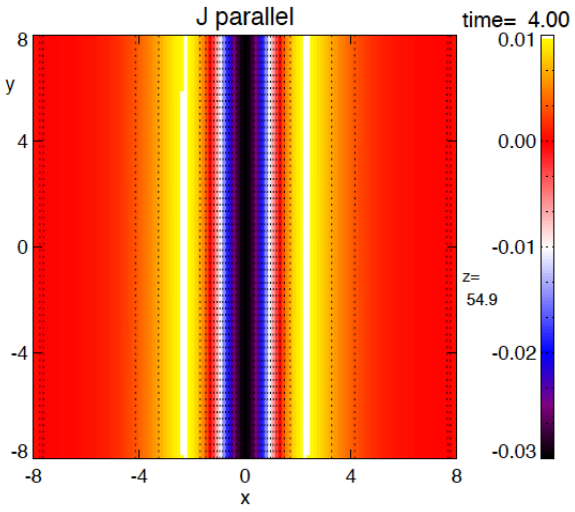

Figure 4.13: Case II: Plot of the generated FAC density ($j_{\parallel}$) in the xy-plane at $z \approx 55$ at time $t = 4$. This plot confirms that the current is generated in the form of a sheet.

(localized) resistivity is explored.

4.3.3 Results: Case III - Localized resistivity of fixed magnitude in the form of a 3D blob

In order to illustrate the Alfvénic perturbations which are imposed by the initial conditions and travel toward the ionospheric boundary, Figure 4.18 shows the magnetic and velocity perturbations in a xy-plane at $t = 20$ at $z \approx 150$. It is seen that the x-components for both δv and δB are negligible. The perturbations (magnetic and velocity) and the associated current layer travel downward and reach the plane shown in Figure 4.18 at $t \approx 5$ and eventually reach the ionospheric boundary (at $t \approx 42$) before reflection.

The FAC density associated with the magnetic field perturbation is presented in Figure 4.19a. The plot shows the presence of the current sheet (at $t = 20$) at the boundary between the two oppositely directed magnetic perturbations consistent with Ampere's law, long before any reflection (at the ionospheric boundary) has taken place.

In case I of Chapter 3 (Subsection 3.2.1), it is observed that in this kind of situation, magnetospheric FAC is enhanced after the reflection from the ionosphere. Figure 4.19b shows the increased FAC density at $z \approx 20$ at time $t = 50$, after reflection. The reflection from the lower boundary starts at $t \approx 42$ and reaches the location of the plot ($z = 20$) at $t \approx 47$. The reflected waves return to the height ($z \approx 80$) of the introduced localized resistivity at $t \approx 62$. So, at any time after $t \approx 62$, the value of $E_{\parallel}$ at $z \approx 80$ also becomes stronger following Equation 4.8.

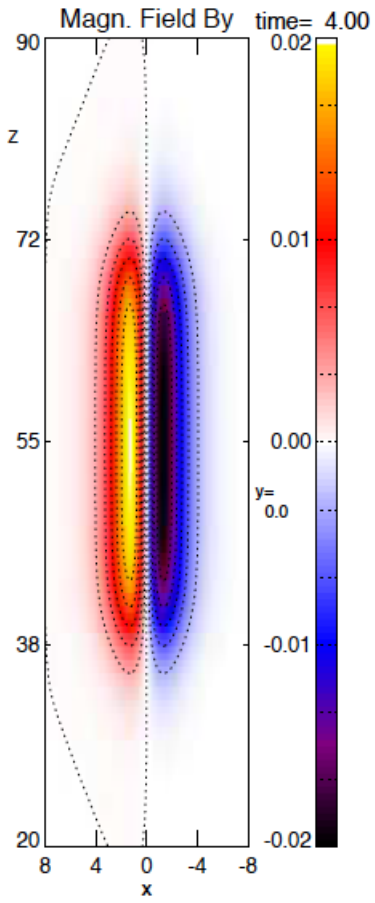

Figure 4.14: Case II: Plot of the generated magneic perturbation (δB_y) in the xz-plane at $y = 0$ at time $t = 4$. This plot shows that the y-components of magnetic perturbation are oppositely directed in the plane of the plot, on the two sides of the central yz-plane through $x = 0$.

In order to understand the evolution it is highly instructive to examine the change of the FAC density and corresponding change in the parallel electric field close to $z \approx 80$. Plots of $j_{\parallel}$ and $E_{\parallel}$ around this site at three different times are shown in Figure 4.20. These plots are taken, respectively, at times, $t = 64$, 80, and 96 in the xy-plane at $z \approx 80$. The plots clearly indicate the increase of both the quantities with time and the thin current sheet gradually grows stronger. In this timespan, the maximum magnitude of $j_{\parallel}$, increases from 2.07 to 3.48 and the corresponding change in the maximum magnitude of parallel electric field is from 0.0970 to 0.1560.

Figure 4.21 illustrate the time variation of the maximum value of parallel electric field ($E_{\parallel,max}$) in the simulation domain. This plot has three distinctively different phases. In the initial phase, before the magnetospheric FAC reaches the location of the resistive blob (at $t \approx 22$), the magnitude of $E_{\parallel,max}$ is zero. After thearrival of the incident Alfvén waves, the value of $E_{\parallel,max}$ increases due to the presence of the FAC carried by the incident perturbations. The next jump in its value is

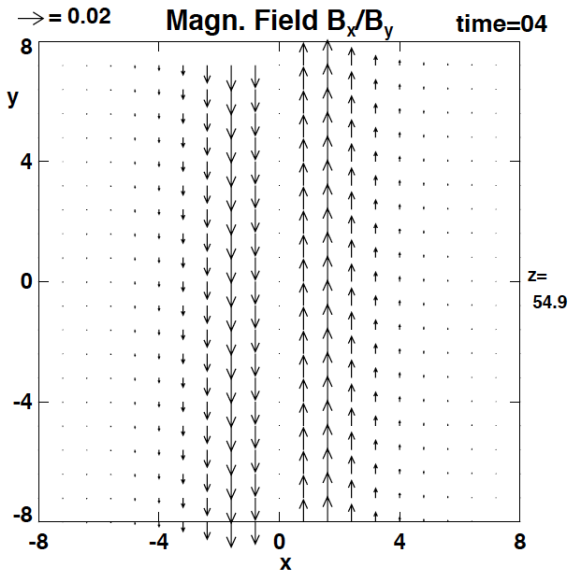

Figure 4.15: Case II: Plot of the generated magnetic perturbations in the xy-plane at $y = 0$ at time $t = 4$. This plot also shows that on the two sides of the central yz-plane the y-components are oppositely directed.

observed at $t \approx 62$ when the reflected waves reach the blob-location. It may be noted that before this time the shear flow is Alfvénic by definition because it is given by the velocity perturbation of the incident Alfvén wave. It has been known for a long time that magnetic reconnection requires

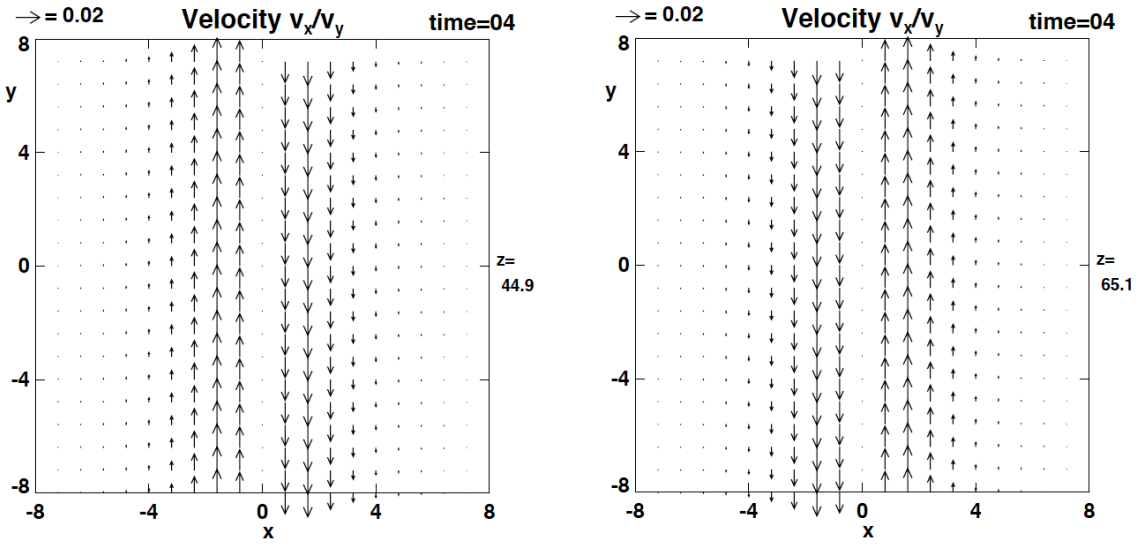

(a) (b)

Figure 4.16: Case II: Plots for velocity perturbations in the xy-plane above and below $z = 55$, the location of introduced $E_{\|}$, at time $t = 4$. (a) Plotted at $z \approx 45$. (b) Plotted at $z \approx 65$

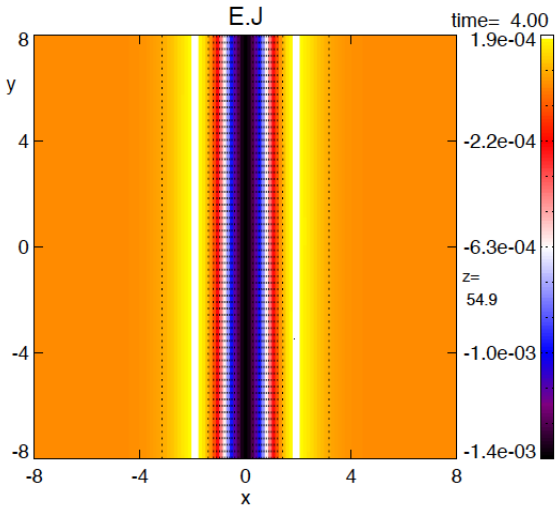

Figure 4.17: Case II: Plot of $\mathbf{E} \cdot \mathbf{j}$ in the xy-plane at $z \approx 55$ at time $t = 4$. The negative values dominate at the locations of the introduced parallel electric field.

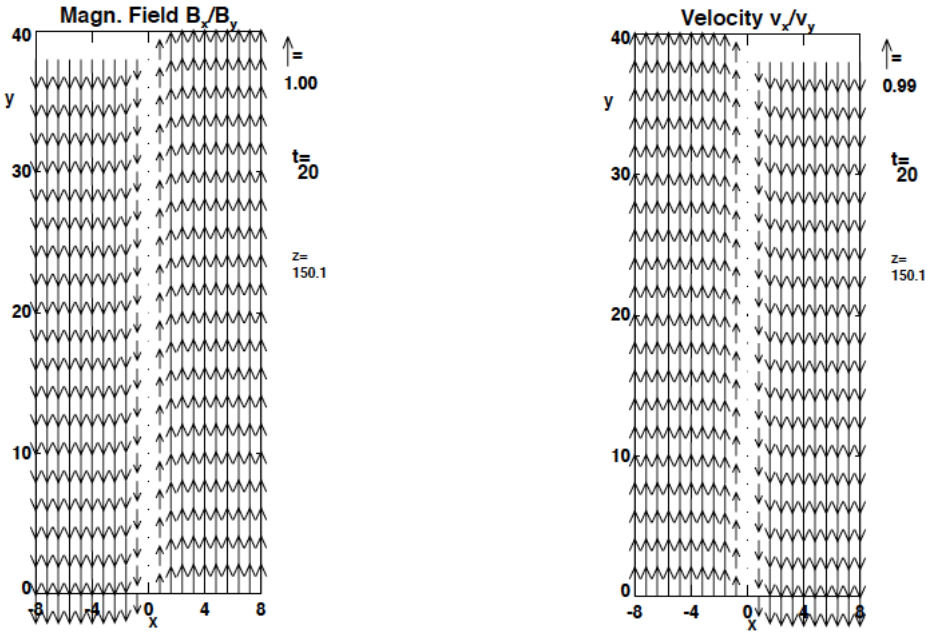

(a) (b)

Figure 4.18: Case III: Plots of introduced magnetic and velocity perturbations. These plots show the (a) magnetic and (b) velocity perturbations introduced at the top 16% of the simulation domain. Then they travel in the downward direction. Plots are in the xy-plane at $z \approx 150$ at time $t = 20$.

sub-Alfvénic flow and is not operating during the incident wave perturbation [113, 114]. But from around $t = 62$ the total magnetic perturbation is enhanced and velocity perturbation is reduced

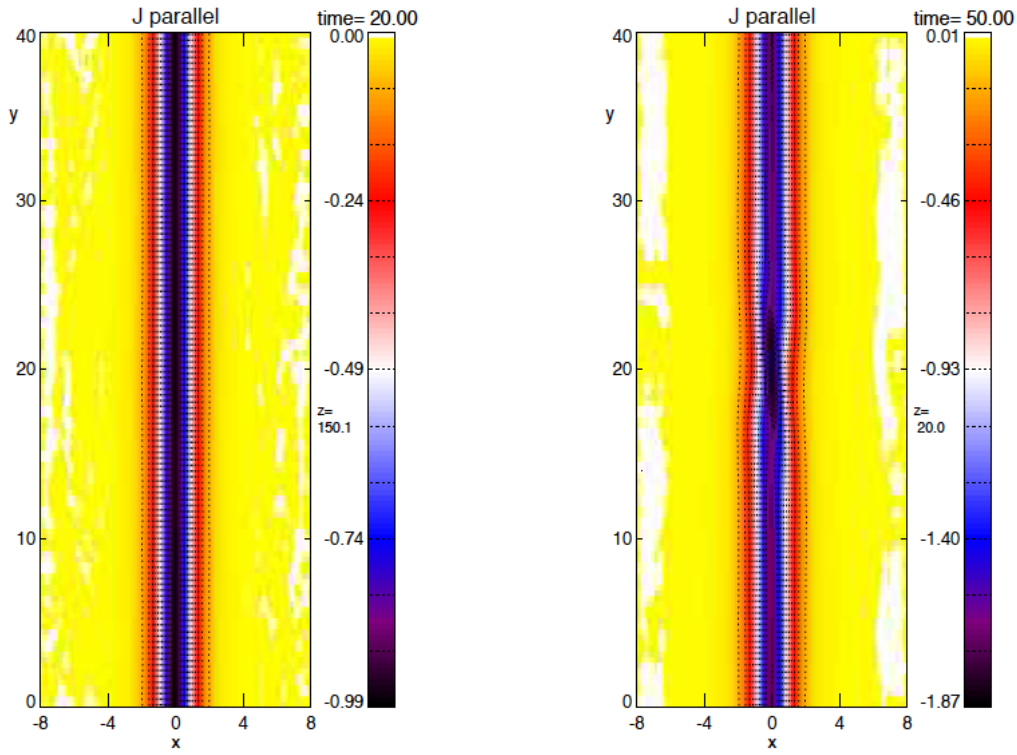

(a) (b)

Figure 4.19: Case III: Plots of $j_{\|}$ associated with the incident and reflected (total) Alfvénic perturbations in the xy-plane. (a) Taken at $t = 20$ at $z \approx 150$ associated with the incident wave. (b) Taken at $t = 50$ at $z = 20$ associated with the superposed (total) wave after reflection. The values of $j_{\|}$ increase after reflection.

from their initial (incident) values because of the superposition with the reflected wave. This situation favors the reconnection thereby causing the increase in the value of $j_{\|}$. Therefore the increase in $E_{\|,max}$ observed in Figure 4.21 characterizes active reconnection after $t \approx 62$.

This evolution and configuration of a very thin current layer and a localized strong parallel electric field are typical for magnetic reconnection. This is confirmed by inspecting the magnetic and velocity perturbations, along with the associated FAC density at the location of the resistivity-blob. Figure 4.22 shows the plots for these three quantities in the xy-plane at $z \approx 80$ at time $t = 96$. Figure 4.22a shows combined x and y-components of the magnetic field in the xy-plane using the arrows. Figure 4.22b shows the vector plot of the combined x and y-components of velocity in the xy-plane. These two plots strongly indicate the occurrence of reconnection. The velocity plot shows the typical plasma jet in the outflow region and the convergence of the flow toward the central region where the parallel electric field is localized. The magnetic field plot shows the typical

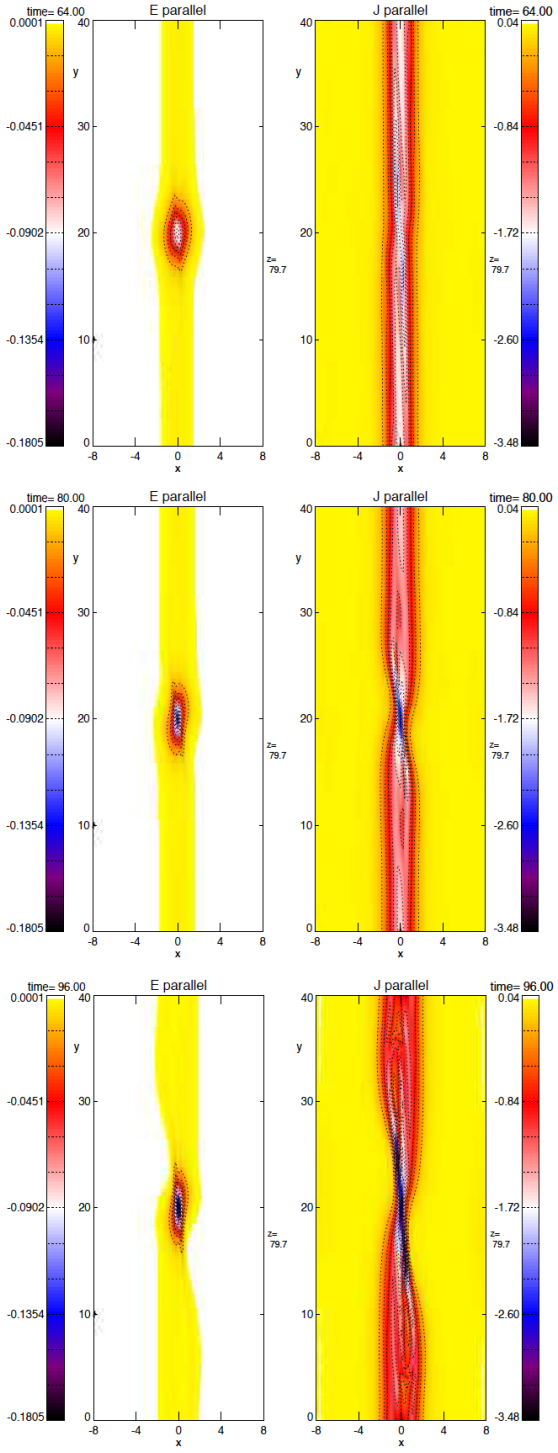

Figure 4.20: Case III: Variation of $E_{\parallel}$ and $j_{\parallel}$ with time. Plots are taken (from top) at $t = 64,\ 80$ and 96 in the xy-plane at $z \approx 80$ (location of the introduced resistivity blob).

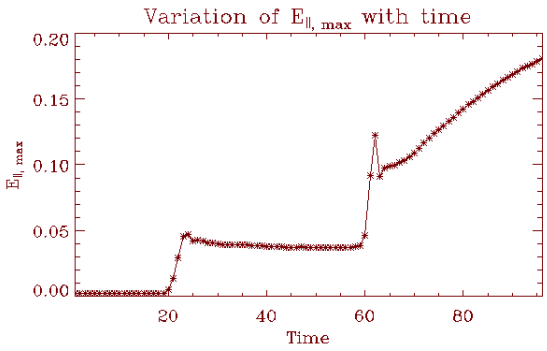

Figure 4.21: Case III: Plot showing the time evolution of maximum parallel electric field ($E_{\parallel,max}$) in the simulation domain.

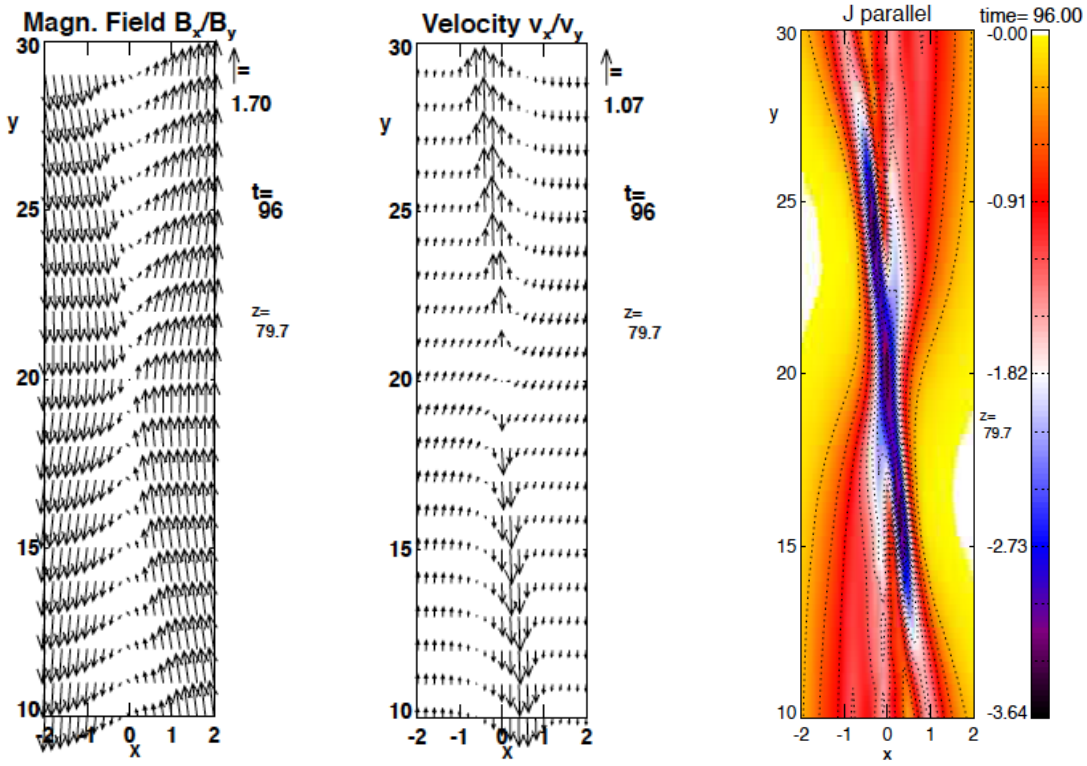

(a) (b) (c)

Figure 4.22: Case III: Plots of Magnetic and velocity perturbations and, FAC density indicating reconnection. These three plots show (a) magnetic perturbation (b) velocity perturbation and (c) FAC density - near the location of localized resistivity at $z \approx 80$ and at time $t = 96$ indicating the presence of strong transport. The FAC is strong enough so that magnetic reconnection takes place.

rotation with a smaller y-component in these outflow regions. Note that the counter streaming slower plasma on the two sides of the outflow region is the residual velocity perturbation from the

partial reflection of the Alfvén wave at the ionospheric (lower) boundary. In Figure 4.22c colors show the z-component of FAC density in the xy-plane. Strong FAC associated with the magnetic and velocity perturbations is observed near the location of magnetic reconnection.

Plots in Figure 4.23 are all showing snap-shots of the horizontal profiles of the FAC density at time, $t = 96$ in a sequence of increasing altitude. These plots show the altitude variation of $j_{\parallel}$ at a time much after the reflection. A close inspection of these plots reveals different important features. All these plots show the presence of thin current layers of $\sim 150m$ (physical value) having high value of current density imbedded in a much wider ($\sim 2\ km$, physical value) layer of current of comparatively lower current density. The plots show the variations in the orientation, strength, length, and thickness of the layers of the FACs. Close to the ionosphere, the overall thickness of the current layer is large but it shows clearly that a very strong and narrow current is embedded into the larger scale current. Also close to the ionosphere this narrow strong current layer is very extended along the y-direction. The overall current configuration with a broad weaker current and a narrow embedded current remains the same but the length of the narrow and intense current decreases up to a height somewhere below the parallel electric field region. Above this height the length of the embedded current increases again. The maximum value of FAC density in the xy-plane also changes with the altitude. Upward from above the ionosphere this value increases up to an altitude (here, $z \approx 60$) and it decreases after that. The values of $E_{\parallel}$ and $j_{\parallel}$ are consistent with the Equations 4.8 and 4.9. Note that the maximization of the current below the localized electric field region is interesting.

Without illustration it is remarked that distribution of $E_{\parallel}$ and $j_{\parallel}$ look very similar in their pattern at sufficient distances away from the location where $\eta_{loc}E_{\parallel}$ is localized. At these locations the resistivity is determined by a background resistivity (η_{bg}) which is uniform, however, so small that it has no influence on the overall evolution.

Another important feature can be observed from these plots. The orientation of the thin current-layer changes gradually, with the change of its altitude. Below the location of the maximum FAC density, the thin current-layer is oriented a small amount away from the $x = 0$ plane in the clockwise direction. Examples are Figures 5.4a or 5.4b. But above that location, the thin current-layer is away from the $x = 0$ plane by a small amount but in the counterclockwise direction. Examples are Figures 5.4d or 5.4e. This feature reveals some important information that will be discussed in a separate subsection.

For the understanding of energy dissipation or generation, $\mathbf{E} \cdot \mathbf{j}$ plot is considered in Figure 4.24. This plot shows that the dominant contribution from $\mathbf{E} \cdot \mathbf{j} > 0$ at the locations of the introduced resistivity which implies the dissipation of energy in the form of heat and thus different from the unphysical result of cases I and II. In the next part some of the interesting aspects of case III are

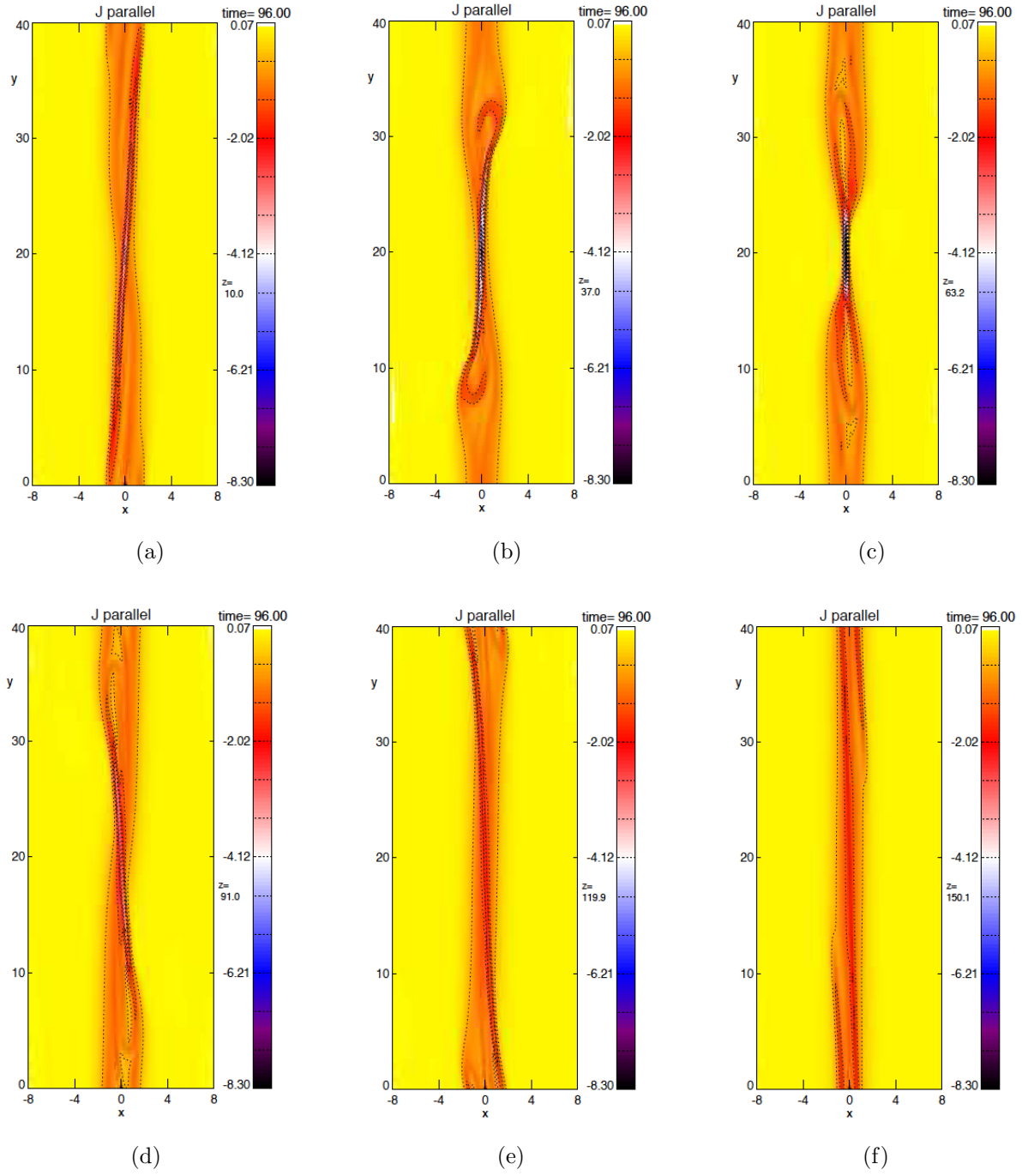

Figure 4.23: Case III: Variation of FAC density with height (z). The plots in the xy-planes are taken at heights (a) ≈ 10, (b)$= 37$, (c)≈ 63, (d)$= 91$, (e)≈ 120 and (f)≈ 150 and at time $t = 96$.

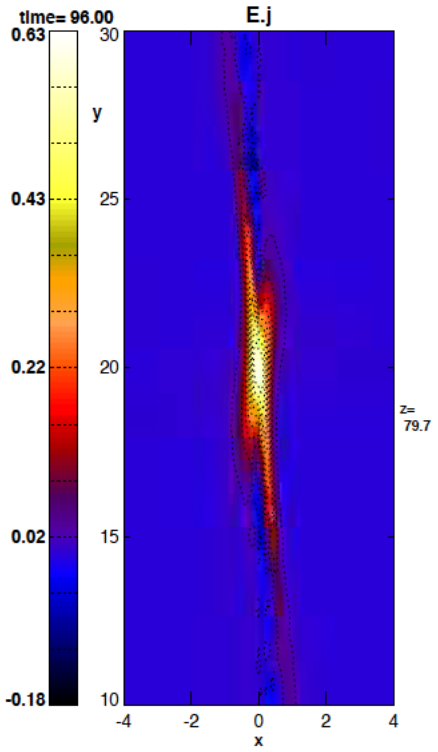

Figure 4.24: Case III: Plot of $\mathbf{E}\cdot\mathbf{j}$ in the xy-plane at $z \approx 80$ at time $t = 96$. The values are positive at the locations of the introduced resistivity.

highlighted.

4.3.3.1 Some of the interesting features of case III

There are different interesting features related to case III. These are the evolution and orientation of thin and strong current layers with respect to the large scale current sheet, a variation of plasma density at the ionosphere, and the association of Pedersen current with the FAC, among others.

Relation between the magnetic reconnection and the thin current sheet: In case III, the reflection of shear Alfvén waves from a highly conductive uniform ionospheric boundary results in the enhancement of magnetospheric FAC and the increased value of FAC favors the process of 3D magnetic reconnection. A cartoon is shown in Figure 4.25 to illustrate the occurrence of reconnection. This diagram shows that the diagonal at the upper boundary that contains the field lines has changed its orientation after the reconnection. Before the reconnection, the diagonal containing the field-lines are extended between the *left-front corner* and the *right-back corner* at the top boundary of the simulation domain. They come closer, as they approach the location of

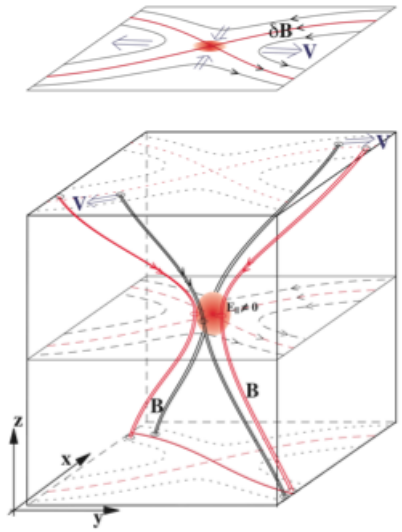

Figure 4.25: Case III: Sketch illustrating the changes in magnetic field lines in presence of FAC ($j_\parallel$) and localized parallel electric field ($E_\parallel$). (Sketch: A Otto, unpublished figure, used with permission)

resistivity blob that creates the strong $E_\parallel$. After reconnection they again spread along a diagonal that is extended between the *left-back corner* and the *right-front corner* of the domain. This change of orientation is understood by comparing the plots in Figures 5.4a and 5.4d which clearly indicate the movement of the current sheet from one side of the central plane to the other side.
The next two Figures (4.26 and 4.27) show the similar results from a different angle. These are the

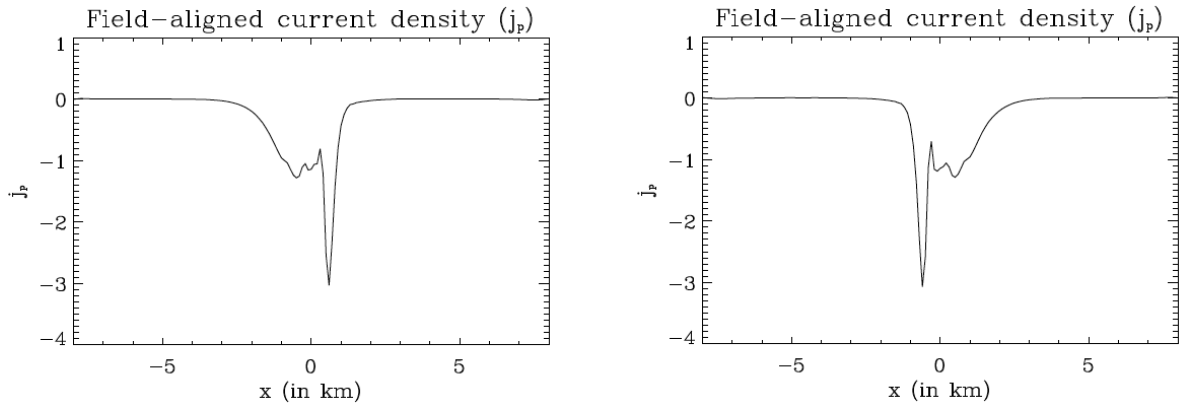

(a) $j_\parallel$ at $y = 10$ (at higher altitude).

(b) $j_\parallel$ at $y = 30$ (at higher altitude).

Figure 4.26: Case III: x-profiles of FAC density ($j_\parallel$) at an altitude $z \approx 100$ i.e., above the location of the resistivity blob and at two different positions along the y-direction. (a) at $y = 10$ and (b) at $y = 30$.

line-plots showing the x-profiles of $j_\parallel$ at different locations. Figure 4.26 shows these plots at two

places along the y-axis at $z \approx 100$. That is somewhere above the location of current-maximum. But Figure 4.27 shows a similar plot for much lower altitude (at $z \approx 8$). These four plots conclu-

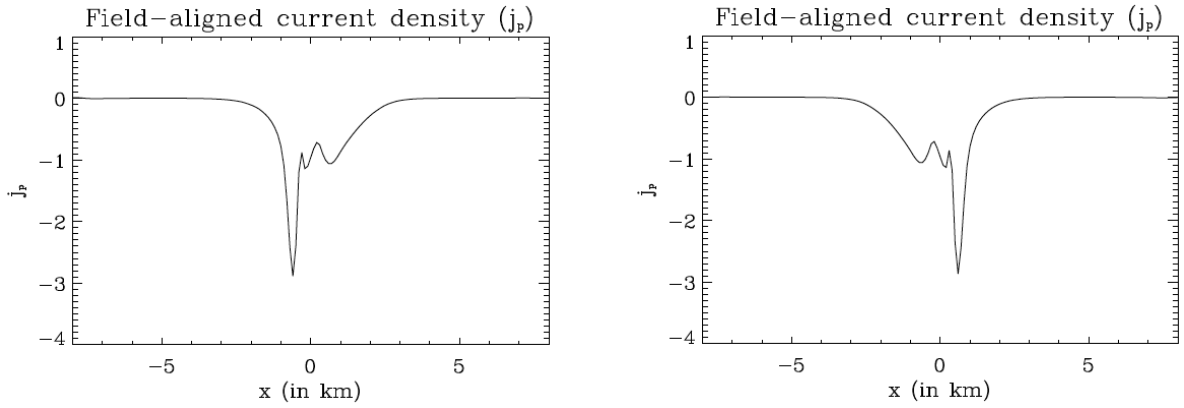

(a) $j_{\parallel}$ at $y = 10$ (at lower altitude).

(b) $j_{\parallel}$ at $y = 30$ (at lower altitude).

Figure 4.27: Case III: x-profiles of FAC density ($j_{\parallel}$) at an altitude $z \approx 8$ i.e., below the location of the resistivity blob and at two different positions along the y-direction. (a) at $y = 10$ and (b) at $y = 30$.

sively show the presence of very thin current sheets having a much higher magnitude of $j_{\parallel}$ (≈ -3, normalized value) embedded in a large scale current sheet ($\sim 2000\ km$) with much lower value of average magnitude of $j_{\parallel}$ (≈ -1, normalized value). The negative values of $j_{\parallel}$ indicate that the direction of the currents are upward.

It can also be noted from the plots that the thin current sheet switches the side from left to right or vice versa above and below the location of current-maximum. Looking from $y = 0$ along the positive y-direction, the thin curtain of FAC shifts from $x > 0$ (located at $y = 10$, in Figure 4.26a) to $x < 0$ (located far away at $y = 30$, in Figure 4.26b) at $z \approx 100$. On the other hand, it shifts from $x < 0$ (located at $y = 10$, in Figure 4.27a) to $x > 0$ (located far away at $y = 30$, in Figure 4.27b) at $z \approx 8$. The average locations of the thin current sheet remain, more or less, same as the large-scale current. There is a possibility that this thin current sheet could be the proxy of the discrete auroral arc.

If the magnetic flux in the thin current layer were conserved, the thickness in the x-direction would decrease as it grows wider in the y-direction. This appears to be supported by these plots. But one needs to note that the FAC is not a conserved quantity along a magnetic flux tube. With the change of the orientation of these field lines, the flow pattern of the charged particles, traveling along these field-lines also changes. This also implies that the field-lines which are very close in the region, having high value of $E_{\parallel}$ can map over a large distance along the FAC sheet at the ionosphere. This is consistent with the results by Otto and Birk [112].

In Figure 4.25, the reconnection plane is shown, separately, above the box representing the simulation domain. This illustrates the inflow and outflow of plasma. The plot in Figure 4.22b clearly shows the flow velocities that are consistent with this illustration. These results show the presence of a structured current system, with narrow sheets embedded in the large-scale overall current. This has been observed by in situ measurements, for example by Dynamic Explorer satellites [115, 116].

Plasma density variation at the ionosphere: Due the movements of the plasma from one place to another, some density variation is expected. Particularly, if the currents, close to the ionosphere are considered, this is more effective. The FACs (basically, carried by the electrons) close at the ionospheric boundary by the Pedersen current. These are already discussed in Chapter-3. Pedersen current is carried, basically, by the (heavier) ions. So, their transport can alter the density profile. A cartoon in Figure 4.28 is used to illustrate this. The diagram shows the plasma-

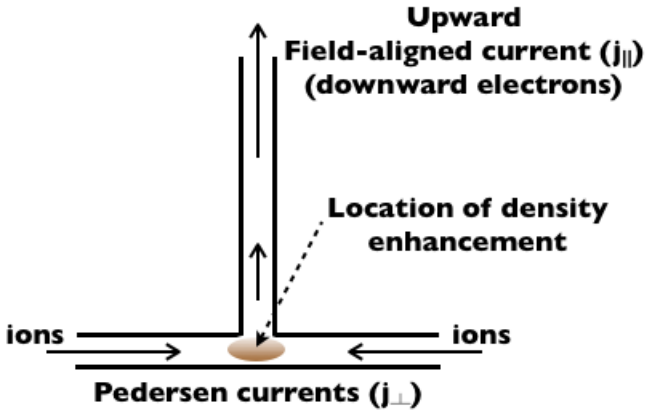

Figure 4.28: Case III: Sketch illustrating the location of density enhancement due to the different currents at the ionospheric E-region when the FAC is upward.

flows in a vertical (xz) plane for upward FAC. For this current to develop, electrons travel inside the current sheet in the downward direction. At the ionosphere, the Pedersen current closes this current sheet. For upward FAC, Pedersen currents are directed toward the foot of the current sheet. So, along the ionospheric foot-point of this kind of current sheet, a density enhancement is probable. This is shown in Figure 4.29. Figure 4.29a shows a plot for the current density of the vertical component of current and the Pedersen current on the xy-plane at $z = 0$. The colors show the vertical component of current density (j_z) and the arrows show the density of Pedersen current (converging to the center of the FAC layer). It may be noted that the vertical component of the current density may well represent the FAC density (with a change of sign). At the lower boundary the Pedersen currents are directed toward the FAC from both the sides. In the plot, j_z is positive.

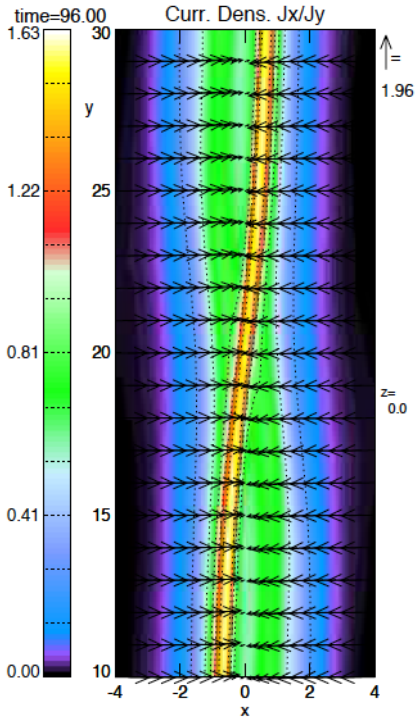

(a) Current densities at the lower boundary.

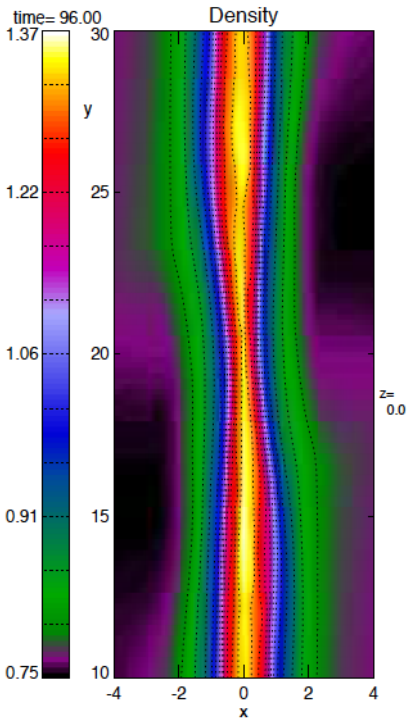

(b) Density variation at the lower boundary

Figure 4.29: Case III: Plots of current densities and plasma density near the lower boundary. These plots show the relation between the density profile and current pattern near the lower boundary. (a) Colors represent the vertical component of current density (j_z) and the arrows are showing the Pedersen currents near the ionospheric boundary. Effectively, $j_z = -j_{\parallel}$, in this case. (b) Density variation at the ionospheric boundary. Enhancement of density is observed along the ionospheric foot-points of FAC.

This means the current is upward forming a negative FAC. Figure 4.29b shows the density plot, also on the xy-plane at the ionospheric boundary (at $z = 0$). The plot shows a clear enhancement of density along the locations where the FACs are closed.

With the enhancement of the density (ρ) at the locations of FACs, the depletion of density is also observed in the surrounding region. Figure 4.30 shows the variation of density with time using the x-profiles of density across the current sheet (at $y = 30$) near the lower boundary (at $z = 0.8$). The straight line at $\rho = 1$ shows the value of density before the Alfvénic perturbations have reached the ionosphere, that is, up to time $t \approx 42$. Densities at three other times ($t \approx 48$, 72, and 96) are shown. These plots illustrate that after the reflection of the perturbation waves and with the development of Pedersen current, the density decreases on the two sides and increases at the base of the FAC sheet.

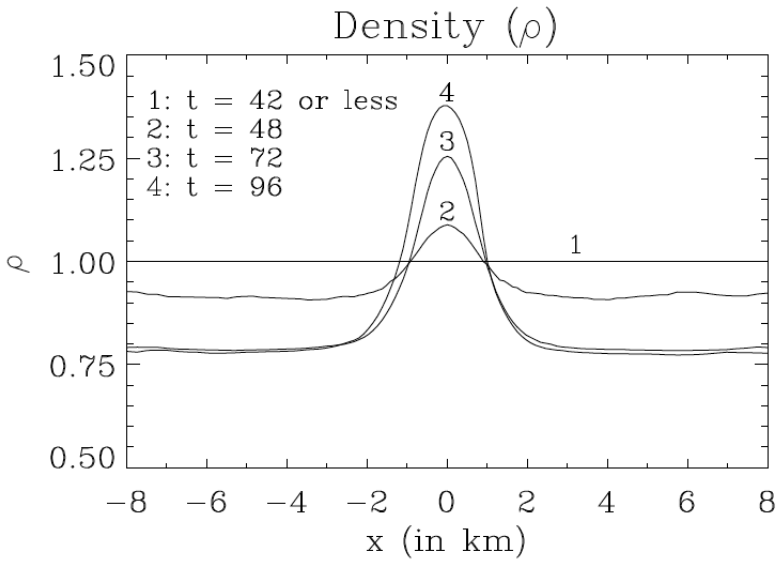

Figure 4.30: Case III: Time evolution of x-profile of plasma density across the FAC-sheet in the E-region (at $y = 30$ and $z = 0.8$). Plot no. 2, 3, and 4 are showing the changes in plasma density with time compared to the initial density value, shown in plot no. 1.

Association of Pedersen current and FAC in the ionosphere: A close inspection of Figure 4.29a may reveal some insight on how the Pedersen current and FAC are associated. This plot shows that the Pedersen currents (i.e. j_x) converge toward the center of the large scale current but the stagnation point of Pedersen current is slightly off the center of the thin embedded FAC (i.e. location of strongest j_z in the plot) and is more pronounced at larger distances from the symmetry point at $y = 20$. This is illustrated in Figure 4.31 which shows the x-profiles of both Pedersen current ($I_{P,x}$, in blue, solid line) and FAC density (j_z, in red, solid line) at a small height above the ionospheric boundary (at $z \approx 3$) through $y = 30$ at time $t = 96$. The magnitude of the gradient of $I_{P,x}$ along the x-direction (i.e. $\partial_x I_{P,x}$) is also plotted (blue, dotted line) in this figure. The plot of j_z shows the presence of a thin and strong and, a wider and weaker FAC layers (i.e. $-j_z$) with their peaks separated by a small distance. Actually, these two peaks almost coincide at $y = 20$ (not illustrated) and away from this location, along both $\pm y$-direction they are separated. Moreover, on either side of $y = 20$ these two peaks switch their sides which is consistent with our observations illustrated in Figure 4.26 and 4.27.

The y-component of the ionospheric horizontal current is negligibly small and thus the region of total FAC layer is associated with the gradient of Pedersen current $I_{P,x}$. Following current continuity equation $\nabla \cdot \mathbf{j} = 0$, we can obtain $\partial_z j_z = -\partial_x j_x$. When integrated along the z-direction, this results in $j_z = -\partial_x I_{P,x}$. As discussed in Chapter 2, j_x is confined, mostly, to a few grid levels near the lower boundary. Hence, an integration over a few grid points (here, from $z(1) = 0$ to $z(9) \approx 3$),

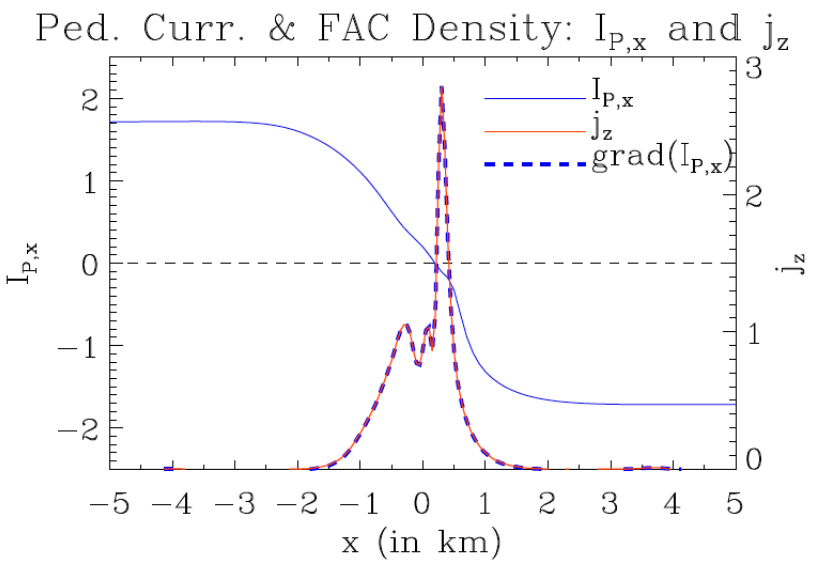

Figure 4.31: Case III: x-profiles for $I_{P,x}$, j_z and the magnitude of $\partial_x I_{P,x}$ at $y = 30$, $z \approx 3$ at time $t = 96$. The variation of $\partial_x I_{P,x}$ is in good agreement with the variation of j_z.

almost includes the total Pedersen current. In Figure 4.31 the x-profiles are taken at $z(9) \approx 3$ and as expected, the plot of j_z has a very good agreement with the plot of $\partial_x I_{P,x}$. The thin current layer with highest magnitude of $j_\parallel$ or j_z is at the location of strongest gradient. Thus it should be noted that this thin current layer need not necessarily be at the location of stagnation of the Pedersen currents. This result is not surprising because the simulation should satisfy $\nabla \cdot \mathbf{j} = 0$, however it presents a nice test of this property. In the next section a summary of all the three cases and a discussion on the main results of these cases are added.

4.4 Summary and discussion

In cases I and II, a localized parallel electric field ($E_\parallel$) is switched on, in a magnetic field that is assumed to be uniform, at the beginning of the simulation. The parallel electric fields are introduced at an altitude corresponding to $\approx 1R_e$ above the ionosphere that is in the magnetospheric region. In case I, the localized $E_\parallel$ is in the form of a 3D blob [shown in Figures 4.5 (left) and 4.6a], the central part of which has the peak-value. The value decreases gradually, with the distance from the center and becomes negligible beyond a certain distance. In case II, $E_\parallel$ is localized along a line, parallel to the y-axis, in the form of a 2D rod-like structure. In both the cases, an immediate generation of FAC [Figures 4.5 (right), 4.6b, 4.11, and 4.12] and of a corresponding magnetic perturbation [Figures 4.7, 4.12, and 4.13] are observed. Upward and downward propagation of magnetic and (associated) velocity perturbation indicates the production of Alfvén waves from the location of the introduced $E_\parallel$.

The interpretation of this result is straightforward. The localized electric field acts as a source for the magnetic field perturbation. This can be easily seen by inspecting the induction eqaution in spherical (for case I) or cylindrical (for case II) coordinates. For example, similar to case I, a localized blob of parallel electric field is assumed to be located at the origin of the coordinate system with a radial (ρ) dependence given by

$$\mathbf{E} = E_{\parallel}\mathbf{e}_z = \frac{q}{\rho^{\alpha}}\mathbf{e}_z \tag{4.10}$$

where q and α are constants and $\alpha > 0$ so that the magnitude of $E_{\parallel}$ decreases rapidly with the distance from the center of the blob. In spherical coordinates, this shape of a localized parallel electric field leads to

$$\frac{\partial \mathbf{B}}{\partial t} = -(\nabla \times \mathbf{E}) = \frac{q(\alpha - 1)}{\rho^{\alpha}} sin\theta \mathbf{e}_{\phi} = (\alpha - 1)E_{\parallel} sin\theta \mathbf{e}_{\phi} \tag{4.11}$$

for the azimuthal magnetic field components. Therefore the magnitude of the parallel electric field determines the amount of azimuthal flux generated. Without any coupling to the ambient magnetic field and plasma this flux would just accumulate, however, it is efficiently transported along the background magnetic field by Alfvén waves away from the localized electric field region. The magnitude of this transport depends again on the amount of flux generated, i.e., on the size and magnitude of the localized parallel electric field.

The plots of $\mathbf{E} \cdot \mathbf{j}$ in these two cases [in Figures 4.8 and 4.14] show that $\mathbf{E} \cdot \mathbf{j} < 0$ is dominant around the location of the $E_{\parallel}$ blob. This indicates a *dynamo action* that is the presence of a *generator* that produces energy. This is unphysical because it implies the production of energy in the absence of a source of free energy.

So, from the results of cases I and II, it can be concluded that the appearance of $E_{\parallel}$ in a vacuum magnetic field violates causality. While it is likely the case that the presence of a parallel electric field has micro-physical causes, the overall macroscopic evolution cannot be separated from current carrying plasma which can provide a net dissipation associated with the presence of the localized $E_{\parallel}$. With the knowledge from the simulation of case I we can, for instance, construct a solution in which no net energy increase would occur. The solution to this is the presence of two torsional Alfvén waves traveling toward the localized $E_{\parallel}$ region which exactly transport and match the amount of magnetic flux produced by the localized $E_{\parallel}$ region. This configuration would present a steady state solution with an $E_{\parallel}$ blob. However, it is obvious that this requires the prior knowledge of magnitude and distribution of any localized $E_{\parallel}$ presence.

In case III, a fixed value of resistivity, localized in the form of a 3D blob is introduced at $\approx 1.25R_e$ at the beginning of the simulation. Ordinarily one would expect that the presence of such a resistive region would also require corresponding microphysical processes that are typically

current dependent. However, as a controlled computer experiment this assumption of a resistivity is acceptable because the resistivity would not alter anything in the absence of electric currents. The simulation experiment of case III assumes perturbations in the magnetic field and velocity at the top part of the simulation domain. These perturbations are along the $\pm y$-direction on the two sides of the yz-plane dividing the simulation domain into two equal halves at $x = 0$. The perturbations are chosen to be consistent with Alfvén waves traveling in the downward direction carrying a sheet of FAC in between. Eventually, this current reaches the level where the resistive blob is present (at $t \approx 22$), then the ionospheric boundary (at $t \approx 42$) before being reflected back. The reflected perturbations once again cross the location of the blob of localized resistivity (at $t \approx 62$). Following Ohm's law ($E_\parallel = \eta j_\parallel$) it can be said that with the passage of FAC, strong parallel electric field is generated at the location of the localized resistivity. Higher the strength of the current, stronger is the electric field.

At the ionospheric boundary, the Pedersen conductance (Σ_P) is adjusted to achieve a high degree ($\approx 80\%$) of reflection of the incident Alfvénic perturbations from the ionosphere. This kind of situation is studied in Chapter-2, Subsection-3.2.1. The enhancement of FAC by the reflection plays an important role. When this stronger FAC reaches the location of introduced localized resistivity magnetic reconnection is observed and a gradual increase in the reconnection rate in indicated by the increase of the parallel electric field around that location. Presence of thin and strong current layer is observed to be embedded in large-scale current sheet. From the time when the reflected perturbation reaches the resistive region thin FAC grows which varies in strength, orientation, length, and thickness along the vertical direction. This thin layer is strongest and of minimum length at some height below the resistive region. In this work the height (z) of maximization of current density is ≈ 60. The location of maximum current density could be an interesting subject of investigation. Below and above this location, the thin current layer becomes wider and is oriented differently on the two sides of the yz-plane at $x = 0$ that separates the oppositely directed sheared perturbations. While the thin sheet of current remains on the clockwise side with respect to this yz-plane below the location of maximum current density, it remains on the counterclockwise side above that location. This change of orientation is explained and explored farther in another subsection which establishes the change of orientation of the thin current sheet that is embedded in the large scale current sheet more clearly.

Plots of $\mathbf{E} \cdot \mathbf{j}$ in the xy-plane at the resistive region shows that its dominant values are positive in the central part that is at the location of introduced resistivity. This indicates the dissipation of the kinetic energy in the form of heat. Therefore the laws of physics are not violated in this case. FAC, which is basically carried by the electrons, tend to develop polarity at its foot-points in the ionosphere. This is neutralized by the ions converging toward the foot-points (of FACs) developing

Pedersen currents. Movements of the (heavier) ions cause some changes in the density configuration of plasma in the ionosphere. Along the foot-points of FAC the density increases while it decreases on the two sides.

In the ionosphere, Pedersen currents converge from the two sides of the FAC before reaching a stagnation point. Therefore j_x changes between a positive and a negative value, only within the range of x-axis where j_z has a nonzero value. This is true as $j_y \approx 0$ in this case. Therefore the total FAC sheet is observed at the locations where $\partial_x j_x$ has nonzero values. This is verified that the magnitude of $\partial_x j_x$ is maximum at the location of strongest FAC and this location may not be the location of the stagnation point for the Pedersen currents.

Case III is producing various aspects well consistent with discrete aurora such as (1) the presence of a thin current sheet embedded in the large scale current sheet, the change of orientation, thickness, length and, strength of the thin current sheet, (2) aspect ratio (small thickness and great length - 10's to 100's of km), (3) dissipation of energy (4) association of Pedersen current and FAC, (4) convection of tangential flow to thin arcs, (5) variation of plasma pressure and density at the ionosphere, while it is difficult to explain the results of cases I and II with sound physical concepts.

Chapter 5
Evolution of dynamic parallel electric fields

Introduction

The basic requirements and properties related to the formation of localized parallel electric fields were explored in Chapter 4. It was illustrated in that chapter that a localized resistive region where FACs are also present, is able to provide the physical explanation for the formation of localized parallel electric fields. Though that study provides a good background on the relation of parallel electric fields, the resistivity that was introduced in the magnetosphere was artificially fixed in magnitude and at a particular location. To overcome this artificial constraint on the resistivity and to make it more realistic, a pattern of current dependent resistivity is introduced at magnetospheric heights and the results are presented in this chapter. The possible processes that cause such resistive interaction suggest a current density dependence of the resistivity. The magnetosphere represents a collisionless plasma because Coulomb collisions are extremely rare. However, The exception to this rule are current sheets, where the velocity of the current carriers surpasses typical wave velocities such as the Alfvén or ion-acoustic speed. Micro-instabilities and turbulence develop for velocities faster than these wave speeds. For instance, a beam of material moving faster than the speed of sound through a background of neutrals can create shockwaves which would decelerate that beam. Similarly, these beams, which carry large current densities, are subject to instabilities (ion-acoustic etc.) or the formation of double layers, which have the effect of a macroscopic resistivity. The precise conditions for the onset of the resistivity (such as a critical current density) and the general current density dependence are determined by the specific microphysical processes and are not well known. However, various studies (e.g. [117, 118]) have demonstrated that the precise current dependence usually is of minor importance for the overall evolution.

To study the basics of parallel electric fields, Chapter 4 provides an introduction to magnetic reconnection. Magnetic reconnection, itself, has been the subject of many analytical and numerical studies. This process plays a fundamental role in many space and laboratory plasma configurations [119, 120]. The conversion of magnetic energy to kinetic energy is one of the important aspects of this process. It has been suggested, that magnetic reconnection plays a major role in the formation of thin discrete auroral arcs (e.g. [121]). In fact, the very definition of magnetic reconnection through a spatially localized parallel electric field [122, 123] suggests a relation to particle acceleration and discrete aurora.

The basic goals of present chapter are to study (a) the dynamic evolution of parallel electric fields by enabling the motion of parallel electric field regions through the introduction of a current dependent resistivity, (b) to investigate the importance of the magnitude of the ionospheric conductance on the

evolution of parallel electric field and the respective reconnection rate, and (c) to study the possible impacts of gradient of the ionospheric conductance on the evolution of parallel electric fields and magnetic reconnection. For this purpose, a magnetospheric FAC carried by the Alfvénic (magnetic and velocity) perturbations, is introduced as in Chapters 3 (cases I & IV) and 4 (case III). For the present chapter, FACs evolve again through propagation and reflection of Alfvén waves, but also in response to the introduced current dependent resistivity. For our reference case the ionosphere has a uniform high value of Pedersen conductance. Two cases with a lower conductance are introduced to study the influence of the magnitude of a uniform ionospheric conductance. Finally, a gradient in conductance is introduced to explore the influence of conductance gradients on magnetic reconnections.

This chapter also employs, the z-components of Poynting flux in order to compare the energy transport of cases when the magnetic perturbations (a) involve magnetic reconnections and (b) no reconnection is present. Note that the energy transport into the ionosphere is given by the z-component of the Poynting flux $S_z = (\mathbf{E} \times \mathbf{B})_z = (\mathbf{E} \times \delta\mathbf{B})$. Note that the Poynting flux actually is the perpendicular convection velocity, for application within ideal MHD. The dominant Poynting flux is in the horizontal direction and a small component of the actual Poynting flux is directed into the ionosphere (along the unperturbed magnetic field). The next sections present a brief summary of the numerical methods, the results, and a summary and discussion.

5.1 Numerical methods

The basic numerical methods for this study are almost same as that of the case III of Chapter 4 (Section 4.2.2). The only difference is in the type of introduced resistivity compared to that case. The introduced resistivity in this chapter is, current dependent with a contribution that depends explicitly on time as well. The actual computation of the resistivity uses a function

$$\eta_{source} = \eta_{cur}(j) + \eta_{io} + \eta_{bg} + \eta_{loc}(x, y, z, t). \tag{5.1}$$

Here, the terms η_{io} and η_{bg} have the same meaning as before (Section 4.2.2). These quantities do not contribute significantly at the magnetospheric heights. The fourth term, $\eta_{loc}(x, y, z, t)$, contributes a significant amount of resistivity that is localized in space and is briefly switched on in time defined by

$$\eta_{loc}(x, y, z, t) = 0.05 \left[\frac{1}{cosh^2\left(\frac{x}{2}\right) cosh^2\left(\frac{y-20}{2}\right) cosh^2\left(\frac{z-80}{3}\right)} \right] \frac{1}{cosh\left(\frac{t-50}{5}\right)}. \tag{5.2}$$

Thus the term $\eta_{loc}(x,\ y,\ z,\ t)$ develops a resistivity that is localized around $(0,\ 20,\ 80)$ of the simulation domain as in Section 4.2.2 but only for a brief period of time, around $t = 50$, to trigger the magnetic reconnection. The first term $\eta_{cur}(j)$ contributes to resistivity, depending on the

local values of current density (j). This term contributes only when the current density exceeds a specified chosen value. Note, that any attempt to trigger reconnection (larger electric fields) any time before the reflected wave arrived at $z \approx 80$ failed (on the considered time scales).

In order to avoid any rapid fluctuation in the value of resistivity (η), the actual resistivity is determined by the equation

$$\frac{\partial \eta}{\partial t} = (\eta - \eta_{source}). \tag{5.3}$$

This equation implies that the resistivity relaxes on a time scale of unity (1 Alfvén time) to η_{source} provided that η_{source} remains constant. The purpose is to avoid very rapid fluctuations of the resistivity, which can cause numerical problems. Compared to the resistivity described in Section 4.2.2 which was fixed in time and space, here, the resistive region can move depending on the values of local FAC density. That means, in the cases in this chapter, the resistivity developes in response to the evolution of FAC density.

5.2 Results

The introduced magnetic and velocity perturbations remain the same as described in Section 4.2.2 for the case with a fixed localized resistivity. Hence, in this case also, Figure 4.18 (Section 4.3.3) illustrates the nature of incident Alfvénic (magnetic and velocity) perturbations from the magnetosphere. Similarly, Figure 4.19 (Section 4.3.3) illustrates the FAC densities ($j_\parallel$), associated with the incident perturbations and with the superposed perturbations, shortly after the reflection in this case too.

Figure 5.1 illustrates the variation of the maximum value of parallel electric fields ($E_{\parallel,max}$), in the entire simulation domain (in blue asterisks). The respective altitude of this maximum parallel

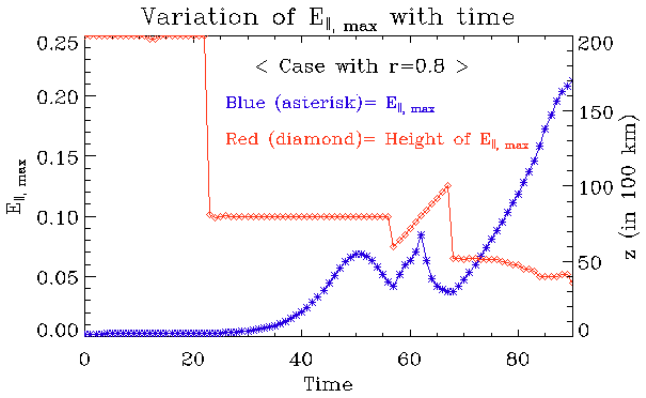

Figure 5.1: Time variation of $E_{\parallel,max}$ and its location in the simulation domain - Plot (in blue) illustrates the time variation of maximum parallel electric field ($E_{\parallel,max}$) in the entire simulation domain. The other plot (in red) shows the location of $E_{\parallel,max}$ using its z-value.

electric field is shown in red (diamonds) in the same figure. Up to about $t = 22$ almost no parallel electric field is present. Only a very small value of $E_{\parallel}$ develops because of the presence of background resistivity (η_{bg}) at the top of the domain once FACs are present. For $t > 22$, i.e., after the arrival of the Alfvénic perturbations at $z \approx 80$, $E_{\parallel}$ increases around the location (0, 20, 80) where η_{loc} is introduced. Note that this is expected because the incoming Alfvén wave maintains an almost constant level of the FAC such that the increasing localized resistivity causes the increasing parallel electric field at $z \approx 80$. After $t = 50$, the resistivity contribution from η_{loc} gradually decreases till $t \approx 57$ when the contribution of $\eta_{cur}(j)$ to the total resistivity (η) becomes dominant in increasing the value of $E_{\parallel,max}$ up to $t \approx 62$. Around this time, the reflected perturbations, with stronger FAC density reach the region of higher value of resistivity. After a short relaxation into this new current state the reflected perturbations and the associated FACs initiate active reconnection and the value of $E_{\parallel,max}$ starts to increase sharply with time after $t = 67$. A comparision between the case of fixed resistivity (Figure 4.21) and this present case shows a larger parallel electric field and more efficient (faster) magnetic reconnection in this case. Here, at time $t = 90$, the value of $E_{\parallel,max} \approx 0.21$ while it is ≈ 0.17 in case of fixed resistivity. Another important feature is the downward displacement of the reconnection site with time. This was observed in the previous case (with fixed resistivity), however, it is more pronounced in these plots. The reconnection site moves down to $z \approx 35$ at $t = 90$ from $z \approx 80$ at $t = 50$.

This motion is actually difficult to explain. Since the resistivity is current dependent this motion of the resistive region implies that the current density is increasing more or faster below z=80. In some physical systems changes of current density can be attributed to simple physical processes such as the compression or stretching of a current sheet. However this is not the case here and the only asymmetries between the region above and below z=80 is the propagation of Alfvén waves across and the boundary conditions.

Figure 5.2 shows the evolution of $E_{\parallel}$ and $j_{\parallel}$ at $z \approx 42$. In order to understand the evolution we examine the variation of the FAC density at a location close to the average location of $E_{\parallel,max}$ after the initiation of reconnection. Here $z \approx 42$ is chosen to examine the evolution of $E_{\parallel}$ and $j_{\parallel}$ at three different times $t = 66,\ 78$, and 90. These plots demonstrate that both $E_{\parallel}$ and $j_{\parallel}$ increase fast with time and the current sheet also grows stronger. The magnitude of $j_{\parallel,max}$ increases from 1.81 to 2.23 in this timespan. The corresponding increase of $E_{\parallel,max}$ is from 0.0245 to 0.2119. In this case the thin current sheet contains more structures.

For a more visual presentation of magnetic reconnection, we should also inspect the magnetic and velocity perturbations and the associated FAC density. Figure 5.3 shows the plots for these three quantities in the xy-plane at $z \approx 44$ and $t = 96$. Though these plots show the similar features as in case of the fixed resistivity in Section 4.3.3, the features are much more pronounced here.

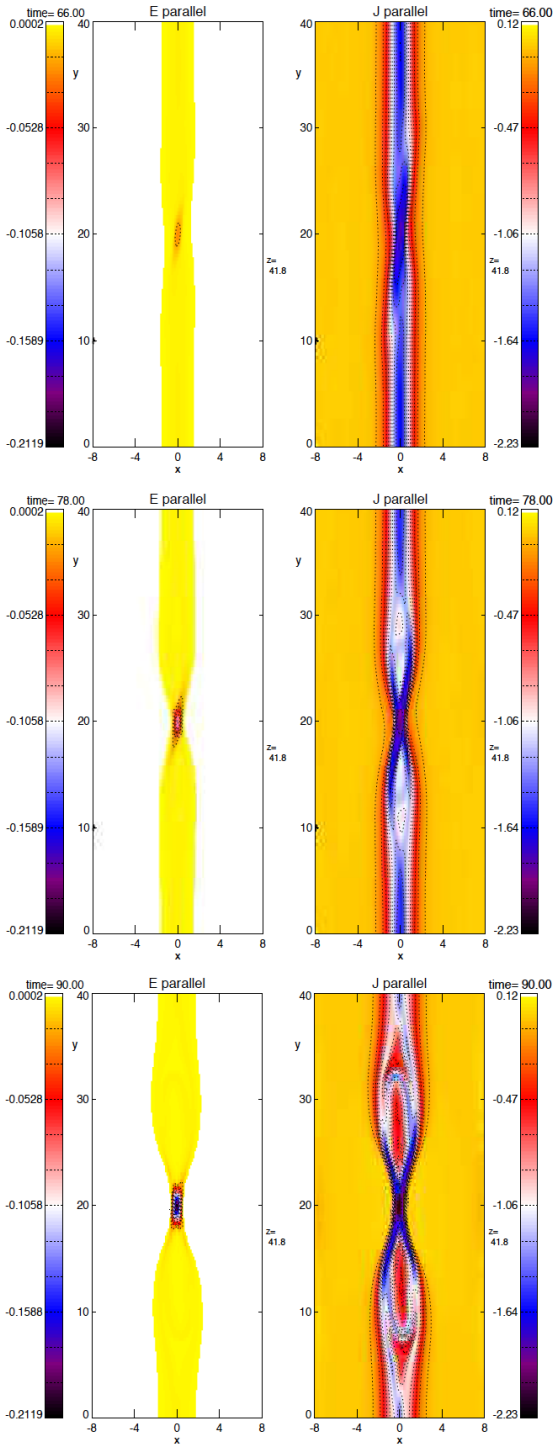

Figure 5.2: Time evolution of $E_{\|}$ and $j_{\|}$ near the location of reconnection. Plots are taken (from top) at $t = 66,\ 78$ and 90 in the xy-plane at $z \approx 42$ (average location of reconnection during this time).

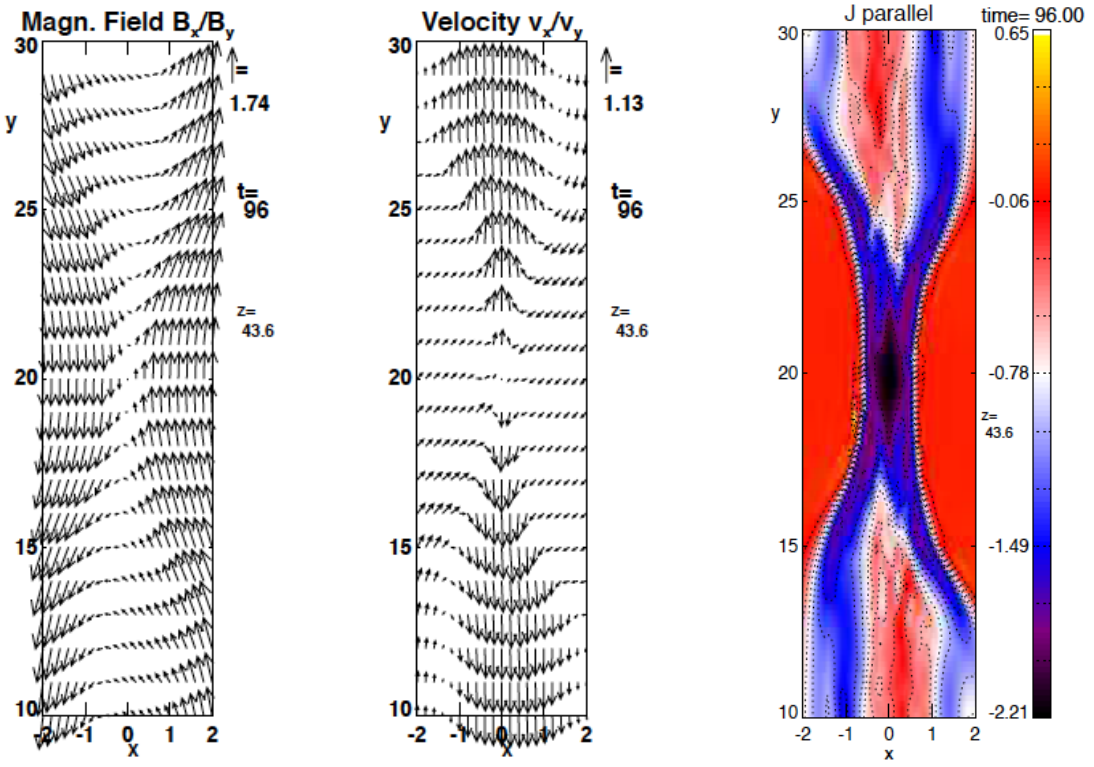

(a) (b) (c)

Figure 5.3: Plots of Magnetic and velocity perturbations and, FAC density indicating reconnection. These three plots show (a) magnetic perturbation (b) velocity perturbation and (c) FAC density - near the region of reconnection at $z \approx 44$ and at time $t = 96$ indicating the presence of strong transport. The FAC is strong enough so that magnetic reconnection takes place.

Figure 5.3a shows the magnetic perturbation and indicates much larger rotation of the incident perturbation compared to the case of fixed resistivity (Figure 4.22). The velocity plot in Figure 5.3b shows a stronger plasma jet, in the outflow region, and faster convergence of the flow toward the central region (see Figure 4.22b). These quantities are typical for the magnetic reconnections. In Figure 5.3c the FAC density is scaled to the same fixed range for all plots. Strong current sheets are observed at the location of reconnection.

For a closer inspection of the altitude variation of the FAC density, Figure 5.4 is added. These plots show snapshots of the horizontal profile of the FAC density at time, $t = 96$ in a sequence of increasing height. This time is much after the reflection and after the triggering of reconnection. Several important features are illustrated in these plots. First, a very strong (prominent) current sheet is observed at the ionospheric boundary (at $z = 0$) of the simulation domain. Probably, it is the consequence of the shift of the reconnection region to a lower height (as illustated in Figure

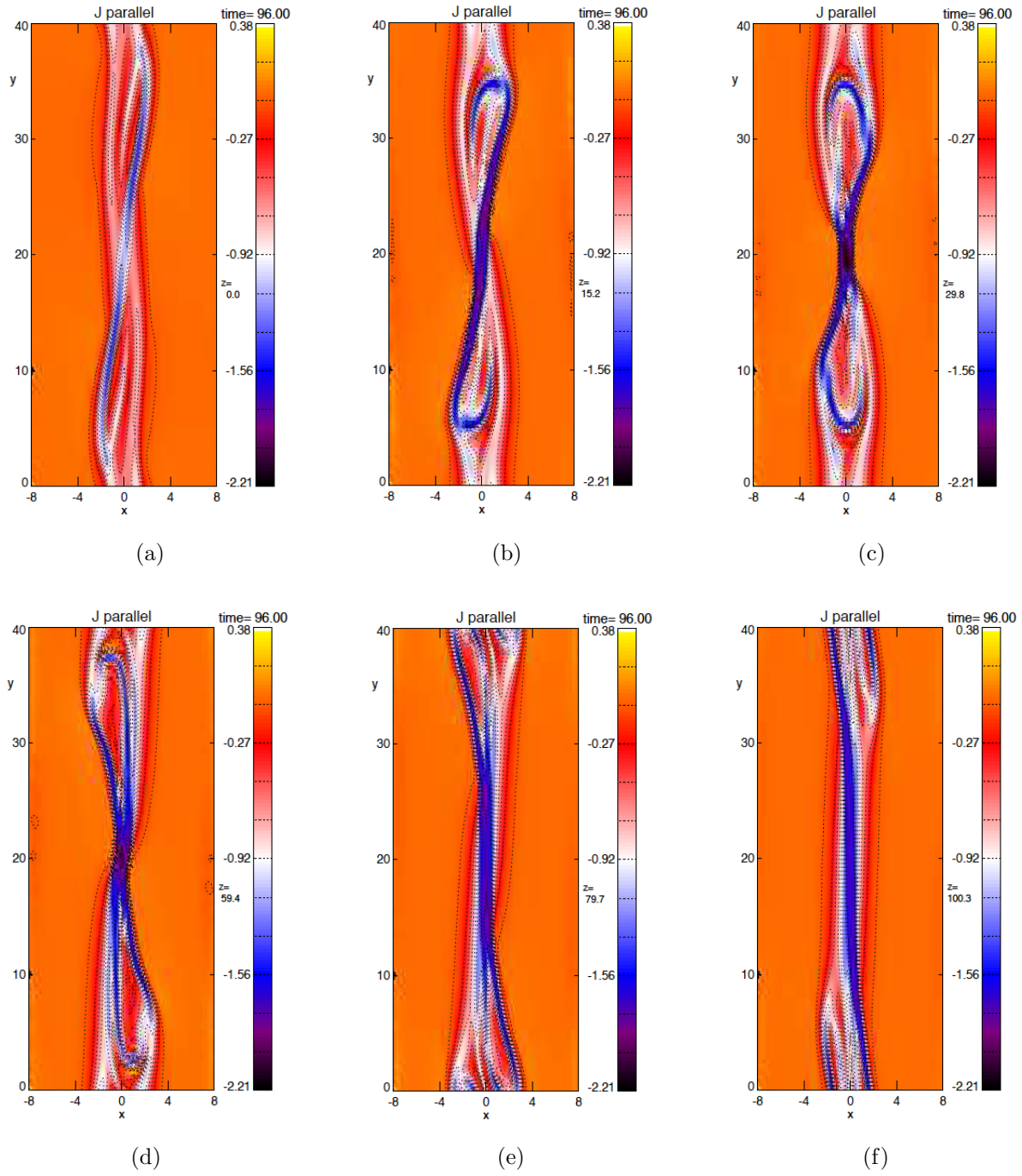

Figure 5.4: Evolution of FAC density with height (z) for dynamic resistivity case. The plots in the xy-planes are taken at or near z = (a) 0, (b) 15, (c) 30, (d) 60, (e) 80 and (f) 100 and at time $t = 96$.

5.1), in this case, (compared to that discussed in Section 4.3.3). Second, the thin current sheets remain embedded inside the large-scale ($\sim 2-4\ km$, physical value) currents (as before). Third, these plots show the presence of more structures in the current system. The narrowest parts of the current sheets are of similar order of magnitudes ($\sim 150-200\ m$, physical value) compared to the case of fixed resistivity but comparatively wider current layers are also present. Fourth, the length of the thin current sheets increase with the increasing distance from the reconnection region and close to this region more structure is present in the current sheets. Last, the magnitude of the FAC density is less than that obtained with the introduction of fixed localized resistivity. Note, however, that this is to some degree arbitrary because it depends on the chosen value of the critical current density above which resistivity is switched on.

For insight into the dissipation of energy, $\mathbf{E}\cdot\mathbf{j}$ is plotted in Figure 5.5 in a xy-plane at $z \approx 42$ and $t = 90$. This plot demonstrates that most of the local dissipation of energy occurs in the form of

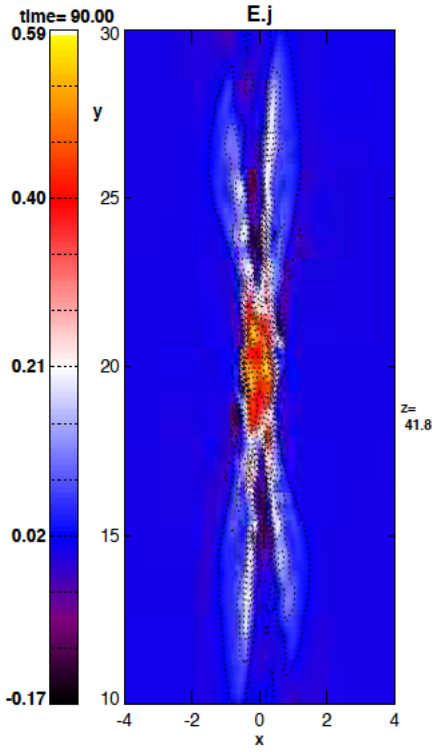

Figure 5.5: Plot of $\mathbf{E}\cdot\mathbf{j}$ in the xy-plane at $z \approx 42$ at time $t = 90$. The dominant positive values indicates the dissipation of energy.

heat in the immediate vicinity of the x-line because the dominant values of $\mathbf{E}\cdot\mathbf{j}$ are positive.

5.2.1 Transport of energy associated with Alfvén wave dynamics and reconnection

To better understand the transport and dissipation of energy for these MI coupling cases a comparative study is conducted for cases with and without reconnection. In all cases, the simulation setup is the same as described, however, with different values of a uniform ionospheric conductance. Figure 5.6 produces a set of plots showing the z-component of the Poynting flux (S_z) in xy-planes. The first plot (Figure 5.6a) shows this Poynting flux (S_z) at $z \approx 150$ at time $t = 50$. At this time, the reflected Alfvén waves have travelled up to $z \approx 32$. Therefore, the first plot presents the Poynting flux of only the incident Alfvén waves which is used in all the cases of Chapter 5 and case III in Chapter 4. The other three plots are showing the Poynting flux (S_z) at $z = 10$ for the three cases of different uniform conductance at the same time. Thus, these plots present the Poynting flux carried by the superposed (total) perturbation after the reflection, at heights not far above the ionospheric boundary. In all of these results the Poynting flux is negative at the locations further from the current sheet while the values are close to zero at or near the locations of the current sheet. A negative value indicates that Alfvén waves carry electromagnetic energy from the magnetosphere toward the ionosphere. The relative values of the maximum magnitudes of the Poynting flux ($S_{z,max}$) are different for the different conductances of the ionosphere. The value of $S_{z,max}$ is largest for the incident perturbations. This value decreases for the reflected perturbations, with increasing conductance of the ionosphere. For the incident perturbation, the value for $S_{z,max} \approx 3.94$ inside the plotted area as obtained from the color-key. However, the corresponding values of $S_{z,max}$ are 1.68, 2.95, and 3.48 when the Pedersen conductances (Σ_P) are 2.25, 0.75, and 0.464, respectively. These conductance values correspond to the reflection coefficients (r) of 80%, 50%, and 30%, respectively. This result indicates that more energy is dissipated in the ionosphere from the magnetosphere if the Pedersen conductance (or the reflectivity) of the ionosphere has a samller value.

Figure 5.7 introduces three plots of the Poynting flux below, at, and above the fixed localized resistivity region for case III from chapter 4. Close inspection of the results in these plots and the respective color scale demonstrates that the major difference for the Poynting flux close to the reconnection site is associated with regions close to the FAC layers. Specifically, above the localized electric field the maximum downward Poynting flux is larger and below the reconnection site the maximum Poynting flux is smaller. This indicates a net Poynting flux into the height where the parallel electric field maximizes. This convergent Poynting flux appears to be present mostly in and close to the FAC regions.

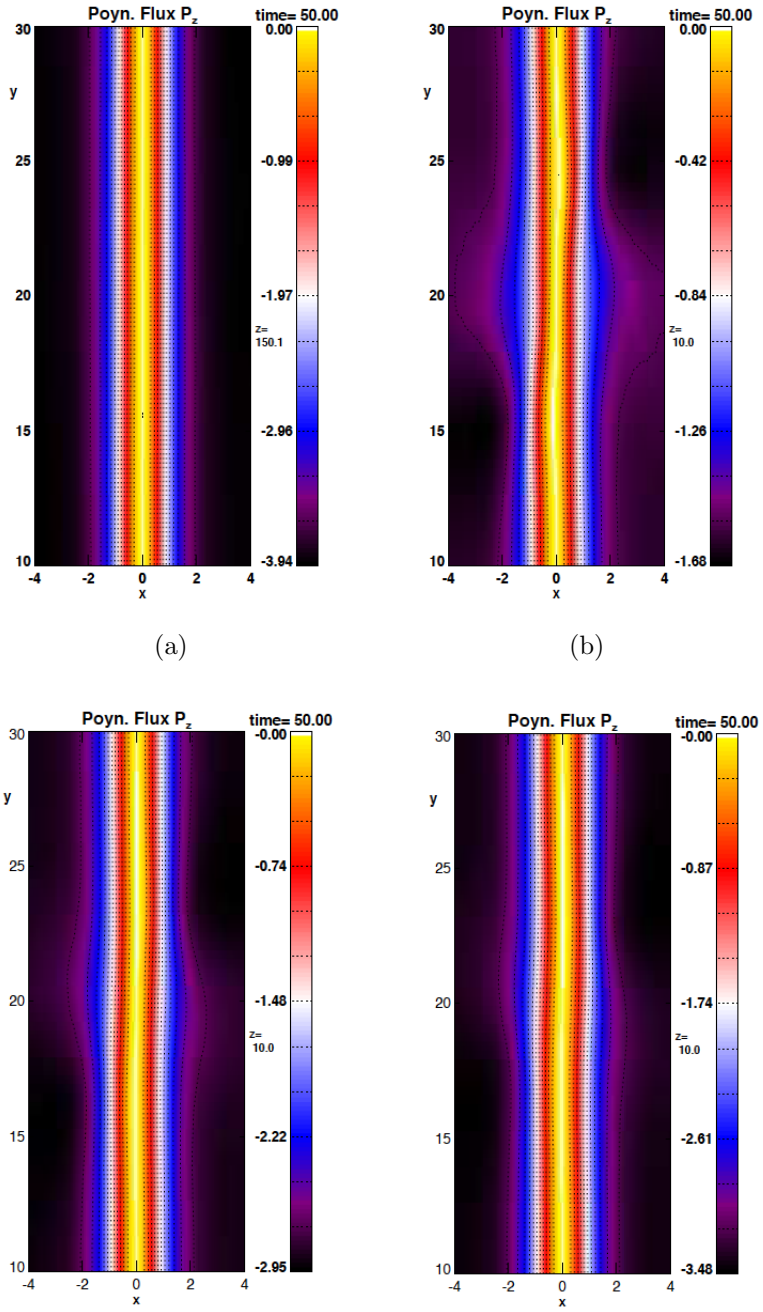

Figure 5.6: Plots of Poynting flux (S_z) for incident and reflected waves. These plots are in the xy-plane at $t = 50$ for (a) the incident wave at $z \approx 150$ and $r \approx 80\%$ (this r is insignificant, here); for the reflected waves for (b) $r \approx 80\%$ at $z \approx 10$; (c) $r \approx 50\%$ at $z \approx 10$; and, for (d) $r \approx 30\%$ at $z \approx 10$.

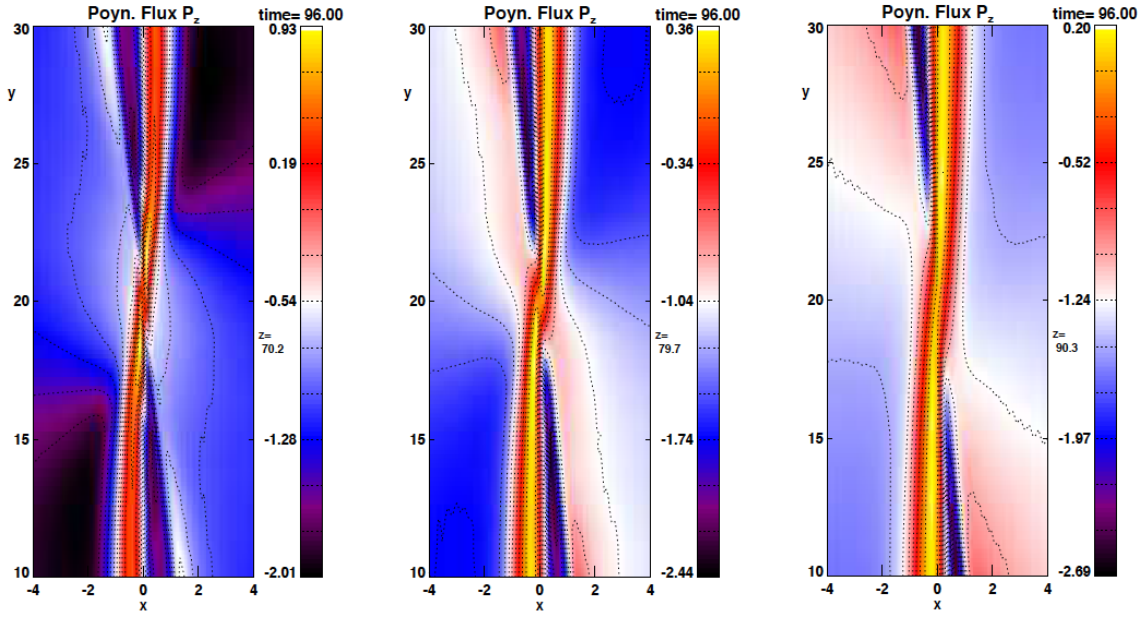

(a) (b) (c)

Figure 5.7: Plots of Poynting flux (S_z) involving magnetic reconnection, at time $t = 96$, below, at, and above the reconnection region, i.e., at heights (a) $z \approx 70$, (b) $z \approx 80$, and (c) $z \approx 90$.

5.2.2 Varying the conductance of the ionospheric boundary

Thus far the investigations were conducted with a uniform ionosphere having a high value of conductance. The ionosphere was set at a reflectivity of 80%. It is important to understand the evolution of reconnection and parallel electric fields in response to the ionospheric conductance. Therefore we included two additional runs with uniform but lower ionospheric conductance. Figure 5.8 shows the results for $E_{\parallel,max}$ when the ionospheric reflectivity values (r) are set at about 30% and 50% (corresponding to $\Sigma_P \approx 0.464$ and 0.75, respectively). The plots use the same format as in Figure 5.1. Comparing these two plots and the plot for $E_{\parallel,max}$ in Figure 5.1 it is evident that the ionospheric reflectivity or the Pedersen conductance has a major influence on magnetic reconnection. Figure 5.8a shows an enhanced electric field for 30% reflectivity, only when the resistivity is switched on temporarily but it turns off after this artificial perturbation. In comparison, Figure 5.8b demonstrates that although the parallel electric field is much smaller than in Figure 5.1 during the late evolution, it is nevertheless steadily increasing toward the end of the run. This shows that reconnection has started to operate on its own without being forced. Therefore, a reflectivity of 30% cannot generate reconnection in this set up while for $r \approx 50\%$, reconnection is observed, though it is not very strong. In this case the reconnection rate increases slowly with time. For a larger value of r, reconnection becomes stronger. For $r \approx 50\%$, the increase of maximum value of parallel

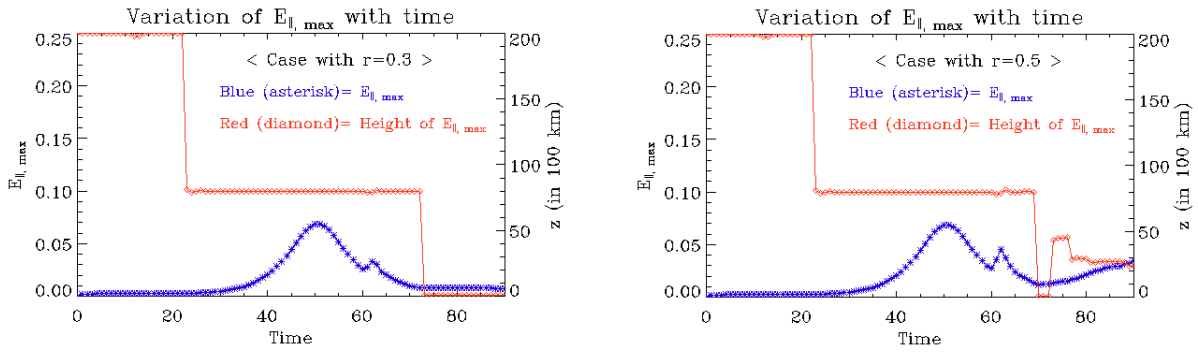

(a) $r \approx 30\%$ (b) $r \approx 50\%$

Figure 5.8: Plots of $E_{\parallel,max}$ and its location for different reflectivities. Plots (in blue) illustrate the time variation of maximum parallel electric field ($E_{\parallel,max}$) in the entire simulation domain and the other plots (in red) show the position of $E_{\parallel,max}$ using its z-value when the ionosphere reflectivities are (a) $\approx 30\%$ and (b) $\approx 50\%$.

electric field i.e. $\Delta E_{\parallel,max} \approx 0.0233$ (from 0.0117 to 0.035) in a timespan of $\Delta t = 20$ (between $t = 70$ and $t = 90$). When the reflectivity is 80%, the corresponding change is $\Delta E_{\parallel,max} \approx 0.1651$ (from 0.0475 to 0.2126). Hence the change is ~ 7 times larger in the later case.

It is noted that this result is somewhat dependent on the specific details of the employed resistivity model. Particularly this model uses a critical current density of 3 in order to turn the current dependent resistivity on. It may be that for a lower value of this critical current density reconnection may still start to operate for lower reflectivity but can be expected at a much lower rate. We can obtain a theoretical estimate of the reconnection rate or the parallel electric field through scaling laws of magnetic reconnection. Note that these scaling laws are based on two-dimensional reconnection and we will discuss the influence of the three-dimensional case later. Without shear flow, the electric field along the z (parallel) direction scales with the product of Alfvén speed, based on the anti-parallel magnetic field components, and the magnitude of the anti-parallel magnetic field [121]. In addition, shear flow can reduce the reconnection rate [113, 114]. Thus the reconnection scales with

$$E_R \sim v_A B_\perp (1 - v_s^2/v_A^2) \tag{5.4}$$

and with the Alfvén speed $v_A = B_\perp/\sqrt{\mu_0 \rho}$ such that

$$E_R \sim B_\perp^2 (1 - v_s^2/v_A^2)/\sqrt{\mu_0 \rho}. \tag{5.5}$$

In our normalized units this becomes

$$E_R \sim B_\perp^2 (1 - v_s^2/v_A^2)/\sqrt{\rho}. \tag{5.6}$$

The perpendicular magnetic field and the shear flow are directly determined by the Alfvén wave of the incoming and reflected wave. Denoting the amplitude of the incoming wave by B_0 and noting that the shearflow is, by definition - the Alfvén speed based on B_0, denoted by $v_{s0} = v_{A0}$. Therefore, based only on the incoming wave, the reconnection electric field scales with

$$E_{R0} \sim E_0(1 - (v_{A0}^2/v_A)^2) = 0 \tag{5.7}$$

where $E_0 = B_0^2/\sqrt{\rho}$ is the scaling for the reconnection rate without any shear flow.
Considering the superposition of reflected and incoming perturbations, the perpendicular magnetic field is $B_1 = B_0(1 + r)$, the shear velocity is $v_{s1} = v_{s0}(1 - r)$ and the new Alfvén speed is $v_{A1} = v_{A0}B_1/B_0$. Since the density does not change significantly we can ignore the density in the scaling. Thus the magnetic field coefficient in the reconnection rate for the superposed wave becomes $B_0^2(1+r)^2$ and the velocity ratio becomes

$$\begin{aligned} (v_{s1}/v_{A1})^2 &= v_{s0}^2(1-r)^2 B_0^2/v_{A0}^2/B_1^2 & (5.8)\\ &= (1-r)^2/(1+r)^2. & (5.9) \end{aligned}$$

Combining the magnetic field and the velocity factors the reconnection rate should scale as

$$\begin{aligned} E_R &\sim E_0(1+r)^2(1-(1-r)^2/(1+r)^2) & (5.10)\\ &= 4rE_0. & (5.11) \end{aligned}$$

This scaling shows the strong dependence of the process on the reflection coefficient. In terms of the physics it is obvious that a high reflection coefficient leads to a higher current density and to smaller shear flow both aspect favoring reconnection.
There are a couple of caveats that are important, in addition to this general scaling. First, the scaling strictly applies to two-dimensional systems. In two dimensions large shear-flow indeed switches off reconnection by forcing the current density at any X-line to 0 [113]. However, in three dimensions with a large guide field (B_z), magnetic perturbations which lead to a 0 current density at the x-line in $2D$ are carried out of the reconnection region along the guide field by Alfvén waves. Therefore large shear-flow does not switch off reconnection totally. Second, the derived reconnection scaling is indeed only a scaling law and the specific properties of the resistivity or of boundary conditions have an additional effect. Therefore the scaling laws should be considered more as a basic limitation to the maximum reconnection rate. Anyhow, the main point in this discussion was to demonstrate that a low conductance is expected to lead to a lower reconnection rate which is qualitatively consistent with the result shown in Figure 5.8.
As it is evident that the magnitude of the Pedersen conductance plays a major role in the evolution of magnetic reconnection, it is also interesting to investigate similar cases where the ionospheric

Pedersen conductance has a gradient. Four cases as studied. The conductance patterns for these four cases are shown in Figure 5.9. In all the four cases the conductance gradients are along the

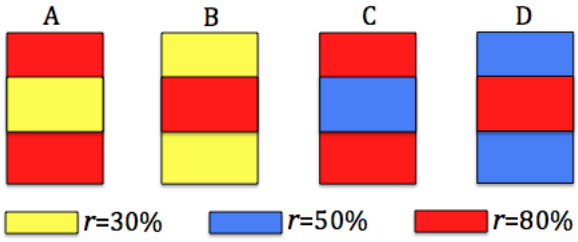

Figure 5.9: 4 Patterns of y-gradient of Pedersen conductance used in the study. The values of different reflection coefficients are shown using the colors.

y-directions and the central conductance region extends from $y = 12$ to $y = 28$. The plots of $E_{\parallel,max}$ are shown in Figure 5.10 for these cases. These plots demonstrate that similar to the magnitude

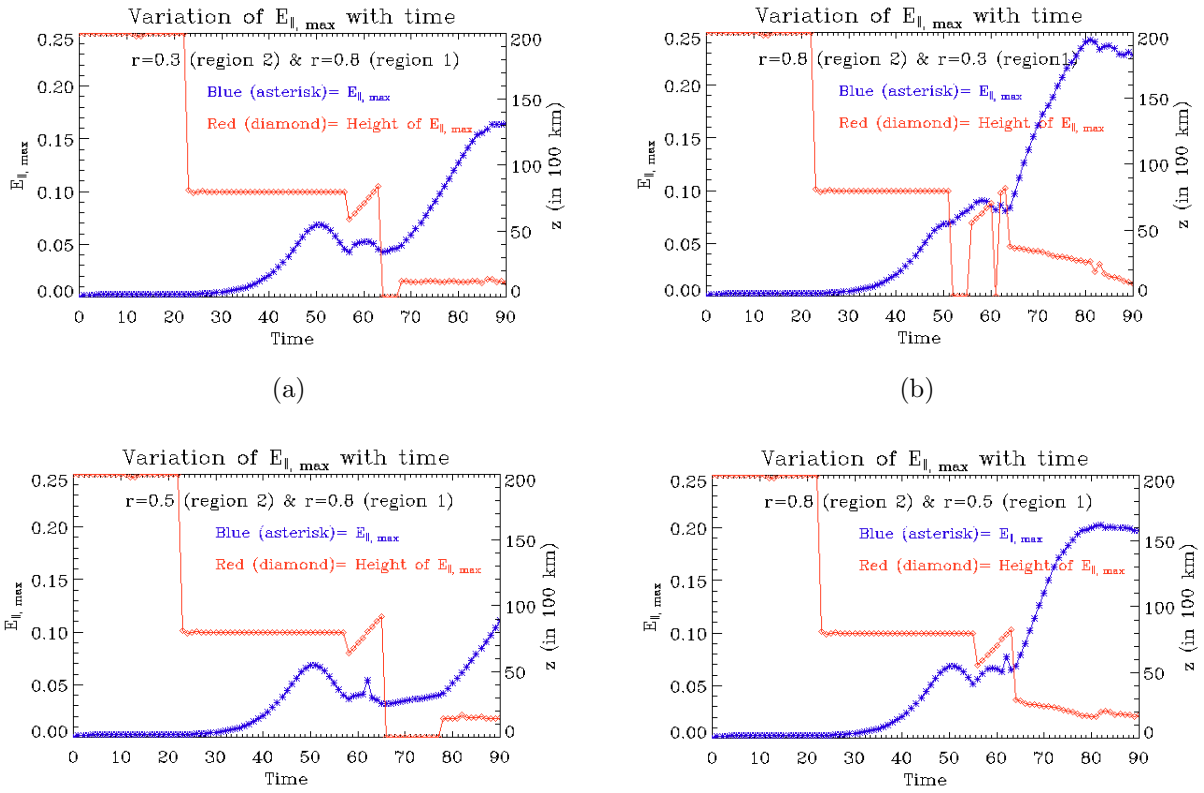

Figure 5.10: Plots showing the time variation of $E_{\parallel,max}$ and its height in the simulation domain when the ionosphere has gradients in its reflectivity (or conductance) such as (a) 30% inside 80%, (b) 80% inside 30%, (c) 50% inside 80%, and (d) 80% inside 50%.

of uniform reflectivity, its gradient has also an important influence on the evolution of magnetic reconnection. Compared to a uniform high reflectivity of 80% (Figure 5.1), the patterns B and D have the same high conductance in the region where reconnection operates in the high uniform conductance case. However, not only is the parallel electric field comparable in the runs with patterns B and D, it develops faster in these two case, and it is largest for pattern B (Figure 5.10b). In this case the region of 80% reflectivity is bound by the regions of much lower (30%) reflectivity, implying a strong gradient along the direction of the polarization of the perturbations. In this case a steep increase in the value of $E_{\parallel,max}$ is observed immediately after the reflected wave passes through the region of the trigger resistivity after t=62.

Similarly surprising are the results for the conductance patterns A and C. In both of these runs the conductance below the reconnection site is lower and for case A the corresponding uniform low conductance actually switched off reconnection. In contrast the reconnection rate for pattern A increased quite rapidly, and although somewhat lower than for the uniform high conductance case, reconnection for pattern A was comparable to the high uniform ionospheric conductance.

For the uniform conductance cases, the height of the maximum parallel electric field was lower for r=0.5 than for r=0.8. A rather low height for the maximum electric field is also seen for all cases with gradients in the conductance. Particularly patterns A and C show that the maximum parallel electric field late in the simulation is at heights corresponding to only 1000 to 1500 km above the conducting boundary.

To shed more light into the distribution of the associated FAC densities, this evolution is shown in Figure 5.11. Consecutive pairs of plots represent the FAC density at the height of the maximum parallel electric field and at the ionospheric boundary (z=0) in the order of the ionospheric patterns described in Figure 5.9. The times and xy-planes, for the plots are chosen, based on time and location of $E_{\parallel,max}$ for each case. Actually, the plots at the ionospheric boundary show the z-components of the current density (effectively, the FAC with a sign change) in colors and the horizontal components of current density with the arrows.

Noteworthy insights from these plots are: (1) reconnection is more likely above the locations of strongest gradient in Pedersen conductance when there is a low conductance strip interlaid in a high conductance background. Cases A and C show two reconnection sites, almost directly above the boundaries between high and low conductance regions (Figures 5.11a and 5.11e). (2) More curls and folds are observed in the current sheets. Examples are Figures 5.11b, 5.11c, 5.11f. (3) The FAC appears to be partially cut off or strongly modified at ionospheric heights for the cases with a high conductance in the center (Figures 5.11d, 5.11h). In fact these cases show FAC filaments with a strong positive (downward) FAC density in the low conductance regions. (4) Similarly, the cases with a low conductance in the center (A and C) show downward FAC filaments in the central (low

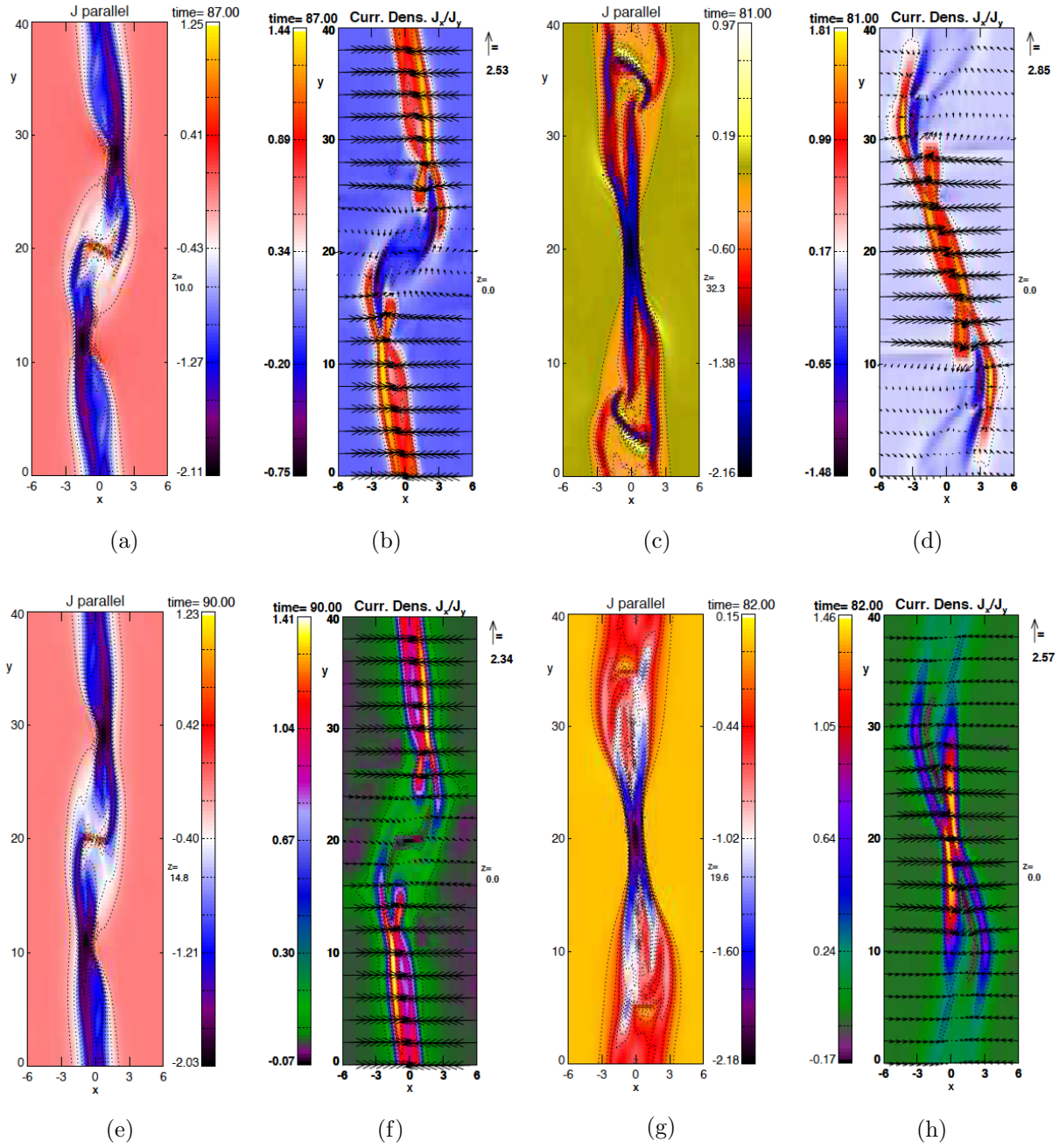

Figure 5.11: Evolution of FAC density for different patterns of ionospheric Pedersen conductance gradients (see Figure 5.9). With: patterns A (at $t = 87$) (a) $z = 10$ and (b) $z = 0$; B (at $t = 81$) (c) $z \approx 32$ and (d) $z = 0$; C ($t = 90$) (e) $z \approx 15$ and (f) $z = 0$; and D ($t = 82$) (g) $z \approx 20$ and (h) $z = 0$.

conductance) region (Figures 5.11c, 5.11g).

Figure 5.12 illustrates the convection patterns at the ionospheric boundary ($z = 0$) for the above mentioned four cases, arranged in the same order. In these plots the arrows represent the horizontal

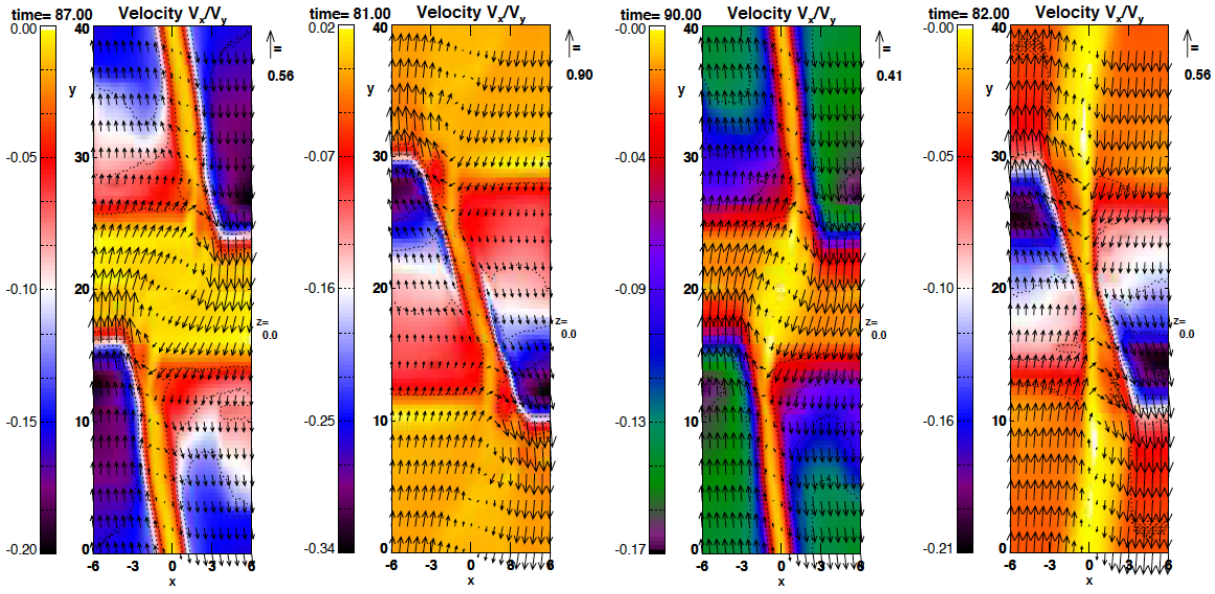

(a) (b) (c) (d)

Figure 5.12: Convection patterns at the ionospheric boundary for the 4 cases illustrated in Figure 5.9. The times corresponds to the time of $E_{\parallel,max}$.

components of velocity perturbation and the colors represent the presence of vertical componets which are not very significant here. The steady state velocity in each case is determined by the incompressibility of the fluid after being influenced by the ionospheric conductances at the time of reflection. Here, velocities are generally larger in regions of lower conductance. It is also seen that regions with high FAC density in the ionosphere (Fig 5.11) have fairly large antiparallel flow component on the two sides of the FAC. Furthermore the plots (a) and (c) show a large convection vortex in the central low conductance region. This is reminisced of the convection vortices of the case IV in Chapter 3 with an incident FAC and conductance gradients along the polarization of the incident Alfvén waves.

The energy transfer between the magnetosphere and the ionosphere is also one aspect of Interest. Plots in Figure 5.13 shows the Poynting flux (S_z) in the xz-planes and integrated along the y-direction for the different cases. The plots follow the same order and times as in last 4 figures. Here, a few interesting features are: (1) The top-part consistently shows the transition from the incident to the reflected waves; (2) Poynting flux is positive around the locations of reconnection; (3) The region of positive Poynting flux is very much localized for case B and D, i.e., for the cases

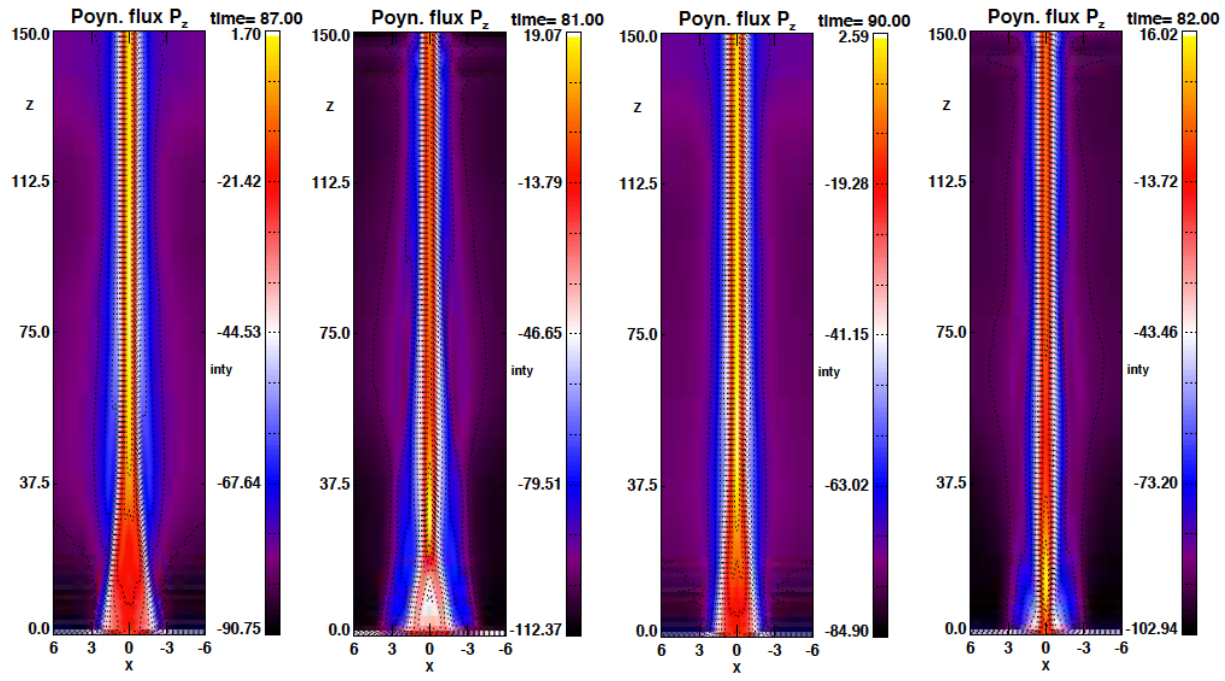

(a) (b) (c) (d)

Figure 5.13: Plots of Poynting flux for the 4 cases illustrated in Figure 5.9. These plots show the total Poynting flux integrated along the y-direction.

with a higher conductance region interlaid in a lower conductance background. This maximum occurs in these cases close to the ionospheric region; (4) In comparison, cases A and C, with a lower conductance strip inside a higher conductance background, show a vertically elongated region of positive Poynting flux; (5) Widening of the lower magnitude of the Poynting flux, at heights close to the ionosphere is another interesting feature. This is not so prominent for case D, in which the reconnection site (i.e., the region of localized positive Poynting flux) shifts close to the ionosphere. Note that the reflected wave boundary (in different cases) is at different heights because the plots are chose at the time of maximum $E_{\parallel}$.

Overall, it can be inferred that the FAC evolution in presence of the gradient in ionospheric Pedersen conductance is more complex. However, in all cases, reconnection starts to operate and in some, reconnection is comparable or faster than in the uniform high conductance example.

5.3 Summary and discussion

The study in this chapter intended to examine the formation and evolution of parallel electric fields by using (a) a more realistic resistivity model which removes the constraint of a fixed parallel electric field region imposed in Chapter 4, and (b) a variety of different ionospheric conductance boundary conditions. While the basic results are, qualitatively, similar to those obtained in the previous

chapter, this study reveals a better understanding of the properties of parallel electric fields. The employed localized resistivity has two important properties. It depends on the magnitude of the local value of current density and it is switched on only when the local current density exceeds a specified critical value. In order to trigger reconnection a localized resistivity at a height $\approx 1.25\ R_E$ is switched on for a brief period of time at $t = 50$. This short-time contribution to the resistivity is used to introduce a magnetic perturbation from which reconnection can grow subsequently. Note that similarly one could have used a small magnetic or velocity perturbation.

For the formation of parallel electric fields, in presence of a resistivity, FACs are required. FACs of magnetospheric origin are introduced in the top 16% of the simulation domain as is done before in several cases. The presence of the FACs associated with the incident perturbations is not enough for a fast magnetic reconnection and the incident perturbation carries an Alfvénic velocity perturbation which tends to inhibit magnetic reconnection. The reference case in this chapter uses a high value of the Pedersen conductance such that a higher fraction ($\approx 80\%$) of the incident Alfvén wave is reflected yielding a higher FAC density for the sum of the incident and reflected perturbation. In presence of the stronger FAC, and the associated reduced value of the total velocity perturbation, magnetic reconnection is triggered. The reconnection rate gradually increases which is indicated by the sharp increase of the value of $E_{\parallel,max}$ inside the domain. With the increase of $E_{\parallel,max}$, a reduction of height of its location is observed. This represents downward displacement of the reconnection region. During reconnection, fast convection is observed in the outflow region indicating the conversion of magnetic energy to kinetic energy. Around the boundary of the outflow region, the perturbation magnetic fields are rotated developing the x-component and reducing the y-component. The modified current sheet shows more structures (curls and folds) compared to the case III studied in Chapter 4. Inspecting the quantity $\mathbf{E} \cdot \mathbf{j}$ demonstrates the dissipation of energy in the form of heat in the region with a maximum value of $E_{\parallel}$.

Alfvén waves carry electromagnetic energy in the form of Poynting flux ($\mathbf{S}$). The results for the z-component of Poynting flux, S_z, being negative show that the incident Alfvén waves carry electromagnetic energy form the magnetosphere to the ionosphere as expected. After reflection (without reconnection), the Poynting flux remains negative although its magnitude decreases. This decrease is more pronounced if the ionospheric Pedersen conductance is higher. This indicates that less energy of the Alfvén wave is dissipated for larger Pedersen conductance of the ionosphere. These results are not unexpected and in fact can be derived analytically because the Poynting flux of the incident and of the reflected wave are determined by the Alfvén wave dynamics. For an magnetic field amplitude δB_y of the incident wave the incident Poynting flux along the vertical direction is $P_{z,i} = v_A \delta B_y^2$. After reflection the velocity decreases by a factor of $(1 - r)$ and the magnetic field increases by $(1 + r)$ such that the vertical Poynting flux becomes $P_{z,r} = v_A \delta B_y^2 (1 - r^2)$.

In the presence of magnetic reconnection, the Poynting flux, away from the current sheet is similar to the cases without reconnection. However, the Poynting flux in the current sheets above and below the region of the maximum parallel electric field is downward and upward, respectively, i.e., converges toward the height of the maximum $E_{\parallel}$. This is consistent with the positive value of $\mathbf{E}.\mathbf{j}$ associated with the maximum $E_{\parallel}$.

In comparison with the reference case with uniform high value of Pedersen conductance, two additional cases with, lower values of a uniform Pedersen conductance are considered. The results demonstrate faster reconnection for higher values of the Pedersen conductance. Magnetic reconnection may not occur at all below a certain uniform value of the Pedersen conductance.

Lastly, several cases are considered to explore the influence of gradients in the ionospheric Pedersen conductance. The current sheets appear more complex in these cases with folds and fairly intense downward current filaments. Particularly, if a lower conductance region is interlaid in a higher conductance background and the conductance gradient is high, reconnection occurs above the regions with a strong conductance gradient. In the cases, where a region of higher conductance is present with a background of lower conductance, fast reconnection measured by the magnitude of the parallel electric field takes place with a sharp increase in the value of $E_{\parallel,max}$. However, the reconnection rate is also considerably enhanced for cases where the reconnection trigger is initially located above a low conductance region. Overall this suggests the conclusion that while reconnection is certainly favored by a highly reflective ionosphere, reconnection seems also enhanced by strong conductance gradients. For all cases the reconnection location gradually shifts downward. This downward displacement is larger for lower conductance and it is particularly strong for cases with strong conductance gradients.

We had briefly discussed such a downward shift of the $E_{\parallel,max}$ region. The location of this $E_{\parallel,max}$ is not easily explained because $E_{\parallel}$ is not transport like other plasma properties such as density of pressure. Rather, the cause for the $E_{\parallel}$ displacement must be the underlying dynamics that determines the current density locally. We note that reconnection itself leads to a smaller width of the FAC, however, why this width should decrease faster below the $E_{\parallel,max}$ region than above is subject to speculation. It may be that the upper regions of the ionosphere with a relatively small collisional resistivity contributes to the thinning of the FAC sheet at these heights and therefore contributes to the downward shift.

Note that for a more realistic system a very low density and its height profile can contribute to the height of the $E_{\parallel,max}$ region because a low density implies a much higher Alfvén speed and therefore a higher electric field in the reconnection scaling. A systematic study of this aspect is beyond the scope of this research and should be conducted later.

The model of magnetic reconnection as a process for the formation of discrete aurora is not en-

tirely new. However, prior work has not investigated this process as a result of the interaction of incident and reflected Alfvén waves or considered the aspect of different ionospheric conductance boundary conditions. In the presented results the Alfvénic interaction is obviously highly important for the results. Particularly, the aspect of Alfvénic shear flow, that is always present for a single Alfvén wave, proofs to be of major importance because this shear flow can turn off reconnection and therefore prevents reconnection to operate. Similarly, the strong influence of the ionospheric conductance is new and also of major importance for this process. A more detailed summary of this process in relation to other works is presented in Chapter 6.

Chapter 6
Summary and Discussion

Introduction

The goal of this thesis research is a better understanding of the coupling between the magnetosphere and the ionosphere, one of the fundamental problems of near-earth space plasma physics. This research has been conducted using three-dimensional plasma simulations of the magnetosphere-ionosphere interaction. The electrodynamical coupling processes between the magnetosphere and the auroral ionosphere are the key to the energy and momentum transfer between these two regions of space [25], where the prevailing characteristics of the ambient spaces are different. This magnetosphere-ionosphere (MI) coupling is determined by field-aligned currents (FACs) and associated parallel electric fields [124]. The FACs are closed in the ionosphere through Pedersen currents [125] and believed to be influenced by the localized electric fields parallel to the geomagnetic fields. Here, the ionosphere is also not merely a passive element in this MI-coupling system, which only react to the input from the magnetosphere. Rather, the ionosphere plays a dynamic role in the evolution of MI-coupling processes through neutral winds and conductance patterns and results in changes which in turn modify FACs and thereby the MI coupling physics.[126].

In this research, I investigated the evolution (i.e. the generation and modification) of FACs by the ionospheric and magnetospheric causes with focus on the role of ionospheric Pedersen conductance, and the basic physical effects associated with and required for the localized parallel electric fields. The first part of this research addresses the influence of the ionospheric Pedersen conductance on FACs. This interaction as well as the subsequent research required the implementation of a partially conducting lower boundary that enabled desired magnitudes and profiles of the ionospheric Pedersen conductance for the simulation experiments. The second part of this study addresses and clarifies the relation of localized parallel electric fields and field-aligned electric currents. Specifically, it shows that a localized parallel electric field is the source of Alfvén waves and is not physically plausible in a magnetic field in the absence of electric currents and it presents basic properties of parallel electric fields within FAC layers. The last part of the presented research combines the first part of the study, i.e., the formation and modification of field aligned current through ionospheric conditions, with the second part addressing the evolution of parallel electric fields. This last part explores the effect of ionospheric conditions on the formation of parallel electric fields, their evolution, and the resulting changes in the FAC distribution. This interaction has also implications on the energy transport and dissipation in the MI coupling process. The following sections contain a summary of the important aspects of this work including the main and significant results, an overall discussion, and future works.

6.1 Summary and main results

6.1.1 Basic methodology

In this study, all the simulations use a 3D-2fluid (ions and neutrals) model originally developed by Birk and Otto [56]. The system under consideration is described by a set of normalized partial differential equations, which describe the basic dynamics of a fully ionized plasma interacting with a neutral fluid. The discretization of the normalized equations uses the DuFort-Frankel method, which provides a second order accurate numerical solution of the combined three-dimensional boundary and initial value problem. The simulation domain assumes its base at about 100 km, and the horizontal and vertical extents of the domain, are chosen in the range of 16–60 km and 2–5 R_E, respectively. Therefore this domain extends, vertically, between the ionosphere and the magnetosphere. The geomagnetic field is assumed to be uniform in the vertically downward direction (for the northern hemisphere) inside this domain.

Simple Alfvénic (magnetic and velocity) perturbations are imposed close to the magnetospheric boundary and travel from the magnetosphere toward the ionosphere. The magnitude of the magnetospheric perturbations is kept constant, thereby representing infinitely long wave trains in order to study the low frequency ionospheric response. A part of this infinitely long wave is reflected back in the upward direction depending on the magnitude of the imposed ionospheric Pedersen conductance. The superposition of the incoming and reflected waves determines the total magnetic and velocity perturbations, above the ionosphere. A simple equation uniquely relates the coefficient of reflection (r) and Pedersen conductence (Σ_P) of the ionosphere. This allows to relate any specific level of reflectivity of the ionosphere with a corresponding value of Σ_P.

If the ionospheric Pedersen conductance is high, strong Pedersen currents develop in the ionosphere following Ohm's law. This Pedersen current is mostly confined to the lower boundary and a minor fraction flows along a few grid levels above the (lower, ionospheric) boundary. This is more pronounced for higher conductance. For all considered cases the entire Pedersen current is contained close to the lower boundary below $z \approx 3$ with much of this current at the actual lower boundary of the system. This approach has better numerical stability and allows much longer integration steps in time than a fully height resolved ionosphere. This basic method for controlling the ionospheric conductance and reflection is then employed in all aspects of this investigation.

6.1.2 Pedersen conductance and FAC formation

Along with the applications with uniform ionospheric conductance it is demonstrated that the gradient in the Pedersen conductance and its orientation have a major influence on the evolution and modification of FACs. In combination with different conductance boundary conditions, this

study uses Alfvénic perturbations with and without FACs in the incident waves. Four different combinations of magnetospheric perturbation types and imposed ionospheric Pedersen conductance patterns are considered. The main results for the different cases are:

Incident FAC interacting with uniform ionospheric conductance: In this case (I) the incident FACs are modified after reflection from the ionosphere in association with the production of Pedersen currents. After reflection, the net FAC into the ionosphere is determined by the incident and reflected Alfvén waves. The ionospheric electric field (based on the total velocity perturbation) has two polarities and combined with Ohm's law ($I_P = \Sigma_P E$) implies a convergent Pederson current which exactly matches the FAC and insures current continuity. If the magnitude of the imposed Pedersen conductance is higher, FAC and Pedersen current are larger. The resulting currents and electric fields can be easily derived from the incident Alfvén wave and the reflection condition in the ionsophere.

Uniform incident perturbation interacting with a nonuniform ionospheric conductance: In these cases (II & III), no FACs are present in the incident perturbation. However, results are different for different orientation of the conductance gradients relative to the polarization of the incident wave. The findings are:

For conductance gradients perpendicular to polarization of the incident wave (case II): FACs are generated along the conductance boundaries. The reflected Alfvénic (magnetic and velocity) perturbations are nonuniform across the conductance boundaries resulting in different values of δB_y above the different conductance regions. This implies a z-component of $\nabla \times \mathbf{B}$ $\left(= \frac{\partial \delta B_y}{\partial x}\right)$ above the conductance boundary. In each conductance region, the Pedersen current is determined by δB_y of the sum of the incident and reflected perturbations. This current is consistent with the respective electric field and conductance values for each conductance region. Both, the total Pedersen current and FAC are independent of the width of the conductance boundary and are fully determined by the incident wave amplitude and ionospheric reflection.

For the gradients aligned with the polarization of the incident wave (case III): Even though this geometry cannot cause FACs, it provides significant insight into a mechanism that can yield a significant local increase of the Pedersen currents above the values inferred by simple Alfvén wave reflection. The basic configuration consists of a strip of high ionospheric conductance embedded in a region of low conductance. Different from the configuration for the other cases, this setup does not lead to a steady state immediately after Alfvén wave reflection. Rather, such a steady state develops over a time period corresponding to the fast mode travel time across the high conductance region. For the final steady state, incompressibility forces the velocity to assume

a uniform value in the high and low conductance regions. This value is determined by the average Pedersen conductance. This creates a dome-like strong magnetic perturbation above the high conductance region with a correspondingly strong Pedersen current. Since the average conductance decreases with decreasing width of the high conductance strip, the uniform electric field and the high conductance magnetic perturbation increases with decreasing width of the high conductance strip.

The explanation of Cowling conductance uses a similar geometry. However, the conducting region is bounded by nonconducting regions on both sides. This geometry also generates an enhanced current along the conducting strip, determined by the Cowling conductance which can be considerably higher than the Pedersen conductance.

In our simulation, no Hall conductance is included and the Pedersen current is enhanced by the constraint of incompressibility, which implies a uniform velocity and electric field. This effect should still be present in cases when Hall conductance is included. However, a complete discussion of this situation requires the inclusion of Hall conductance. Such an investigation would also provide insight into a more generalized Cowling conductance where the condition of no conductance (boundary) is replaced by low conductance. Unlike the Cowling case, here the relative widths of the different conductance regions have a strong influence on the resulting high conductance current.

Incident FAC interacting with a nonuniform ionospheric conductance: In general, magnetospheric currents are modified after reflection from the ionosphere. The complexity of the modification depends on the pattern of the conductance at the lower boundary. This case (IV) is practically a combination of cases I and III and the final steady state is a truly three-dimensional configuration. Here, the gradient of conductance is aligned with the polarization of the Alfvénic perturbations. As a result the uniform FAC-sheet becomes nonuniform (and enhanced), along its length, after reflection from the ionosphere. An intense central FAC over the high conductance region is embedded in a wider FAC with lower current density. Lower FAC density is generated outside the (main) current sheet. Closure of these FACs generates nonuniform, convergent (or divergent) Pedersen current. In this case different quantities like electric field, velocity and Pedersen current vary in a fully three-dimensional (complex) manner.

In contrast to case III, the steady state velocity is different over the different conductance regions and develops flow vortices at the edges of the low conductance regions close to the FAC sheet. Away from the FAC sheet, the velocity gradually tends to become uniform (similar to case III). Consequently, the Pedersen currents are distinctly different in the different conductance regions at locations, close to the FAC sheet. However, away from the FAC sheet, they tend to become more uniform over the different conductance regions.

In an additional case the interaction between a uniform perturbation and a high conductance patch inside a low conductance background is studied. Here, strong Pedersen currents result inside the high conductance patch, which close two FAC filaments on two opposite edges of the patch (separating the high and low conductance regions). All these cases highlight that the incompressibility of the plasma flow plays a highly significant role in the steady state velocity distribution, which in turn determines the electric field at the ionospheric boundary. Combined with the Pedersen conductance, the electric field generates the required Pedersen current. Current continuity links the evolution of Pedersen currents with the evolution of FACs.

6.1.3 Properties and effects of localized parallel electric fields

Chapter 4 explores basic properties of the relation between parallel electric fields and field-aligned electric currents. This study has two main parts. First, a localized electric field along a uniform magnetic field (representing the geomagnetic field), is introduced in the form of a blob (3D localization) and of a horizontal rod (2D localization) at heights corresponding to $\approx 1\ R_E$.
The presence of the parallel electric field gives rise to an immediate and continuous generation of an azimuthal magnetic perturbation caused by the horizontal gradients of the electric field. The magnetic perturbations imply the presence of a FAC, and they expand in the up and downward directions in the form of Alfvén waves. An inspection of the induction equation demonstrates that the generation of azimuthal (magnetic) flux is determined by the magnitude and the horizontal gradient of the parallel electric field. The value of the actual magnetic perturbation depends on the balance between the rate at which magnetic flux is produced and the Alfvén speed which determines the flux transport rate along the magnetic field away from the localized parallel electric field.
However, an inspection of $\mathbf{E} \cdot \mathbf{j}$ shows that this quantity is mostly negative, which implies that a localized parallel electric field acts as a generator of energy, which is consistent with simple physical intuition, i.e., a magnetic perturbation and magnetic energy travel away from the localized electric field. This is physically not plausible because the uniform magnetic field cannot provide a source for the energy transport out of the $E_\parallel$ region.
A steady state solution with a localized $E_\parallel$ is possible if two Alfvén waves (torsional for case I and sheared for case II) which exactly match the properties of the expanding waves but have opposite magnetic polarity would converge toward the $E_\parallel$ region. However, this violates causality as it requires a prior knowledge (by the outer world) about the localized $E_\parallel$. Therefore this result implies that a parallel electric field can form only in response to field-aligned electric current and cannot be simply postulated. Nevertheless, this numerical experiment also implies that a localized

parallel electric field causes a magnetic flux perturbation and Alfvén waves traveling away from the localized $E_{\parallel}$ region.

The second part explores the formation of parallel electric fields by introducing localized blob of resistivity into the system in which a FAC is introduced by two Alfvén wave trains traveling from the magnetosphere down into the ionosphere. In this case the Alfvénic perturbations and the associated FACs travel downward and eventually reach the location of the resistivity blob (of fixed magnitude). Then they are reflected at the ionospheric boundary, and travel back to the resistive region. In the presence of the FACs, parallel electric fields are formed in the resistive region, the magnitudes of which vary with the intensity of the FACs. FACs increase further after the reflected wave passes the resistive region. In the chosen example with a reflection coefficient of 0.8, magnetic reconnection is initiated in the resistive region. This process leads to a further increase of the parallel electric field and is documented by the magnetic field, electric current density, and horizontal flow configuration at the height of the resistive patch, and may initiate reconnection depending on its strength.

The location of the maximum value of parallel electric field ($E_{\parallel,max}$) is the site of the reconnection. During reconnection the value of $E_{\parallel,max}$ increases sharply for the chosen Pedersen conductance. Other noteworthy features are a downward shift of the reconnection site, positive values of $\mathbf{E} \cdot \mathbf{j}$ indicative of energy dissipation, and, the formation of very thin current sheets. These thin FAC current sheets spread from the reconnection site up and down the field line and are embedded in a much wider FAC system.

As the FAC intensity increases, ions converge from two sides toward the FAC sheet. It is expected that this generates an increase of density and pressure at the base of an upward FAC filament in the ionosphere. It is verified that the density is indeed enhanced along the foot-points of the upward FAC sheet and depleted away from this current sheet. It is also demonstrated that the FAC current density exactly matches that of the gradients in the Pederson current, which also implies an excellent validity of current continuity ($\nabla \cdot \mathbf{j} = 0$) in the simulation.

6.1.4 Evolution of dynamic parallel electric fields

This study is intended to investigate more realistic parallel electric field evolution. Different from the resistivity with fixed magnitude and location (used in the prior chapter 4), here, the introduced resistivity is current dependent and becomes active only when it exceeds a certain threshold value. Therefore, this model removes the constraints of a fixed location and magnitude for the resistivity, and it has more freedom in its formation, which results in the dynamic evolution of parallel electric fields. A small localized resistivity is still switched on only for a brief period of time to trigger reconnections. Without this trigger the evolution of reconnection would occur slower than that by

including the resistive perturbation.

The reference case in this study employs the same high conductance used in the prior chapter and the overall evolution is rather similar. After the incident Alfvén wave with the FAC layer passes the resistive trigger, a moderate parallel electric field develops with the resistive perturbation. This parallel electric field increases significantly only after the reflected wave passes this region. Comparison runs with lower uniform conductance show that an amplification occurs still for a reflection coefficient of 0.5 but reconnection is turned off for a reflection coefficient of only 0.3. Two reasons for this behavior are: (1) that higher conductance (and reflectivity) generates higher magnetic field perturbations and therefore principally high reconnection rates and (2) lower conductance leads to higher velocity perturbations and reconnection is reduced or can be switched off entirely for faster shear flow.

Interesting results are obtained with nonuniform ionospheric conductances. This comparison includes 4 cases, 2 of which use a central region of high conductance embedded in a lower conductance background and 2 employ a central region of lower conductance embedded in a background of high conductance. The reconnection trigger is switched on only above the central region, i.e., for two cases above a lower conductance region. In all of the cases, reconnection start to operate as identified by the magnitude of the parallel electric field. Reconnection is faster than in the cases of corresponding uniform ionospheric conductance. In all cases, the FAC layers exhibit more complex patterns. The cases with a central lower conductance region, result in reconnection, approximately, above the location of conductance gradient. Reconnection is very fast, surpassing the uniform high conductance case, for a central strip of high conductance. In all cases with current dependent resistivity, the reconnection site, characterized by the maximum value of the parallel electric field, move closer to the ionosphere, which is more pronounced for the conductance gradient cases. Among these, the maximum parallel electric field is at a height of only 1000 to 1500 km when reconnection operates.

An important aspect of MI coupling is the energy flux and dissipation. For the simple system of an incident and reflected Alfvén wave the vertical component can be computed from the properties of the incident wave and ionospheric reflection. An examination of the z-component of the Poynting flux (being negative) shows that this flux is fully consistent with the analytic value away from the FAC sheet for all cases. This flux is strongly reduced by the reflected wave compared to the incident perturbations. This reduction increases strongly with increasing conductance where the z-component of the Poynting flux of the superposed incident and reflected waves is $P_{z,r} = (1-r^2)P_{z,i}$ with the incident flux $P_{z,i} = \delta B_y^2 v_A$.

The Poynting flux for all reconnection is modified strongly close to the FAC layer. Inside the current sheets the Poynting flux can be positive, and there is a net Poynting flux toward the height

of the maximum parallel electric field from above and below. This is particularly noticeable below the $E_{\parallel,max}$ region where a positive contribution to the Poynting flux extends to a wider region from the unperturbed FAC layer.

Clearly, the evolution of strong upward parallel electric fields should be related to downward electron acceleration and precipitation. The fluid simulation has no microphysical process directly related to the acceleration of particles but it is possible to construct a proxy for auroral arc location by integrating the parallel electric field from the ionospheric boundary upward along magnetic field lines. In an electrostatic configuration (steady state) this integral would correspond to a potential difference, but since this evolution is not electrostatic a better terminology might be a 'quasi-potential' or 'parallel potential'. The results are shown in Figure 6.1 where the first plot (Figure 6.1a) corresponds to a uniform high conductance ($r = 80\%$) of the ionosphere. The other

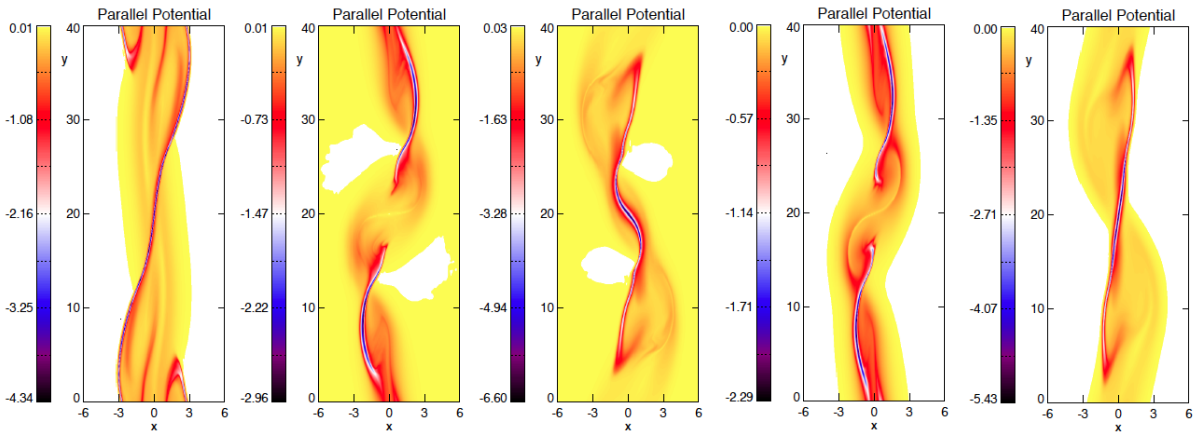

Figure 6.1: Plots of parallel potentials for different ionospheric conductance patterns: (a) uniform high conductance, (b-e) representing the cases illustrated in Figure 5.9, in order.

plots, in order, correspond to the 4 cases, illustrated in Figure 5.9. Here the highest values actually correspond to highest precipitating particle energy rather than energy flux.

Figure 6.1 illustrates that the highest quasi-potential is located in filaments even thinner than the embedded current sheets from the simulation. Generally, the morphology of a very narrow precipitation region extended over a large distance is highly reminiscent of discrete auroral arcs. Similarly the evolution of folds or curls reminds of some auroral structure. Note that in comparison to the location of the FAC and the fact that convection is strongly sheared across the potential filaments (compare Figures 5.11 and 5.12).

There is a clear distinction also between the uniform and the nonuniform conductance cases where the nonuniform cases show filaments with the highest quasi-potential above high conductance re-

gions and curls or folds above low conductance regions. Note, that the folds can in part be attributed to the velocity vortices at the conductance boundaries.
It is instructive to compare the parallel potential difference (see quasi-potential scale in Figure 6.1) to the maximum parallel electric field, which demonstrates that for all cases the parallel electric field must at least extend to several 10 distance units (or several 1000 km) along the magnetic field in the vertical direction.
One has to be careful not to interpret these results too literally for actual discrete arcs because of several idealizations and an artificially imposed ionospheric conductance pattern. However, the results still demonstrate many similarities to actual discrete aurora and the importance of the ionospheric conductance for the evolution of parallel electric field and auroral acceleration regions.

6.2 Discussion

Research on the coupling between the magnetosphere and the ionosphere has been conducted for a long time (e.g., [17, 27, 29, 30]). For the processes of different temporal and spatial scale size, various models have developed (e.g., [22, 24, 28]). These models help to understand how the coupling operates and how this coupling effects important space plasma processes that participate in the MI coupling (e.g., [18, 19, 127, 25]). The investigations in this study are based on three-dimensional simulations of the MI system and have the objective to better understand the magnetospheric and ionospheric influences on the formation and evolution of field-aligned electric currents and their role and influence on the evolution of field-aligned electric fields. This research applies to low frequency coupling processes that are dominant in establishing ionospheric convection and current systems. The most important results of this thesis are:

- The ionospheric conductance and conductance gradient are a major factor in the formation and modification of FACs:
  (a) A high value of ionospheric conductance strongly amplifies FACs that are imposed on the ionosphere from the magnetosphere;
  (b) Conductance gradients can generate strong FACs even if the incident perturbation does not carry any significant FAC;
  (c) Localized high conductance regions can generate Pedersen currents much larger than inferred by simple Alfvén wave reflection when the polarization of the incident wave has a component along the conductance gradient;
  (d) Interaction between the FACs, imposed from the magnetosphere, and the ionospheric conductance gradient yields nonuniform FACs with the generation of additional FACs outside the imposed one. This results in nonuniform Pedersen currents in the ionosphere.

- Localized parallel electric fields act as a source of local magnetic flux generation and associated Alfvén waves. Such fields are not physically plausible in a magnetic field without the presence of FACs.

- Localized parallel electric fields can form in FAC layers as a result of locally enhanced (anomalous) resistivity:
  (a) They are strongly enhanced by magnetic reconnection if the FAC is amplified by high ionospheric conductances;
  (b) Strongly enhanced fields cause very thin and intense embedded FAC layers with characteristic fast tangential convection and perpendicular fields pointing toward the FAC layer for upward current;
  (c) Ionospheric conductance gradients have a major influence on the magnitude, evolution, and height of the localized parallel electric fields. Conductance gradients increase the electric field in all cases considered in this study;
  (d) Parallel electric fields can be switched off entirely for low ionospheric reflectivity;
  (e) the ionospheric morphology of FACs, convection, electric fields, and likely precipitation regions have many similarities with discrete auroral arcs.

Some aspects of these finding are not entirely new or unexpected such as the amplification of FAC by high ionospheric conductance, however, in combination these results produce a new systematic picture of the ionospheric role for MI coupling.

This entire research can be broadly discussed in two parts. The first part of this dissertation presents a systematic study of the magnetospheric and ionospheric influences on the evolution and modification of FACs with focus on the role of ionospheric Pedersen conductance and its gradients. FACs are typically generated in the magnetosphere and are carried into the ionosphere by Alfvén waves. During their reflection from the ionosphere these FACs are modified depending on the magnitude and distribution of ionospheric conductance. For conductance gradients, along the polarization of the wave, strong Pedersen currents can be generated which in turn enhance the FAC as well.

The second part of this dissertation addresses the properties and evolution of parallel electric fields in an attempt to better understand the formation of discrete auroral arcs in response to the evolution of FACs for predetermined ionospheric conductance patterns. First, it is demonstrated that localized parallel electric fields generate magnetic flux such that their presence in a uniform magnetic field is not plausible. It is shown that parallel electric fields generated in a FAC in the presence of a (anomalous) resistivity represent a load and can provide physical explanation for the auroral acceleration geometry. The results demonstrate that such electric fields can be significantly

enhanced by Alfvén wave reflection where both magnitude and gradients of the ionospheric conductance are important. The strongly enhanced parallel electric field is associated with magnetic reconnection and modifies the FAC system such that thin current layers (with curls and folds) are observed to be embedded in the large scale current system.

Ionospheric conductance and FAC evolution: Many studies address aspects of FACs and ionospheric conductances. For instance, Cloutier [128] investigated ionospheric effects related to the production, maintenance, and control of FACs; in a paper on the east-west variation of magnetic field at the mid-latitudes, Nakano et al. [129] concluded that the variation of FACs are due to the variation of ionospheric polar cap conductivity; Ridley et al. [130] focused their study on quantifying the influence of the ionospheric conductance on the magnetospheric configuration during steady southward IMF conditions.

However, almost no studies attempt a systematic relation between the local ionospheric conductance and its direct influence on the evolution or modification of such currents. A particularly poorly understood topic appears to be the role of conductance gradients. While it has been long established that such gradients are important for the local electric field and current configuration in the ionosphere, for instance in the model of the Cowling conductance, a systematic study of this interaction is not available. This represents a major lack of insight of the currents associated with large conductance gradient such as during an auroral substorm or at the terminator where the sunlit ionosphere has a much higher conductance than the dark ionosphere. It has also been speculated that discrete arc formation may require nightside conditions or strong conductance gradients [131]. Furthermore, many global MHD simulations use ionospheric conductance boundaries and therefore implicitly make use of the FAC-conductance physics.

Traditionally, the Cowling geometry has been considered as the only possibility of a strong increase in the ionospheric currents. Such an increase is deemed important, for instance, associated with the Harang discontinuity or substorm expansion [23, 24]. The presented results demonstrate that an important element for a high ionospheric current can indeed be a thin strip of high conductance. However, in the results in our models, the dominant aspect for convection across such a strip is incompressibility, which forces a uniform value of the normal component of the convection (or a constant value of the tangential electric field). In our model the normal component of the convection is determined by the average ionospheric Pedersen conductance, which can be rather low in the night side ionosphere causing fast flow and a large convection electric field. Very large electric fields have indeed been observed around narrow discrete arcs (e.g. [28]). A narrow strip of very large conductance can therefore cause a major increase of the ionospheric current within this strip. This can lead to strong turbulence in the ionosphere, if the current increase is large enough so that the current carrying ions reach the speed of sound.

It is also noted that convection across the day - night terminator appears continuous (W. Bristow, private communication). At least the continuous normal component of this convection is explained by the ionospheric incompressibility as demonstrated in the results in our model. However, this would also imply a significant change of the horizontal ionospheric currents, tangential to the conductance boundary.

In our model, Hall current is not included in the current system. It is argued that in case of simple configurations Hall current is not significant in the closure of FACs. However, for the cases with complex combinations of ionospheric configurations and magnetospheric perturbation, incorporation of Hall current into the ionospheric current system would be desirable.

Field-aligned electric fields, currents, and ionospheric conductance: This topic is of central importance for the formation of discrete auroral arcs and has produced a wealth of research. For instance, Block and Falthammar [102] investigated the role of parallel electric field in auroral acceleration and discussed the significance of the fluctuations in (perpendicular and parallel) electric fields as observed by the satellites; Sugiura et al. [115, 116] used DE-2 satellite data to find a correlation between the FACs and electric field; Sugino et al [126] worked on the determination of relative contribution of the ionospheric conductivity and the electric field to the ionospheric current based on EISCAT radar data.

Early research has suggested that field-aligned electric fields form as U or V shaped electric potentials assuming micro-physical processes such as double layers or electrostatic shocks (e.g. [132, 44, 100]) as the mechanisms for the electric field formation. Observations of perpendicular electric fields which point toward a vertical layer of field-aligned accelerated particles ([133, 134]) have been considered as evidence for such U or V shaped postulated potentials. Our results of imposing a localized parallel electric field shows that such localized electric field represent a continuous source for the production of magnetic flux. In our results this flux is transported along the background magnetic field away from the localized $E_{\parallel}$ through Alfvén waves. Since these waves require a source of energy, which is not available in a uniform or dipole magnetic field, it is not plausible that localized parallel electric fields can exist without associated currents. This intuitive expectation is confirmed through the product $\mathbf{E} \cdot \mathbf{j}$ which demonstrates that the localized electric field region represent a dynamo process without an energy source in the absence of currents.

This situation changes entirely when localized electric fields form as a result of a resistivity within a FAC layer. Various authors have considered this situation (e.g., [43, 48]). A comprehensive review of theoretical models of discrete arc formation has been provided by Borovsky [97], which lists 21 mechanisms. However, except for models based on inertial Alfvén wave acceleration [135] and models based on localized electric fields [121, 111], models were, generally, found to be unable to provide an explanation for the observed width and length of discrete auroral arcs. A similar model

described as magnetic fracture [136, 137] has been proposed, which also considers the effects from the presence of a parallel electric field along a FAC layer. These models are similar also in the aspect that the presence of a parallel electric field breaks the so-called frozen-in condition which implies that the actual motion of the auroral arc/precipitation is different from the convection in the ionosphere [136, 138, 139].

The results in this thesis research use a model similar to the one described by Otto and Birk [121, 111], and Birk and Otto [140]. These models postulated the presence of a FAC layer as an equilibrium condition, however, none of these models actually considered a partially conducting boundary or the actual formation of a FAC layer in response to incident Alfvén waves from the magnetosphere. Except for the studies by Otto and Birk, no models actually have ever been investigated quantitatively in the framework of numerical simulation.

The result presented for case III in Chapter 4 show characteristics similar to the Otto and Birk models in terms of the evolution of magnetic reconnection (flow, magnetic field, and current evolution), and confirms earlier model results. However, the results presented in Chapter 5, actually, remove the constraint of a fixed location of the parallel electric field region, and they include the effect that a partially conducting ionosphere has on the presence and evolution of a parallel electric field. Specifically, they demonstrate that a low conducting ionospheric boundary can switch-off the electric field formation. Furthermore, they demonstrate clearly that that the electric field formation and magnitude is very different in response to the incident wave compared to the response to the combined incident and reflected wave. In the first case, fast Alfvénic convection prevents a strong increase of the parallel field while the latter situation can yield a significant increase of the electric field if a large ionospheric conductance and reflection reduces the fast shear flow and increase the magnetic perturbation and FAC intensity.

An examination of the magnetic field-aligned Poynting flux also demonstrates that a significant fraction of this Poynting flux is absorbed well above the ionosphere in the acceleration region, demonstrating considerable perpendicular plasma acceleration and energy dissipation at the height of the acceleration region. Case studies of different ionospheric conductance patterns further demonstrate that conductance gradient yield higher values of the parallel electric field than corresponding uniform ionospheric conductance. Although these conductance patterns are imposed as a boundary condition and not self-consistently generated through precipitation, these results indicate that a varying ionospheric conductance may be important for the auroral acceleration for discrete arcs.

A more self-consistent approach to determine ionospheric conductance would use the potential computed from the parallel electric fields as a proxy for ionization and ionospheric conductance variation. A self-consistent interaction of electric field, FACs and conductance is difficult to predict but a few observational and theoretical aspects are notable. Intense FACs can be expected

in regions of high conductance or strong conductance gradients while intense precipitation almost instantly causes a strong enhancement of the ionospheric conductance. Hence, the evolution of ionospheric conductance can be highly dynamic. Typically, discrete auroral arcs move relative to the ambient ionospheric plasma such that they should be expected at the boundary between the low and high conductance regions in the ionosphere. An important aspect here is the relative location of the most intense precipitation and the location of the highest current density. These are not necessarily coincident, and in fact a comparison of Figures 5.11 and 6.1 illustrates that the largest field-aligned potential difference is at the outer or leading edge of the FAC distribution. This is in part explained by the different travel times of the precipitating electrons and of the evolving FAC, which propagates at the Alfvén speed. However the exact interplay of FAC and discrete electron precipitation is difficult to predict. Large parallel electric fields can develop only in regions of high conductance or conductance gradients. Discrete arcs can therefore propagate only into a low conductance region if the parallel potential maps into regions of low conductance thereby allowing the propagation of the FAC and parallel electric field region.

It is also interesting to note that the onset of the auroral expansion of substorms typically occurs when the so-called growth phase or onset arc has moved close to or into the region of diffuse precipitation which is characterized by higher conductance. Prior to onset, the growth phase arc is weak and propagates slowly equatorward without significant changes in brightness. The growth phase arc for much of this evolution may not necessarily be the result of field-aligned particle acceleration but rather be caused by scattering of electrons into the loss cone at the earthward edge of the electron plasma sheet.

The presented results may also shed some light on the magnetic fracture model [141, 137]. This model is, as mentioned, similar to the reconnection/localized electric field model by Seyler [135], and by Otto and Birk [121]. However, different from the latter two models, the fracture model does not consider the electric field localized along the FAC layer. A physical reason and distinction of these may be the difference between the evolution for the incident wave and the superposed incident and reflected wave. Considering only the incident wave, a sufficiently thin FAC sheet may still cause anomalous resistivity through micro-turbulence. However, in this case the parallel electric field is purely driven by the maintained presence of the FAC through the Alfvén waves and the Alfvénic shear flow prevents a tearing instability. In this sense the electric field represents an approximately steady state solution in the presence of micro-turbulence. In contrast, the superposed incident and reflected waves (for high conductance or conductance gradients) is unstable with respect to the tearing mode and magnetic reconnection. This is clearly demonstrated in all of our cases with conductance gradients or high conductance. The difference is that the electric field in this case becomes strongly localized along the FAC sheet while it can be present over a long distance along

the current sheet for the incident wave alone.

Similar to the first part of this thesis there are several important aspects, which are not included in the present model where the lack of a Hall conductance has already been mentioned. Two other idealizations include the assumption of a uniform magnetic field, which does not contain the convergence of the dipole field into the ionosphere. A second related aspect is the constancy of the plasma density in the initial configuration. Both of these aspects are currently considered through an appropriate normalization, which can be chosen height dependent to distinguish temporal effects at acceleration region heights compared to ionospheric heights. Here the decreasing density and decreasing dipole field strength with height partially compensate each other such that the actual height dependence of the Alfvén speed is less than, the effect from the density decrease alone. However, it is known that, in particular, the acceleration region has very low density and therefore a high Alfvén speed. The presented result shows that the localized $E_{\parallel}$ tends to shift toward lower heights at later times. This may change with a more realistic height dependence of the Alfvén speed. Finally, a potentially important aspect, related to our simulation, is the evolution of inertial Alfvén wave which carry a magnetic field. This wave develops a significant parallel electric field if the component of the wave vector perpendicular to be is comparable to the inverse plasma skin depth c/ω_{pe}. However, the consideration of the corresponding electron inertial physics would require a much higher spatial resolution and much shorter time scales, which are beyond the capability of current supercomputers.

6.3 Future works

In various ways, the present research can be continued farther. Though our model provides significant insight on the role of ionospheric conductance and conductance-gradient on MI coupling, still it has some drawbacks concerning the current-conductance relation, which deserve to be addressed in future research.

The most important of these, for a full description of horizontal ionsopheric current, is the lack of Hall physics. We have argued that this is secondary for the closure of FACs, which is certainly true in simple configurations and the respective Hall current can be computed from a Hall conductance without any change in the Pedersen current and FAC configuration. However this is less clear for conductance gradients and a polarization of the incoming wave in the direction of the conductance gradient. It would be very desirable to extend the present research to incorporate the Hall current in these configurations to reconcile our results with the traditional Cowling conductance and to extend the Cowling conductance to configurations where a high conductance region is bound by nonzero but low conductance regions.

A second aspect of future work should be a more self-consistent distribution and generation of iono-

spheric conductance. Here conductance should increase according to particle precipitation where one would use the potential computed from the parallel electric field as input for ionization and conductance changes in the ionosphere. This appears to be a central issue to obtain a more self-consistent model of the ionospheric feedback onto the evolution of parallel electric fields. Finally, a worthy topic of future work could be a quantitative test of other discrete arc models, particularly, the magnetic fracture model by Haerendel [141, 137].

References

[1] R. L. Lysak. Propagation of Alfvén waves through the ionosphere. *Physics and Chemistry of the Earth*, 22(7-8):757–766, 1997.

[2] C-G. Fälthammar. Space physics, August 2001. URL `https://www.kth.se/social/upload/521f2beaf276542c27bf78f4/Falthammar.pdf`.

[3] T. Gold. Motions in the magnetosphere of the earth. *Journal of Geophysical Research*, 64 (9):1219–1224, 1959.

[4] V. M. Vasyliunas. Fundamentals of planetary magnetospheres. In *Heliophysics - Plasma Physics of the Local Cosmos*. .

[5] Encyclopædia Britannica. Geomagnetic field, 2014. URL `http://www.britannica.com/EBchecked/topic/229754/geomagnetic-field`.

[6] R. J. Walker and C. T. Russell. Solar-wind interactions with magnetized planets. In *Introduction to Space Physics*.

[7] A. Otto. Lecture notes on magnetospheric physics, January 2014. URL `http://how.gi.alaska.edu/ao/msp/index.html#list`.

[8] V. M. Vasyliunas. Comparative magnetospheres. In *Solar Trrestrial Physics*. .

[9] M. Kallenrode. *Space Physics - An introduction to Plasmas and Particles in the Heliosphere and Magnetosphere*. Springer, New York, 2004.

[10] J. R. Kan and S. -I. Akasofu. A model of the open magnetosphere. *Journal of Geophysical Research*, 79(10):1379–1384, 1974.

[11] H. Rishbeth and O. K. Garriott. *Introduction to Ionospheric Physics*. Academic Press, New York and London, 1969.

[12] Encyclopædia Britannica. ionosphere and magnetosphere, 2014. URL `http://www.britannica.com/EBchecked/topic/1369043/ionosphere-and-magnetosphere`.

[13] Tony T. Giang. Low-energy ion outflow from the sub-auroral region, 2010.

[14] M. Nicolet. The constitution and composition of the upper atmosphere. In *Proceedings of the IRE*, volume 47, pages 142–147, 1959.

[15] W. Baumjohann and R. A. Treumann. *Basic Space Plasma Physics*. Imperial College Press, London, 1997.

[16] P. Muralikrishna and V. H. Kulkarni. On the height variation of the E-region Cowling conductivity - effect of charged dust particles. *Annales Geophysicae*, 24:2949–2957, 2006.

[17] R. G. Roble and M. H. Rees. Time-dependent studies of the aurora: Effects of particle precipitation on the dynamic morphology of ionospheric and atmospheric properties. *Planetary and Space Science*, 25:991–1010, 1977.

[18] T. J. Fuller-Rowell and D. Rees. A three-dimensional time-dependent global model of the thermosphere. *Journal of Atmospheric Sciences*, 37(11):2545–2567, 1980.

[19] M. Harel, R. A. Wolf, P. H. Reiff, R. W. Spiro, W. J. Burke, F. J. Rich, and M. Smiddy. Quantitave simulation of a magnetospheric substorm - 1. Model Logic and Overview. *Journal of Geophysical Research*, 86(A4):2217–2241, 1981.

[20] R. L. Lysak. Coupling of the dynamic ionosphere to auroral flux tubes. *Journal of Geophysical Research*, 91(A6):7047–7056, 1986.

[21] R. G. Roble, E. C. Ridley, and R. E. Dickinson. On the global mean structure of the thermosphere. *Journal of Geophysical Research*, 92(A8):8745–8758, 1987.

[22] J. J. Sojka. Global scale, physical models of the F-region ionosphere. *Reviews of Geophysics*, 27(3):371–403, 1989.

[23] J. R. Kan. A global magnetosphere-ionosphere coupling model of substorm. *Journal of Geophysical Research*, 98(A10):17,263–17,275, 1993.

[24] J. R. Kan. A globally integrated substorm model: Tail reconnection and magnetosphere-ionosphere coupling. *Journal of Geophysical Research*, 103(A6):11,787–11,795, 1998.

[25] M. H. Rees, D. Lummerzheim, and R. G. Roble. Modeling of the atmosphere-magnetosphere-ionosphere system MAMI. *Space Science Reviews*, 71:691–703, 1995.

[26] R. L. Lysak. Propagation of Alfvén waves through the ionosphere: Dependence on the ionospheric parameters. *Journal of Geophysical Research*, 104(A5):10,017–10,030, 1999.

[27] H. Zhu, A. Otto, D. Lummerzheim, M. H. Rees, and B. S. Lanchester. Ionosphere-magnetosphere simulation of small-scale structure and dynamics. *Journal of Geophysical Research*, 106(A2):1795–1806, 2001.

[28] B. S. Lanchester, M. H. Rees, D. Lummerzheim, A. Otto, K. J. F. Sedgemore-Schulthess, H. Zhu, and I. W. McCrea. Ohming heating as evidence for strong field-aligned currents in filamentary aurora. *Journal of Geophysical Research*, 106(A2):1785–1794, 2001.

[29] R. L. Lysak. Magnetosphere-Ionosphere coupling by Alfvén waves at mid-latitudes. *Journal of Geophysical Research*, 109(A07201):33–87, 2004.

[30] A. Yoshikawa, H. Nakata, A. Nakamizo, T. Uozumi, M. Itonaga, S. Fujita, and K. Yumoto and. Alfvénic-coupling algorithm for global and dynamical magnetosphere-ionosphere coupled system. *Journal of Geophysical Research*, 115(A04211), 2010.

[31] R. L. Lysak. Electrodynamic coupling of the magnetosphere and ionosphere. *Space Science Reviews*, 55:33–87, 1988.

[32] A. J. Zmuda, J. H. Martin, and F. T. Heuring. Transverse magnetic disturbances at 1100 kilometers in the auroral region. *Journal of Geophysical Research*, 71(21), 1966.

[33] A. J. Zmuda, J. C. Armstrong, and F. T. Heuring. Characteristics of transverse magnetic disturbances observed at 1100 kilometers in the auroral oval. 75(25), 1970.

[34] W. D. Cummings and A. J. Dessler. Field-aligned currents in the magnetosphere. *Journal of Geophysical Research*, 72(3):1007–1013, 1967.

[35] T. Iijima and T. A. Potemra. The amplitude distribution of field-aligned currents at northern high latitudes observed by Triad. *Journal of Geophysical Research*, 81(13):2165–2174, 1976.

[36] T. Iijima and T. A. Potemra. Field-aligned currents in the dayside cusp observed by Triad. *Journal of Geophysical Research*, 81(34):5971–5979, 1976.

[37] T. Iijima and T. A. Potemra. Large-scale characteristics of field-aligned currents associated with substorm. *Journal of Geophysical Research*, 83(A2):599–615, 1978.

[38] T. Iijima and. Field-aligned currents in geospace: Substance and significance. In *Magnetospheric Current System*.

[39] G. Haerendel. Field-aligned currents in the earth's magnetosphere. In *Physics of Magnetic Flux Ropes*.

[40] M. R. Lessard and D. J. Knudsen. Ionospheric reflection of small-scale Alfvén waves. *Geophysical Research Letters*, 28(18):3573–3576, 2001.

[41] H. Alfvén. On the theory of magnetic storms and aurorae. *Tellus*, 10:104–116, 1958.

[42] R. E. Ergun, L. Andersson, Y. J. Su, D. L. Newman, M. V. Goldman, W. Lotko, C. C. Chaston, and C. W. Carlson. Localized parallel electric fields associated with inertial Alfvén waves. *Physics of Plasmas*, 12(072901), 2005.

[43] D. W. Swift. A mechanism for energizing electron in the magnetosphere. *Journal of Geophysical Research*, 70:3061–3073, 1965.

[44] L. P. Block. A double layer review. *Astrophysics and Space Science*, 55(1):59–83, 1978.

[45] R. E. Ergun, C. W. Carlson, J. P. McFadden, F. S. Mozer, L. Muschietti, I. Roth, and R. J. Strangerway. Debye-scale plasma structures associated with magnetic-field-aligned electric fields. *Physical Review Letters*, 81(4):826–829, 1998.

[46] E. C. Whipple, Jr. The signature of parallel electric fields in a collisionless plasma. *Journal of Geophysical Research*, 82(10):1525–1531, 1977.

[47] S. Knight. Parallel electric fields. *Planetary and Space Science*, 21:741–750, 1973.

[48] K. Papadopoulos. A review of anomalous resistivity for the ionosphere. *Reviews of Geophysics and Space Physics*, 15(1):113–127, 1977.

[49] C. T. Russell. High altitude observations of Birkeland currents. *Annales Geophysicae*, 33(4): 435–442, 1977.

[50] L. P. Block. Three-dimensional potential structure associated with Birkeland currents. In *Magnetospheric Currents*.

[51] W. B. Lyatsky and A. M. Hamza. Possible role of magnetosphere-ionosphere coupling in auroral arc formation. *Annales Geophysicae*, 18:1108–1117, 2000.

[52] T. Sato and T. E. Holzer. Quiet auroral arcs and electrodynamic coupling between the ionosphere and the magnetosphere. *Journal of Geophysical Research*, 78(25):7314–7329, 1973.

[53] W. B. Lyatsky. Conductivity waves in the magnetosphere-ionosphere system. *Geomagn. Aeron.*, 27(25):965–970, 1987.

[54] R. L. Lysak. Feedback instability of the ionospheric resonant cavity. *Journal of Geophysical Research*, 96:1553–1568, 1991.

[55] A. Kozlovsky and W. B. Lyatsky. Instability of the magnetosphere-ionosphere convection and formation of auroral arcs. *Annales Geophysicae*, 12(25):636–641, 1994.

[56] G. T. Birk and A. Otto. A three-dimnsional plasma-neutral gas-fluid code. *Computational Physics*, 125:513–525, 1996.

[57] A. Otto. Lecture notes on fundamentals of plasma physics, 2013. URL `http://how.gi.alaska.edu/ao/plasma/index.html`.

[58] M. G. Kivelson. Physics of space plasmas. In *Introduction to Space Physics*.

[59] C. A. J. Fletcher. *Computational Techniques for Fluid Dynamics*. Springer, 1991.

[60] R. Courant, R. K. Friedrichs, and H. Lewy. On the partial differential equations of mathematical physics. *IBM Journal of Research and Developement*, 11:215–234, 1967.

[61] A. Otto. Lecture notes on methods of numerical simulation in fluids and plasmas, 2013. URL `http://how.gi.alaska.edu/ao/sim/index.html#Notes`.

[62] G. D. Smith. *Numerical solution of partial differential equations : finite difference methods*. Clarendon Press, 1985.

[63] Luciano Rezzolla. Numerical methods for the solution of partial differential equations, September 2011. URL `http://www.aei.mpg.de/~rezzolla/lnotes/Evolution_Pdes/evolution_pdes_lnotes.pdf`.

[64] H. Alfvén. The existence of electromagnetic-hydrodynamic waves. *Nature*, 150:405–406, 1942.

[65] T. K. Allen, W. R. Baker, R. V. Pyle, and J. M. Wilcox. Experimental generation of plasma Alfvén waves. *Physical Review Letters*, 2(9):383–385, 1959.

[66] P. H. Jephcott. Alfvén waves in a gas discharge. *Nature*, 150:1652–1654, 1959.

[67] J. M. Wilcox, F. I. Boley, and G. L. Siscoe. Experimental study of Alfvén wave properties. *Physics of Fluids*, 3:15–19, 1960.

[68] George Parks. *Physics of Space Plasmas - an introduction*. Addision-Wesley Publishing Company, Redwood City, CA, 1991.

[69] D. J. Knudsen, M. C. Kelley, and J. F. Vickrey. Alfvén waves in the auroral ionosphere: A numerical model compared with measurements. *Journal of Geophysical Research*, 97(A1): 77–90, 1992.

[70] D. Leneman. Reflection of Alfvén waves from boundaries with different conductivities. *Physics of Plasmas*, 14(122109), 2007.

[71] M. Scholer. On the motion of artificial ion clouds in the magnetosphere. *Planetary and Space Science*, 18:977–1004, 1970.

[72] G. Le, J. A. Slavin, and R. J. Strangerway. Space technology 5 observations of the imbalance of regions 1 and 2 field-aligned currents and its implication to the cross-polar cap Pedersen currents. *Journal of Geophysical Research*, 115(A07202), 2010.

[73] J. W. Dungey. *Geophysics - the Earth's Environment*. Gordon and Breach, New York, 1963.

[74] A. J. Zmuda and J. C. Armstrong. The diurnal variation of the region with vector magnetic field changes associated with field-aligned currents. *Journal of Geophysical Research*, 79(16): 2501–2502, 1974.

[75] A. J. Zmuda and J. C. Armstrong. The diurnal flow pattern of field-aligned currents. *Journal of Geophysical Research*, 79(31):4611–4619, 1974.

[76] G. Rostoker, J. C. Armstrong, and A. J. Zmuda. Field-aligned current flow associated with intrusion of the substorm-intensified westward electrojet into the evening sector. *Journal of Geophysical Research*, 80(25):3571–3579, 1975.

[77] M. C. Kelly. *The Earth's Ionosphere*. Academic Press, INC., San Diego, California, 1989.

[78] J. W. Dungey. *Physics of the Geomagnetic Phenomena*. Academic Press, New York, 1967.

[79] M. Itonaga, A. Yoshikawa, and S. Fujita. A wave equation describing the generation of field-aligned current in the magnetosphere. *Earth Planets Space*, 52:503–507, 2000.

[80] C. K. Goertz and R. W. Boswell. Magnetosphere-ionosphere coupling. *Journal of Geophysical Research*, 84(A12):7239–7246, 1979.

[81] Y. Kamide. *Electrodynamic Processes in the Earth's Ionosphere and Magnetosphere*. Kyoto Sangyo University Press, Kyoto, Japan, 1988.

[82] P. Janhunen and A. Olsson. Auroral potential structures and current-voltage relationship : Summary of a recent results. *Physics and Chemistry of the Earth*, 26(1-3):107–111, 2001.

[83] C-G. Fälthammar. Magnetic-field aligned electric fields in a collisionless plasmas - a brief review. *Geofísica Internacional*, 43(2):225–239, 2004.

[84] H. Alfvén. On the existence of electro-magnetic-hydrodynamic waves. *Arkiv fór matematik, astronomi och fysik*, 29B(2):1–7, 1943.

[85] H. Alfvén and C-G. Fälthammar. *Cosmical Electrodynamics - Fundamental Principles*. Clarendon Press, Oxford, 1963.

[86] R. Lüst. *The Century of Space Science*. Kluwer Academic Publishers, Netherlands, 2001.

[87] C. E. McIlwain. Direct measurement of particles producing visible auroras. *Journal of Geophysical Research*, 1960.

[88] R. D. Albert. Energy and flux variations of nearly monoenergetic auroral electrons. *Journal of Geophysical Research*, 72(23):5811–5815, December 1967.

[89] D. S. Evans. The observations of a nearly monoenergetic flux of auroral electrons. *Journal of Geophysical Research (Space Physics)*, 1968.

[90] G. Haerendel, E. Rieger, A. Valenzuela, H. Foeppl, H. C. Stenbaek-Nielsen, and E. M. Wescott. The skylab barium first observations of electrostatic acceleration of barium ions into the magnetosphere. *European Space Agency*, pages 203–211, 1976.

[91] E. M. Wescott, H. C. Stenbaek-Nielsen, and T. N. Davis. The skylab barium plasma injection experiments 1. Convection observations. *Journal of Geophysical Research*, 81(25):4487–4494, 1976.

[92] H. C. Stenbaek-Nielsen, T. J. Hallinan, and E. M. Wescott. Acceleration of barium ions near 8000 km above an aurora. *Journal of Geophysical Research*, 1984.

[93] E. M. Wescott, T. J. Hallinan, H. C. Stenbaek-Nielsen, D. W. Swift, and D. D. Wallis. Rapid ray motions in barium plasma clouds and auroras. *Journal of Geophysical Research*, 1993.

[94] H. C. Stenbaek-Nielsen, E. M. Wescott, and T. J. Hallinan. Observed barium emission rates. *Journal of Geophysical Research*, 1993.

[95] A. Olsson, A. I. Eriksson, and P. Janhunen. On the current-voltage relationship in auroral breakups and westwards-travelling surges. *Annales Geophysicae*, 14:1265–1273, 1996.

[96] L. P. Block and C-G. Fälthammar. Mechanisms that may support magnetic-field-aligned electric fields in the magnetosphere. *Annales Geophysicae*, 32(1):161–174, 1976.

[97] J. E. Borovsky. Auroral arc thicknesses as predicted by various theories. *Journal of Geophysical Research*, 98(A4):6101–6138, 1993.

[98] W. Baumjohann. *Advanced Space Plasma Physics*. Imperial College Press, London, 1997.

[99] J. M. Cornwall and Y. T. Chiu. Ion distribution effects of turbulence on a kinetic auroral arc model. *Journal of Geophysical Research*, 87(A3):1517–1527, 1982.

[100] M. Temerin, K. Cerny, W. Lotko, and F. S. Mozer. Observation of double layers and solitary waves in the auroral plasma. *Physical Review Letters*, 48:1175–1179, 1982.

[101] M. Mozer and M. Temerin. Solitary waves and double layers as the source of parallel electric fields in the auroral acceleration region. In *High-Latitude Space Plasma Physics*.

[102] L. P. Block and C-G. Fälthammar. The role of magnetic-field-aligned electric fields in auroral acceleration. *Journal of Geophysical Research*, 95(A5):5877–5888, 1990.

[103] B. Hultqvist. On the production of a magnetic-field-aligned electric field by the interaction between the hot magnetospheris plasma and the cold ionosphere. *Planetary and Space Science*, 19:749–759, 1971.

[104] B. Hultqvist. Downward ion acceleration at auroral latitudes: Cause of parallel electric field. *Annales Geophysicae*, 20:1117–1136, 2002.

[105] K. Rönnmark. Auroral current-voltage relation. *Journal of Geophysical Research*, 107(A12), 2002.

[106] M. Bohm, N. Brenning, and C-G. Fälthammar. Dynamic trapping: Neutralization of positive space charge in a collisionless magnetized plasma. *Physical Review Letters*, 65(7):859–862, 1990.

[107] C. T. Elvey. Problems of auroral morphology. *Proc. Nat. Acad. Sci., Wash.*, 43:63–75, 1957.

[108] S. -I. Akasofu. Thickness of an active auroral curtain. *Journal of Atmospheric and Terrestrial Physics*, 21:287–288, 1961.

[109] J. E. Maggs and T. N. Davis. Measurements of the thicknesses of auroral structures. *Planetary and Space Science*, 16:205–209, 1968.

[110] G. Haerendel. Origin and dynamics of thin auroral arcs. *Advanced Space Research*, 23(10): 1637–1645, 1999.

[111] A. Otto and G. T. Birk. Formation of thin auroral arcs by current striation. *Geophysical Research Letters*, 20(24):2833–2836, 1993.

[112] A. Otto and G. T. Birk. Formation of thin discrete auroral arcs. In *Proceedings of the Second International Conference on Substorms*, 1994.

[113] A. L. La Belle-Hamer, A. Otto, and L. C. Lee. Magnetic reconnection in the presence of sheared flow and density asymmetry: Application to the Earth's magnetopause. *Journal of Geophysical Research*, 100(A7):11,875–11,889, 1995.

[114] P. A. Cassak and A. Otto. Scaling of the magnetic reconnection rate with symmetric shear flow. *Physics of Plasmas*, 18(074501):1–4, 2011.

[115] M. Sugiura, N. C. Maynard, W. H. Farthing, J. P. Heppner, B. G. Ledley, and L J. Cahill, Jr. Initial results on the correlation between the magnetic and electric fields observed from the DE-2 satellite in the field-aligned current regions. *Geophysical Research Letters*, 9(9): 985–988, 1982.

[116] M. Sugiura, T. Iyemori, R. A. Hoffman, N. C. Maynard, J. L. Burch, and J. D. Winningham. Relationships between field-aligned currents, electric fields, and particle precipitation as observed by Dynamics Explorer-2. In *Magnetospheric Currents*.

[117] E. Adamson, A. Otto, and K. Nykyri. 3-d mesoscale MHD simulations of a cusp-like magnetic configuration: method and first results. *Annales Geophysicae*, 29:759–770, 2011.

[118] E. Adamson, J. Büchner, and A. Otto. On the role of current dissipation in the energization of coronal bright points. *Astronomy and Astrophysics*.

[119] Magnetic reconnection: A kinetic treatment. In *Physics of the Magnetopause*.

[120] L. C. Lee. A review of magnetic reconnection: MHD models. In *Physics of the Magnetopause*.

[121] A. Otto and G. T. Birk. The dynamical evolution of small-scale auroral arc phenomena due to a resistive instability. *Journal of Geophysical Research*, 97(A6):8391–8397, 1992.

[122] M. Hesse and K. Schindler. A theoretical foundation of general magnetic reconnection. *Journal of Geophysical Research*, 93(A6):5559–5567, 1988.

[123] K. Schindler, M. Hesse, and J. Birn. General magnetic reconnectionp, arallel electric fields, and helicity. *Journal of Geophysical Research*, 93(A6):5547–5557, 1988.

[124] C. R. Stark, A. p. Cran-McGreehin, and A. N. Wright. Contributions to the magnetospheric parallel electric field. *Journal of Geophysical Research*, 116(A07216):1–13, 2011.

[125] G. Rostoker and R. Boström. A mechanism for driving the gross Birkeland current configuration in the auroral oval. *Journal of Geophysical Research*, 81(1):235–244, 1976.

[126] M. Sugino, R. Fujii, S. Nozawa, , H. J. Opgenoorth, and A. Brekke. Relative contribution of ionospheric conductivity and electric field to ionospheric current. *Journal of Geophysical Research*, 107(A10):1330–1344, 2002.

[127] Y. Kamide and W. Baumjohann. *Magnetosphere-Ionosphere Coupling*. Springer-Verlag, Berlin, 1993.

[128] P. A. Cloutier. Topical Reviews: Ionospheric effects of Birkeland currents. *Reviews of Geophysics and Space Physics*, 9(4):987–996, 1971.

[129] S. Nakano, T. Iyemori, and S. Yamashita. Net field-aligned currents controlled by the polar ionospheric conductivity. *Journal of Geophysical Research*, 107(A5), 2002.

[130] A. J. Ridley, T. I. Gombosi, and D. L. DeZeeuw. Ionospheric control of the magnetosphere: Conductance. *Annales Geophysicae*, 22:567–584, 2004.

[131] P. T. Newell, C. -I. Meng, and K. M. Lyons. Supperession of discrete aurorae by sunlight. *nature*, 381:777–767, 1996.

[132] R. Boström. Ionosphere-Magnetosphere coupling. In *Magnetospheric Physics*.

[133] N. Singh, H. Thiemann, and R. W. Schunk. Simulation of auroral current sheet equilibria and associated V-shaped potential structures. *Geophysical Research Letters*, 10(8):745–748, 1983.

[134] P. Janhunen, A. Olsson, F. S. Mozer, and H. Laakso. How does the U-shaped potential close above the acceleration region? A study using polar data. *Annales Geophysicae*, 17:1276–1283, 1999.

[135] C. E. Seyler. A mathematical model of the structure and evolution of small-scale discrete auroral arcs. *Journal of Geophysical Research*, 95(A10):17,199–17,215, 1990.

[136] G. Haerendel, S. Buchert, C. La Hoz, B. Raaf, and E. Rieger. On the proper motion of auroral arcs. *Journal of Geophysical Research*, 98(A4):6087–6099, 1993.

[137] G. Haerendel. Magnetic fractures or reconnection of type ii. In *Proceedings IAU Symposium*, number 274, 2010.

[138] H. U. Frey, G. Haerendel, D. Knudsen, S. Buchert, and O. H. Bauer. Optical and radar observations of the motion of auroral arcs. *Journal of Atmospheric and Terrestrial Physics*, 58(1-4):57–69, 1996.

[139] H. U. Frey, O. Amm, C. C. Chaston, S. Fu, , L. Juusola, , B. Lanchester, R. Nakamura, N. Østgaard, T. Sakanoi, E. Séran, D. Whiter, J. Weygand, K. Asamura, and M. Hirahara. Small and mesoscale properties of a substorm onset auroral arc. *Journal of Geophysical Research*, 115(A10209), 2010.

[140] G. T. Birk and A. Otto. On the role of macroscopic resistive instabilities in the auroral ionosphere-thermosphere system. *Advanced Space Research*, 20(6):1301–1304, 1997.

[141] G. Haerendel. Auroral particle acceleration - An example of a universal plasma process. *ESA Journal*, 4(3):197–210, 1980.